

MODEL-BASED ESTIMATION OF WIND FIELDS OVER THE OCEAN
FROM WIND SCATTERMENTS

David G. Long

A Dissertation Presented to the
FACULTY OF THE GRADUATE SCHOOL
UNIVERSITY OF SOUTHERN CALIFORNIA

In Partial Fulfillment of the
Requirements for the Degree
DOCTOR OF PHILOSOPHY
(Electrical Engineering)

January 1989

Copyright 1989 David G. Long

(document has been reformatted from the original with graphics scanned from photocopies)

MODEL-BASED ESTIMATION OF WIND FIELDS OVER THE OCEAN
FROM WIND SCATTERMENTS

David G. Long
University of Southern California
Los Angeles, California

Jan. 1989.

ABSTRACT

The traditional point-wise approach to the estimation of winds over the ocean from wind scatterometer measurements relies only on the measurements associated with a given sample point to estimate the wind at that sample point. Further, the nature of the relationship between the scatterometer measurement and the wind vector leads to non-unique estimates of the wind. A second step, known as dealiasing, is needed to select a single wind estimate. This dissertation proposes a new model-based approach to wind estimation. In this fundamentally new approach to wind estimation, the values of the parameters of a model of the wind field, based on physical principles, are estimated from the noisy scatterometer measurements, and then the wind field is computed from the estimated model parameters. The model-based approach takes advantage of the inherent correlation in the wind field between sample points to provide more accurate estimates of the wind field. This dissertation: provides proofs of the identifiability of both point-wise and model-based wind estimation from scatterometer measurements, describes the development of the wind field model, evaluates the modeling error for the wind field model, formulates the model parameter estimation problem, describes procedures for estimating the model parameters and computing the wind field estimate, and provides a detailed comparison, via simulation, of the accuracy of the estimates obtained for point-wise and model-based wind field estimation. The results indicate that the model-based approach results in significantly improved estimates of the wind field.

Portions of this Ph.D. dissertation were published in:

D. G. Long and J. M. Mendel, "Model-Based Estimation of Wind Fields over the Ocean From Scatterometer Measurements Part I: The Wind Field Model," *IEEE Transactions on Geoscience and Remote Sensing*, Vol. 28. No. 2, pp. 349-360, May 1990.

D. G. Long and J. M. Mendel, "Model-Based Estimation of Wind Fields over the Ocean From Scatterometer Measurements Part II: Estimation of the Model Parameters," *IEEE Transactions on Geoscience and Remote Sensing*, Vol. 28. No. 2, pp. 361-373, May 1990.

D. G. Long and J. M. Mendel, "Identifiability in Wind Estimation from Wind Scatterometer Measurements," *IEEE Transactions on Geoscience and Remote Sensing*, Vol. 29, No. 2, pp. 268-276, 1991.

UNIVERSITY OF SOUTHERN CALIFORNIA
THE GRADUATE SCHOOL
UNIVERSITY PARK
LOS ANGELES, CALIFORNIA 90089

This dissertation, written by

David G. Long

*under the direction of his..... Dissertation
Committee, and approved by all its members,
has been presented to and accepted by The
Graduate School, in partial fulfillment of re-
quirements for the degree of*

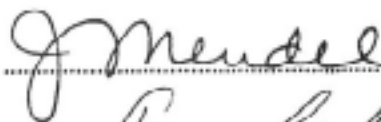
DOCTOR OF PHILOSOPHY



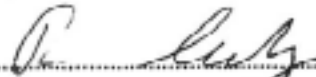
Dean of Graduate Studies

Date January 27, 1989

DISSERTATION COMMITTEE



Chairperson



Acknowledgments

Without the guidance of my advisor, Dr. Jerry Mendel, this dissertation would not have been possible. I extend my heartfelt thanks to him. I thank Dr. Mike Freilich, an oceanographer with NASA's Jet Propulsion Laboratory, for his advice and critiques of my work. He has been an inspiration to me. I am grateful to Dr. Fuk Li for his encouragement, advice, and friendship. He, too, has been an inspiration and a role model for me. I also thank Barbara Cline for her support.

Lastly, I acknowledge the support given me by my wife and family and the encouragement given by my parents, Walter and Lenna Long.

Contents

List of Figures	vii
List of Tables	x
Glossary of Symbols	xiii
1 Introduction	1
1.1 Background	1
1.2 Problem Motivation	2
1.3 Solution Approach	2
1.4 Results Summary	2
1.5 Dissertation Overview	3
2 Fundamentals of Wind Scatterometry	5
2.1 Overview	5
2.2 Ocean Winds	5
2.3 The Geophysical Model Function	6
2.3.1 The SASS ¹ Model Function	7
2.3.2 The Wentz Model Function	7
2.3.3 NSCAT Tabular Model Function	9
2.4 Wind Scatterometer Theory	9
2.4.1 The Scatterometer Measurement Process	10
2.5 Traditional Wind Estimation	13
2.5.1 Step One: Point-Wise Wind Estimation	13
2.5.2 Multiple Solutions and Ambiguity Removal	15
2.5.3 Step Two: Dealiasing (Ambiguity Removal)	20
2.6 Short-Comings of Point-Wise Wind Estimation	22
3 Identifiability in Point-Wise Wind Estimation	30
3.1 The Relationship Between σ^o and the Vector Wind	30
3.2 Identifiability of the Set D_p^c	42
3.3 Summary	50

4	Development of the Wind Field Model	51
4.1	Wind Field Model Requirements	51
4.2	Wind Field Model Assumptions	52
4.3	Model Development	54
4.4	Parameterizing the Boundary Conditions	66
4.5	Evaluating the Wind Field Model	68
4.5.1	NB Model Error	73
4.5.2	PBC Model Error	75
4.6	Conclusion	80
5	Formulating Model-Based Wind Field Estimation	81
5.1	Objective Function Formulation	81
5.2	Identifiability of the Model Parameters	83
5.3	Gradient of the Objective Function	86
5.4	Summary	89
6	Objective Function Optimization	90
6.1	Optimization Considerations	90
6.2	Field-Wise Dealiasing	91
6.3	Initial Value Computation	91
6.3.1	Point-Wise Wind Estimation	92
6.3.2	Point-Wise Dealiasing	92
6.3.3	Model Parameter Initial Value Computation	96
6.4	Gradient-Search Optimization	100
6.5	Resolution Considerations	101
6.6	Computational Considerations	101
6.7	Summary	102
7	Performance of Model-Based Wind Field Estimation	103
7.1	50 km Resolution Results Example	103
7.2	25 km Resolution Results Example	119
7.3	Summary	127
8	Conclusions and Recommendations for Future Work	134
8.1	Conclusions	134
8.2	Recommendations for Future Work	134
A	Additional Background	145
A.1	Meteorology Fundamentals	145
A.1.1	Atmospheric Thermodynamics	145
A.1.2	Turbulence	149
A.2	Oceanography Fundamentals	152
A.2.1	Wind Generated Wave Spectrum	153

A.3	Scattering Theory	155
A.3.1	The Radar Equation	156
A.3.2	Surface Scattering	158
A.3.3	Scattering Theory	159
A.4	The Geophysical Model Function	166
A.4.1	Historical Background	166
A.4.2	Wind-to-Backscatter Modeling	167
A.5	The SASS ¹ Geophysical Model Function	168
B	Detailed Derivations for Point-Wise Identifiability	170
C	The Geostrophic Equation	177
C.1	Derivation of the Geostrophic Equations	177
C.2	Divergence of the Geostrophic Wind Field	181
C.3	Curl of a Non-divergent, Isotropic Wind Field	182
D	Simulation of “Real” Mesoscale Wind Fields	186
D.1	Computation of “Realistic” Mesoscale Wind Fields	186
D.2	The Divergence and Curl of “Realistic” Mesoscale Wind Fields	187
E	Detailed Derivations for the Wind Field Model	190
E.1	Computation of K^{-1}	190
E.2	Linear Independence of the Columns of F	192
E.3	Rank of $GK^{-1} + 4I$ and $HK^{-1} - 4I$	194
F	Options for the Wind Field Model	196
F.1	Zero Vorticity, Zero Divergence Model	196
F.2	Constant Vorticity, Constant Divergence Model	197
F.3	Polynomial Vorticity and Divergence	198
F.4	Fourier Series Vorticity and Divergence	200
F.5	Isotropic Vorticity and Divergence	201
F.6	Parameterization of the Boundary Conditions	201
G	Modeling Error for Various Model Options	204
H	Simulation of the NSCAT Scatterometer	206
H.1	Instrument Measurement Simulation Model	206
H.2	Simulation Procedure	210
I	Initial Value Computation Methods	211
I.1	The Two-Dimensional Optimization Method	211
I.2	Model Extrapolation	212
I.2.1	Preliminaries	213
I.2.2	Model Parameter Vector Extrapolation	213

I.2.3	Discussion	221
-------	----------------------	-----

List of Figures

2.1	σ° versus χ for $\theta = 30^\circ$ (SASS ¹ model function, vertical polarization).	8
2.2	Diagram of the NSCAT measurement Swath	11
2.3	Plot illustrating point-wise WLS wind estimation.	17
2.4	Plot illustrating point-wise WLS wind estimation for a 0 deg true wind.	18
2.5	Plot of the J_{ML} likelihood function for 45 deg true wind.	19
2.6	Directional histogram from simulated wind retrieval — 2 alias case	23
2.7	Directional histogram from simulated wind retrieval — 3 alias case	24
2.8	Directional histogram from simulated wind retrieval — 4 alias case	25
2.9	An example of a wind field at 50 km resolution.	26
2.10	Ambiguity sets generated from simulated NSCAT σ° measurements	27
2.11	Dealiased wind field	28
2.12	Typical wind field features.	29
3.1	Illustration of multiple solutions for point-wise estimation for a true wind direction of 0°	33
3.2	Illustration of multiple solutions for point-wise estimation for a true wind direction of 45°	34
3.3	Illustration of multiple solutions for point-wise estimation for a true wind direction of 90°	35
3.4	Illustration of multiple solutions for point-wise estimation for a true wind direction of 135°	36
3.5	Illustration of multiple solutions for point-wise estimation for a true wind direction of 180°	37
3.6	The true ambiguity set map for 3 m/s wind speed and the SASS configuration with an incidence angle of 40°	38
3.7	The true ambiguity set map for 3 m/s wind speed and the SASS configuration with an incidence angle of 20°	39
3.8	The true ambiguity set map for 3 m/s wind speed, the NSCAT configuration, and an incidence angle of 40°	40
3.9	The true ambiguity set map for 3 m/s wind speed, the NSCAT configuration, and an incidence angle of 20°	41
3.10	Histogram of the directions of the aliases in the noisy ambiguity sets versus true wind direction for the SASS Configuration for an incidence angle of 40°	43

3.11	Histogram of the directions of the aliases in the noisy ambiguity sets versus true wind direction for the SASS Configuration for an incidence angle of 20°.	44
3.12	Histogram of the directions of the aliases in the noisy ambiguity sets versus true wind direction for the NSCAT Configuration for an incidence angle of 40°.	45
3.13	Histogram of the directions of the aliases in the noisy ambiguity sets versus true wind direction for the NSCAT Configuration for an incidence angle of 20°.	46
4.1	Region sampling diagram example	56
4.2	An example of a uniformly sampled wind field.	70
4.3	Best-fit “model” wind field	71
4.4	Example mesoscale wind Field.	72
6.1	An example of a simulated wind field uniformly sampled with $h = 25$ km over a 300×300 km region. A vector length equal to the sample spacing corresponds to 15 m/s.	93
6.2	The “true model” wind field resulting from fitting the PB model with $M_c = M_d = 2$ and $N = 8$ to the wind field shown in Fig. 6.1. Plotting conventions and scale are the same as in Fig. 6.1.	94
6.3	Noisy ambiguity sets resulting from point-wise estimation of the wind field in Fig. 6.1 using simulated σ^o measurements from NSCAT.	95
6.4	The result of applying the median-filter-based dealiasing algorithm described in the text to Fig. 6.3.	97
6.5	The initial value wind field computed from Fig. 6.4 (see text for explanation of computational method).	98
6.6	The wind field computed using the optimized model parameters.	99
7.1	Diagram of the model-based estimation procedure.	104
7.2	Diagram of the region segmentation scheme for the 50 km resolution example.	105
7.3	True wind field over both NSCAT observation swaths at 50 km resolution. .	107
7.4	True model field corresponding to Fig. 7.3.	108
7.5	The closest alias to the true wind vector in point-wise noisy ambiguity sets computed using simulated σ^o measurements from NSCAT. The true wind field is shown in Fig. 7.3.	109
7.6	Dealiased point-wise wind field estimate.	110
7.7	Initial value wind field computed from Fig. 7.6.	111
7.8	Optimized wind field (model-based wind field estimate) resulting from the initial value wind field in Fig. 7.7. Compare Fig. 7.3 and Fig. 7.6.	112
7.9	Enlargement of region F of the true wind field in Fig. 7.3.	120
7.10	Enlargement of region F of the dealiased wind field in Fig. 7.6.	121
7.11	Enlargement of region F of the initial value wind field in Fig. 7.7.	122
7.12	Enlargement of region F of the optimized wind field in Fig. 7.8.	123
7.13	A second 50 km resolution example of a true wind field over both NSCAT observation swaths. Plotting convention is similar to Fig. 7.3.	124

7.14	Dealiased point-wise wind field estimate corresponding to Fig. 7.12.	125
7.15	Optimized wind field (model-based wind field estimate) corresponding to Fig. 7.12.	126
7.16	A 25 km resolution example of a true wind field over both NSCAT observation swaths. Plotting convention is similar to Fig. 7.3.	128
7.17	Closest ambiguity to the true wind field in Fig. 7.15.	129
7.18	Point-wise dealiased wind field estimate corresponding to Fig. 7.15. Dealiasing was done at 25 km resolution.	130
7.19	The 50 km reference field. This field was determined by first computing the point-wise wind estimates and dealiasing at 50 km resolution. The 25 km resolution point-wise ambiguities closest to the corresponding 50 km dealiased winds are shown.	131
7.20	The 25 km resolution initial value field computed from Fig. 7.17	132
7.21	Optimized wind field (model-based wind field estimate) corresponding to Fig. 7.17.	133
A.1	Schematic diagram of a wind scatterometer.	157
D.1	Example of the vorticity of a mesoscale wind field.	188
D.2	Example of the divergence of a mesoscale wind field.	189
I.1	Diagram of two overlapping regions	214

List of Tables

2.1	$\alpha(k)$, $\beta(k)$ and $\gamma(k)$ values in the noise variance expression	12
2.2	Ambiguity set statistics.	20
4.1	Summary of the S ³ Wind measurement accuracy requirements for future space- borne wind scatterometers	52
4.2	RMS difference between the true wind field in Fig. 4.2 and the field in Fig. 4.3.	69
4.3	Wind-field-model error for the NB model, with $M_c = M_d = 2$, as a function of N for simulated mesoscale wind fields.	73
4.4	NB-model Error for $N = 8$, versus M_c and M_d	74
4.5	NB-model Error for $N = 12$, versus M_c and M_d	76
4.6	PBC-model Error for $N = 8$ and $M_c = M_d = 2$, versus M_l	77
4.7	PBC-model error, with $M_l = 8$ and $M_c = M_d = 2$, as a function of N for simulated mesoscale wind fields.	77
4.8	PBC-model Error for $N = 8$ and $M_l = 8$, versus M_c and M_d	78
4.9	PBC-model error for $N = 12$ and $M_l = 8$, versus M_c and M_d	79
6.1	Wind Field Estimate Error	100
6.2	Wind Field Model Fit Error	100
7.1	Region A (at 1,73) Wind Estimation Performance	113
7.2	Region B (at 13,73) Wind Estimation Performance	113
7.3	Region C (at 1,85) Wind Estimation Performance	113
7.4	Region D (at 13,85) Wind Estimation Performance	114
7.5	Region E (at 1,97) Wind Estimation Performance	114
7.6	Region F (at 13,97) Wind Estimation Performance	114
7.7	Region G (at 1,109) Wind Estimation Performance	115
7.8	Region H (at 13,109) Wind Estimation Performance	115
7.9	Region I (at 1,121) Wind Estimation Performance	116
7.10	Region J (at 13,121) Wind Estimation Performance	116
7.11	Region K (at 1,133) Wind Estimation Performance	117
7.12	Region L (at 13,133) Wind Estimation Performance	117
7.13	Total Wind Field Estimate Error	118
7.14	Total Wind Field Estimate Error for Example 2	119
7.15	Total Wind Field Estimate Error for the 25 km Resolution Example	127

I.1 Extrapolated vorticity coefficients for region \mathcal{L}_1 in terms of the vorticity coefficients for region \mathcal{L} 216

Glossary of Symbols

a :	<ol style="list-style-type: none"> 1. Incidence angle and polarization dependent coefficient in Wentz geophysical model function. First used in Eq. (2.3). 2. Friction coefficient. First used in Eq. (A.16). 3. Empirical constant in wave number spectrum. Used in Eq. (A.52).
$a(k)$:	Time-independent term in measurement variance expression. First used in Eq. (2.19).
a_0 :	<ol style="list-style-type: none"> 1. Radian length, $a_0 = 2\pi/L$. First used in Eq. (A.80). 2. Lowest-order coefficient in boundary polynomial parameterization. First used in Section I.1.
a_2 :	Second lowest-order coefficient in boundary polynomial parameterization. First used in Section I.1.
$a_x(x, y)$:	Component of $A(x, y)$ vector field in the x direction. First used in Eq. (C.45).
$a_y(x, y)$:	Component of $A(x, y)$ vector field in the y direction. First used in Eq. (C.45).
A :	<ol style="list-style-type: none"> 1. Target or resolution element area in radar equation. First used in Eq. (A.61). 2. Coefficient in trigonometric model function expansion. First used in Eq. (A.113).
$A(x, y)$:	General irrotational vector field. First used in Eq. (C.41).
\bar{A} :	Equivalent target or resolution element area in radar equation. First used in Eq. (A.63).
${}_1A$:	$N^2 \times N^2$ matrix. Defined in Eq. (4.61).
${}_2A$:	$N^2 \times N^2$ matrix. Defined in Eq. (4.62).

${}_3A$:	$N^2 \times N^2$ matrix. Defined in Eq. (4.63).
${}_4A$:	$N^2 \times N^2$ matrix. Defined in Eq. (4.64).
A_0 :	Term in the definition of the Wentz geophysical model function. First used in Eq. (2.2).
A_1 :	Term in the definition of the Wentz geophysical model function. First used in Eq. (2.2).
A_2 :	Term in the definition of the Wentz geophysical model function. First used in Eq. (2.2).
A_e :	Antenna effective area. First used in Eq. (A.58).
A_n :	Scattered field Fourier expansion coefficient. First used in Eq. (A.87).
$A_x(k_x, k_y)$:	Fourier coefficients of the x component of the field $A(x, y)$. First used in Eq. (C.54).
$A_y(k_x, k_y)$:	Fourier coefficients of the y component of the field $A(x, y)$. First used in Eq. (C.55).
A_f^c :	Field-wise maximum likelihood estimate set. Defined in Eq. (5.22)
A_p^c :	Point-wise maximum likelihood estimate set. Defined in Eq. (3.7)
b :	<ol style="list-style-type: none"> 1. Incidence angle and polarization dependent coefficient in Wentz geophysical model function. First used in Eq. (2.3). 2. Isotropic energy spectrum power-law coefficient. Used in Eq. (A.34). 3. Empirical constant in wave number spectrum. Used in Eq. (A.52). 3. Term in Taylor series expansion of $C(u)$. First used in Eq. (A.101).
$b(k)$:	Time-independent term in measurement variance expression. First used in Eq. (2.19).
$b(n)$:	Function of wavenumber used in space harmonic expansion. First used in Eq. (A.81).
$b_{i,j}$:	Element of the $N \times N$ matrix B . Defined in Eq. (4.20).
$b_{i,j}^r$:	Element of the $N \times N$ matrix B^r . Defined in Eq. (4.26).
$b_{i,j}^{ru}$:	Element of the $N \times N$ matrix B^{ru} . Defined in Eq. (I.1).
$b_{i,j}^u$:	Element of the $N \times N$ matrix B^u . Defined in Eq. (4.24).

$b_{i,j}^v$:	Element of the $N \times N$ matrix B^v . Defined in Eq. (4.25).
$b_x(x, y)$:	Component of $B(x, y)$ vector field in the x directiuon. First used in Eq. (C.45).
$b_y(x, y)$:	Component of $B(x, y)$ vector field in the y directiuon. First used in Eq. (C.45).
B :	<ol style="list-style-type: none"> 1. $N \times N$ matrix containing pressure field boundary conditions with elements $b_{i,j}$. First used in Eq. (4.17). 2. Coefficient in trionometric model function expansion. First used in Eq. (A.113).
$B(x, y)$:	General non-divergent vector field. First used in Eq. (C.41).
B_n :	Pertubation expansion constant. Defined in Eq. (A.84).
B^r :	$N \times N$ matrix containing part of the pressure field boundary conditions with elements $b_{i,j}^r$. First used in Eq. (4.23).
B^{ru} :	$N \times N$ matrix containing part of the pressure field boundary conditions with elements $b_{i,j}^{ru}$. First used in Eq. (I.2).
B^u :	$N \times N$ matrix containing part of the pressure field boundary conditions with elements $b_{i,j}^u$. First used in Eq. (4.23).
B^v :	$N \times N$ matrix containing part of the pressure field boundary conditions with elements $b_{i,j}^v$. First used in Eq. (4.23).
$B_x(k_x, k_y)$:	Fourier coefficients of the x component of the field $B(x, y)$. First used in Eq. (C.56).
$B_y(k_x, k_y)$:	Fourier coefficients of the y component of the field $B(x, y)$. First used in Eq. (C.57).
\overline{B} :	N^2 element vector containing lexicographic-ordered B matrix. First used in Eq. (4.30).
$\overline{\overline{B}}$:	N^2 element vector containing extrapolated \overline{B} . First used in Eq. (I.23).
c :	<ol style="list-style-type: none"> 1. Incidence angle and polarization dependent coefficient in Wentz geophysical model function. First used in Eq. (2.4). 2. Empirical constant in directional spectrum. Used in Eq. (A.53). 3. Vorticity parameter for the constant vorticity model. First used in Eq. (F.4).

$c(k)$:	Time-independent term in measurement variance expression. First used in Eq. (2.19).
$c(x, y)$:	Curl field. First used in Eq. (C.48).
$c_{m,n}$:	Coefficient of wind field vorticity model. First used in Eq. (4.9).
$\underline{c}_{m,n}$:	Coefficient of wind field vorticity model for region \mathcal{L}_1 . First used in Eq. (I.12).
C :	<ol style="list-style-type: none"> 1. $N \times N$ matrix with elements $\eta_{i,j}$ containing wind field vorticity. First used in Eq. (4.17). 2. Radar equation inversion factor. Defined in Eq. (A.61). 3. Coefficient in trionometric model function expansion. First used in Eq. (A.113).
$C(k)$:	Radar equation inversion factor for k th measurement. First used in Eq. (H.4).
$\widehat{C}(k)$:	Noisy value of radar equation inversion factor for k th measurement. First used in Eq. (H.8).
$C(u)$:	Autocorrelation of a Gaussian random surface. First used in Eq. (A.99).
$C(k_x, k_y)$:	Fourier coefficients of the curl field $c(x, y)$. First used in Eq. (C.58).
$C(\mathbf{p}, t)$:	Space-time correlation function of the ocean's surface. Defined in Eq. (A.41).
C_{Dn} :	Neutral stability drag coefficient. First used in (A.7).
$C_{Dn[10m]}$:	Neutral stability drag coefficient at an altitude of 10 m. First used in Eq. (A.9).
C_p :	Coriolis parameter. First used in Eq. (C.27).
\overline{C} :	<ol style="list-style-type: none"> 1. N^2 element vector containing the lexicographic-ordered C matrix. First used in Eq. (4.30).
\underline{C} :	<ol style="list-style-type: none"> 1. $N \times N$ vorticity field matrix for region \mathcal{L}_1. First used in Section (I.2.2). 2. Equivalent radar equation inversion factor. Defined in Eq. (A.61).
d :	<ol style="list-style-type: none"> 1. Incidence angle and polarization dependent coefficient in Wentz geophysical model function. First used in Eq. (2.4).

	2. Divergence parameter for the constant divergence model. First used in Eq. (F.4).
$d(x, y)$:	Divergence field. First used in Eq. (C.48).
$d_{m,n}$:	Coefficient of wind field divergence model. First used in Eq. (4.10).
$d_{i,j}^s$:	Elements of the D^s matrix. Defined in Eq. (4.40).
D :	<ol style="list-style-type: none"> 1. $N \times N$ matrix with elements $\delta_{i,j}$ containing wind field divergence. First used in Eq. (4.17). 2. Function used in the definition of the directional spectrum. Defined in Eq. (A.56). 3. Thickness of the region of vertical motion. First used in Eq. (C.20).
$D(k_x, k_y)$:	Fourier coefficients of the divergence field $d(x, y)$. First used in Eq. (C.59).
D^s	Unit subdiagonal $N \times N$ matrix with elements $d_{i,j}^s$. Defined in Eq. (4.41).
D_f^c :	Field-wise true ambiguity set. Defined in Eq. (5.13).
D_p^c :	Point-wise true ambiguity set. Defined in Eq. (3.1).
$D(\mathbf{K}, \omega)$:	Space-time power spectrum of the ocean's surface. Defined in Eq. (A.40).
\bar{D} :	N^2 element vector containing lexicographic-ordered D matrix. First used in Eq. (4.31).
e :	<ol style="list-style-type: none"> 1. Incidence angle and polarization dependent coefficient in Wentz geophysical model function. First used in Eq. (2.5). 2. Natural number. Used in Section A.1.
\mathbf{E}_i :	Incident electromagnetic field. First used in Section A.3.3.
\mathbf{E}_s :	Reflected electromagnetic field. First used in Eq. (A.78).
\mathbf{E}_s :	Scattered electromagnetic field. First used in Section A.3.3.
$\mathbf{E}_i(p)$:	Incident electromagnetic field with polarization p . First used in Eq. (A.72).
$\mathbf{E}_s(p)$:	Scattered electromagnetic field with polarization p . First used in Eq. (A.72).
$E(k_x, k_y)$:	Two-dimensional energy spectrum. First used in Eq. (A.25).
$\hat{E}(k)$:	One-dimensional isotropic energy spectrum. First used in Eq. (A.30).

$E[\cdot]$:	Expectation operator. First used in Eq. (2.12).
f :	<ol style="list-style-type: none"> 1. Incidence angle and polarization dependent coefficient in Wentz geophysical model function. First used in Eq. (2.5). 2. Coriolis parameter. First used in Eq. (4.6).
$f_{i,j}$:	Element of the matrix \mathcal{F} . Defined in Eq. (4.101).
$f'_{i,j}$:	Element of the matrix \mathcal{F}' . Defined in Eq. (F.42).
F :	<ol style="list-style-type: none"> 1. $2N^2 \times (4N - 2)$ model matrix. First used in Eq. (4.68). 2. $2N^2 \times N_u$ wind field model matrix (augmented form of definition 1). First used in Eq. (4.101).
F_1 :	$2N^2 \times (N - 1)$ matrix used to construct F matrix. First used in Eq. (4.69).
F'_1 :	$2N^2 \times N$ matrix used to construct \mathcal{F} matrix. First used in Eq. (4.98).
F_2 :	$2N^2 \times (N - 1)$ matrix used to construct F matrix. First used in Eq. (4.69).
F_3 :	$2N^2 \times N$ matrix used to construct F matrix. First used in Eq. (4.69).
F_4 :	$2N^2 \times (N - 1)$ matrix used to construct F matrix. First used in Eq. (4.69).
F_{cd} :	$2N^2 \times 4N$ wind field model matrix. Defined in Eq. (F.8).
F_r :	$2N^2 \times (4N + 4)$ wind field model matrix. Defined in Eq. (4.91).
$F_{n,p}$:	Element of the general matrix F . First used in Eq. (5.25).
F_s :	Model matrix. First used in Section F.4.
F_u :	One-dimensional u component spectrum. First used in Eq. (A.28).
F_v :	One-dimensional v component spectrum. First used in Eq. (A.29).
F^\dagger :	Pseudo-inverse of F . First used in Eq. (4.101).
F^a :	$2N^2 \times (4N - 2 + N_c + N_d)$ model matrix. Defined in Eq. (F.22).
F_{cd}^\dagger :	$4N \times 2N^2$ pseudo-inverse of F_{cd} . First used in Eq. (F.10).
F_r^\dagger :	$(4N + 4) \times 2N^2$ pseudo-inverse of F_r . First used in Eq. (4.93).
\mathcal{F} :	<ol style="list-style-type: none"> 1. $2N^2 \times M_l$ modelling matrix with elements $f_{i,j}$. First used in Eq. (4.100).

	2. Force. First used in Eq. (C.3).
\mathcal{F}' :	$2N^2 \times M_l$ modelling matrix with elements $f'_{i,j}$. First used in Eq. (F.41).
g :	Gravitational constant. First used in Eq. (A.2).
g_* :	Modified gravitational constant. First used in Eq. (A.47).
$g(\cdot)$:	Operator for number of unknowns in polynomial. Defined in Eq. (4.106).
G :	1. $N^2 \times N^2$ block Jordan-form matrix. Defined in Eq. (4.46). 2. Antenna Gain. First used in Eq. (A.58).
\bar{G} :	1. Equivalent antenna gain used in radar equation. First used in Eq. (A.63).
$G(\theta, \chi, p)$:	Term in SASS ¹ model function definition. First used in Eq. (2.1).
h :	1. Sample grid spacing. First used in Eq. (4.11). 2. Height. First used in Eq. (A.2).
h_h^2 :	Height variance. First used in Eq. (A.99).
$h(x)$:	One-dimensional surface height as a function of x . Used in Section A.3.2.
$h(x, y)$:	Surface height as a function of x and y . Used in Section A.3.2.
\bar{h} :	Mean surface height. Defined in Eq. (A.65).
$\overline{h^2}$:	Variance of surface height. Defined in Eq. (A.66).
H :	1. $N^2 \times N^2$ block tridiagonal matrix. Defined in Eq. (4.47). 2. Scale height. Defined in Eq. (A.4).
$H(k_x, k_y)$:	Two-dimensional cross-spectrum. First used in Eq. (A.35).
$H(\theta, \chi, p)$:	Term in SASS ¹ model function definition. First used in Eq. (2.1).
$\hat{H}(k)$:	One-dimensional cross-spectrum. First used in Eq. (A.35).
\mathbf{i} :	Unit vector in the x or i direction. First used in Eq. (A.16).
I :	General identity matrix. First used in Eq. (A.43).
I_N :	$N \times N$ identity matrix. First used in Eq. (E.30).
I_{N^2} :	$N^2 \times N^2$ identity matrix. First used in Eq. (E.29).

$Im\{\cdot\}$:	Imaginary part of argument. First used in Eq. (A.36).
\mathbf{j} :	Unit vector in the y or j direction. First used in Eq. (A.16).
$J(a_0, a_1)$:	Two-dimensional PBC model-based objective function. First used in Section I.1.
$J(\bar{X})$:	Generic field-wise objective function of \bar{X} . First used in Section 6.1.
$J(\theta)$:	PBC model-based objective function as a function of angle between lowest-order boundary polynomial coefficients. First used in Section I.1.
$J_{ML}(u, v)$:	Point-wise maximum likelihood objective function. Defined in Eq. (2.23).
$J_{WLS}(u, v)$:	Point-wise weighted least-squares objective function. Defined in Eq. (2.24).
$J_f(u, v)$:	Field-wise maximum likelihood objective function for \bar{x} . Defined in Eq. (5.9).
$J_p(u, v)$:	Point-wise maximum likelihood objective function for u and v . Defined in Eq. (3.6).
k :	<ol style="list-style-type: none"> 1. Observation index. First used in Eq. (2.7). 2. Spatial spectrum wavenumber. First used in Section A.1.2.
\mathbf{k} :	Unit vector in z (vertical) direction. First used in Section 4.1.
k_x :	Wave number in the x direction. First used in Eq. (A.21).
k_y :	Wave number in the y direction. First used in Eq. (A.22).
k_z :	Wave number in the z direction. First used in Eq. (A.77).
K :	<ol style="list-style-type: none"> 1. $N^2 \times N^2$ matrix. Defined in Eq. (4.32). 2. Magnitude of the wave number vector. First used in Eq. (A.44).
\mathbf{K} :	Wave number vector. First used in Eq. (A.40).
K_1 :	$N^2 \times N^2$ matrix. First used in Eq. (E.32).
K_d :	Wave number transition threshold. First used in Eq. (A.106).
K_p :	Normalized standard deviation of σ^o measurement. Defined in Eq. (2.10).
$K_{pc}(k)$:	Normalized standard deviation of radar communication error in σ^o measurement. First used in Eq. (H.6).

$K_{pm}(k)$:	Normalized standard deviation of geophysical model error. First used in Eq. (H.3).
$K_{pr}(k)$:	Normalized standard deviation of σ^o retrieval error. First used in Eq. (H.8).
K_t :	Wave number cutoff threshold. First used in Eq. (A.52).
\widehat{K}_p :	Weighting factor for point-wise weighted least-squares objective function. Defined in Eq. (2.25).
\mathcal{K}_{-1} :	$N^2 \times N^2$ matrix used for model extrapolation in the $-j$ direction. Defined in Eq. (I.24).
\mathcal{K}_{+1} :	$N^2 \times N^2$ matrix used for model extrapolation in the $+j$ direction. Defined in Eq. (I.41).
l :	Region boundary sample index. Defined in Eq. (4.96).
$l(\overline{X})$:	Field-wise log-likelihood function for model parameter vector \overline{X} . First used in Eq. (5.7).
L :	<ol style="list-style-type: none"> 1. Scale length or characteristic length. First used in Section A.1.2. 2. Wave length. First used in Eq. (A.39).
L_n :	Number of σ^o measurements at the lexicographic index sample point n . First used in Eq. (5.7).
$L_p(u, v)$:	Point-wise log-likelihood function for u and v . Defined in Eq. (2.22).
\mathcal{L} :	Square region of interest for defining wind field model. First used in Section 4.1.
\mathcal{L}_1 :	Second region overlapping \mathcal{L} . First used in Section I.2.2.
M_c :	Wind field vorticity model order. First used in Eq. (4.9).
M_d :	Wind field divergence model order. First used in Eq. (4.10).
M_l :	Boundary polynomial model order. First used in Eq. (4.99).
M_{-1} :	$N_p \times N_p$ model parameter extrapolation matrix for the $-j$ direction. First used in Eq. (I.31).
M_{+1} :	$N_p \times N_p$ model parameter extrapolation matrix for the $+j$ direction. First used in Eq. (I.46).
M_{-1}^{bb} :	$M_l \times M_l$ extrapolation matrix for the $-j$ direction. Defined in Eq. (I.33).

M_{+1}^{bb} :	$M_l \times M_l$ extrapolation matrix for the $+j$ direction. Defined in Eq. (I.48).
M_{-1}^{bc} :	$M_l \times N_c$ extrapolation matrix for the $-j$ direction. Defined in Eq. (I.34).
M_{+1}^{bc} :	$M_l \times N_c$ extrapolation matrix for the $+j$ direction. Defined in Eq. (I.49).
M_{-1}^{cc} :	$N_c \times N_c$ extrapolation matrix for the $-j$ direction. Defined in Eq. (I.35).
M_{+1}^{cc} :	$N_c \times N_c$ extrapolation matrix for the $+j$ direction. Defined in Eq. (I.50).
M_{-1}^{dd} :	$N_d \times N_d$ extrapolation matrix for the $-j$ direction. Defined in Eq. (I.36).
M_{+1}^{dd} :	$N_d \times N_d$ extrapolation matrix for the $+j$ direction. Defined in Eq. (I.51).
\mathcal{M} :	Geophysical model function relating wind and radar backscatter.
$\mathcal{M}\{(u, v), k\}$:	Geophysical model function relating the wind vector (u, v) to σ° at the observation angle k . First used in Eq. (2.7).
\mathcal{M}' :	Modified geophysical model function relating wind and radar backscatter.
$\mathcal{M}'\{(u, v), k\}$:	Modified geophysical model function relating the wind vector (u, v) to σ° at the observation angle k . Defined in Eq. (2.14).
n :	Lexicographic index corresponding to i, j . $n = (j + 1)N + i$.
\bar{n} :	Unit normal vector. First used in Eq. (A.73).
N :	Size, in samples, of region of interest. First used in Section 4.3.
N_c :	Number of parameters in polynomial vorticity model. $N_c = (M_c + 1)(M_c + 2)/2$. First used in Section 4.3.
N_d :	Number of parameters in polynomial divergence model. $N_d = (M_d + 1)(M_d + 2)/2$. First used in Section 4.3.
N_p :	<ol style="list-style-type: none"> 1. Number of transmit pulses integrated into one observation of σ°. Used in Section 2.4.1. 2. Number of unknowns in the PBC wind field model. First used in Section I.2.2.
N_s :	Number of vectors in the set $\{\mathbf{U}_1, \mathbf{U}_2, \dots, \mathbf{U}_{N_s}\}$. First used in Eq. (6.1).
N_u :	Number of unknowns in wind field model. First used in Eq. (4.106).
$O(\cdot)$:	Order-of operator. First used in Eq. (C.9).

p :	<ol style="list-style-type: none"> 1. Polarization indicator in model function. First used in Eq. (2.1). 2. Geostrophic pressure field. First used in Eq. (4.6). 3. Magnitude of the vector \mathbf{p}. First used in Eq. (A.95).
\mathbf{p} :	Position vector. First used in Eq. (A.40).
p' :	Horizontal pressure gradient. First used in Eq. (C.22).
\mathbf{p}' :	Position vector. First used in Eq. (A.46).
$\bar{\mathbf{p}}$:	Unit vector in the direction of \mathbf{p} . First used in Eq. (A.95).
$p(k)$:	Polarization of k th observation of σ° . First used in Eq. (3.2).
$p(h_x)$:	Probability density of a Gaussian surface. First used in Eq. (110).
$p(l)$:	Pressure field along region boundary. First used in Section 4.4.
$p'(r, \theta, \phi)$:	Pressure field resulting from fluid motion. First used in Eq. (C.14).
p_l :	Pressure field along region boundary. Shorthand for $p(l)$. First used in Section 4.4.
$p_{i,j}$:	Value of pressure field at (i, j) . First used in Eq. (4.20).
$p_s(r)$:	Pressure field which exist without fluid motion. First Used in Eq. (C.14).
P :	<ol style="list-style-type: none"> 1. $N \times N$ matrix containing sampled pressure field with elements $p_{i,j} = \psi_{i,j}$. First used in Eq. (4.17). 2. Wave Period. First used in Eq. (A.39).
$P(n)$:	Fourier series coefficients for a periodic surface. First used in Eq. (A.79).
P_n :	Radar noise-only power. First used in Eq. (H.7).
P_r :	Received radar power. First used in Eq. (A.59).
$P_r(k)$:	True received signal power for the k th measurement. Defined in Eq. (H.4).
$\widehat{P}_r(k)$:	Noisy value of received signal power for the k th measurement. Defined in Eq. (H.5).
P_t :	Transmitted radar power. First used in Eq. (A.59).
\bar{P} :	N^2 element vector containing lexicographic-ordered P matrix. First used in Eq. (4.30).

\underline{P} :	$N \times N$ pressure field matrix for region \mathcal{L}_1 . Defined in Eq. (I.7).
\overline{P} :	N^2 element vector of lexicographic-ordered pressure field of region \mathcal{L}_1 . Defined in Eq. (I.9).
$q_{i,j}$:	Element of the $N \times N$ matrix Q . First used in Eq. (4.19).
$q_{i,j}^{-1}$:	Element of the $N \times N$ inverse matrix Q^{-1} . First used in Eq. (E.6).
${}_k q_{m,n}$:	Element of the vector $Q_{m,n}$. Defined in Eq. (4.82).
${}_k q_m^c$:	Element of the vector Q_m^c . Defined in Eq. (F.34).
${}_k q_m^s$:	Element of the vector Q_m^s . Defined in Eq. (F.33).
${}_k q_{m,n}^c$:	Element of the vector $Q_{m,n}^c$. Defined in Eq. (F.28).
${}_k q_{m,n}^s$:	Element of the vector $Q_{m,n}^s$. Defined in Eq. (F.27).
Q :	$N \times N$ matrix with elements $q_{i,j}$. First used in Eq. (4.17).
Q_1 :	$N \times N$ matrix. First used in Eq. (E.32).
Q_d :	Energy dissipation in the energy transport equation. First used in Eq. (A.48).
Q_i :	Input energy due to surface winds in the energy transport equation. First used in Eq. (A.48).
$Q_{m,n}$:	N^2 vector with elements ${}_k q_{m,n}$. First used in Eq. (4.80).
Q_n :	Energy exchange in the energy transport equation. First used in Eq. (A.48).
Q_m^c :	N^2 vector with elements ${}_k q_m^c$. First used in Eq. (F.32).
Q_m^s :	N^2 vector with elements ${}_k q_m^s$. First used in Eq. (F.32).
$Q_{m,n}^c$:	N^2 vector with elements ${}_k q_{m,n}^c$. First used in Eq. (F.26).
$Q_{m,n}^s$:	N^2 vector with elements ${}_k q_{m,n}^s$. First used in Eq. (F.26).
r :	1. Distance from the earth's center. First used in Eq. (A.11). 2. Radial distance for vector in polar form. First used in Section I.1.
\mathbf{r} :	Position vector. First used in Eq. (A.73).
\mathbf{r}' :	Position vector. First used in Eq. (A.73).

r_0 :	Radius of the earth. First used in Eq. (C.31).
\bar{r} :	Unit vector in the direction of \mathbf{r} . First used in Eq. (A.73).
R :	<ol style="list-style-type: none"> 1. Gas constant. First used in Eq. (A.1). 2. Empirical function of wind speed used in directional spectrum. Defined in Eq. (A.55). 3. Distance or range of target from radar. First used in Eq. (A.59).
R_E :	Radius of the earth. First used in Eq. (A.13).
R^c :	$2N^2 \times N^2$ matrix relating wind field to curl field. First used in Eq. (4.68).
R^d :	$2N^2 \times N^2$ matrix relating wind field to divergence field. First used in Eq. (4.69).
\bar{R} :	Equivalent distance or range of target from radar. First used in Eq. (A.63).
\bar{R}^c :	$2N^2$ vector with elements \bar{R}_k^c . First used in Eq. (4.85).
\bar{R}^d :	$2N^2$ vector with elements \bar{R}_k^d . First used in Eq. (4.85).
\bar{R}_x^c :	$2N^2$ vector with elements $\bar{R}_{x_k}^c$. First used in Eq. (4.85).
\bar{R}_y^c :	$2N^2$ vector with elements $\bar{R}_{y_k}^c$. First used in Eq. (4.85).
\bar{R}_x^d :	$2N^2$ vector with elements $\bar{R}_{x_k}^d$. First used in Eq. (4.85).
\bar{R}_y^d :	$2N^2$ vector with elements $\bar{R}_{y_k}^d$. First used in Eq. (4.85).
R^{2N^2} :	$2N^2$ -dimensional space of real numbers. Used in Section 5.2.
R^{N_u} :	N_u -dimensional space of real numbers. Used in Section 5.2.
s :	Empirical constant in directional spectrum. Used in Eq. (A.53).
$s(k)$:	Modified measurement parameter. $s^2(k) = \sigma^o(k)$. Defined in Eq. (2.14).
$s_n(k)$:	Modified measurement parameter at n . $s_n^2(k) = \sigma_n^o(k)$. First used in Eq. (5.15).
$s_t(k)$:	Value of $s(k)$ corresponding to true wind vector (u_t, v_t) . Used in Section 3.2.
$s_{nt}(k)$:	Value of $s_n(k)$ corresponding to true wind at n . First used in Eq. (5.17).

S :	<ol style="list-style-type: none"> 1. $N \times N$ matrix with elements $s_{i,j} = \chi_{i,j}$. First used in Eq. (4.17). 2. A closed surface. Used in Section A.3.3.
SNR:	Measurement signal-to-noise ratio. Defined in Eq. (H.7).
S_x :	Surface x dimension length. Used in Section A.3.2.
S_y :	Surface y dimension length. Used in Section A.3.2.
S_I :	Scatterometer instrument skill. Used in Section 2.5.2.
$S(K)$:	Amplitude spectrum. First used in Eq. (A.44).
\bar{S} :	N^2 element vector containing lexicographic-ordered S matrix. First used in Eq. (4.31).
t :	Time. First used in Eq. (A.13).
$t_{i,j}$:	Elements of the matrix T . Defined in Eq. (4.48).
T :	<ol style="list-style-type: none"> 1. Length of measurement integration time. Used in Section 2.4.1. 2. $N \times N$ matrix with elements $t_{i,j}$. Defined in Eq. (4.48). 3. Temperature in degrees Kelvin. First used in Eq. (A.1).
T_g :	Length of integration time for a single transmit pulse used for measurement of σ^o . Used in Section 2.4.1.
u :	<ol style="list-style-type: none"> 1. Component of wind vector in the x or i direction. First used in Eq. (2.7). 2. Zonal component of the wind velocity. First used in Eq. (A.13). 3. Argument of autocorrelation function. First used in Eq. (A.99).
\mathbf{u} :	Wind velocity vector. First used in Eq. (C.2).
u_n :	u component of wind vector at lexicographic index n . First used in Eq. (5.4).
u_t :	u component of true wind vector. First used in Eq. (3.1).
$u_{i,j}$:	u component of wind vector at sample index (i, j) . First used in Eq. (5.2).
u_* :	Friction velocity of the wind at the ocean's surface. First used in Eq. (A.5).

\mathbf{u}_H :	Horizontal wind velocity vector. First used in Eq. (C.2).
U :	1. $N \times N$ matrix containing u -components of wind vector field. First used in Eq. (4.38). 2. Wind speed. First used in Eq. (2.1).
$U(h)$:	Wind speed profile. First used in Eq. (A.5).
U_n :	Wind speed at lexicographic index sample point n . Defined in Eq. (5.27).
\bar{U} :	N^2 element vector containing lexicographic-ordered U matrix. First used in Eq. (4.42).
$U_{12.5}$:	Wind speed at 12.5 m in a neutral stability atmosphere. First used in Eq. (A.55).
$U_{19.5}$:	Wind speed at 19.5 m in a neutral stability atmosphere. First used in Eq. (A.50).
\mathbf{U} :	Wind vector $\mathbf{U} = (u, v)^T$. First used in Section 4.2.
v :	1. Component of wind vector in the y or j direction. First used in Eq. (2.7). 2. Meridonal component of the wind velocity. First used in Eq. (A.14).
\mathbf{U}_i :	i th vector of the set $\{\mathbf{U}_1, \mathbf{U}_2, \dots, \mathbf{U}_{N_s}\}$. First used in Eq. (6.1).
\mathbf{U}_m :	Median vector. First used in Eq. (6.1).
v_n :	v component of wind vector at lexicographic index n . First used in Eq. (5.4).
v_t :	v component of true wind vector. First used in Eq. (3.1).
$v_{i,j}$:	v component of wind vector at sample index (i, j) . First used in Eq. (5.3).
V :	$N \times N$ matrix containing v -components of wind vector field. First used in Eq. (4.39).
$V(k)$:	Variance corresponding to $s(k)$. First used in Eq. (3.9).
$V_n(k)$:	Variance corresponding to $s_n(k)$. First used in Eq. (5.14).
$V_t(k)$:	True variance corresponding to $s_t(k)$. First used in Eq. (3.8).

\bar{V} :	N^2 element vector containing lexicographic-ordered V matrix. First used in Eq. (4.43).
\mathbf{V} :	Horizontal velocity vector. First used in Eq. (A.16).
$\mathbf{V}(x, y)$:	Vector velocity field. First used in Eq. (A.1.2).
\mathbf{V}_g :	Geostrophic wind velocity vector. Defined in Eq. (A.19).
w :	<ol style="list-style-type: none"> 1. Ratio of u and v components of wind. Defined in Eq. (5.30). 2. Vertical component of the wind velocity. First used in Eq. (A.15).
$w_1(k)$:	Zero-mean Gaussian random noise term associated with σ^{o2} used in σ^o measurement model. First used in Eq. (2.13).
$w_2(k)$:	Zero-mean Gaussian random noise term associated with σ^o used in σ^o measurement model. First used in Eq. (2.13).
$w_3(k)$:	Zero-mean Gaussian random noise term used in σ^o measurement model. Used in Eq. (2.13).
w_s :	Median-filter-based ambiguity removal (dealiasing) algorithm window size. First used in Section 6.3.2.
\bar{W} :	$2N^2$ element vector consisting of the concatenation of the wind field component vectors \bar{U} and \bar{V} . Defined in Eq. (4.67).
\bar{W}^b :	$2N^2$ element vector of the lexicographic wind field due only to boundary conditions. First used in Eq. (4.76).
\bar{W}^c :	$2N^2$ element vector of the lexicographic wind field due only to vorticity field. First used in Eq. (4.76).
\bar{W}^d :	$2N^2$ element vector of the lexicographic wind field due only to divergence field. First used in Eq. (4.76).
\bar{W}_t :	$2N^2$ element true wind field vector. First used in Section 4.5.
\mathbf{x} :	Unit vector in the x direction. First used in Section C.1.
x_i :	Sample index location $x_i = ih$. First used in Eq. (4.11).
x_m^c :	Coefficient of the isotropic discrete Fourier series vorticity model. First used in Eq. (F.30).
x_m^d :	Coefficient of the isotropic discrete Fourier series divergence model. First used in Eq. (F.31).

$x_{m,n}^c$:	Coefficient of the discrete Fourier series vorticity model. First used in Eq. (F.24).
$x_{m,n}^d$:	Coefficient of the discrete Fourier series divergence model. First used in Eq. (F.25).
\overline{X} :	<ol style="list-style-type: none"> 1. Lexicographic-ordered boundary conditions. Defined in Eq. (4.65). 2. General N_u-dimensional model parameter vector for polynomial boundary conditions. Defined in Eq. (4.97).
\overline{X}_{cd} :	$4N$ element vector of consisting of \overline{X} augmented by the constant vorticity and divergence model coefficients c and d . Defined in Eq. (F.7).
\overline{X}_r :	<ol style="list-style-type: none"> 1. $4N + 4$ model parameter vector. Defined in Eq. (4.92). 2. rth element of \overline{X}. First used in Eq. (5.29). 3. Augmented model parameter vector. First used in Section F.4.
\overline{X}_t :	N_u -dimensional true model parameter vector. First used in Eq. (5.13).
\overline{X}^a :	$(4N - 2 + N_c + N_d)$ -dimensional model parameter consisting of the concatenation of \overline{X} , \overline{X}^c , and \overline{X}^d . Defined in Eq. (F.21).
\overline{X}^b :	Vector consisting of concatenation of \overline{Y} , \overline{X}^c , and \overline{X}^d . Defined in Eq. (I.30).
\overline{X}^c :	N_c -dimensional vector of the vorticity polynomial coefficients. First used in Eq. (F.16).
\overline{X}^d :	N_d -dimensional vector of the divergence polynomial coefficients. First used in Eq. (F.16).
$\underline{\overline{X}}^c$:	N_c -dimensional vector of the extrapolated vorticity polynomial coefficients. First used in Eq. (I.21).
$\underline{\overline{X}}^d$:	N_d -dimensional vector of the extrapolated divergence polynomial coefficients. First used in Eq. (I.21).
\mathbf{y} :	Unit vector in the y direction. First used in Section C.1.
y_j :	Sample index location $y_j = jh$. First used in Eq. (4.13).
y_m^c :	Coefficient of the isotropic discrete Fourier series vorticity model. First used in Eq. (F.30).

y_m^d :	Coefficient of the isotropic discrete Fourier series divergence model. First used in Eq. (F.31).
$y_{m,n}^c$:	Coefficient of the discrete Fourier series vorticity model. First used in Eq. (F.24).
$y_{m,n}^d$:	Coefficient of the discrete Fourier series divergence model. First used in Eq. (F.25).
$Y(k)$:	Time-independent portion of variance corresponding to $s(k)$. First used in Eq. (3.13).
$Y_t(k)$:	True time-independent portion of variance corresponding to $s_t(k)$. First used in Eq. (3.12).
\mathbf{z} :	Unit vector in the z direction. First used in Section C.1.
$z(k)$:	Noisy measurement of $\sigma^o(k)$. Defined in Eq. (2.9).
$z_n(k)$:	Noisy measurement of $\sigma_n^o(k)$. First used in Eq. (5.6).
$Z(\omega)$:	Frequency spectrum of the ocean's surface. First used in Eq. (A.42).
Z_0 :	Surface roughness length. First used in Eq. (A.6).
Z_p :	Point-wise σ^o measurement vector. First used in Eq. (2.21).
$\alpha(k)$:	<ol style="list-style-type: none"> 1. Coefficient in K_p expression. First used in Eq. (2.11). 2. Arbitrary constant. First used in Section A.1.2.
$\alpha_1(k)$:	Term in variance expression. First used in Eq. (H.18).
α_H :	Horizontal polarization function of incidence angle. Defined in Eq. (A.93).
α_P :	Function of incidence angle for polarization P . First used in Eq. (A.92).
α_V :	Vertical polarization function of incidence angle. Defined in Eq. (A.93).
$\beta(k)$:	Coefficient in K_p expression. First used in Eq. (2.11).
$\beta_1(k)$:	Term in variance expression. First used in Eq. (H.18).
β_a :	Coefficient in power-law expansion of trigonometric expansion of model function. First used in Eq. (A.114).
β_b :	Coefficient in power-law expansion of trigonometric expansion of model function. First used in Eq. (A.115).

β_c :	Coefficient in power-law expansion of trigonometric expansion of model function. First used in Eq. (A.116).
$\gamma(k)$:	1. Coefficient in K_p expression. First used in Eq. (2.11). 2. Ratio of surface tension to water density. First used in Section A.1.2.
$\gamma_1(k)$:	Term in variance expression. First used in Eq. (H.18).
γ_a :	Coefficient in power-law expansion of trigonometric expansion of model function. First used in Eq. (A.114).
γ_b :	Coefficient in power-law expansion of trigonometric expansion of model function. First used in Eq. (A.115).
γ_c :	Coefficient in power-law expansion of trigonometric expansion of model function. First used in Eq. (A.116).
δ :	Divergence. First used in Eq. (4.2).
$\delta(x, y)$:	Divergence field. First used in Eq. (4.10).
ϵ :	1. Dielectric constant. First used in Section A.3.2. 2. Rossby number. Defined in Eq. (C.1).
ζ :	Vorticity. First used in Eq. (4.1).
$\zeta(x, y)$:	Vorticity field. First used in Eq. (4.9).
$\zeta_{i,j}$:	Vorticity field in region \mathcal{L}_1 . First used in Eq. (I.11).
η_0 :	Impedence of free space. First used in Eq. (A.73).
θ :	1. Incidence angle of radar at ocean's surface. 2. Angle of vector in polar form. First used in Section I.1.
λ :	1. Longitude. First used in Eq. (A.11). 2. Wavelength of radar. First used in Eq. (A.11).
$\lambda(k)$:	Short-hand for $\lambda_{k,k}$. First used in Eq. (E.8).
$\lambda^q(k)$:	Element of main diagonal of the matrix Λ^q and an eigenvalue of the Q matrix. First used in Eq. (E.8).
$\lambda^{K^{-1}}(k)$:	Eigen value of the matrix K^{-1} . First used in Eq. (E.10).
$\lambda_{k,k}^{K^{-1}}$:	Eigen value of the matrix K^{-1} . First used in Eq. (E.10).

$\lambda_{k,k}$:	Eigenvalue of the K matrix and a diagonal element of the matrix Λ . Defined in Eq. (E.8).
Λ :	$N^2 \times N^2$ diagonal matrix with diagonal elements $\lambda_{k,k}$. First used in Eq. (E.7).
Λ^q :	$N \times N$ diagonal matrix. Defined in Eq. (E.5).
$\nu(k)$:	$\sigma^o(k)$ measurement noise. First used in Eq. (2.9).
$\nu_1(k)$:	Normal random variable. First used in Eq. (H.3).
$\nu_2(k)$:	Normal random variable. First used in Eq. (H.5).
$\nu_3(k)$:	Normal random variable. First used in Eq. (H.8).
ρ :	Density. First used in Eq. (A.1).
$\rho(t)$:	Normalized autocorrelation of a one-dimensional surface. Defined in Eq. (A.68).
$\rho'(r, \theta, \phi)$:	Density resulting from fluid motion. First used in Eq. (C.15).
ρ_s :	Atmospheric density. First used in Eq. (4.6).
$\rho_s(r)$:	Density without fluid motion. First used in Eq. (C.15).
σ :	Standard deviation of the surface height. Defined in Eq. (A.67).
σ^o :	Normalized radar backscatter. First used in Section 1.1.
σ_c^o :	Crosswind value of σ^o . First used in Eq. (A.119)
σ_d^o :	Downwind value of σ^o . First used in Eq. (A.118)
σ_u^o :	Upwind value of σ^o . First used in Eq. (A.117)
$\sigma^o(k)$:	True value of k th observation of σ^o . First used in Eq. (2.7).
$\sigma^o(\theta)$:	σ^o as a function of incidence angle θ . First used in Eq. (A.100).
$\sigma^o(\theta, \chi, p)$:	Normalized radar backscatter as a function of incidence angle, relative azimuth angle, and polarization. First used in Eq. (A.72).
$\sigma_m^o(k)$:	Value of $\sigma^o(k)$ computed from geophysical model function. Defined in Eq. (H.2).
$\sigma_q^o(\theta)$:	Large-scale scattering (σ^o) as a function of incidence angle θ . First used in Eq. (A.108).

$\sigma_s^o(\theta)$:	Small-scale scattering (σ^o) as a function of incidence angle θ . First used in Eq. (A.109).
$\sigma_H^o(\theta)$:	Horizontal polarization σ^o as a function of incidence angle θ . First used in Eq. (A.90).
$\sigma_P^o(\theta)$:	σ^o as a function of incidence angle θ for polarization P . First used in Eq. (A.92).
$\sigma_V^o(\theta)$:	Vertical polarization σ^o as a function of incidence angle θ . First used in Eq. (A.91).
$\overline{\sigma^o}$:	Equivalent σ^o used in radar equation. First used in Eq. (A.63).
τ :	<ol style="list-style-type: none"> 1. Time. First used in Eq. (A.41). 2. Time scale of motion. First used in Section C.1.
τ_{-1}^c :	$N_c \times N_c$ vorticity coefficient extrapolation matrix for $-j$ direction. First used in Eq. (I.14).
τ_{+1}^c :	$N_c \times N_c$ vorticity coefficient extrapolation matrix for $+j$ direction.
τ_{-1}^d :	$N_d \times N_d$ divergence coefficient extrapolation matrix for $-j$ direction. First used in Eq. (I.22).
τ_{+1}^d :	$N_d \times N_d$ divergence coefficient extrapolation matrix for $+j$ direction. First used in Eq. (I.51).
Υ :	$N^2 \times M_l$ matrix relating boundary polynomial coefficients to pressure field. First used in Eq. (I.3).
Υ^c :	$N^2 \times N_c$ matrix relating the polynomial coefficient vector to the vorticity field matrix. Defined in Eq. (F.17).
Υ^d :	$N^2 \times N_d$ matrix relating the polynomial coefficient vector to the divergence field matrix. Defined in Eq. (F.18).
Υ^{ru} :	$N^2 \times M_l$ matrix relating boundary polynomial coefficients to a portion of the pressure field. First used in Eq. (I.3).
Υ^u :	$N^2 \times M_l$ matrix relating boundary polynomial coefficients to pressure field. First used in Eq. (I.4).
ϕ :	<ol style="list-style-type: none"> 1. Wind direction. First used in Eq. (2.8). 2. Latitude. First used in Eq. (A.11). 3. Conservative potential. First used in Eq. (C.3).

ϕ_n :	Wind direction at lexicographic index sample point n . First used in Eq. (5.28).
Φ :	<ol style="list-style-type: none"> 1. Geopotential height. First used in Eq. (A.16). 2. Fourier Coefficient. Used in Section A.1.2.
$\Phi(\phi)$:	Directional spectrum. First used in Eq. (A.44).
$\Phi_u(k_x, k_y)$:	Two-dimensional spatial Fourier coefficient. First used in Eq. (A.21).
$\Phi_v(k_x, k_y)$:	Two-dimensional spatial Fourier coefficient. First used in Eq. (A.21).
χ :	<ol style="list-style-type: none"> 1. Relative azimuth angle between radar illumination and wind direction. See Eq. (2.8). 2. Velocity Potential. First used in Eq. (4.3).
$\chi(k)$:	Relative azimuth angle between radar illumination and wind direction for k th observation. First used in Eq. (3.2).
ψ :	<ol style="list-style-type: none"> 1. Stream function. First used in Eq. (4.3). 2. Atmospheric stability. First used in Eq. (A.5).
$\psi(k)$:	Azimuth angle of radar illumination for k th observation. First used in Eq. (3.2).
$\psi_{i,j}$	Element of the sine transformation matrix Ψ . Defined in Eq. (E.3).
Ψ :	<ol style="list-style-type: none"> 1. Azimuth angle of radar illumination. First used in Eq. (2.8). 2. $N \times N$ unitary sine transformation matrix with elements $\psi_{i,j}$. Defined in Eq. (E.3).
$\Psi(\mathbf{K})$:	Wavenumber spectrum. Defined in Eq. (A.43).
$\Psi_l(K)$:	Large-scale component of wavenumber spectrum. Defined in Eq. (A.106).
$\Psi_s(K)$:	Small-scale component of wavenumber spectrum. Defined in Eq. (A.107).
ω :	Radian frequency. First used in Eq. (A.40).
$\omega(K)$:	Dispersion relationship. Used in Section A.1.2.
Ω :	Angular velocity of rotation of the earth. First used in Section A.1.
$\mathbf{\Omega}$:	Angular velocity vector of the earth. First used in Section C.1.
\otimes :	Kronecker or right-direct product. First used in Eq. (4.32).

- $\lfloor \cdot \rfloor$: Lexicographic index operator, $\lfloor k \rfloor = \text{int}[(k - 1)/N] + 1$. First used in Eq. (4.82).
- $\lceil \cdot \rceil$: Lexicographic index operator, $\lceil k \rceil = \text{mod}(k - 1, N) + 1$. First used in Eq. (4.82).
- \dagger : Matrix pseudo-inverse. First used in Eq. (4.95).
- $\|\cdot\|_2$: L_2 norm. First used in Section 5.2.
- $\langle \cdot \rangle$: Statistical expectation. First used in Eq. (A.41).

Chapter 1

Introduction

1.1 Background

While most of the planets in our solar system have some atmosphere, the oceans of planet Earth make it one of the most unique. The oceans of the Earth work in concert with the atmosphere to control and regulate the environment. Fed by the sun, the interaction of land, ocean, and atmosphere produces the phenomenon we call weather. Meteorology is the science of studying weather. For centuries, meteorologists have struggled to understand the complexities of weather. Only in the past half century have meteorologists begun to understand weather patterns well enough to produce relatively accurate, though limited, forecasts of future weather patterns [2, 25]. One of the limitations of predicting future weather is that meteorologists do not adequately know the *current* weather [40, 74]. An accurate understanding of current weather patterns is required to predict future weather patterns. Until recently, detailed local weather conditions were available only from sparsely arrayed weather stations, ships on commercial shipping lanes and sparsely distributed ocean bouys. Meteorological conditions over large regions of the ocean have been unavailable [99].

The advent of satellites for remote sensing has improved the situation significantly. Satellite remote sensing has the potential to provide local weather conditions at an unprecedented frequency and spatial resolution [1, 36]. Such information should significantly impact our understanding of the world weather systems and improve the reliability of weather forecasting. Of primary import in the remotely sensed data, is the determination of accurate, high resolution wind fields over the ocean's surface [4, 6, 86]. Until recently such data has been unavailable. In 1978 the experimental SeaSat radar scatterometer (SASS) first demonstrated the ability to accurately infer vector winds over the ocean's surface from space [5, 13, 14, 23, 27, 37, 42, 47, 51, 106].

A wind scatterometer is an active radar remote sensing instrument which provides measurements of the normalized radar backscatter (σ^o) at Ku-band (14 GHz) of the ocean's surface [1, 38, 81, 84, 87, 102]. From these noisy measurements of σ^o , the speed and direction of the wind over the ocean's surface can be inferred using a relationship between the wind vector and σ^o , known as the "geophysical model function" [24, 91, 93, 102, 105].

The early demise of the SeaSat satellite (due to a spacecraft power failure) limited the data length from this pioneering instrument platform though SeaSat data is still being studied. The dramatic success of SASS [100] prompted NASA to design and build an advanced scatterometer known as NSCAT (for *NASA scatterometer*) for flight in the 1990's [75]. The NSCAT scatterometer offers several significant design improvements over SASS, including additional antennas and an onboard digital signal processor to permit better cell coregistration and improved resolution [30, 60, 61, 68, 66]. While the feasibility of the method is demonstrated for NSCAT, the method is applicable for other classes of scatterometers, e.g., [82].

1.2 Problem Motivation

The techniques for estimating winds developed for SASS are planned for use in processing of NSCAT data. Unfortunately, the traditional approach to wind estimation has significant limitations. Due to the nature of the geophysical model function relating σ^o and winds, the traditional technique of estimating the wind results in a non-unique estimate of the wind vector [3, 93, 109]. A second step, known as *dealiasing*, must be used to select a single vector. This latter step is typically based on *ad hoc* considerations, is error-prone, and is difficult to analyze.

The difficulties and limitations of this traditional approach have spurred interest in the development of improved techniques for estimating the wind field from the scatterometer measurements (see, for example, [43, 44]); the need for improved techniques is recognized [3, 47, 108].

1.3 Solution Approach

In this dissertation, a new estimation-theory based approach to wind field estimation is proposed; it uses a model of the underlying wind field that is based on fundamental physical principles. In this model-based approach, the scatterometer measurements of σ^o are used to estimate the parameters of the wind field model. The wind field estimate is then computed from the estimated model parameters. This approach is fundamentally different from the traditional point-wise approach to wind field estimation. Unlike the traditional approach, the proposed model-based approach takes advantage of the inherent correlation in the wind field at different sample points, giving significantly improved accuracy for the wind field estimate.

1.4 Results Summary

In this research, the feasibility of model-based wind field estimation from wind scatterometer measurements is demonstrated. As shown by simulation, the proposed model-based wind

estimation approach produces more accurate estimates of the wind field than does the traditional point-wise approach. This accuracy improvement comes at the expense of additional computation.

The specific contributions of this dissertation include: a proof of the set-wise identifiability of the point-wise wind estimate, development of a descriptive model for near-surface mesoscale wind fields, an evaluation of the model accuracy against realistic mesoscale wind fields, formulation of the estimation problem for estimating the wind field model parameters from the wind scatterometer measurements in terms of an objective function, a proof of the identifiability of the model parameters from the wind scatterometer measurements, an approach to optimization of the objective function based on a gradient-type search algorithm, computation of initial values obtained from the point-wise wind estimates, and a detailed comparison of accuracies of the wind field estimates obtained via the model-based and point-wise wind field estimation approaches. The latter result is demonstrated using simulated NSCAT measurements.

1.5 Dissertation Overview

In Chapter 2 a tutorial background in the fundamentals of wind scatterometry, including a description of the operation of a spaceborne wind scatterometer, the measurement model, and the traditional point-wise method of estimating the wind from the scatterometer measurements, is given. A discussion on the short-comings of the traditional approach is included.

In Chapter 3 a proof of the identifiability of point-wise wind estimation is given for the first time. It is shown that point-wise wind estimation is *set-wise* identifiable.

In Chapter 4 a model for mesoscale wind fields over the ocean is developed. The model is based on the geostrophic equation of wind motion and various assumptions on the wind field vorticity and divergence. The modeling error versus model order is evaluated for realistic wind fields and a model order is chosen.

In Chapter 5 a model-based approach is formulated for estimating the wind field over the entire swath simultaneously. It takes advantage of the inherent correlation in the wind at different points within the swath. Identifiability of the estimates is shown and the gradient of the model-based objective function is derived.

In Chapter 6 optimization of the model-based estimation objective function, to obtain the maximum likelihood estimate of the wind field model parameters, is considered. Various methods of optimizing the multimodal objective function are described. A gradient-based optimization approach is selected for this research. The gradient-based approach relies on the selection of suitable initial values. Various methods of computing initial values, including methods which first use a point-wise wind estimation, are considered. The limitations of these approaches are described.

In Chapter 7 the performance of the model-based wind field estimation procedure is compared against the point-wise approach. Using simulations, the accuracy of estimates of the wind field, obtained by the traditional point-wise approach to wind estimation and the

proposed model-based approach, is evaluated and compared.

Finally, in Chapter 8 conclusions are drawn and recommendations for future work are given.

The Appendixes provide additional background, detailed derivations and results, and, other supplementary information. Appendix A provides a brief tutorial on the fields of meteorology, oceanography, and electromagnetic scattering theory. Appendix B provides detailed derivations of various results required to show the set-wise identifiability of point-wise wind estimates. Appendix C summarizes the derivation of the geostrophic equation which forms the basis of the wind field model developed in this dissertation and considers properties of the geostrophic wind field. Appendix D describes how simulated mesoscale wind fields were developed for the evaluation of the wind field model. Simulated results were used due to the limited availability of suitable “real” mesoscale wind field data. Appendix E provides detailed proofs of various results required in the development of the wind field model. Appendix F describes alternate formulations considered for the wind field model. Appendix G provides detailed results for the modeling errors of various wind field modelling options. Appendix H describes the NSCAT scatterometer simulation used to generate the simulated σ^o measurements used to evaluate wind estimation accuracy. Appendix I describes alternate approaches to determining initial values to begin the gradient-search optimization.

Chapter 2

Fundamentals of Wind Scatterometry

2.1 Overview

The purpose of this chapter is to provide background in the field of wind scatterometry. Historical background and more detailed information are included in Appendix A. This chapter is organized in the following manner: Section 2 introduces the concepts related to *mesoscale wind fields* over the ocean and provides a backdrop for the interaction of winds and waves. Section 3 discusses the relationship of winds and waves to radar backscatter and describes several of the most common geophysical model functions relating wind and backscatter. Section 4 describes the operation of a wind scatterometer and describes the sampling scheme and measurement model. Section 5 describes the traditional point-wise approach for wind estimation. Section 6 discusses the short-comings of this traditional point-wise approach to wind estimation.

2.2 Ocean Winds

Meteorologists traditionally have separated the vertical and horizontal motions of the atmosphere. Vertical motions of the atmosphere are termed *updrafts* or *downdrafts* while horizontal air motions are called *winds* [104]. Meteorologists and oceanographers commonly talk about the *zonal* (east-west) and *meridional* (north-south) components of the wind velocity. Positive zonal winds are called *westerlies* (from the west) with negative zonal winds called *easterlies* (from the east). Positive and negative meridional winds are called *southerly* and *northerly*, respectively. On wind field maps, it is common to use *streamlines* to indicate the wind direction. Streamlines are arbitrarily spaced lines that are everywhere parallel to the horizontal velocity vector [104].

Horizontal motions of the planetary atmosphere are divided into a number of more or less distinct scales of motion. The definitions are not precise and depend on context. The very broadest features of the global circulation patterns, at scales comparable to oceans and continents, are termed *planetary-scale motions*. *Synoptic-scale motions*, while smaller

than planetary-scale motions, consist of weather patterns large enough to be resolved by conventional weather station sampling with stations spaced several hundred kilometers apart. Weather maps displayed on the evening news are generally synoptic-scale. What we consider daily weather is primarily associated with synoptic-scale motions. *Mesoscale motions* range in size from 10 km to 1000 km. Generally, mesoscale motions are too small to be resolved by conventional weather stations and are much less well understood. However, mesoscale motions are of prime interest in weather forecasting.

Until recently, weather forecasting relied exclusively on subjective analysis of synoptic weather charts. The development of computers permitted meteorologists to employ numerical solutions of the equations of motion in their analysis. While the numerical prediction models are far superior to earlier techniques, the lack of a complete knowledge of the current weather conditions still limit their usefulness [104]. Numerical weather prediction (NWP) modeling is based on a set of primitive equations derived from Newton's laws of motions, atmospheric continuity constraints, and the laws of thermodynamics. The measurement accuracy and spatial sampling characteristics of the initial weather conditions used to initialize the NWP models dictate the accuracy of the NWP results. Recent study results point to the improvements in forecast accuracy by use mesoscale weather data, including surface wind fields, to initialize the NWP models (see [5, 38, 43, 44, 86]). Mesoscale wind fields are also important in the study of various oceanographic, climatological, and meteorological studies [3, 35, 47, 53, 84, 107].

Early scatterometers were airborne instruments [49]. The first space-borne wind scatterometer, known as SASS, was flown on the the Seasat spacecraft in the late 1970's [29, 48, 81, 102]. SASS first demonstrated that accurate measurements of winds over the ocean could be obtained from space [47, 51, 99, 100]. NASA is currently constructing an advanced wind scatterometer, known as NSCAT, for launch in the mid 1990's [60, 61].

Since wind scatterometers are the *only* instruments which can provide vector measurements of winds under all weather conditions, they are considered an essential ingredient in future plans for Earth remote sensing instruments (e.g., NASA's Earth Remote Sensing [EOS] program) [84].

2.3 The Geophysical Model Function

As wind blows over the ocean's surface, friction between the lower layers of the atmosphere (known as the *surface boundary layer*, the top of which may be from tens to many hundreds of meters above the earth's surface), transfers energy from the wind to the ocean surface. This slows the wind flow at the surface and induces currents and waves on the ocean's surface. Wind generated waves vary in size from the smallest *capillary* waves (less than 10 cm) to very long wavelength *gravity* waves [54]. The radar backscatter of the ocean's surface is sensitive to the capillary waves generated by the air flow over the surface in a manner which makes it possible to infer the speed and direction of the wind over the ocean's surface from measurements of the radar backscatter of the surface. The relationship between the wind and the radar backscatter is known as the *geophysical model function* and will be denoted

by \mathcal{M} .

The theory of the scattering of electromagnetic (EM) radiation from the ocean’s surface is complex. The relationship between winds and radar backscatter has been widely studied [11, 24, 28, 49, 50, 62, 91, 93, 105, 108]. A brief summary and historical background on the development of the geophysical model function are given in Appendix A. In the following sections, the most widely accepted forms of the geophysical model function relating winds to radar backscatter at 14 GHz are described. These are known as the SASS¹ and the Wentz or SASS². A number of other geophysical model functions have been proposed, e.g., [91]. While the model functions differ in detail, they share a $\cos 2\chi$ dependence on wind direction (discussed below).

2.3.1 The SASS¹ Model Function

Based primarily on empirical observations of σ^o from space and from aircraft measurement, but also including the two-scale scattering theory (see Appendix A), the science working team for the SeaSat scatterometer, developed the SASS¹ model function. The SASS¹ has been the most commonly used geophysical model function. The SASS¹ model function expresses σ^o in a tabular power-law formulation known as a *G/H Table* [11, 52], i.e.,

$$\sigma^o = G(\theta, \chi, p) U^H(\theta, \chi, p) \quad (2.1)$$

where U is the wind speed, θ is the incidence angle of the microwave radiation on the ocean’s surface, χ is the relative azimuth angle between the microwave radiation and the wind direction, and p indicates the polarization of the radar.

The tabulated G and H coefficients exhibit a $\cos 2\chi$ dependence on the wind direction. Fig. 2.1 illustrates the relationship between σ^o , χ , θ , and U for SASS¹. The $\cos 2\chi$ dependence of σ^o on wind direction is evident. The SASS¹ model function has been extensively studied and evaluated (see Appendix A).

2.3.2 The Wentz Model Function

Analysis of the winds measured using the SeaSat scatterometer against conventional ship and bouy measurements has shown that the SASS¹ model function has a slight 0.5 *m/s* wind speed bias [33]. Recently, Wentz [105] proposed a variation of the model function which, although producing very similar σ^o values for given χ and θ , does not exhibit the wind speed bias. The Wentz model function, known either as the Wentz or SASS² model function, is expressed [105],

$$\sigma^o = A_0 + A_1 \cos \chi + A_2 \cos 2\chi \quad (2.2)$$

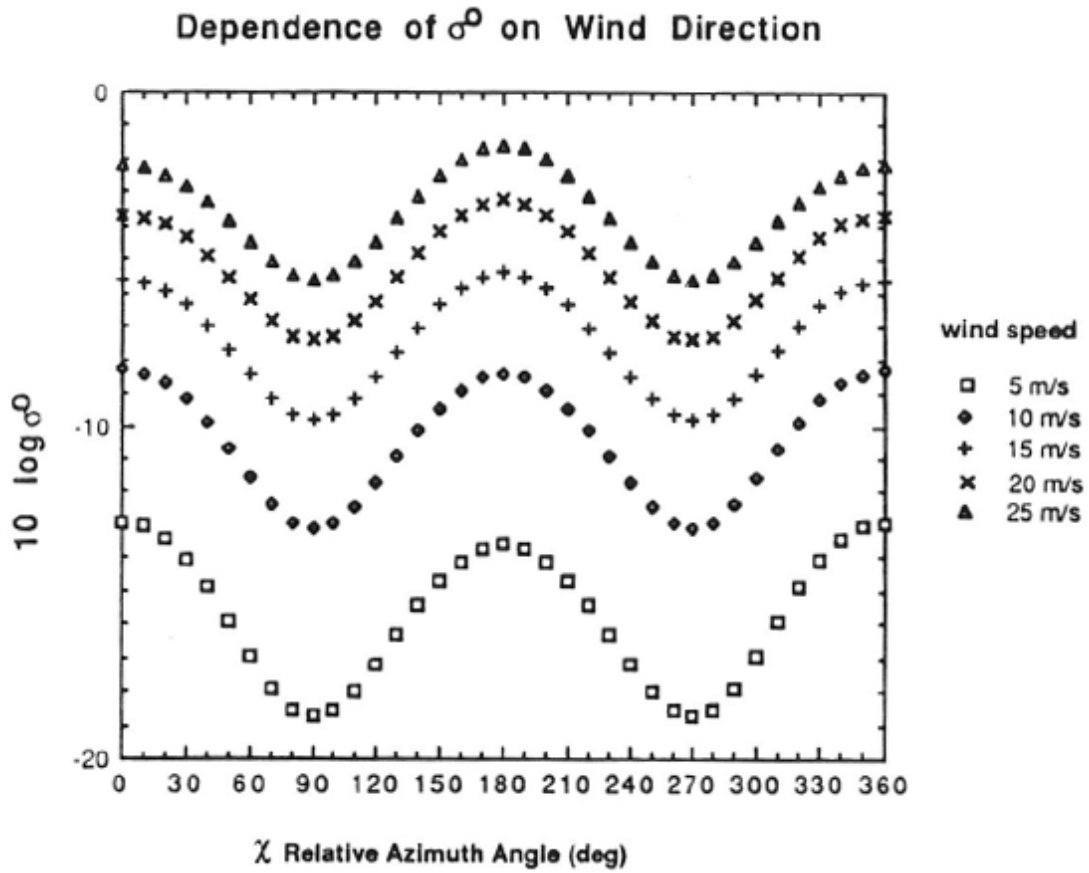


Figure 2.1: σ^o versus χ for $\theta = 30^\circ$ (SASS¹ model function, vertical polarization).

with

$$A_0 = a U^d \tag{2.3}$$

$$A_1 = A_0(b + e \log U) \tag{2.4}$$

$$A_2 = A_0(c + f \log U) \tag{2.5}$$

where a , b , c , d , e , and f are tabulated functions of incidence angle θ and polarization p . Since, in general, $A_2 \gg A_1$, the $\cos 2\chi$ dependence of σ^o on wind direction is apparent.

2.3.3 NSCAT Tabular Model Function

To provide the greatest possible processing flexibility, the NSCAT project will not be assuming that \mathcal{M} has any particular form, but will tabularize σ^o as a function of wind speed (U), relative azimuth angle (χ), incidence angle (θ), and polarization (p), i.e.,

$$\sigma^o = TAB(U, \chi, \theta, p) \tag{2.6}$$

where $TAB(U, \chi, \theta, p)$ consists of a table of values which is interpolated. The table of values is currently determined by evaluating the SASS¹ model function or the Wentz model function at the desired points in the parameter space. The hope is that later basic research into the relationship between σ^o and the wind will permit refinement of the table values. Throughout this research the NSCAT tabular form of the model function is used.

2.4 Wind Scatterometer Theory

The scatterometer does not directly measure the wind, but infers the normalized radar backscatter σ^o from noisy measurements of the radar backscatter from the ocean's surface (see Appendix A and Appendix H). Essentially, the radar scatterometer transmits a radar pulse of known power towards the ocean's surface. A portion of this power is reflected, or backscattered, toward the radar. This reflected "signal" power is measured by the scatterometer. The amount of power which is received is a function of the known radar parameters and σ^o which is a function of the wind blowing over the ocean surface. Unfortunately, the measured power is corrupted by additive noise power. A separate measurement of the noise-only power is made and subtracted from the signal+noise power measurement. This provides the measurement of the backscattered signal power. The σ^o measurement is obtained from the signal power measurement using the well-known radar equation [102]. σ^o is related to the wind by the geophysical model function \mathcal{M} .

Since \mathcal{M} has a multi-valued inverse, several measurements of σ^o from different azimuth angles must be used to determine the wind vector [102]. SASS used two fan-beam antennas on either side of the spacecraft to provide two azimuth-angle observations of each resolution element [48]. The NSCAT design will use three antennas on each side of the spacecraft to provide three azimuth-angle observations of each resolution element, or cell. NSCAT will

provide measurements of σ^o at 25 km resolution over a 600 km wide swath on either side of the spacecraft ground track as diagrammed in Fig. 2.2. Details of the SASS design may be found in [48] while the NSCAT design is described in [60, 61, 68].

The advanced NSCAT design has a number of significant advantages over the SASS design. An important difference is the uniformity of the σ^o sampling grid. The design of SASS resulted in very non-uniform sampling of σ^o (see [68]). The NSCAT design will be assumed throughout the majority of the dissertation (see Appendix H).

2.4.1 The Scatterometer Measurement Process

The wind scatterometer provides essentially instantaneous measurements of σ^o over a grid of sample points in each of the measurement swaths (refer to Fig. 2.2). For NSCAT, the sample points, or “cells”, as they are often referred to in literature, are separated by 25 km. At each sample point, noisy measurements, denoted $z(k)$, of the true σ^o , denoted $\sigma^o(k)$, are obtained for each of 3 azimuth angles. For NSCAT, the center antenna beam is dual-polarized so that there are 3 azimuth angles but four observations of σ^o ; hence, k ranges from 1 to 4 [21, 70].

$\sigma^o(k)$ is related to the wind at the sample point by the geophysical model function,

$$\sigma^o(k) = \mathcal{M}\{(u, v), k\} \quad (2.7)$$

where u and v are the components of the wind at the sample point and the k index in \mathcal{M} subsumes the dependence of σ^o on the antenna observation azimuth angle Ψ , the incidence angle θ , and polarization p . Note that the relative azimuth angle χ is

$$\chi = \Psi - \phi \quad (2.8)$$

where ϕ is the wind direction. σ^o is always positive for any wind or k .

Let us consider the measurement process for a particular azimuth angle observation k at a particular sample point. The noise model for the noisy measurement $z(k)$ of the true σ^o value may be expressed, as

$$z(k) = \sigma^o(k) + \nu(k) \quad (2.9)$$

where $\nu(k)$ is a zero mean Gaussian random variable whose variance is dependent on the true σ^o , $\sigma^o(k)$, and the time length T of the measurement [102].

A commonly accepted metric for evaluating the noise-level in the scatterometer measurement is the so-called K_p parameter [19, 34], which is defined as the normalized standard deviation of the σ^o measurement. The K_p of $z(k)$, denoted $K_p(k)$, is,

$$K_p(k) \triangleq \frac{\{Var[z(k)]\}^{1/2}}{\sigma^o(k)}. \quad (2.10)$$

The variance of the signal power measurement (and hence the σ^o measurement) is a quadratic function of $\sigma^o(k)$ [19, 34]. The variance of $z(k)$ can be expressed, as [21] (see also

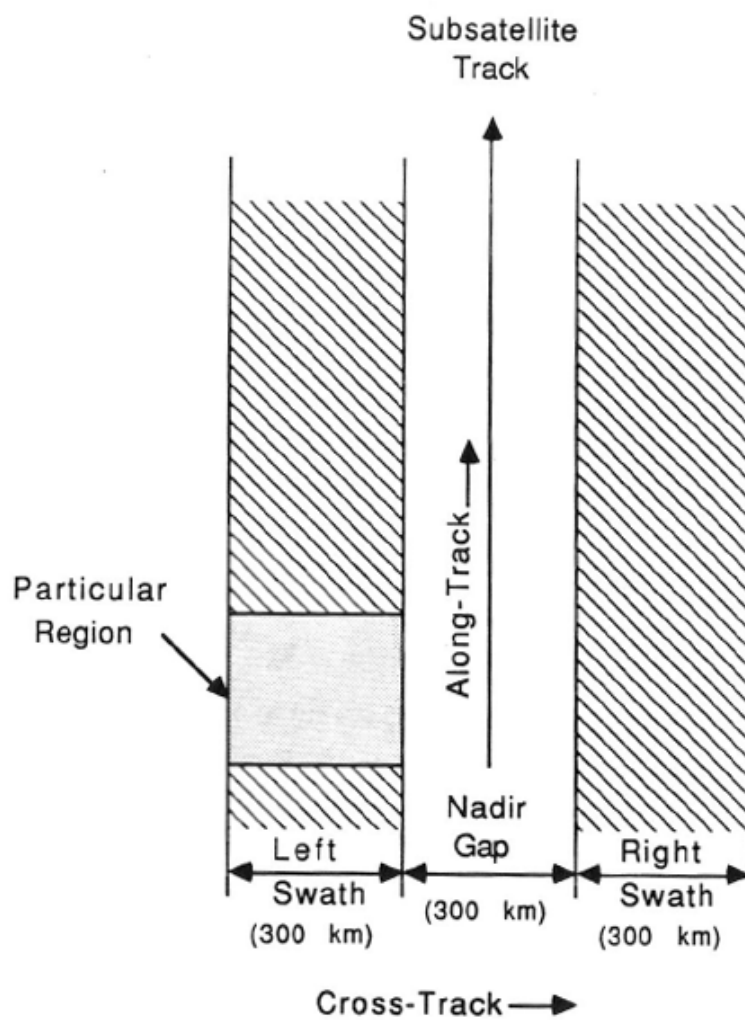


Figure 2.2: Diagram of the NSCAT measurement Swath

Appendix H)

$$\text{Var}[z(k)] = K_p^2(k)\sigma^{o2}(k) = \alpha^2(k)\sigma^{o2}(k) + \beta^2(k)\sigma^o(k) + \gamma^2(k) \quad (2.11)$$

where $\alpha(k)$, $\beta(k)$, and $\gamma(k)$ depend on the known observation azimuth angle and the length $T = N_p T_g$ of the integration, where N_p is the number of pulses summed and T_g is the energy integration period length. When only radar communication noise is considered, $\alpha(k)$, $\beta(k)$, and $\gamma(k)$ are all proportional to $1/\sqrt{T}$ (see Appendix H). We note that,

$$E[z(k)] = \sigma^o(k) \quad (2.12)$$

where $E[\cdot]$ denotes the expectation operation. Typical values for $\alpha(k)$, $\beta(k)$ and $\gamma(k)$ coefficients are shown in Table 2.1. Note that $\text{Var}[z(k)]$ can only be computed when $\sigma^o(k)$ is available and hence only when the true wind vector is known.

Table 2.1: $\alpha(k)$, $\beta(k)$ and $\gamma(k)$ values in the noise variance expression

k	Near Swath Cells			Mid Swath Cells			Far Swath Cells		
	α $\times 10^{-2}$	β $\times 10^{-3}$	γ $\times 10^{-3}$	α $\times 10^{-2}$	β $\times 10^{-5}$	γ $\times 10^{-6}$	α $\times 10^{-2}$	β $\times 10^{-5}$	γ $\times 10^{-6}$
1	4.58	1.87	1.67	4.84	7.44	1.05	5.29	6.96	4.93
2	4.80	3.08	1.48	5.04	12.5	1.76	5.18	5.12	1.88
3	4.80	3.08	1.48	5.04	12.5	1.76	5.18	5.12	1.88
4	4.57	1.87	1.67	4.84	7.44	1.05	5.31	7.40	5.21

The general noise model for the measurements may be expressed, as

$$z(k) = \sigma^o(k) + \nu(k) = \sigma^o(k)[1 + w_1(k)] + \sqrt{\sigma^o(k)}w_2(k) + w_3(k) \quad (2.13)$$

where $w_1(k)$, $w_2(k)$, and $w_3(k)$ are independent, zero mean Gaussian random variables with known variances $\alpha^2(k)$, $\beta^2(k)$, and $\gamma^2(k)$, respectively.

To simplify the notation, $s(k)$ is defined, as

$$s(k) \triangleq \sqrt{\sigma^o(k)} = \mathcal{M}\{(u, v), k\} = \sqrt{\mathcal{M}\{(u, v), k\}} \quad (2.14)$$

Using this definition, Eq. (2.13) can be written in terms of the modified measurement parameter $s(k)$, as

$$z(k) = s^2(k)[1 + w_1(k)] + s(k)w_2(k) + w_3(k) \quad (2.15)$$

Since the noise sources are independent, the mean and variance of $z(k)$ are,

$$E[z(k)] = s^2(k) \quad (2.16)$$

and

$$\text{Var}[z(k)] = \alpha^2(k)s^4(k) + \beta^2(k)s^2(k) + \gamma^2(k). \quad (2.17)$$

The conditional probability distribution of $z(k)$ given $s(k)$ is

$$p(z(k)|s(k)) = \frac{1}{\sqrt{2\pi} [\alpha^2(k)s^4(k) + \beta^2(k)s^2(k) + \gamma^2(k)]^{1/2}} \cdot \exp\left\{-\frac{1}{2}[z(k) - s^2(k)]^2/[\alpha^2(k)s^4(k) + \beta^2(k)s^2(k) + \gamma^2(k)]\right\}. \quad (2.18)$$

The measurement $z(k)$ is a random variable due to the presence of the noise. Since $\alpha^2(k)$, $\beta^2(k)$, and $\gamma^2(k)$ can be expressed, as

$$\begin{aligned} \alpha^2(k) &= \frac{1}{T}a(k) \\ \beta^2(k) &= \frac{1}{T}b(k) \\ \gamma^2(k) &= \frac{1}{T}c(k) \end{aligned} \quad (2.19)$$

where $a(k)$, $b(k)$, and $c(k)$ are positive constants that are independent of T , we see that as $T \rightarrow \infty$, $\alpha^2(k) \rightarrow 0$, $\beta^2(k) \rightarrow 0$, and $\gamma^2(k) \rightarrow 0$. This corresponds to reducing the measurement noise to zero, which is equivalent to reducing K_p . Because,

$$\text{Var}[z(k)] = \frac{1}{T} [a(k)s^4(k) + b(k)s^2(k) + c(k)] \quad (2.20)$$

is non-negative for all T , it follows that $\text{Var}[z(k)] \rightarrow 0$ as $T \rightarrow \infty$; hence, $z(k)$ converges in probability to the deterministic quantity $s^2(k) = \sigma^o(k)$. This fact will be utilized in the next chapter to show that the wind vector is identifiable from wind scatterometer measurements.

2.5 Traditional Wind Estimation

Traditionally, estimation of wind fields from wind scatterometer measurements has involved a two step process. The first step consists of point-wise estimation of the wind at each sample point. As will be shown in the next chapter, point-wise wind estimation is non-unique and a number of ambiguous solutions are produced. To resolve this ambiguity, the second step consists of various *ad hoc* schemes to select a single vector from the set of possible solutions at each sample point by examining neighboring points so that a unique wind field is produced. Each step in this process is considered in the following sections.

2.5.1 Step One: Point-Wise Wind Estimation

Historically, wind estimation (or *retrieval* as it is commonly called in wind scatterometry literature) has been done only on a point-wise basis, i.e., the relationship between adjacent sample points is ignored in the wind estimation algorithm. Only the set of σ^o measurements at each sample point is used to estimate the wind vector at that sample point.

In the traditional approach to estimating the wind at a given sample point, the wind vectors which minimize an objective function, that is formed from the σ^o measurements, are determined. The most commonly used objective functions are based on maximum-likelihood (ML) and weighted least-squares (WLS). Due to computational requirements, the WLS approach has been most commonly used, although the ML approach is considered the best [21].

The Point-Wise ML Objective Function

The ML objective function, J_{ML} , is defined as the negative of the log-likelihood function for the σ^o measurements occurring at a single measurement point. Minimization of J_{ML} must be numerically performed over the two-dimensional space of u and v (or, equivalently, wind speed and wind direction). The amount of computation required for minimization of J_{ML} is significant. This has led to the common use of the WLS algorithm. In this research, however, all point-wise results are based on the ML objective function.

To evaluate the point-wise log-likelihood function, let Z_p be the vector of σ^o measurements at a single point, i.e., $Z_p = (z(1), \dots, z(N))^T$; its elements are statistically independent. From Eq. (2.18) the conditional probability of Z_p given (u, v) is

$$p(Z_p|u, v) = \prod_k \frac{1}{\sqrt{2\pi}} \frac{1}{[\alpha^2(k)s^4(k) + \beta^2(k)s^2(k) + \gamma^2(k)]^{1/2}} \cdot \exp\left\{-\frac{1}{2}[z(k) - s^2(k)]^2/[\alpha^2(k)s^4(k) + \beta^2(k)s^2(k) + \gamma^2(k)]\right\} \quad (2.21)$$

The log-likelihood function [78] $L_p(u, v)$ is given, as

$$L_p(u, v) = \sum_k \left\{ -\frac{1}{2} \log[\alpha^2(k)s^4(k) + \beta^2(k)s^2(k) + \gamma^2(k)] - \frac{1}{2}[z(k) - s^2(k)]^2/[\alpha^2(k)s^4(k) + \beta^2(k)s^2(k) + \gamma^2(k)] \right\} \quad (2.22)$$

The ML objective function, J_{ML} , is defined, as

$$J_{ML}(u, v) \triangleq -L_p(u, v) \quad (2.23)$$

The Point-Wise WLS Objective Function

Historically, the WLS objective function, which is known as the sum-of-squares (SOS) algorithm in the wind scatterometer literature, has been the most widely used. It was used to process the SeaSat Scatterometer data set in the late 1970's. The WLS algorithm is based on the first-order approximation $\log(1 + x) \approx x$ for small x . Using this approximation, the noise model is approximately Gaussian in the log domain [21].

Using the approximate noise model and associated variance, J_{WLS} is just the weighted

least squares [21] objective function for $\log \sigma^o(k)$. The weights are $\widehat{K}_p^2(k)$; i.e.,

$$J_{WLS}(u, v) = \sum_k \left[\frac{\log z(k) - \log \sigma^o(k)}{K_p(k)} \right]^2 \quad \forall z(k) > 0 \quad (2.24)$$

where \widehat{K}_p^2 is [21]

$$\widehat{K}_p^2 \triangleq \alpha^2(k)z^2(k) + \beta^2(k)z(k) + \gamma^2(k). \quad (2.25)$$

When minimizing J_{WLS} , there is a closed form for the wind speed solution at a given wind direction ϕ , when the SASS¹ model function is used. The minimum over wind direction is evaluated numerically. Thus, minimization of J_{WLS} is essentially one dimensional and requires much less computation than minimization of J_{ML} . As a result, the WLS algorithm has been most widely used.

For large $K_p(k)$ (corresponding to low SNR), the approximations used in deriving the J_{WLS} are not very good [21]. Furthermore, when $K_p(k)$ is large, $z(k)$ can be negative. Since negative measurements [due to $\log z(k)$] can not be used, the estimated wind is biased [32].

2.5.2 Multiple Solutions and Ambiguity Removal

Due to the nature of \mathcal{M} , the point-wise wind estimation objective function J (either $J_{ML}(u, v)$ or $J_{WLS}(u, v)$) has a number of local minima and may have several global minima. In the traditional point-wise approach, all of the values of (u, v) which correspond to local minima of J are determined and used in a later step known as *dealiasing*. Collectively, the set of (u, v) vectors which maximize J will be termed the *noisy ambiguity set*. Typically, members of the noisy ambiguity set have similar wind speed but differ widely in direction. In the next chapter, the identifiability of the wind vector from the scatterometer measurements is shown. Historically, the set of wind vectors corresponding to the set of local minima of the objective function (the noisy ambiguity set) are also called the “wind retrieval” or “ambiguity” set. The members of the noisy ambiguity set are termed *ambiguities* or *aliases* [56, 59, 94, 109].

Associated with each ambiguity is the value of its objective function which can be used to rank them. The ambiguity with the smallest objective function is the 1st alias, with the rest following in sequence. Note that J often has multiple global minima so that there may be several “1st aliases”. This difficulty arises due to the harmonic nature of \mathcal{M} .

From an estimation point of view, the 1st alias(es) is (are) “the most likely”; however, since the other aliases have very similar objective functions, and due to the sinusoidal nature of the σ^o predicted by the model function, the 1st alias is not always, intuitively, the “best”. Consequently, the entire ambiguity set has been historically used as the result of the wind estimation process rather than just the 1st alias. Later processing has been used to “select” the ambiguity thought to be closest to the true wind. This last step has been termed *dealiasing* [94, 109].

To gain insight into the reasoning for why this has been done, consider the following discussion of a “typical” wind estimation situation using J_{WLS} . Similar conclusions can be

drawn using J_{ML} . Fig. 2.3 depicts curves of the possible wind speeds and directions for each of the σ^o measurements corresponding to a true wind speed of 10 m/s with a true wind direction of 45 deg. For these σ^o measurements zero noise is added. A sketch of the value of the WLS objective function J_{WLS} is also shown (see caption for detailed discussion). As is evident, there are two local minima of the objective function and thus two aliases. One alias occurs at the correct wind direction of 45 deg while the other alias occurs at 225 deg.

Some combinations of true wind direction and added noise produce additional aliases. A plot similar to the previous plot for a true wind direction of 0 degrees is shown in Fig. 2.4. Note that there are 4 local minima in the the objective function of which two are global minima. Depending on the realization of the noise up to four aliases can be produced. From these plots, the following observation can be made: the set of wind vector ambiguities can be thought of as “a correct” vector and a set of spurious vectors of similar wind speed but widely dispersed directions.

Similar statements can be made about the ML objective function J_{ML} . In fact, the number of aliases, their wind directions and speeds obtained using the ML objective function are very similar to those obtained using the WLS objective function. A plot of J_{ML} for a true wind direction of 0 deg is illustrated in Fig. 2.5.

There is no method for choosing the alias which is closest to the direction of the true wind vector, unless the closest alias is “always” the 1st alias; however, this is not always the case. Figs. 2.6, 2.7 and 2.8 give plots of directional histograms of the aliases produced by simulating scatterometer measurements at a particular sample point. The simulation was conducted by choosing a true wind speed and direction, determining the true $\sigma^o(k)$ values for each azimuth angle k , and then simulating the measurement process by adding a gaussian random value of the appropriate variance, as indicated in Eq. (2.11), to the true $\sigma^o(k)$ value. Using the ML objective function, the ambiguity set was determined. The realizations of the noise were repeated a total of 5000 times to produce 5000 ambiguity sets. The ambiguity sets were classified by the number of aliases in each set. The directional histograms for each alias in each class were produced. The true wind speed was 10 m/s and the true direction was 0 deg. The values of α , β , γ , θ , and p correspond to NSCAT at near swath. Of the 5000 realizations, none produced ambiguity sets with only one alias, 665 produced ambiguity sets with two aliases, 326 produced ambiguity sets with three aliases, and 4006 produced ambiguity sets with four aliases. For 3 realizations an ambiguity set could not be determined. Typically, the aliases are about 180 deg apart for the 2 alias case, and about 90 deg apart of the 4 alias case. The percentage of time that the 1st alias is the closest alias to the “true” wind direction of all the aliases in the ambiguity set (as determined by counting the number of times the 1st alias is the closest alias to the true for a large number of ambiguity sets generated from Monte Carlo realizations of simulated noisy σ^o measurements) is known as the scatterometer *instrument skill* and is denoted by S_I . As indicated in Table 2.2, the 1st alias is the closest alias to the true wind direction only about 53 percent of the time, i.e., the instrument skill is 53 %.

These results are typical for all true wind directions and speeds. For a true wind direction of 180 deg, the frequency histograms are essentially “flipped over” or mirrored about the 90

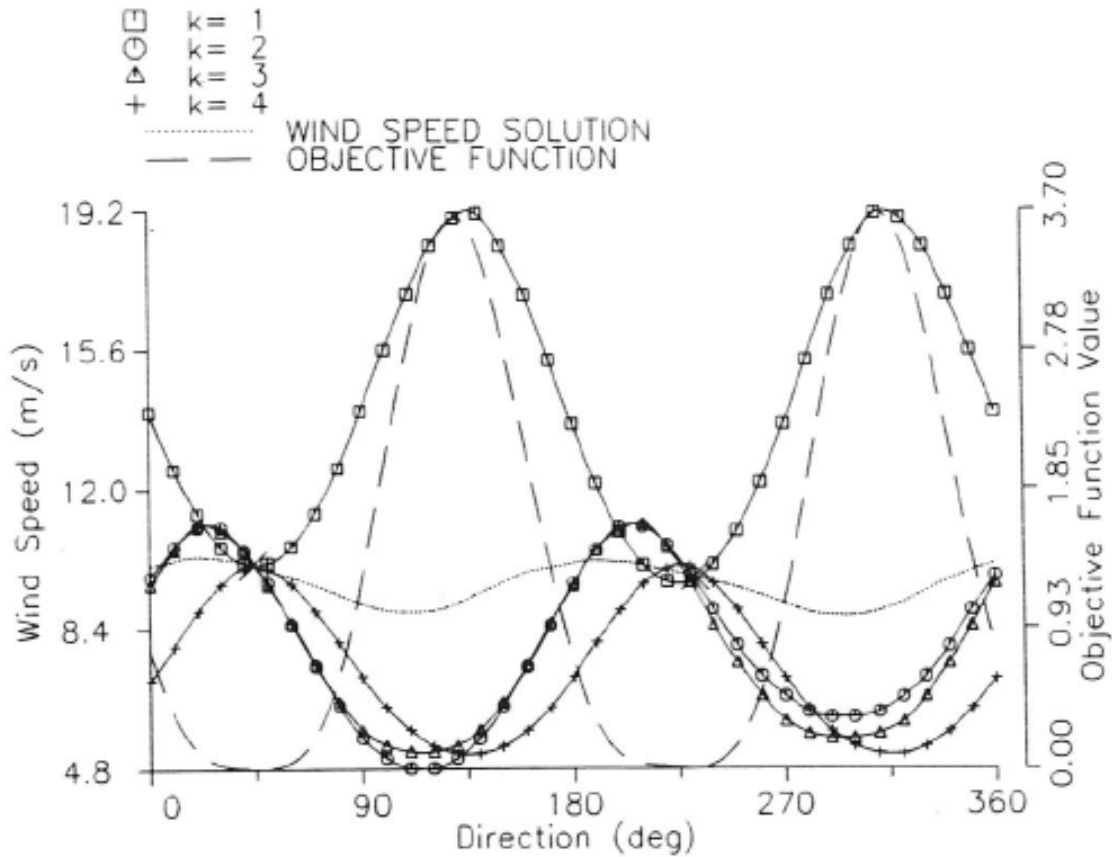


Figure 2.3: Plot illustrating point-wise WLS wind estimation. The true wind speed is 10 m/s while the true wind direction is 45 deg.

This plot was generated by computing the values of $\sigma^o(k)$ for $k = 1, 2, 3, 4$ given the known wind vector (u, v) . No noise was added, i.e., $z(k) = \sigma^o(k)$. The WLS objective function, J_{WLS} , was computed. The wind speed which minimized J_{WLS} as a function of wind direction is shown as a dotted line. The value of J_{WLS} at this minimum wind speed is plotted as a function of direction as the dashed line. Note that there are 2 global minima. The four curves with symbols (corresponding to $k = 1, 2, 3, 4$) were generated by determining the u and v for which $\mathcal{M}\{u, v, k\} = z(k)$. Note the double sinusoidal nature of these curves. J_{WLS} is minimized at the wind speeds and directions at which these four curves all intersect. For this case, this occurs at the true wind speed of 10 m/s and the true wind direction of 45 deg and again at a wind speed of 10 m/s with the wind direction of 230 deg. Intuitively, when noise is added, the σ^o curves (lines with symbols) shift vertically relative to one another. This leads to inexact intersections with spurious near-intersections possibly occurring at other wind directions (e.g., 30 and 210 deg for this case).

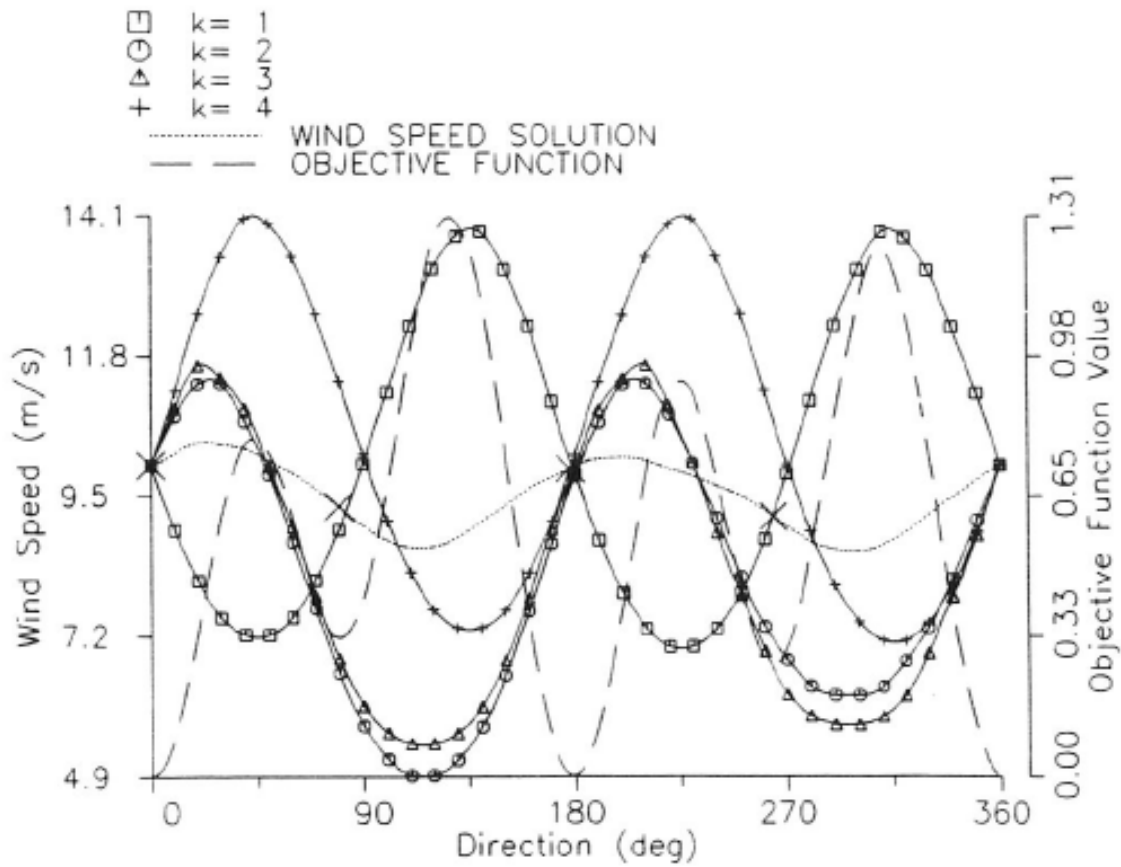


Figure 2.4: Plot illustrating point-wise WLS wind estimation for a 0 deg true wind. Refer to the caption of Fig. 2.3 for a detailed explanation about the construction and meaning of the plots.

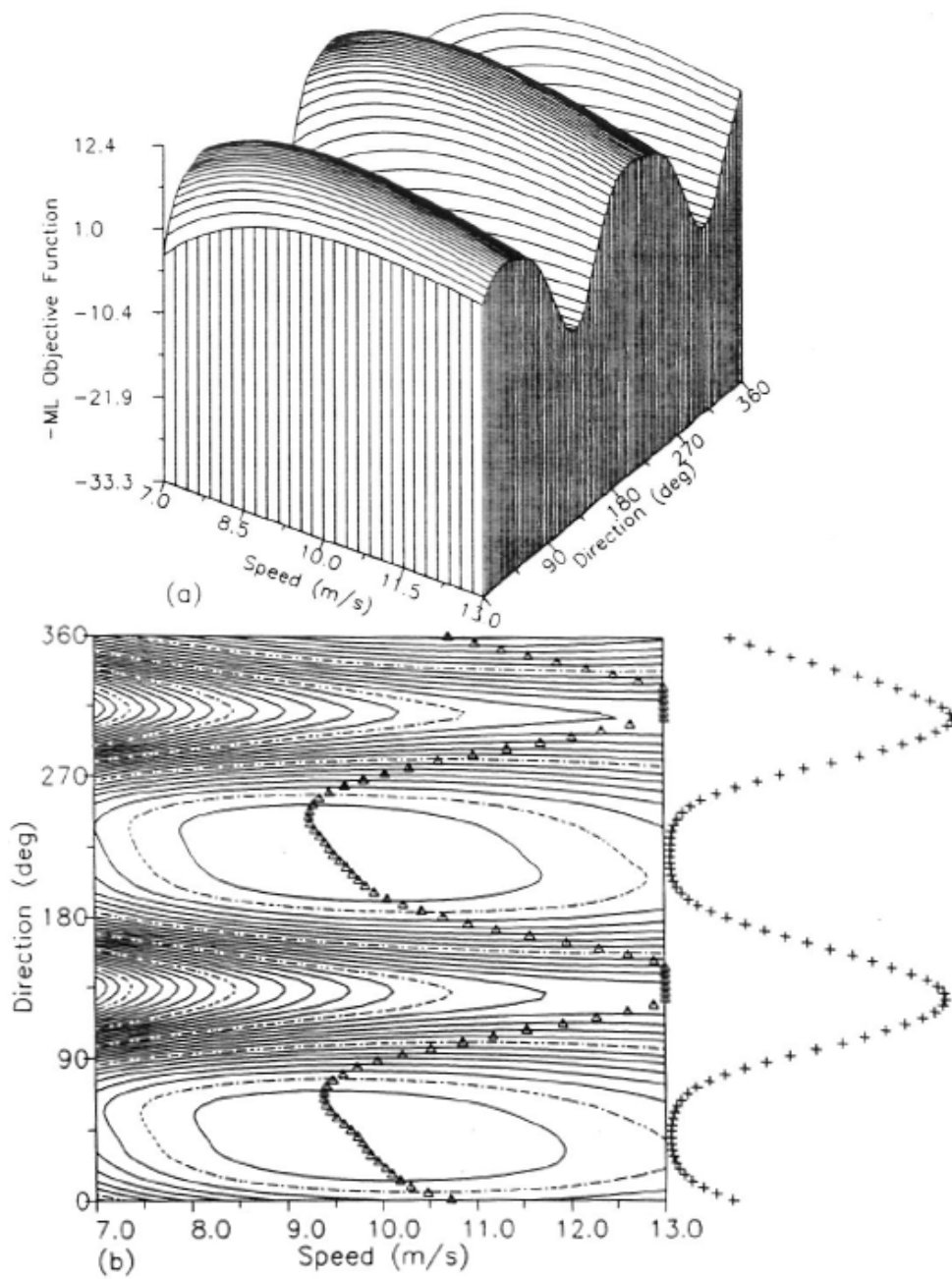


Figure 2.5: Plot of the J_{ML} likelihood function for 45 deg true wind. For clarity, a perspective plot of $-J_{ML}$ is shown in (a). The triangles on the contour plot of J_{ML} in (b) mark the trajectory of a ravine search used to find the local minima. The crosses off to the right of the plot indicate the value of the objective function along the ravine search path. The contour intervals are arbitrary.

to 270 deg line.

Table 2.2: Ambiguity set statistics.

Number of Aliases	Number of Occurrences	Number of Times the First Alias is the Closest to True Wind	Instrument Skill (%)
2	665	359	54
3	326	216	66
4	4006	2060	51
Totals	4997	2635	53

The previous observations motivated earlier experimenters to always retain all the aliases, rather than using only the “most likely” 1st alias, and, then to use later processing to “choose” the alias which corresponds to the “best” wind direction. Typically, this has been done by comparing the ambiguity sets from adjacent sample points, applying heuristic real-world constraints, and attempting to manually identify weather patterns. From this a plausible selection of one ambiguity from the ambiguity set at each sample set is determined to generate a wind vector field. This process of “dealiasing” has traditionally been done by human experts [94, 109].

This wind estimation approach is not well founded in theory and is essentially *ad hoc* in nature. It does, however, work reasonably well as computer simulations and SeaSat Scatterometer experience have demonstrated [94, 109].

2.5.3 Step Two: Dealiasing (Ambiguity Removal)

Application of point-wise wind estimation to each sample point of the wind field produces an ambiguity set at the sample points. The purpose of the “dealiasing” procedure is to select a single vector from each ambiguity set to produce a unique wind field estimate. Typically, dealiasing relies on various *ad hoc* considerations for selection of a unique wind vector. Dealiasing is error-prone.

As an illustration, Fig. 2.9 shows an example wind field. Using a simulation of NSCAT, σ^o measurements were generated and the noisy ambiguity set at each sample point was determined. The noisy ambiguity sets are shown in Fig. 2.10. The closest ambiguity to the true wind is shown as a solid vector, while the other ambiguities are shown as dotted vectors. For this example wind field, the ambiguity removal algorithm was unable to correctly select the ambiguities closest to the true wind direction. The resulting dealiased wind field, which is the point-wise wind field estimate, is shown in Fig. 2.11.

Previous work on the removal of ambiguous wind directions from scatterometer measurements has been done using SASS data [47] and simulated scatterometer data [94, 109]. Data from SASS was manually processed by a team of experts to select unambiguous wind fields in conjunction with the JASIN experiment, an intensive ocean/atmosphere study conducted

in the northeast Atlantic in 1978 [47] (see also [109]). Pattern recognition of significant meteorological wind patterns (see Fig. 2.12 [109]) was employed by researchers to aid in manual selection of the “correct” wind direction. Results indicated that “correct” wind solutions (as compared to ship and bouy measurements of the wind direction) of high quality SASS data could be selected most of the time. The manual method, however, is unsuited for an operational scatterometer (such as NSCAT) due to the amount of man-time required to process the data [47, 109].

In the early 1980’s NASA sponsored a study to develop an automated wind vector selection algorithm for a proposed scatterometer (which has since been canceled) known as NOSS [94]. The NOSS scatterometer was similar to SeaSat but had higher resolution. A computer simulation of NOSS was used to generate a number of data sets for algorithm development. Three different algorithms were developed by various organizations: the University of Wisconsin, the University of Kansas, and the Remote Sensing Systems Corporation (RSS). Developers were given a number of simulated data sets to “tune” their algorithm; then, each of the algorithms were rigorously compared using a number of independent data sets. Overall results indicated that ambiguities could be correctly removed almost all of the time when S_I was small. No study of the effects of larger S_I values was conducted. Each of the 3 approaches showed both strengths and weaknesses. A discussion of each approach follows. Additional information is given in [3] and [94].

The Wisconsin method ranked the ambiguous vectors by residual and used the very lowest residual vectors to define an initial streamline field pattern (a streamline is a line of constant wind direction). A low-pass filter was used to weight each vector ambiguity with respect to direction. The weighted ambiguity closest to the streamline was selected to feed into the next iteration of filtering and selection. The low-pass filter technique was designed to smooth the wind field and minimize the error due to incorrect ambiguity choices. Unfortunately, it also tends to smooth the resultant wind field. One advantage of this technique was the ability to extend the streamlines beyond the data swath to interpolate gaps between measurement swaths. Most errors were close to the edges of the measurement swath, indicating that the lack of data beyond the swath edge degraded performance.

The Kansas method consisted of histogram analysis, averaging, and curve fitting in a simplified pattern recognition approach. Histograms of wind speed, direction and gradient were computed over 10 by 10 processing grids. For regions of small wind variations, the lowest residual ambiguities were selected. For regions of high wind variation, a least-squares method of fitting the lowest residual ambiguities to streamlines of typical wind patterns was used. In these high variation regions the ambiguity closest to the resulting pattern was selected. The algorithm failed to select a unique vector 15% of the time with errors concentrated in large regions along the swath edges.

The RSS method selects the “mostly likely” ambiguity by minimizing both the wind direction difference and the residual between adjacent measurements. The wind direction was assumed to be correlated within 30 degrees over 50 km. Several fields which minimized the selection criteria were often produced. When this occurred, the field with the smallest total residual was selected. Performance was strongly dependent on the contents of the

wind field. The algorithm often “locked on” to vectors 180 degrees out of phase to the true direction over extended regions.

Most recently, a median filtering algorithm has been used to “de-alias” simulated NSCAT data [95, 96]. An iterative median filter is initialized by the lowest residual wind vectors. On each pass, the median vector is replaced by the ambiguity closest to the median vector. Depending on the variation of S_I , 10-20 iterations were required for convergence. This algorithm works remarkably well under most conditions, but may exhibit poor performance in regions of low wind speed and/or instrument skill. The performance of this algorithm has led to its being selected for use in processing NSCAT data. It has been used for generating the point-wise wind field estimates in this research (e.g., see Fig. 2.11). A more detailed description of the algorithm is given in Chapter 6. Only limited direct comparisons with other methods have been published [3, 96].

Recently, Hoffman [43, 44] developed a technique of assimilating the point-wise ambiguity sets into numerical weather prediction models with simultaneous dealiasing. While his research demonstrated the utility of his approach, the accuracy of the dealiasing was inconclusive.

Using Ekman boundary layer dynamics, Yu [110] developed a technique for deducing the wind direction from measurements of the wind speed over a region. He applied his technique to measurements made by both the Seasat altimeter and scatterometer. His method, however, is limited to low resolution estimates of the wind field, i.e., it does not resolve subsynoptic scale features of the wind field [110]. His method also does not use the fact that the scatterometer measurements are sensitive to the wind direction as well as wind speed.

2.6 Short-Comings of Point-Wise Wind Estimation

The traditional two-step point-wise wind estimation approach results in multiple solutions at each sample point in the first step which must be resolved by dealiasing. This second dealiasing step, which traditionally has been based either on manual methods or on various *ad hoc* considerations, is error-prone and may result in estimates of the wind field with large regions of significant directional errors, due to selection of the wrong alias. Although much research effort has been expended on the development of improved dealiasing algorithms (e.g., [3, 109]), the difficulties remain unsolved. Because of the *ad hoc* nature of the dealiasing step, error analysis of the wind estimates is difficult. Even when the dealiasing is perfect (i.e., the alias closest to the true wind direction is *always* selected), the point-wise approach often produces very noisy estimates of the wind field due to the high noise levels in the σ^o measurements. This is often resolved by spatial averaging of the resulting wind field estimates [90]; however, this reduces the spatial resolution of the results.

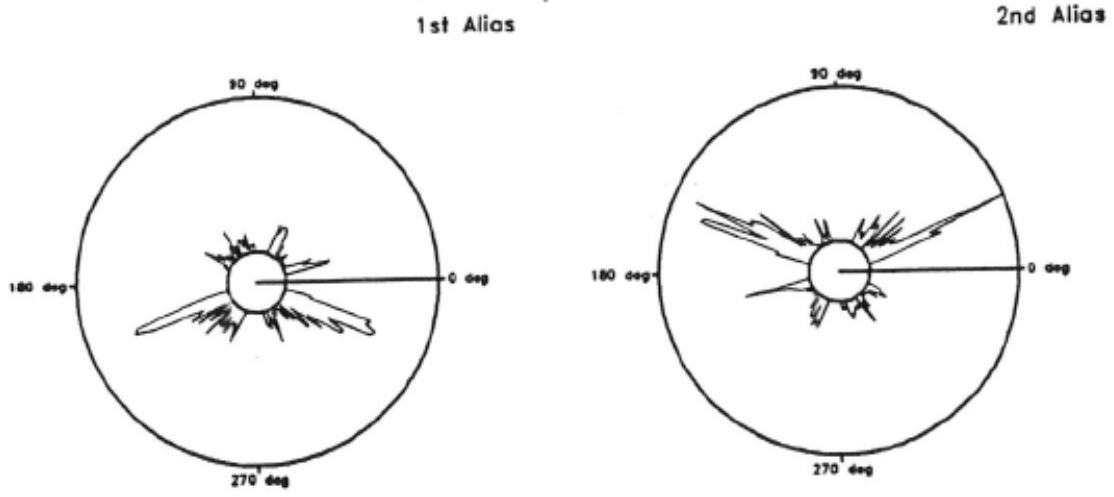


Figure 2.6: Directional histogram from simulated wind retrieval — 2 alias case

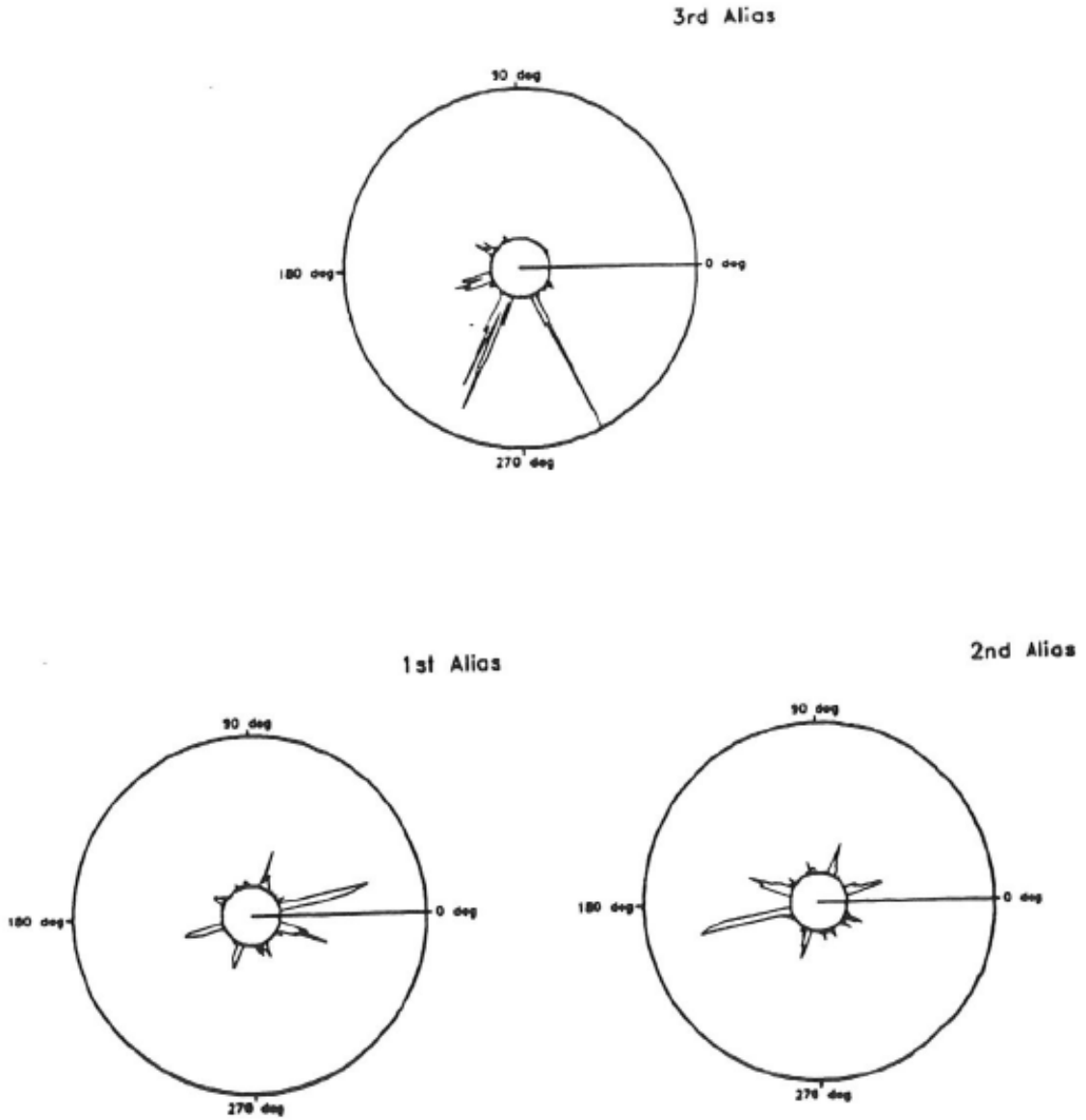


Figure 2.7: Directional histogram from simulated wind retrieval — 3 alias case

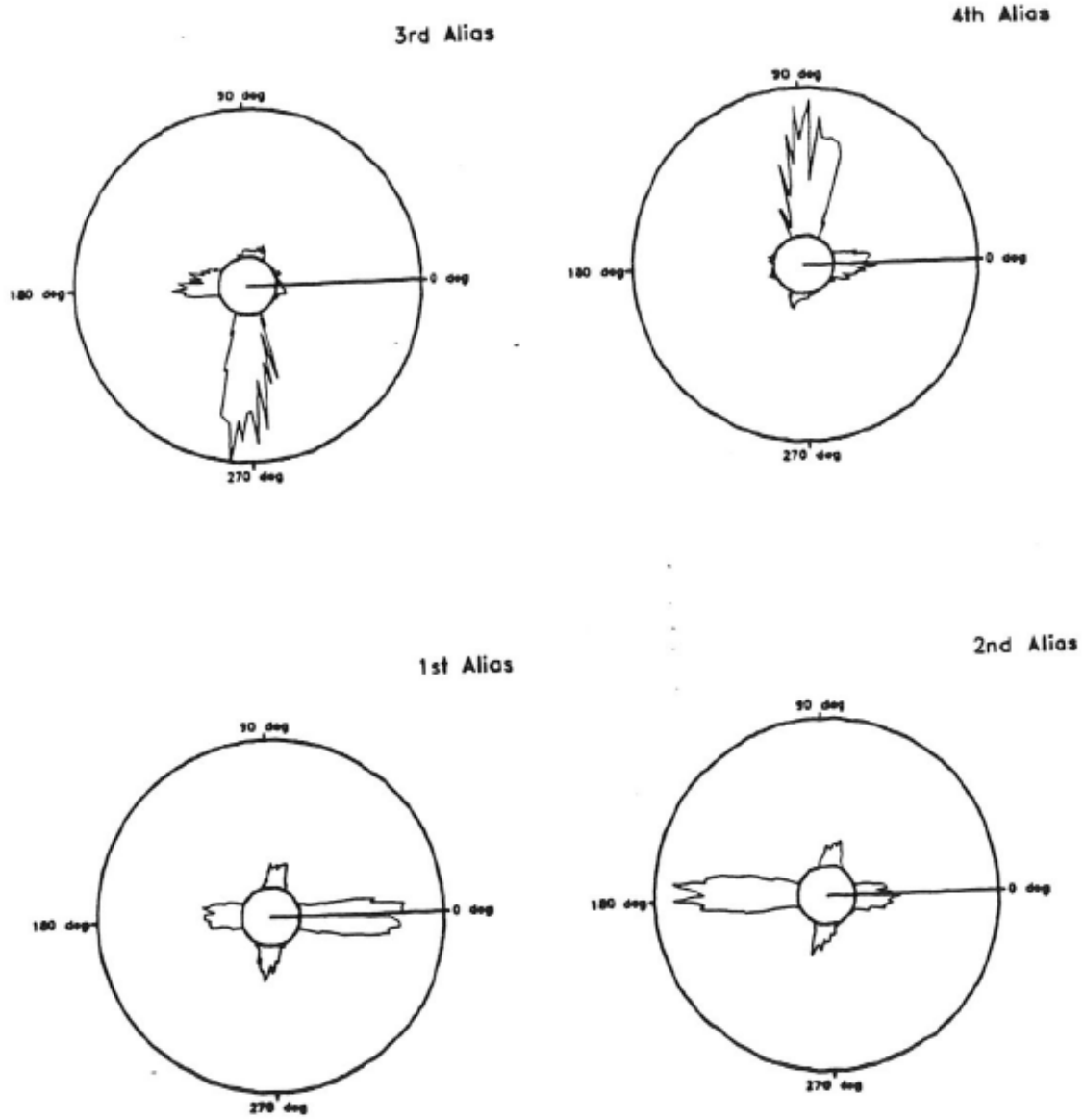


Figure 2.8: Directional histogram from simulated wind retrieval — 4 alias case

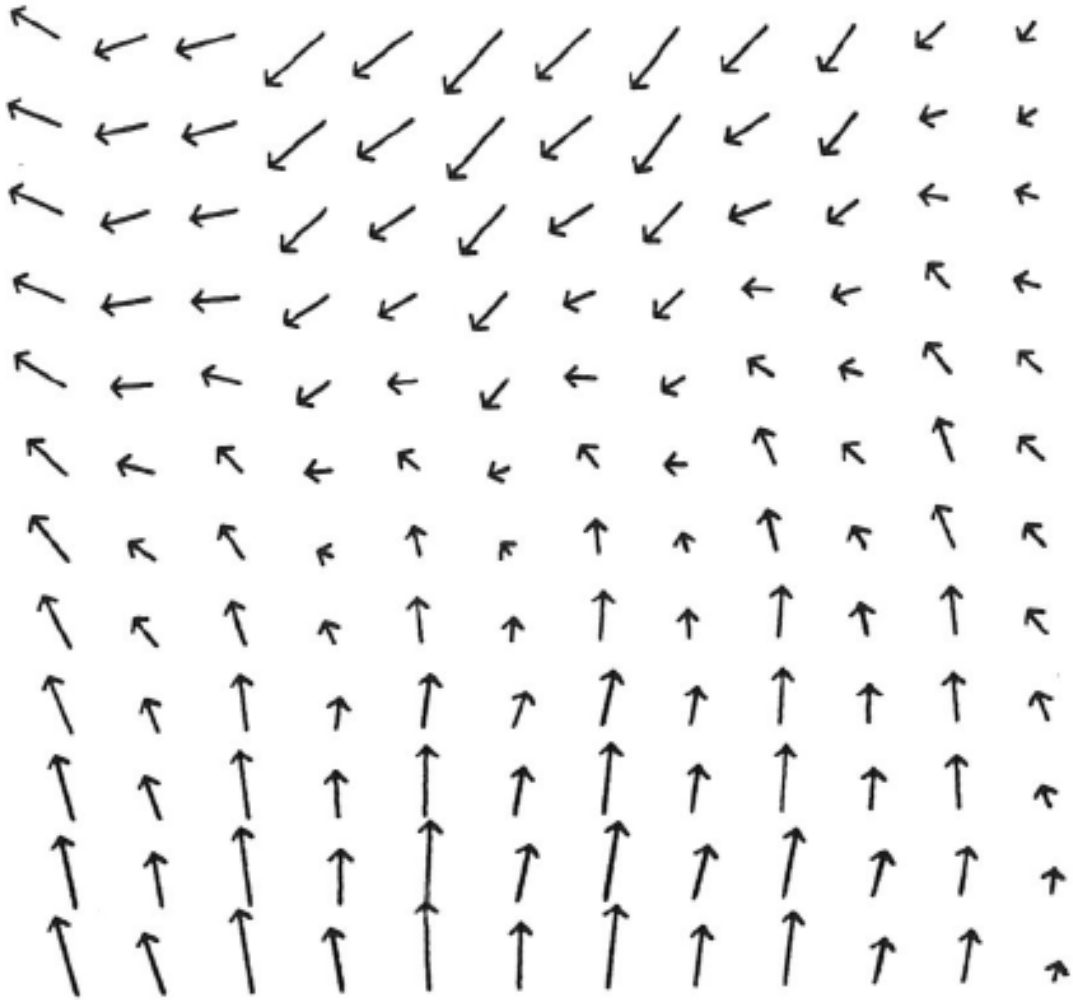


Figure 2.9: An example of a wind field at 50 km resolution.

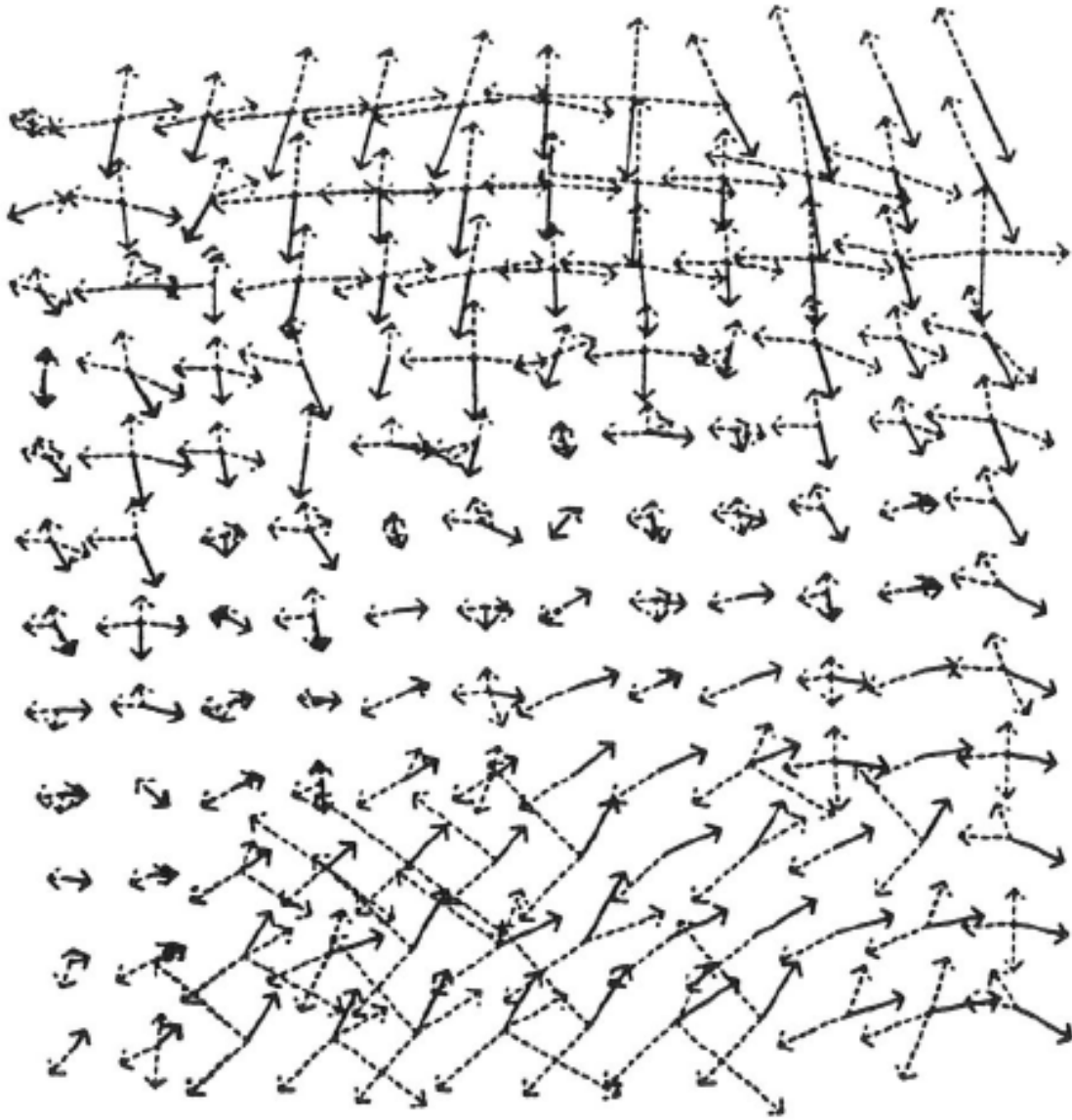


Figure 2.10: Ambiguity sets generated from simulated NSCAT σ^o measurements of the wind field in Fig. 2.9. Solid vectors are the ambiguities closest to the true wind field.

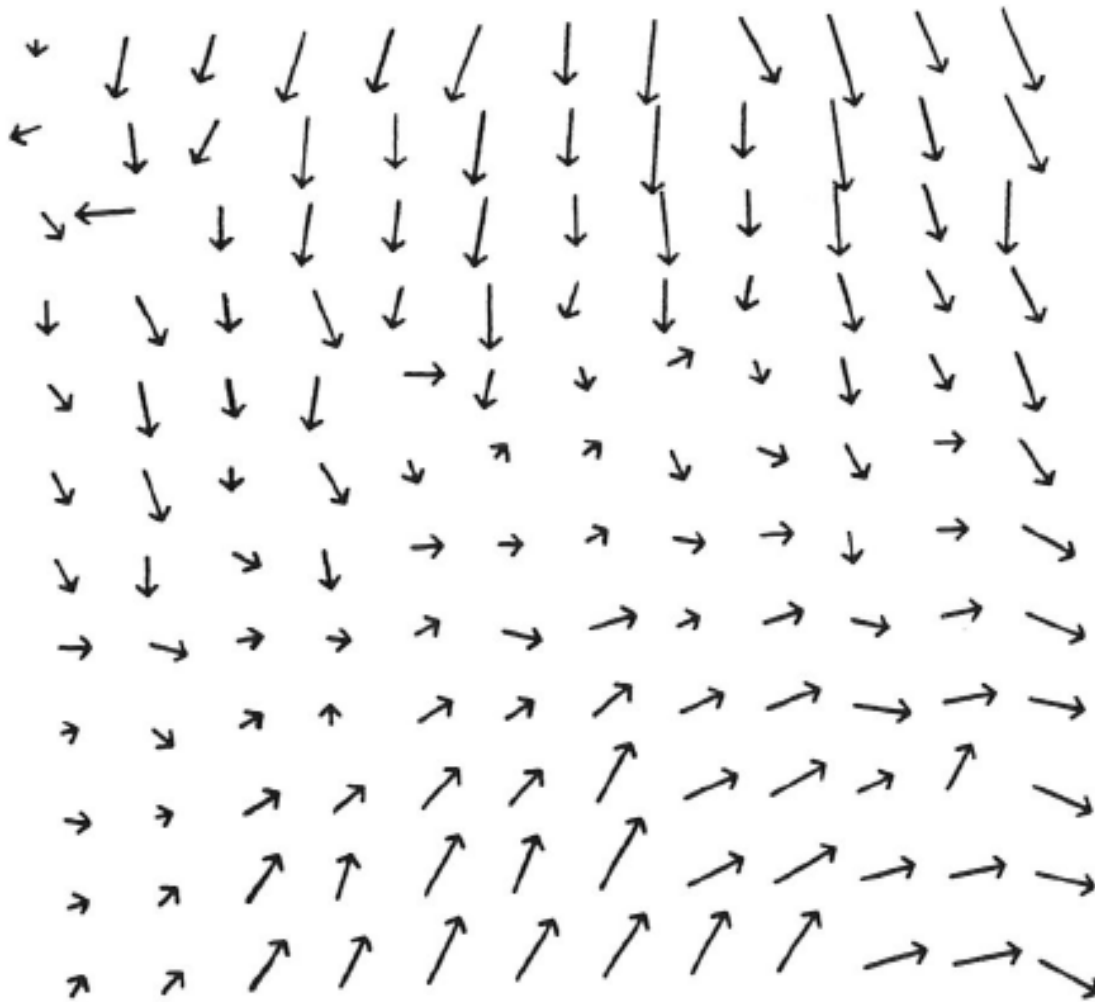
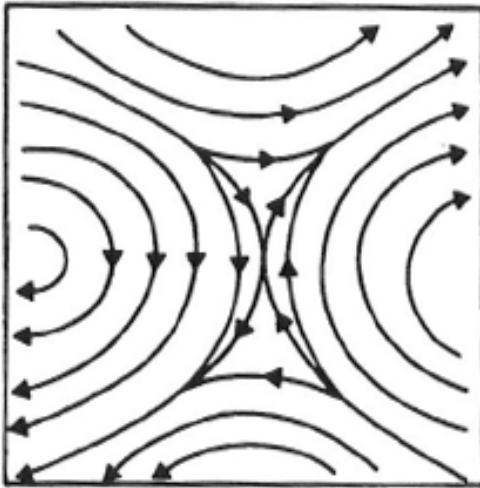
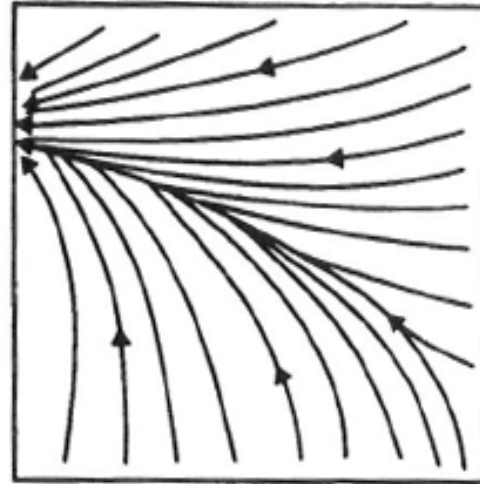


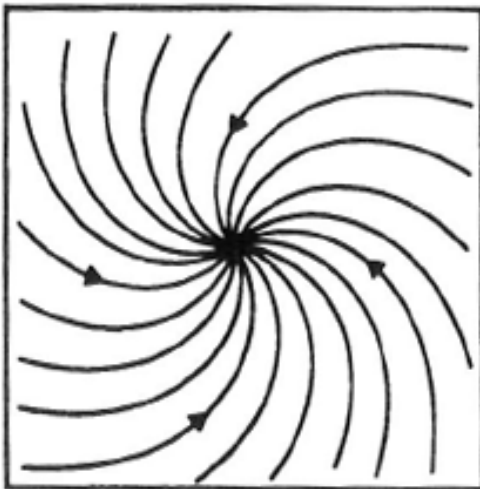
Figure 2.11: Dealiased wind field corresponding to Fig. 2.10. The NSCAT median filter-based ambiguity removal algorithm was used.



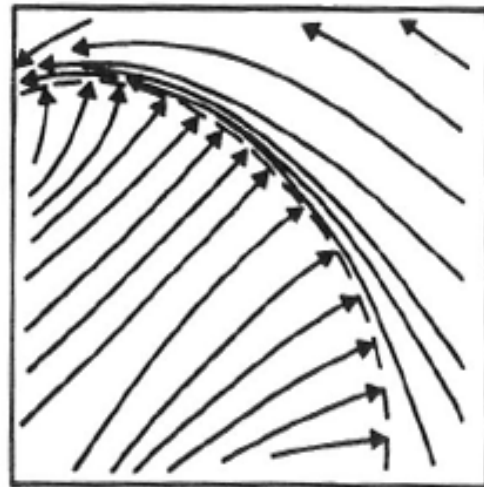
Col Point



Convergence Zone



Cyclonic Vortex



Front

Figure 2.12: Typical wind field features.

Chapter 3

Identifiability in Point-Wise Wind Estimation

The estimation theory concept of “identifiability” indicates whether or not an estimated quantity can be uniquely determined from the available measurements [26, 78]. In this chapter, the identifiability of the wind vector estimated from wind scatterometer measurements of the radar backscatter of the ocean’s surface is shown. Due to the nature of the relationship between backscatter and the wind vector, traditional wind estimation approaches produce multiple estimates of the wind direction, which occur at the local minima of an objective function formed from the noisy backscatter measurements.

In this chapter wind vector estimation is shown to be set-wise identifiable, i.e., there is a unique set of wind vectors that could have given rise to the observed backscatter values. Within this set, there is no way to select a unique wind vector estimate from the measurements at a single sample point. This provides a theoretical basis for dealiasing. This is a new result. Details of the proof presented in this chapter are used in Chapter 5 to show the indentifiability of model-based wind field estimation.

3.1 The Relationship Between σ^o and the Vector Wind

In this Chapter we will assume that the relationship between the wind and σ^o is precisely known, i.e., the geophysical model error is zero. The $\cos 2\chi$ dependence of σ^o on the wind direction for the SASS¹ geophysical model function has been noted. While other model functions (e.g., [24, 91, 105]) differ in detail, they share a similar $\cos 2\chi$ dependence on wind direction. This characteristic of the model function is primarily responsible for the difficulties in obtaining unique estimates of the wind vector from σ^o measurements.

In the traditional point-wise approach, the estimate of the wind vector is obtained by minimizing an objective function, typically based on maximum likelihood, formed from the σ^o measurements. Due to the double cosine nature of \mathcal{M} , the objective function has several local minima with similar wind speed but differing direction. The wind vectors corresponding to these local minima are called the *noisy ambiguity set*. Members of this set are commonly

termed “aliases” [109]. From the noisy ambiguity set a single wind vector is selected in a post-estimation “de-aliasing” step, using a variety of tactics including continuity considerations (see [94, 109]). To-date, no one has shown that the wind is uniquely identifiable using this two-step approach. We will show that, whereas the wind estimate is not unique in the first step, it is set-wise identifiable, i.e., there is a unique set of wind vectors corresponding to the observed σ^o values, which can not be distinguished from one another using only σ^o measurements. Identifiability for the second dealiasing step can not be shown since it relies on information not present in the σ^o measurements.

Due to the nature of \mathcal{M} and the fact that σ^o is observed from only a small set of azimuth angles, there may be several wind vectors which give rise to the same set of σ^o values (one value for each observation azimuth angle). Define D_p^c to be the set of all possible true wind velocity vectors, denoted by (u_t, v_t) , which give rise to the same set of $\sigma^o(k)$'s, i.e.,

$$D_p^c \triangleq \left\{ (u, v) \mid \mathcal{M}\{(u, v), k\} = \mathcal{M}\{(u_t, v_t), k\} \forall k \right\} \quad (3.1)$$

Note that by definition, $(u_t, v_t) \in D_p^c$.

Because members of the set D_p^c produce exactly the same set of $\sigma^o(k)$ values, they can not be distinguished from one another even if the measurements are noise free. We refer to D_p^c as the *true ambiguity set*. The membership in the set D_p^c depends on the model function, the set of relative azimuth angles (and the corresponding incidence angles and polarizations of the antenna beams), and the true wind vector. Depending on these factors, D_p^c will contain one or more members. The fact that D_p^c may contain multiple members is a property inherent to the model function and the measurement geometry.

In effect, the geophysical model function is a many-to-one mapping of wind velocity vectors to the set of $\sigma^o(k)$'s corresponding to the observed azimuth angles. The best we can ever expect to do is identify all members of D_p^c . Selection of a unique wind vector from D_p^c requires additional information not contained in the σ^o measurements for a single sample point of the ocean's surface; hence, the need for dealiasing in which data from other sample points (or, from other sources) are used in conjunction with dynamical constraints, continuity considerations, etc., to select a wind vector field which (hopefully) is “close” to the true field [94, 109].

To illustrate the membership of D_p^c for various true wind vectors, let us consider the well-known SASS¹ model function [93], for which \mathcal{M} is expressed, as

$$\sigma^o(k) = \mathcal{M}\{(u, v), k\} = G(\theta(k), \chi(k), p(k))U^H(\theta(k), \chi(k), p(k)) \quad (3.2)$$

where $U = |(u, v)|$ is the wind speed, $\chi(k) = \psi(k) - \phi$ where $\phi = \tan^{-1}(v/u)$ is the wind direction and $\psi(k)$ is the azimuth angle of the k^{th} antenna beam, and $p(k)$ is the radar polarization. χ is known as the relative azimuth angle. G and H are tabular functions. For given values of θ and p , $G(\theta, \chi, p) \sim \cos 2\chi$ and $H(\theta, \chi, p) \sim 2$ [93]. For given values of $\sigma^o(k)$,

$\chi(k)$, $\theta(k)$, and $p(k)$, U can be computed, as

$$U = \exp \left\{ \frac{1}{H(\theta(k), \chi(k), p(k))} \ln \left[\frac{\sigma^o(k)}{G(\theta(k), \chi(k), p(k))} \right] \right\} \quad (3.3)$$

Consider the SASS antenna configuration with two azimuth angles (both vertically polarized in this example) separated by 90° . For the true wind vector (u_t, v_t) , the set of true σ^o values are denoted $\sigma^o(k=1) = \mathcal{M}\{(u_t, v_t), k=1\}$ and $\sigma^o(k=2) = \mathcal{M}\{(u_t, v_t), k=2\}$. Now consider the two curves in wind vector space (u, v) , defined by $\mathcal{M}\{(u_1, v_1), 1\} = \sigma^o(1)$ and $\mathcal{M}\{(u_2, v_2), 2\} = \sigma^o(2)$. These curves are depicted in Fig. 3.1 for a true wind speed of 3 m/s and a true wind direction of 0° where the wind vector (u, v) has been converted to speed and direction relative to the antenna azimuth angle for plotting. $k=1$ corresponds to the relative observation azimuth angle of 0° , while $k=2$ corresponds to 90° . To generate this curve for $k=1$ given $\sigma^o(1)$ and the respective $\psi(1)$, $\theta(1)$, and $p(1)$ values, for each possible value of ϕ , a wind speed U was computed using Eq. (3.3) such that $\mathcal{M}\{(U \cos \chi(1), U \sin \chi(1)), 1\} = \sigma^o(1)$. The curve for $k=2$ was similarly computed.

These curves intersect several times. The points along these curves for which $(u_1 = u_2, v_1 = v_2)$ at which the curves intersect, define the true ambiguity set D_p^c . Curves for other true wind directions are also shown in Figs. 3.2-3.5. Note, that depending on the wind direction, the number of elements in D_p^c varies from 1 to 4.

Figures 3.6 and 3.7 show maps of D_p^c for a true wind speed of 3 m/s at two different incidence angles. To prepare Fig. 3.6, a true wind direction (along the horizontal axis) was first selected and D_p^c for that true wind direction was computed. The wind direction of each of the elements of D_p^c (the directions of each of the elements of the “true ambiguity set”) was then marked along the vertical corresponding to the true wind direction. This process was repeated for each true wind direction. The result graphically illustrates how D_p^c changes with true wind direction for the SASS¹ model function. The vertical lines labeled (a)-(e) correspond to the plots shown in Figs. 3.1-3.5, respectively. Figure 3.7 was generated in a similar manner, but for a different incidence angle.

For the purpose of comparison, Figs. 3.8 and 3.9 were prepared in the same manner as Figs. 3.6 and 3.7 but for the three-azimuth-angle NSCAT scatterometer configuration, with all vertically polarized antennas. Note, that the additional azimuth angle reduces the number of intersections at a given true wind direction to 1 or 2.

Figures 3.6 through 3.9 can be misleading since they show the *true* ambiguity set. The true ambiguity set can only be obtained from noise-free σ^o measurements. In the real world, the σ^o measurements are always noisy. When the σ^o measurements are noisy, additional intersections may be produced, or the curves may not intersect at all. When the measurements are noisy, an objective function [21] (such as the maximum-likelihood objective function given in Section 4) is formulated from the measurements and minimized to provide estimates of the wind vector [21]. In the noisy case, the wind vectors corresponding to the local minima of the objective function define the noisy ambiguity set. The number of minima depends on the true wind, observation angles, etc. To contrast the difference between the true and noisy ambiguity sets, Figs. 3.10 through 3.13 were prepared with Figs.

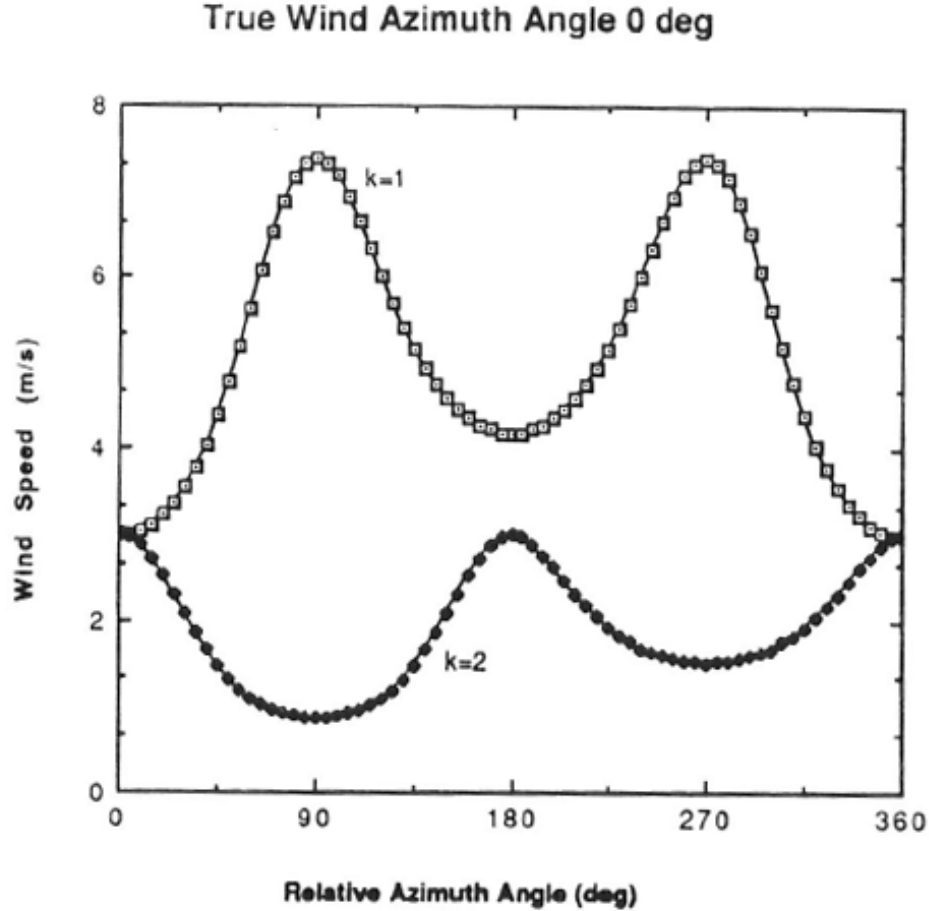


Figure 3.1: Illustration of multiple solutions for point-wise estimation for a true wind direction of 0° . The curves in (u, v) space, along which $\mathcal{M}\{(u, v), k\} = \mathcal{M}\{(u_t, v_t), k\}$ for $k = 1, 2$ where (u_t, v_t) is the true wind vector are shown. The wind vector (u, v) has been converted to speed and direction relative to the antenna azimuth angle for plotting. (u_t, v_t) is the true wind with speed of 3 m/s and azimuth angle (relative to the first antenna beam) of 0° where the observation azimuth angles are 0° and 90° , for $k = 1$ and $k = 2$, respectively. Both antennas were vertically polarized with an incidence angle of 40° . The SASS¹ model function was used to generate this plot.

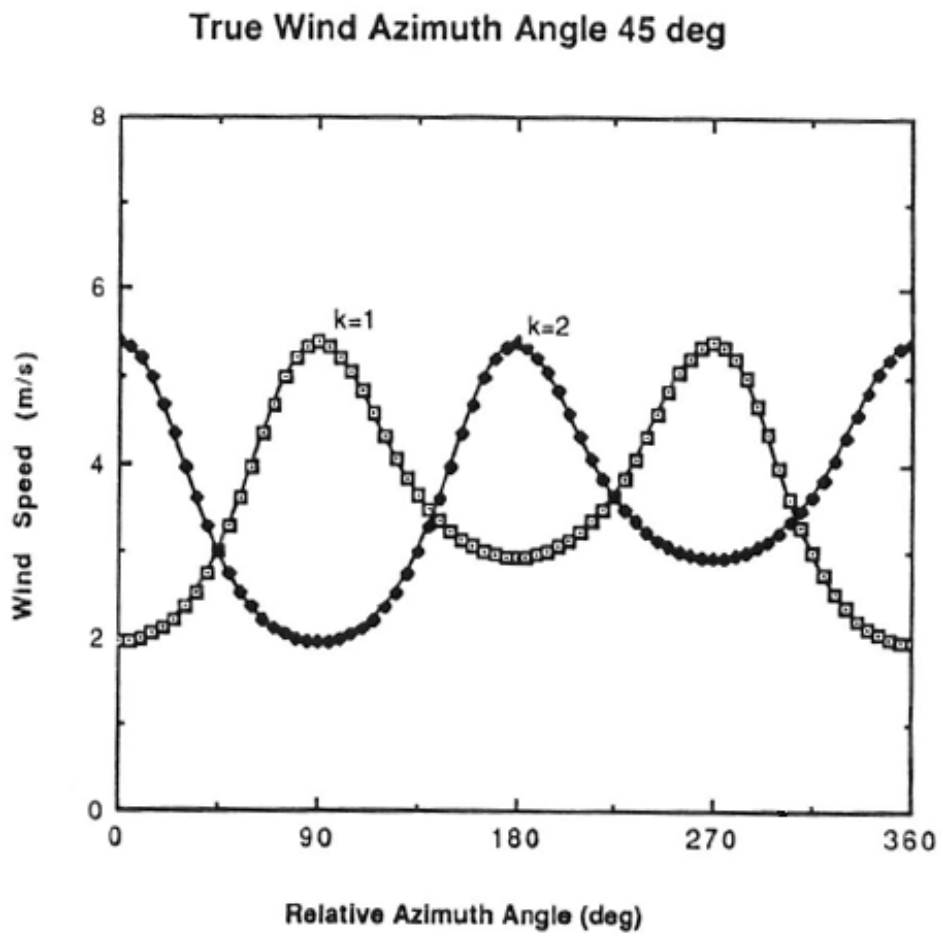


Figure 3.2: Illustration of multiple solutions for point-wise estimation for a true wind direction of 45° . See the caption for Fig. 3.1 for explanation of curves.

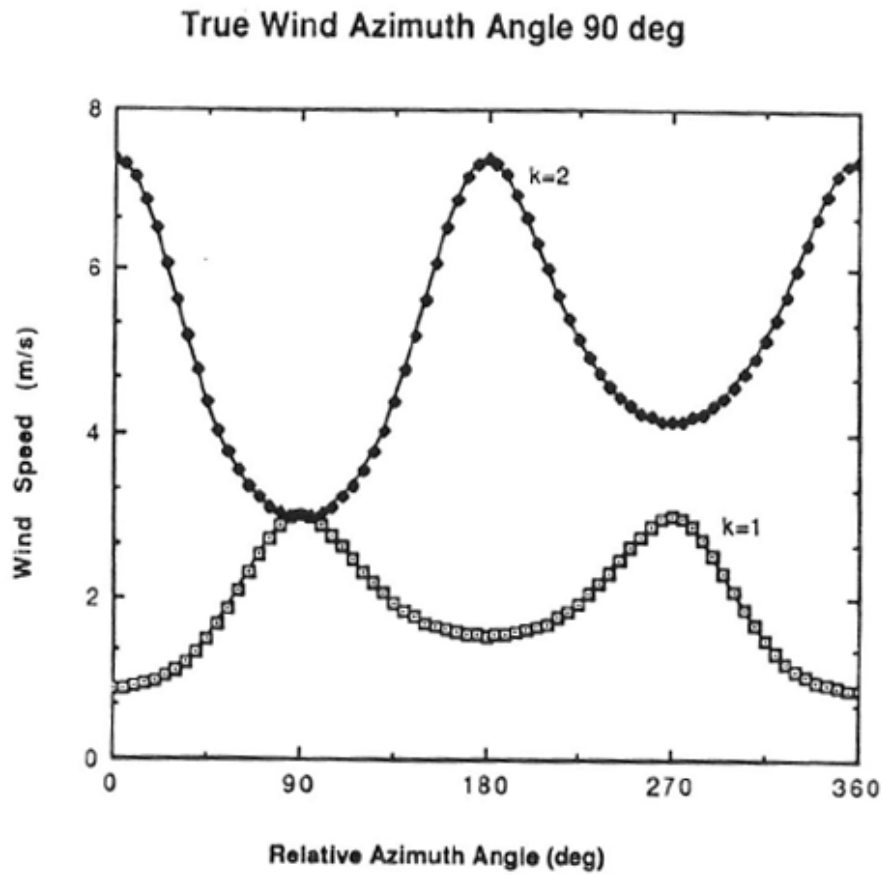


Figure 3.3: Illustration of multiple solutions for point-wise estimation for a true wind direction of 90° . See the caption for Fig. 3.1 for explanation of curves.

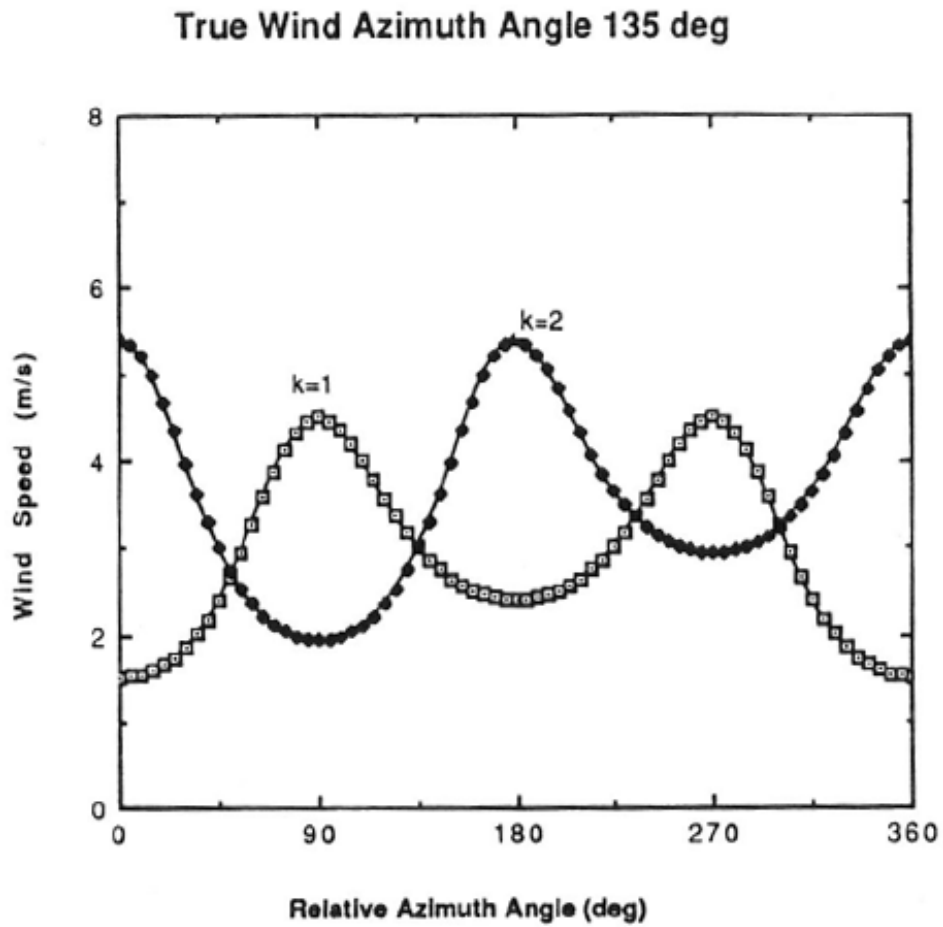


Figure 3.4: Illustration of multiple solutions for point-wise estimation for a true wind direction of 135° . See the caption for Fig. 3.1 for explanation of curves.

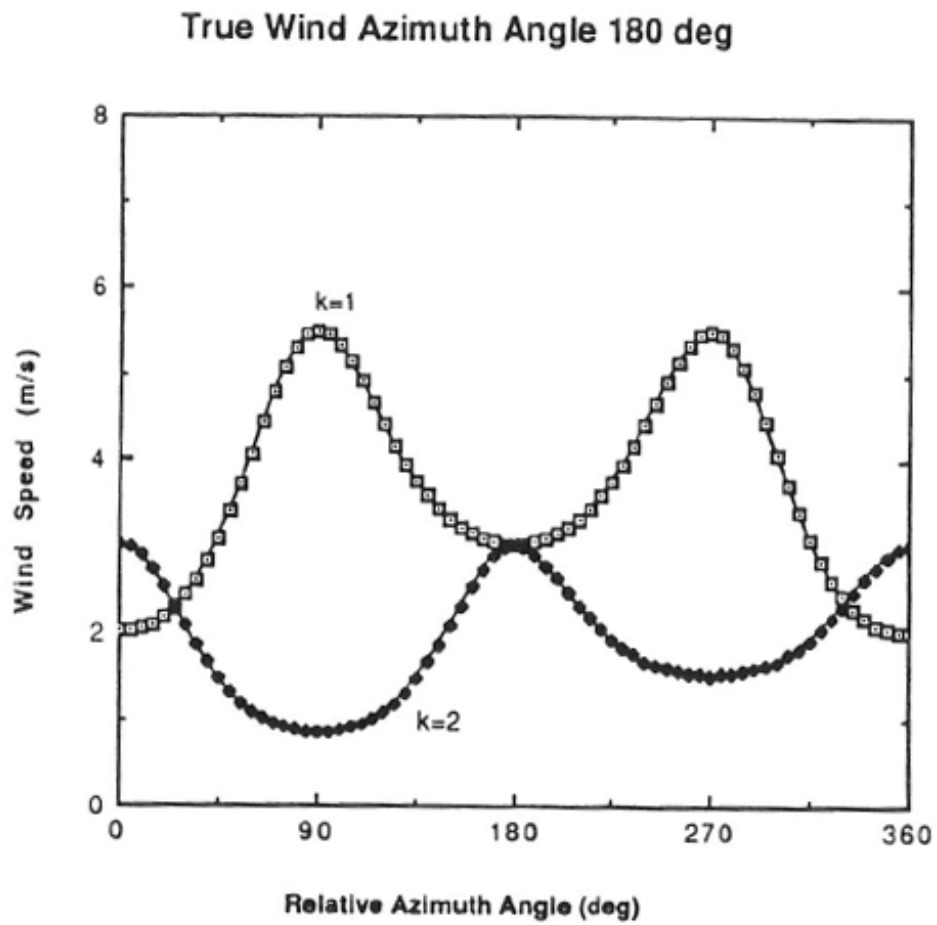


Figure 3.5: Illustration of multiple solutions for point-wise estimation for a true wind direction of 180° . See the caption for Fig. 3.1 for explanation of curves.

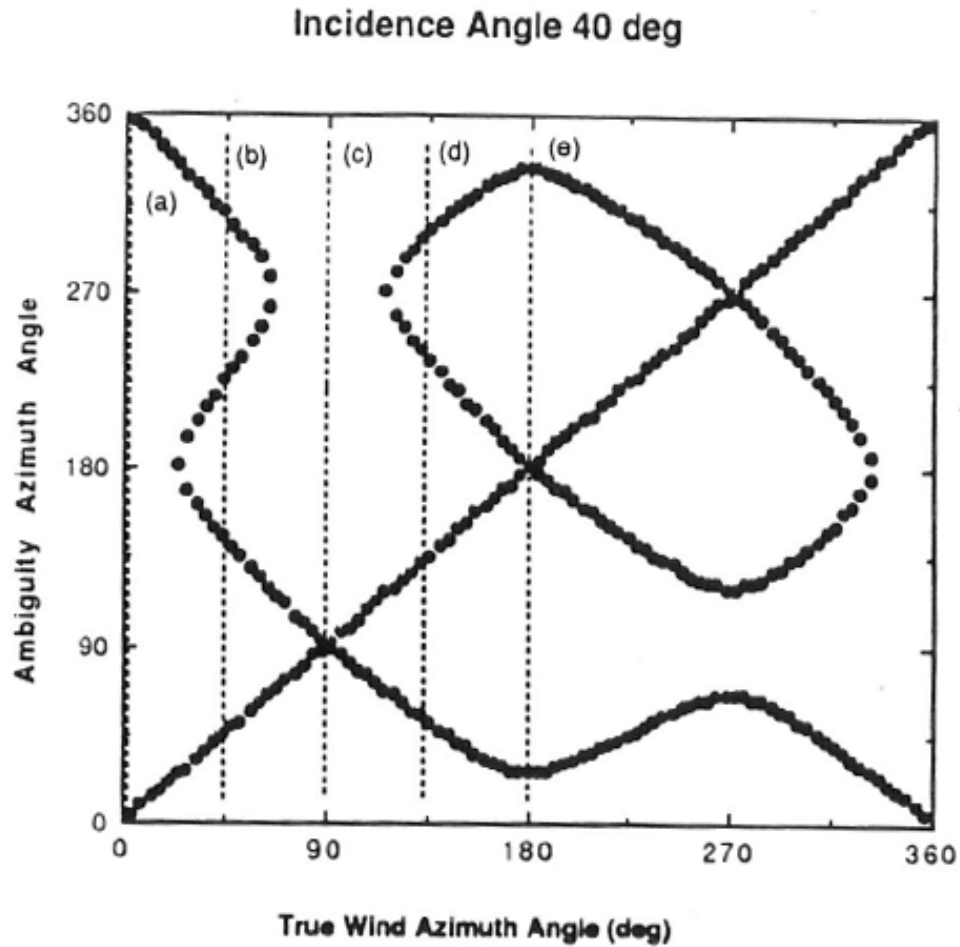


Figure 3.6: The true ambiguity set map for 3 m/s wind speed and the SASS configuration with an incidence angle of 40° . The labeled vertical lines correspond to results from the plots shown in Figs. 3.1-3.5, respectively. Two observation azimuth angles, at 0° and 90° (SASS configuration), both vertically polarized, were used with the SASS¹ model function (see text).

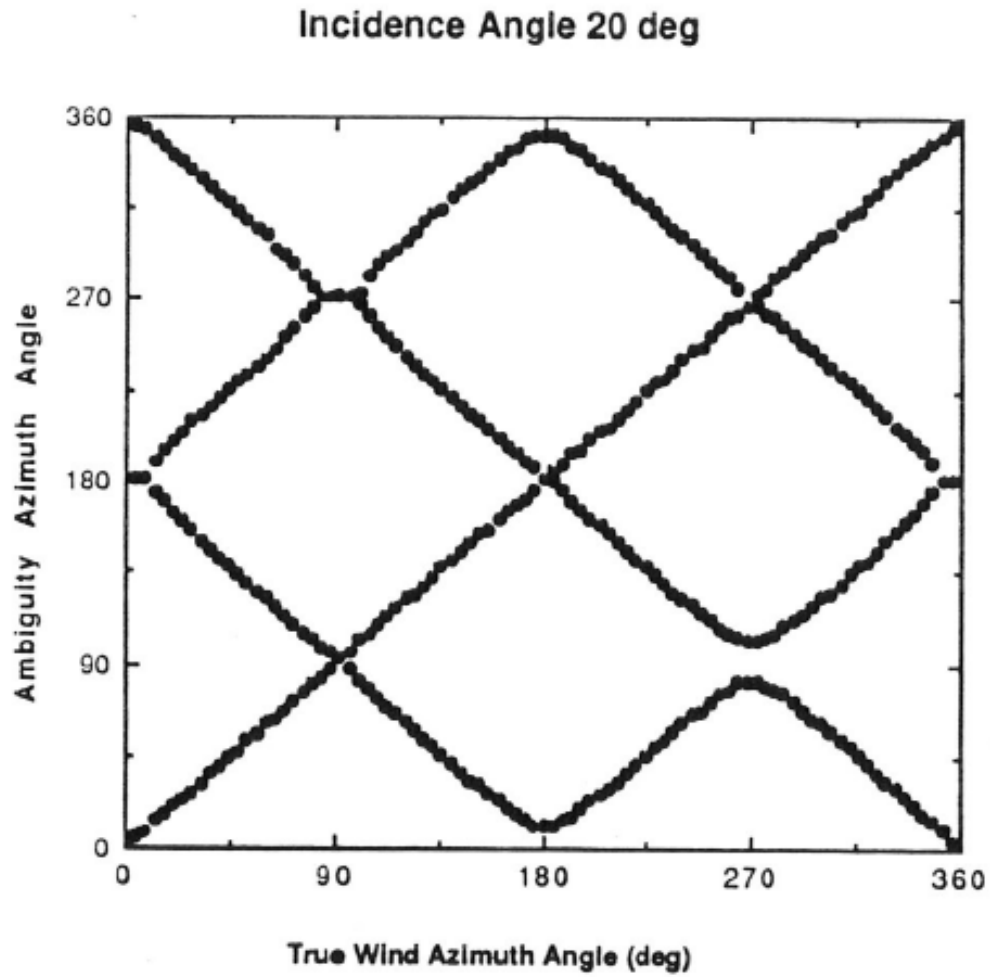


Figure 3.7: The true ambiguity set map for 3 m/s wind speed and the SASS configuration with an incidence angle of 20° . Two observation azimuth angles, at 0° and 90° (SASS configuration), both vertically polarized, were used with the SASS¹ model function (see text).

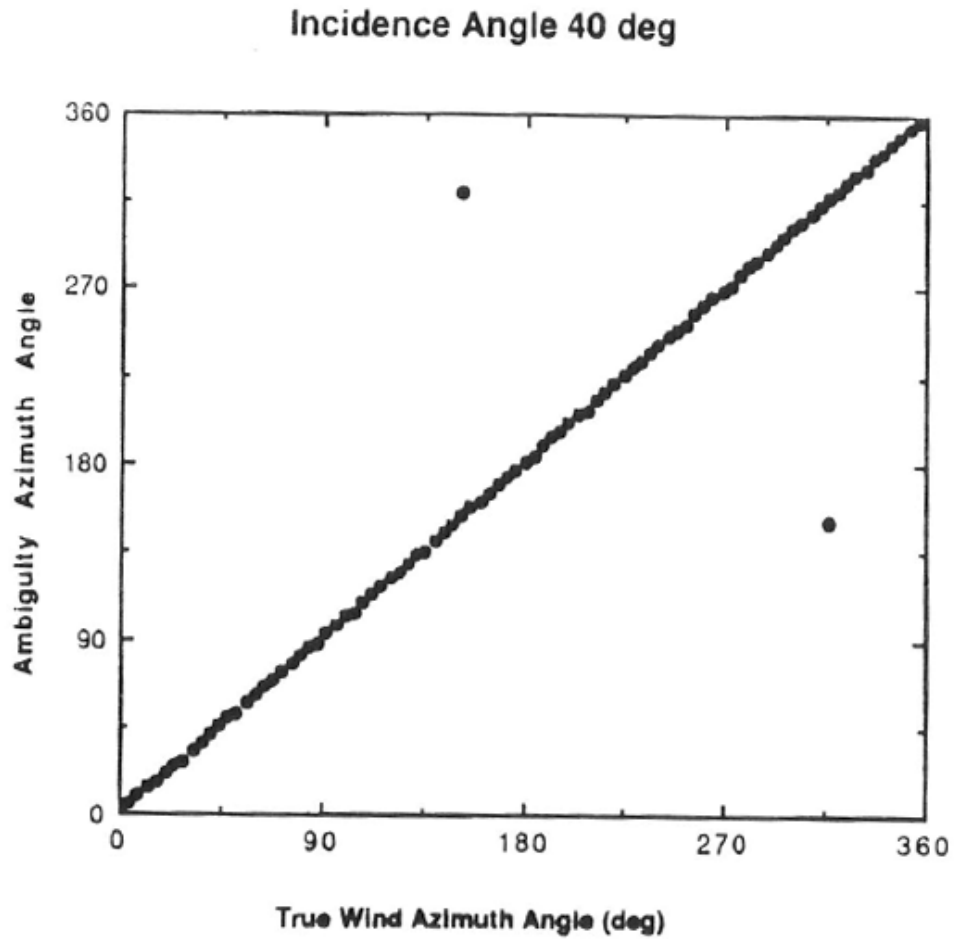


Figure 3.8: The true ambiguity set map for 3 m/s wind speed, the NSCAT configuration and an incidence angle of 40°. Same as Fig. 3.6, but for the three observation azimuth angle (0°, 65°, and 90°) NSCAT configuration (all vertically polarized).

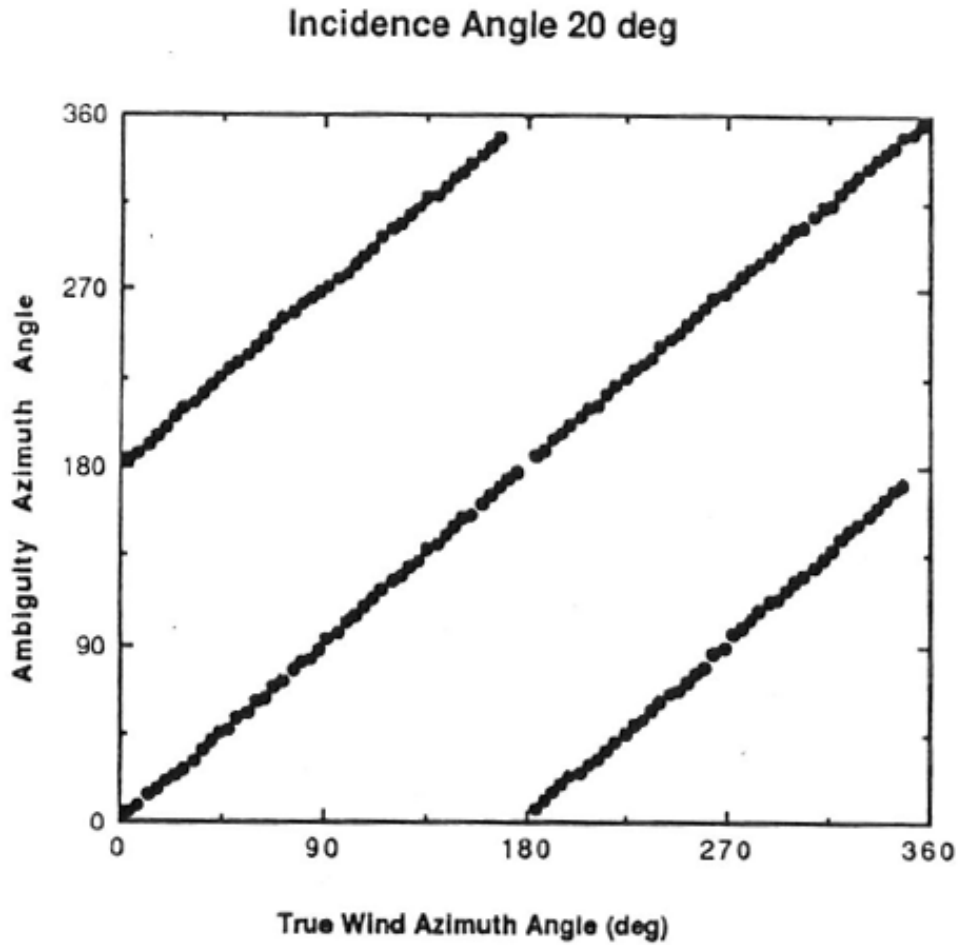


Figure 3.9: The true ambiguity set map for 3 m/s wind speed, the NSCAT configuration and an incidence angle of 20°. Same as Fig. 3.7, but for the three observation azimuth angle (0°, 65°, and 90°) NSCAT configuration (all vertically polarized).

3.10 and 3.11 corresponding to the SASS antenna configuration, and Figs. 3.12 and 3.13 to the NSCAT configuration. Figures 3.10 and 3.11 should be compared with Figs. 3.6 and 3.7, respectively, whereas Figs. 3.12 and 3.13 should be compared with Figs. 3.8 and 3.9, respectively. Figures 3.10 through 3.13 were prepared as follows. For a given true wind direction, the true σ^o set was computed. Noisy σ^o measurements were simulated by Monte Carlo methods and the noisy ambiguity set corresponding to each realization of the noisy σ^o sets was determined [21]. While details vary with choice of objective function (see [21]), the general characteristics remain the same. A histogram of the direction of the elements of the noisy ambiguity sets was computed. This was repeated for each true direction and the results were plotted. For a given true wind direction, the average number and location of the wind directions corresponding to the noisy ambiguity set can be seen. Note that there are typically 2 to 4 members of the noisy ambiguity set regardless of the number of members of the true ambiguity set.

The increased number of elements of the noisy ambiguity set relative to the true ambiguity set is due to the presence of noise. We will show, that, as the measurement noise level is reduced (by increasing measurement time) the noisy ambiguity set (corresponding to the maximum-likelihood objective function) converges to the true, multi-membered ambiguity set. Even if we could choose the observation angles to ensure that the true ambiguity set D_p^c contains a single member for all true winds, the noisy ambiguity set will most likely be multi-membered. In either case, if a unique wind estimate is desired, dealiasing is required.

3.2 Identifiability of the Set D_p^c

Let us consider the identifiability of u and v (or, equivalently, the wind speed and direction). As mentioned above, (u_t, v_t) is the true wind vector and D_p^c is the corresponding true ambiguity set. By definition, $(u_t, v_t) \in D_p^c$. Let $Z_p = (z(1), \dots, z(N))^T$; its elements are statistically independent. From Eq. (2.18) the conditional probability of Z_p given (u, v) is

$$p(Z_p|u, v) = \prod_{k=1}^N \frac{1}{\sqrt{2\pi}} \frac{1}{[\alpha^2(k)s^4(k) + \beta^2(k)s^2(k) + \gamma^2(k)]^{1/2}} \cdot \exp\left\{-\frac{1}{2}[z(k) - s^2(k)]^2/[\alpha^2(k)s^4(k) + \beta^2(k)s^2(k) + \gamma^2(k)]\right\}. \quad (3.4)$$

The log-likelihood function [78] $L_p(u, v)$ is given, as

$$L_p(u, v) = \sum_{k=1}^N \left\{ -\frac{1}{2} \log[\alpha^2(k)s^4(k) + \beta^2(k)s^2(k) + \gamma^2(k)] - \frac{1}{2}[z(k) - s^2(k)]^2/[\alpha^2(k)s^4(k) + \beta^2(k)s^2(k) + \gamma^2(k)] \right\}. \quad (3.5)$$

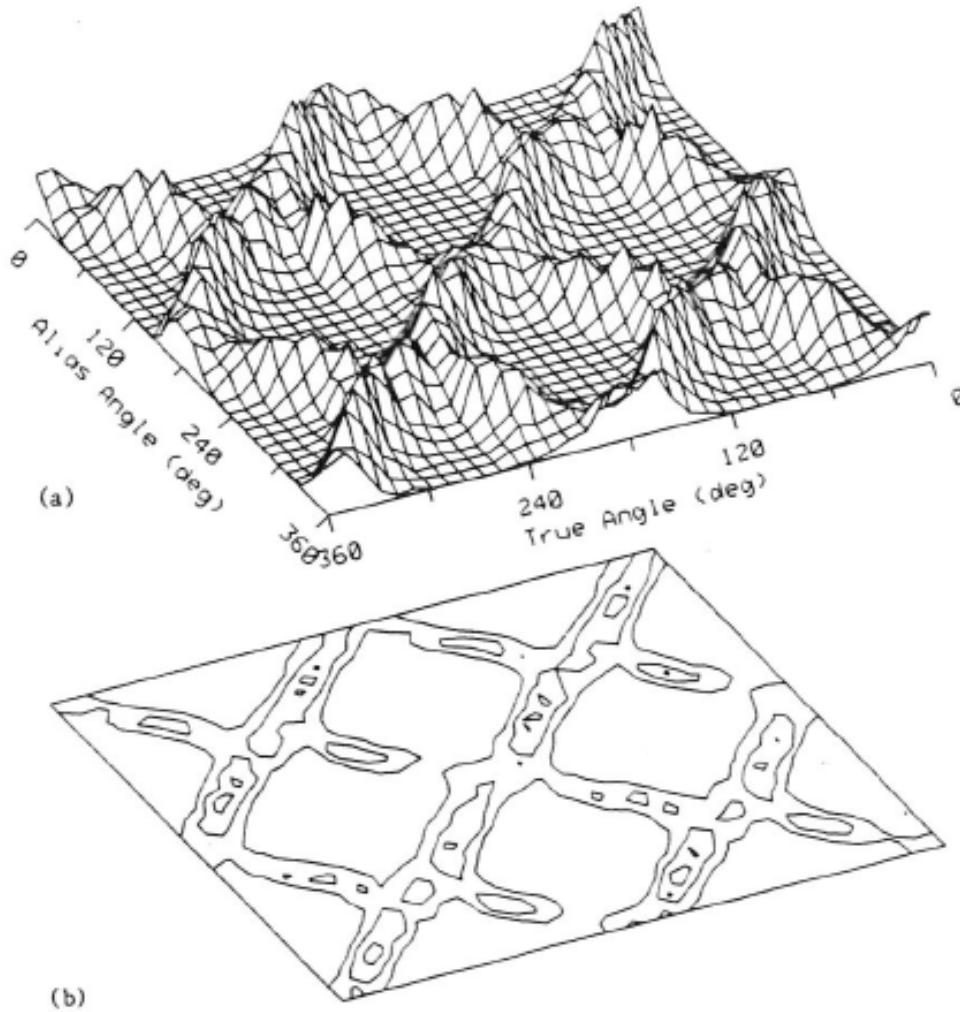


Figure 3.10: Histogram of the directions of the aliases in the noisy ambiguity sets versus true wind direction for the SASS Configuration for an incidence angle of 40° created by Monte Carlo simulations of noisy σ^o measurements using the WLS (SOS) objective function. The true wind speed is 3 m/s. Vertically polarized antenna beams in the SASS configuration with the SASS¹ model function were used. For clarity, (a) shows a perspective plot while (b) shows a contour plot.

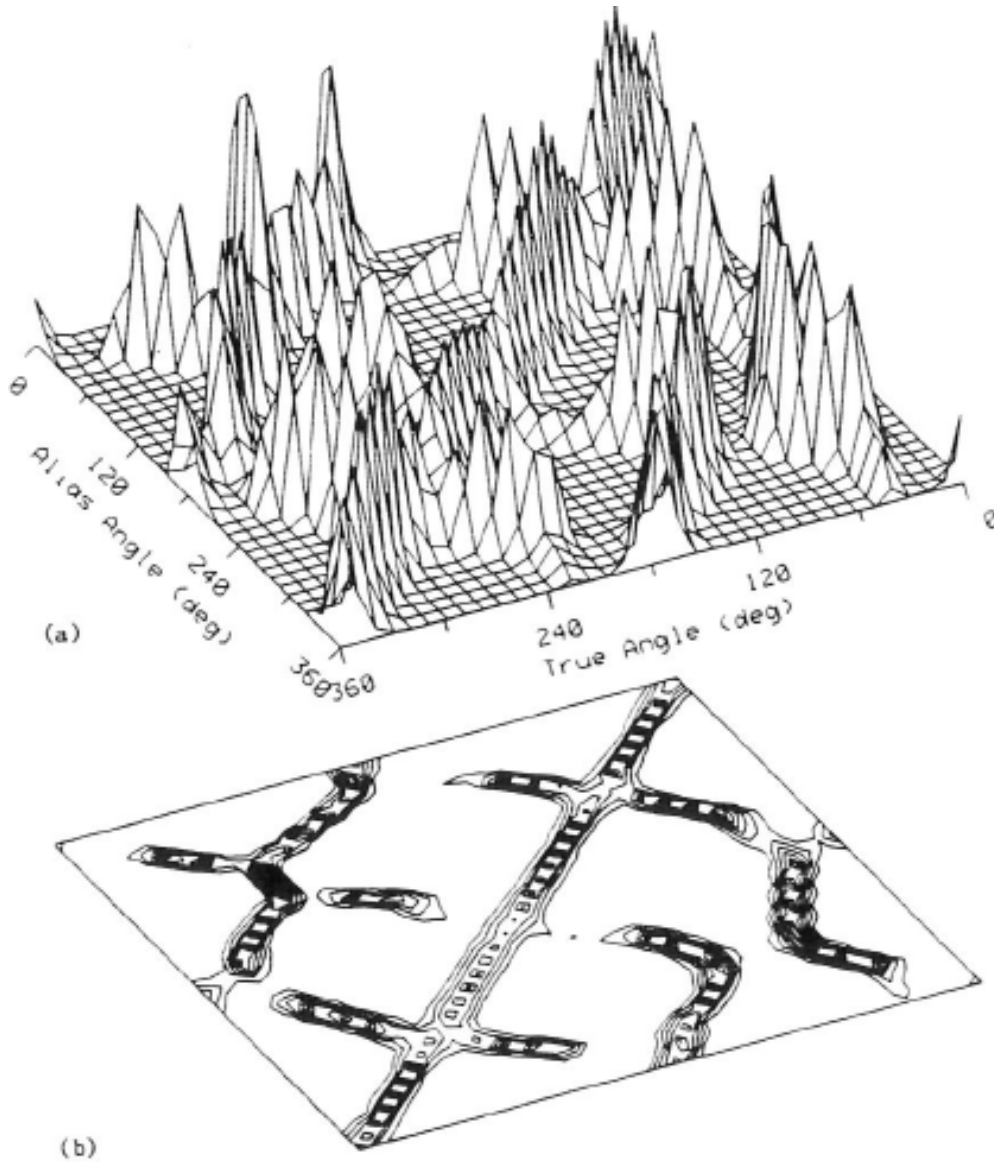


Figure 3.11: Histogram of the directions of the aliases in the noisy ambiguity sets versus true wind direction for the SASS Configuration for an incidence angle of 20° . See the caption of Fig. 3.10 for an explanation of the plots.

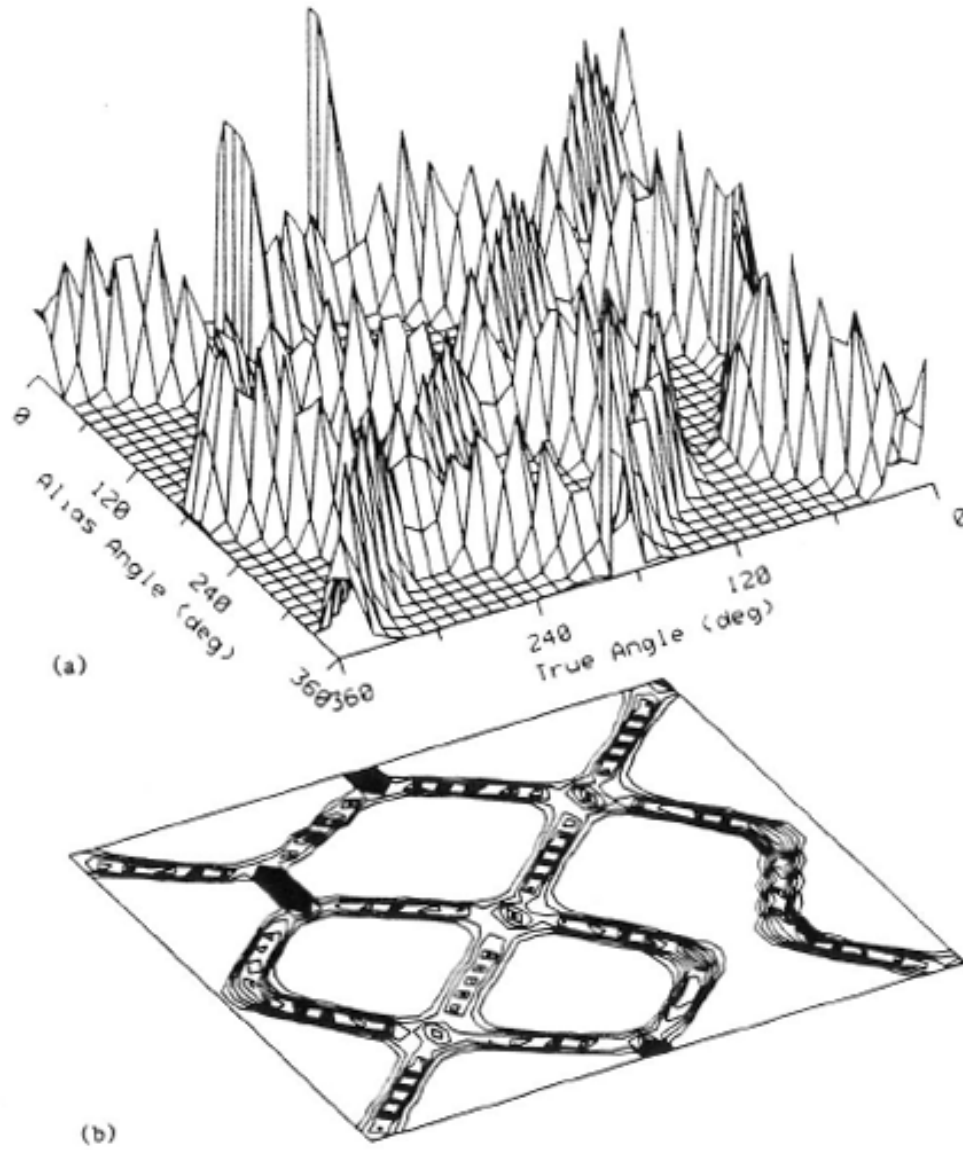


Figure 3.12: Histogram of the directions of the aliases in the noisy ambiguity sets versus true wind direction for the NSCAT Configuration for an incidence angle of 40° . Same as Fig. 3.10, but for the NSCAT configuration with all vertically-polarized beams.

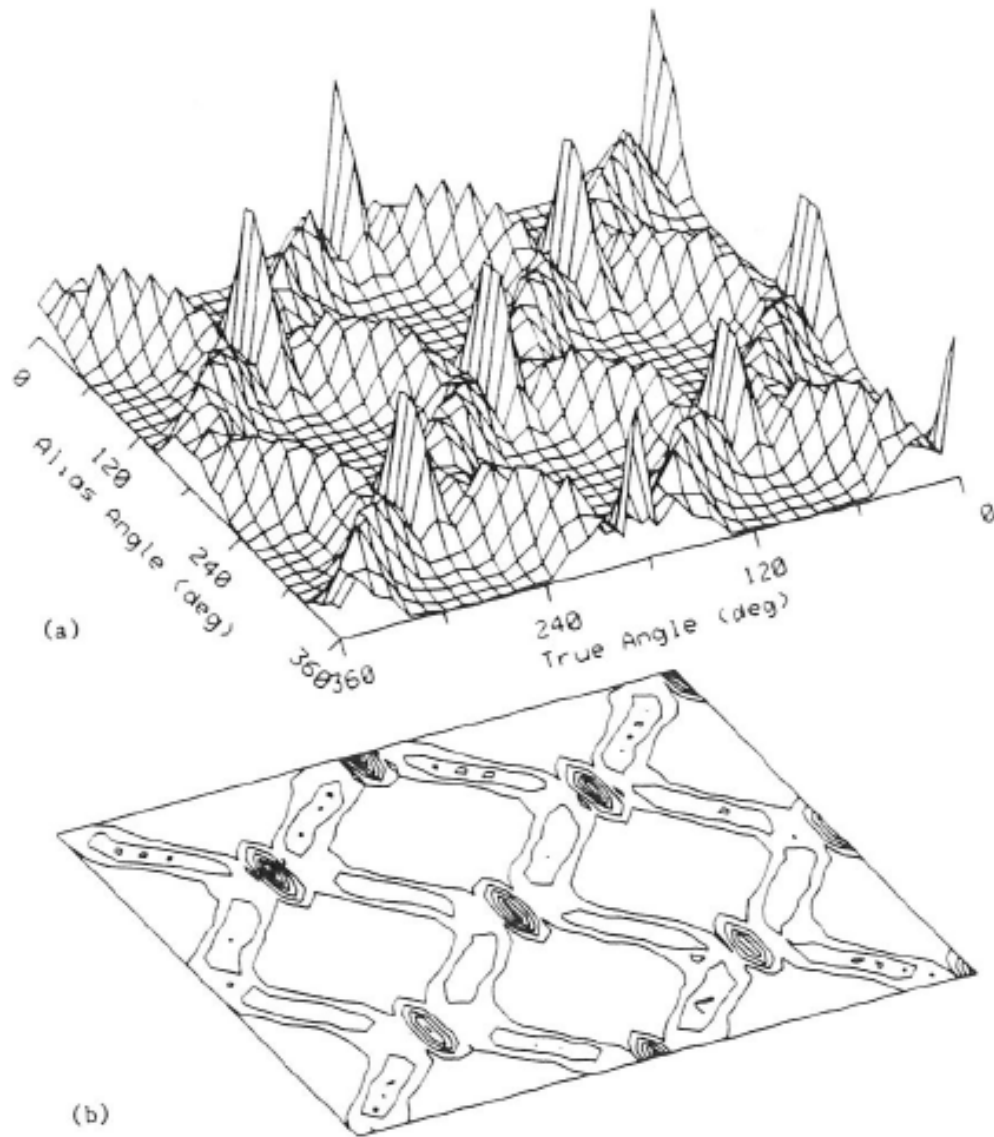


Figure 3.13: Histogram of the directions of the aliases in the noisy ambiguity sets versus true wind direction for the NSCAT Configuration for an incidence angle of 20° . Same as Fig. 3.11, but for the NSCAT configuration with all vertically-polarized beams.

The maximum-likelihood objective function, $J_p(u, v)$, is defined, as

$$J_p(u, v) \triangleq -L_p(u, v). \quad (3.6)$$

To show identifiability of the point-wise estimation scheme, we need to show that as $T \rightarrow \infty$ [corresponding to a longer and longer measurement (for which the noise variance goes to zero)] the locations of global minima of $J_p(u, v)$ converge in probability to the members of D_p^c [26]. To show convergence in probability we will show that: (A) $J_p(u, v)/T$ converges in the mean-squared sense (which is stronger than convergence in probability) to the deterministic function $E[J_p(u, v)/T]$ and (B) the set of maximum-likelihood estimates of u and v converge in probability to the location of the minimum of $E[J_p(u, v)/T]$. Doing this is equivalent to showing that the set, A_p^c , of the (u, v) which minimize $J_p(u, v)/T$ for $T \rightarrow \infty$ is equal to D_p^c , where A_p^c is defined as [18, 26]

$$A_p^c = \left\{ (u_1, v_1) \left| \lim_{T \rightarrow \infty} E \left[\frac{J_p(u_1, v_1)}{T} \right] = \min_{u, v} \lim_{T \rightarrow \infty} E \left[\frac{J_p(u, v)}{T} \right] \right\}. \quad (3.7)$$

If $J_p(u, v)/T$ converges in mean-square to the function $E[J_p(u, v)/T]$ (which is deterministic), the location of the minima of $J_p(u, v)/T$ converge in probability to the location of the minima of $E[J_p(u, v)/T]$, which is equivalent to saying that the maximum-likelihood estimates of u, v converge in probability to the locations of the minima of $E[J_p(u, v)/T]$ [26]. The set A_p^c is the set of maximum-likelihood estimates of (u, v) as $T \rightarrow \infty$. If $A_p^c = D_p^c$, the maximum-likelihood estimate is consistent and the unknowns are identifiable [26].

To show (A), we first compute $E[J_p(u, v)]$. To clarify and simplify notation we define $s_t(k) = \mathcal{M}'\{(u_t, v_t), k\} = \sqrt{\mathcal{M}\{(u_t, v_t), k\}}$ to be the true value of $s(k)$ corresponding to the k^{th} observation of the true wind (u_t, v_t) . Additionally, we define.

$$V_t(k) \triangleq \alpha^2(k)s_t^4(k) + \beta^2(k)s_t^2(k) + \gamma^2(k) \quad (3.8)$$

and

$$V(k) \triangleq \alpha^2(k)s^4(k) + \beta^2(k)s^2(k) + \gamma^2(k) \quad (3.9)$$

where $V_t(k)$ is the true variance of the k^{th} measurement $z(k)$ (which depends on the true value, $s_t(k)$, of $s(k)$). Non-subscripted $V(k)$ and $s(k)$ are place holders for the estimated $V(k)$ and $s(k)$, whereas a t subscript is used to denote the true values of $V(k)$ and $s(k)$. From Eq. (2.19) we note that $V_t(k)$ and $V(k)$ can also be written, as

$$V_t(k) = \frac{1}{T} Y_t(k) \quad (3.10)$$

and

$$V(k) = \frac{1}{T} Y(k) \quad (3.11)$$

where

$$Y_t(k) \triangleq a(k)s_t^4(k) + b(k)s_t^2(k) + c(k) \quad (3.12)$$

and

$$Y(k) \triangleq a(k)s^4(k) + b(k)s^2(k) + c(k) \quad (3.13)$$

Applying these definitions, and noting the independence of the noise terms, we find that

$$E[z(k)] = s_t^2(k) = \sigma^o(k) \quad (3.14)$$

$$\begin{aligned} E[z^2(k)] &= (1 + \alpha^2(k))s_t^4(k) + \beta^2(k)s_t^2(k) + \gamma^2(k) \\ &= V_t(k) + s_t^4(k) \end{aligned} \quad (3.15)$$

$$\text{Var}[z(k)] = V_t(k) \quad (3.16)$$

$$E[z(j)z(k)] = s_t^2(j)s_t^2(k) \quad \forall j \neq k \quad (3.17)$$

The point-wise objective function $J_p(u, v)$ can be expressed, as

$$J_p(u, v) = \sum_{k=1}^N \left\{ \frac{1}{2} \log V(k) + \frac{1}{2} [z(k) - s^2(k)]^2 / V(k) \right\} \quad (3.18)$$

Taking the expectation of (3.18) and using Eq. (B.8) [Appendix B], we find that

$$\begin{aligned} E[J_p(u, v)] &= E \left[\sum_{k=1}^N \left\{ \frac{1}{2} \log V(k) + \frac{1}{2} [z(k) - s^2(k)]^2 / V(k) \right\} \right] \\ &= \frac{1}{2} \sum_{k=1}^N \left\{ \log V(k) + E \left[[z(k) - s^2(k)]^2 / V(k) \right] \right\} \\ &= \frac{1}{2} \sum_{k=1}^N \left\{ \log V(k) + [V_t(k) + [s_t^2(k) - s^2(k)]^2] / V(k) \right\} \end{aligned} \quad (3.19)$$

which is deterministic. Using Eqs. (3.10) through (3.13), we can write $E[J_p(u, v)]$ explicitly in terms of T , as

$$E[J_p(u, v)] = \frac{1}{2} \sum_{k=1}^N \left\{ \log Y(k) - \log T + T \left[Y_t(k)/T + [s_t^2(k) - s^2(k)]^2 \right] / Y(k) \right\} \quad (3.20)$$

so that

$$\begin{aligned} E \left[\frac{1}{T} J_p(u, v) \right] &= \frac{1}{2} \sum_{k=1}^N \left\{ \frac{1}{T} \log Y(k) - \frac{1}{T} \log T + \right. \\ &\quad \left. \left[Y_t(k)/T + [s_t^2(k) - s^2(k)]^2 \right] / Y(k) \right\} \end{aligned} \quad (3.21)$$

Taking the limit of Eq. (3.21) as $T \rightarrow \infty$, we obtain

$$\lim_{T \rightarrow \infty} E \left[\frac{1}{T} J_p(u, v) \right] = \frac{1}{2} \sum_{k=1}^N [s_t^2(k) - s^2(k)]^2 / Y(k) \quad (3.22)$$

We now wish to show, that

$$\lim_{T \rightarrow \infty} E \left\{ \left[\frac{1}{T} J_p(u, v) - \frac{1}{T} E[J_p(u, v)] \right]^2 \right\} = 0 \quad (3.23)$$

We first note that,

$$\begin{aligned} E \left\{ \left[\frac{1}{T} J_p(u, v) - \frac{1}{T} E[J_p(u, v)] \right]^2 \right\} &= E \left[\frac{1}{T^2} J_p^2(u, v) \right] - \\ &\quad 2E \left[\frac{1}{T^2} J_p(u, v) E[J_p(u, v)] \right] \\ &\quad + \frac{1}{T^2} E^2 [J_p(u, v)] \end{aligned} \quad (3.24)$$

Substituting Eqs. (B.12), (B.13), and (B.17) from Appendix A into Eq. (3.24), and taking the limit as $T \rightarrow \infty$, we find that all terms cancel; hence,

$$\lim_{T \rightarrow \infty} E \left\{ \left[\frac{1}{T} J_p(u, v) - \frac{1}{T} E[J_p(u, v)] \right]^2 \right\} = 0 \quad (3.25)$$

which proves the desired result (A).

We now must show (B). Since $J_p(u, v)/T$ converges in the mean-square to the deterministic function $E[J_p(u, v)/T]$, the locations of the minima of $J_p(u, v)/T$ converge in probability to the minima of $E[J_p(u, v)/T]$. We need only show that $A_p^c = D_p^c$.

From Eq. (3.22),

$$\lim_{T \rightarrow \infty} E \left\{ \frac{J_p(u, v)}{T} \right\} = \sum_{k=1}^N [s_t^2(k) - s^2(k)]^2 / Y(k) \geq 0. \quad (3.26)$$

Equality occurs only when

$$\sum_{k=1}^N [s_t^2(k) - s^2(k)]^2 = 0. \quad (3.27)$$

which is the minimum value of Eq. (3.26). It follows that $s^2(k) = s_t^2(k)$ for all k is the minimum of $\lim_{T \rightarrow \infty} E \left\{ \frac{J_p(u, v)}{T} \right\}$; hence, the set of (u, v) , A_p^c , which minimize $J_p(u, v)$ in the limit, is, by definition, the set D_p^c . This proves result (B).

Wind vector estimation is therefore identifiable to the multimember set D_p^c . The wind estimate will be uniquely identifiable (i.e., to a single (u, v) estimate) if and only if D_p^c contains a single member.

3.3 Summary

In this Chapter the identifiability of wind vectors estimated from wind scatterometer measurements of σ° is considered. It has been shown that wind vectors are set-wise identifiable. Due to the nature of \mathcal{M} , there will be a set of wind solutions which minimize the maximum-likelihood objective function. This is the first time that an estimation-theory-based explanation has been given for why several ambiguities arise in wind vector estimation from wind scatterometer measurements; this provides a theoretical foundation for why dealiasing is needed.

Chapter 4

Development of the Wind Field Model

In this Chapter a parametric descriptive model for near-surface mesoscale wind fields over the ocean, suitable for use in a new estimation-theory-based approach to estimating the wind vector field from scatterometer measurements, is developed.

In this Chapter, the requirements for the wind field model are first described, and then the assumptions used to derive the wind field model are presented. This is followed by the mathematical development of the wind field model. Two model options are considered. Finally, the ability of the resulting model to describe “realistic” near-surface mesoscale wind fields is evaluated. Additional model options are considered in Appendix F. Appendix G contains additional model error analysis for the various model options.

4.1 Wind Field Model Requirements

For model-based wind field estimation we need a mathematical model for describing and/or representing the wind field. This model must be capable of representing near-surface mesoscale wind fields. Since other data sources are not always available, we require that the model use only scatterometer data. To be useful for wind field estimation, the model must be computationally tractable and lend itself to a model parameter estimation formulation [65, 67, 77]. Note that, while we will base the model formulation on physical principles, the model does not necessarily have to be based on atmospheric dynamics, since the model is used only for describing a snapshot of the near-surface wind field and not for propagating winds (see [63, 64]).

In this paper we present a particularly simple wind field model that is based on the geostrophic equation and some rather simplistic assumptions regarding the divergence and curl of the horizontal wind field. We show that this model is adequate for use in wind field estimation.

We require that the wind field model must: (1) be capable of accurately describing near-surface mesoscale wind fields; (2) be based only on scatterometer data (i.e., no other instrument or *in situ* data is assumed to be available); (3) be computationally tractable; and (4) lend itself to a model parameter estimation formulation.

Table 4.1: Summary of the S³Wind measurement accuracy requirements for future space-borne wind scatterometers

Wind Speed Range	Speed Accuracy	Direction Accuracy	Resolution
< 3 m/s	—	—	—
3-6 m/s	± 2 m/s	± 20 deg	100 km
6-100 m/s	± 2 m/s or 10% of wind speed	± 20 deg	≤ 50 km

The role of the wind field model in model-based wind field estimation is to provide a description of the wind field over the scatterometer measurement swath at a fixed instant of time and a resolution of from 25 to 50 km (corresponding to the scatterometer sampling); hence, our wind field model need only be for a sampled wind field. To simplify matters we restrict our attention to limited-area regions with a maximum spatial extent of approximately 600 km (corresponding to the maximum scatterometer swath width [60, 61]).

Based on experience with the SEASAT scatterometer data, the Satellite Surface Stress (S^3) working group [84] recommended wind estimate accuracy requirements for use in the next generation of scatterometers. Their requirements are summarized in Table 4.1. Based on these requirements and the performance of the model-based wind estimation approach presented in subsequent chapters, we have been able to show that only relatively mild requirements are needed on the accuracy of the wind field model. For example, an acceptable RMS wind direction modeling error of < 6 deg and an RMS wind speed error of < 7.5 % are considered acceptable for use in scatterometer wind estimation. These mild requirements permit us to use a very simple parametric wind field model, one with only a small number of parameters. This simplifies the use of the model in the wind field estimation process.

4.2 Wind Field Model Assumptions

Denote the near-surface horizontal wind field of interest (e.g., the neutral stability wind at 19.5 m) by $\mathbf{U} = (u, v)^T$. We are interested in a mathematical model that provides a reasonably accurate description of \mathbf{U} over a (limited-area) region \mathcal{L} . The vorticity ζ and divergence δ of \mathbf{U} are defined, as

$$\zeta = \mathbf{k} \cdot \nabla \times \mathbf{U} \quad (4.1)$$

$$\delta = \nabla \cdot \mathbf{U}. \quad (4.2)$$

Using the Helmholtz Theorem, \mathbf{U} may be defined by a streamfunction ψ and velocity potential χ , according to

$$\mathbf{U} = \mathbf{k} \times \nabla\psi + \nabla\chi \quad (4.3)$$

where $\mathbf{k} \times \nabla\psi$ is a nondivergent vector field and $\nabla\chi$ is a curl-free vector field [10].

Taking the divergence and curl, respectively, of Eq. (4.3) we obtain Poisson equations for ψ and χ [72],

$$\nabla^2\psi = \zeta \quad (4.4)$$

$$\nabla^2\chi = \delta \quad (4.5)$$

These equations appear in the classic problems of partitioning a given wind field into its rotational and non-divergent components and reconstructing a wind field from specified vorticity and divergence [10, 41, 72, 97]. For this latter problem, Lynch [72] argues that the reconstruction is not unique over a limited domain; an arbitrary harmonic function may be added to χ , provided ψ is also altered, to produce the same wind field. From this he concludes that the boundary values of χ may be set arbitrarily. He shows that setting the boundary values of χ to zero minimizes the divergent component of the kinetic energy. Choosing $\chi = 0$ on the boundary ensures a unique reconstruction of the wind field.

Following this line of reasoning, our *first* modeling assumption is to assume that $\chi = 0$ on the boundary of \mathcal{L} which corresponds to assuming that the wind field has a minimum of divergent kinetic energy. Assuming that $\chi = 0$ on the boundary, Eqs. (4.4) and (4.5), the vorticity and divergence fields, and the boundary conditions for ψ , are sufficient for describing the wind vector field.

To obtain simple boundary conditions we make a *second* major modeling assumption by attributing ψ to geostrophic motion. This second assumption is that the streamfunction ψ is proportional to the geostrophic pressure field p , i.e.,

$$\psi = \frac{1}{\rho_s f} p \quad (4.6)$$

where ρ_s is the density and f is the Coriolis parameter. This represents a departure from Lynch's [72] direct method for reconstructing a wind field from the normal velocity component along the boundary and the vorticity and divergence fields. Our approach allows further simplification of the model at a later step.

Note that in a strictly geostrophic formulation, the wind field would be non-divergent and χ would be identically zero. Mesoscale winds, however, may exhibit non-zero divergence; hence, we adopt a more general formulation in which χ is not set to zero. Instead, χ is attributed to the *ageostrophic* component of the wind. This generalization allows us to apply the model to mesoscale wind fields which depart from strict geostrophy. Inclusion of the ageostrophic flow permits the model to span a wider space in describing the wind field. Note that in applying the wind field model, ψ and χ will be determined from the observed wind field.

By making our second modeling assumption, we are able to specify the boundary values for Eqs. (4.4) and (4.5) in terms of the geostrophic pressure field. This avoids the difficulties of using velocity boundary conditions, which may yield an overdetermined system (see the discussion in [72]).

Our *third* modeling assumption is that, over the region of interest, $\rho_s f$ is essentially

constant (i.e., an f -plane approximation); we do this to simplify the mathematics. Again, to simplify the mathematics, we normalize the pressure field by $\rho_s f$ so that $\psi = p$. Applying this pressure field normalization, Eq. (4.3) can be written in component form, as

$$u = -\frac{\partial p}{\partial y} + \frac{\partial \chi}{\partial x} \quad (4.7)$$

$$v = \frac{\partial p}{\partial x} + \frac{\partial \chi}{\partial y} \quad (4.8)$$

These two equations, along with Eqs. (4.4) (in which $\psi = p$) and (4.5) form the basis of our wind field model.

To complete the wind-field model, descriptions of the vorticity and divergence fields are needed. Our *fourth* and final modeling assumption is that the vorticity and divergence fields are continuous, relatively smooth, and vary slowly over the region of interest, \mathcal{L} ; hence, the vorticity and divergence fields can be parameterized using only a small number of unknowns. This is consistent with some of the limited data available [14, 16, 39, 73, 89, 90, 92, 107].

We have considered a number of different parameterizations of the curl and divergence fields (see Appendix F) and have found that for our application (wind estimation from wind scatterometer measurements), bivariate polynomial approximations for these fields result in adequate accuracy, i.e.,

$$\zeta(x, y) \triangleq \sum_{m=0}^{M_c} \sum_{\substack{n=0 \\ m+n \leq M_d}}^{M_c} c_{m,n} x^m y^n \quad (4.9)$$

$$\delta(x, y) \triangleq \sum_{m=0}^{M_d} \sum_{\substack{n=0 \\ m+n \leq M_d}}^{M_d} d_{m,n} x^m y^n \quad (4.10)$$

where M_c and M_d are the model orders and $c_{m,n}$ and $d_{m,n}$ are vorticity and divergence coefficients. Note that the coefficients of the polynomials will be derived from the observed wind fields.

The model orders can be selected arbitrarily (depending on the desired accuracy of the model); however, we have found, based on the results presented below, that $M_c = M_d = 2$ is adequate for wind estimation.

4.3 Model Development

To further develop our simple wind field model, for the purposes of wind field estimation from scatterometer measurements, we discretize Eqs. (4.4), (4.5), and (4.7) - (4.10), on an $N \times N$ equally-spaced grid with spacing h over the region \mathcal{L} . For our purposes the value of h is selected to correspond to the 25-50 km sampling resolution of the wind scatterometer. The swath is segmented into abutting along-track regions (see Figure 1). In the case of

NSCAT, $N = 24$ and $h = 25$ km will cover the entire left or right swath width [30, 60, 61]. By further segmenting the swath into adjacent cross-track regions N may be chosen to be less than 24. In this case, the $Nh \times Nh$ dimensions of the region \mathcal{L} are reduced. We have found that choosing $N = 8$ or 12 provides a good tradeoff between the number of unknowns in the model and the model's accuracy.

The discretization of Eqs. (4.4), (4.5), and (4.7) - (4.10) is stable and will converge assuming that the boundary conditions of the pressure fields are bounded and have bounded higher-order derivatives [80, 85].

We will show below that a simple linear equation can be used to relate the wind vector field at the sample points to the boundary conditions for ψ (i.e., the geostrophic pressure field along the region boundary) and the parameters of the vorticity and divergence field models.

Applying the first-order difference approximations [80],

$$\frac{\partial}{\partial x} a(x) \Big|_{x=ih} \approx \frac{1}{h} [a(x_i) - a(x_{i-1})] \quad (4.11)$$

$$\frac{\partial^2}{\partial x^2} a(x) \Big|_{x=ih} \approx \frac{1}{h^2} [a(x_{i+1}) - 2a(x_i) + a(x_{i-1})] \quad (4.12)$$

to Eqs. (4.4), (4.5), (4.7), and (4.8) and scaling by the discretization interval h , we obtain the following finite-difference equation (FDE) system,

$$u(x_i, y_j) = -[p(x_i, y_j) - p(x_i, y_{j-1})] + [\chi(x_i, y_j) - \chi(x_{i-1}, y_j)] \quad (4.13)$$

$$v(x_i, y_j) = [p(x_i, y_j) - p(x_{i-1}, y_j)] + [\chi(x_i, y_j) - \chi(x_i, y_{j-1})] \quad (4.14)$$

$$\zeta(x_i, y_j) = p(x_{i+1}, y_j) + p(x_i, y_{j+1}) + p(x_{i-1}, y_j) + p(x_i, y_{j-1}) - 4p(x_i, y_j) \quad (4.15)$$

$$\delta(x_i, y_j) = \chi(x_{i+1}, y_j) + \chi(x_i, y_{j+1}) + \chi(x_{i-1}, y_j) + \chi(x_i, y_{j-1}) - 4\chi(x_i, y_j) \quad (4.16)$$

where $i = 1, \dots, N$ and $j = 1, \dots, N$, and where, for convenience, $\zeta(x_i, y_i)$ and $\delta(x_i, y_i)$ have been scaled by an additional factor of h . The boundary conditions for the p field are the geostrophic pressure field $p(x_0, y_j)$ and $p(x_{N+1}, y_j)$ for $j = 1, \dots, N$ and $p(x_i, y_0)$ and $p(x_i, y_{N+1})$ for $i = 1, \dots, N$ (refer to Fig. 4.1). The boundary conditions of the χ field are assumed to be zero.

For notational simplicity we write the discretized streamfunction $p(x_i, y_j)$ as $p_{i,j}$, where $x_i = ih$ and $y_j = jh$. A similar notation will be used for the velocity, vorticity, divergence, and potential velocity fields.

Collecting the finite-difference equations for the streamfunction and potential velocity fields at each point of the square lattice covering \mathcal{L} , Eqs. (4.15) and (4.16) can be written

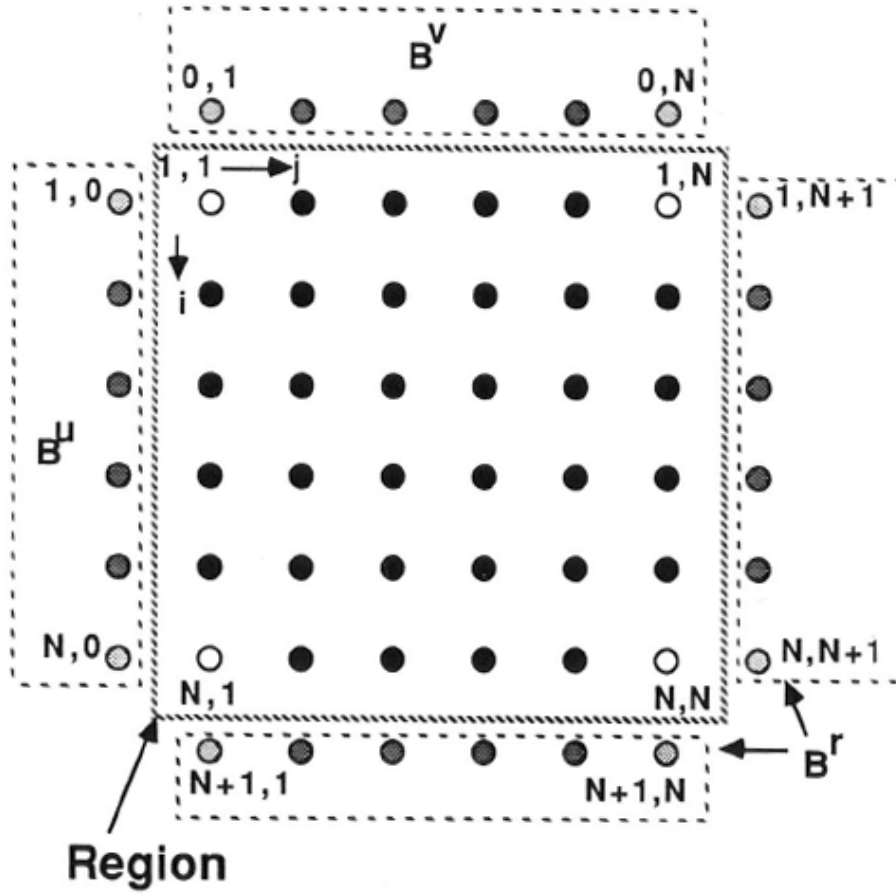


Figure 4.1: A diagram showing the region sample grid for $N = 6$ with boundary conditions and coordinate system. The dark sample points and open circles are the locations of the samples in the region of interest. The grey samples points indicate the locations of the boundary conditions for the pressure field (see text).

as two matrix equations, i.e.,

$$QP + PQ = \frac{1}{4}B + \frac{1}{4}C \quad (4.17)$$

$$QS + SQ = \frac{1}{4}D \quad (4.18)$$

where P , S , C , and D are $N \times N$ matrices with elements $p_{i,j}$, $\chi_{i,j}$, $\zeta_{i,j}$ and $\delta_{i,j}$, respectively; Q is an $N \times N$ tridiagonal, symmetric, Toeplitz matrix with elements $q_{i,j}$ [45, 46], where,

$$q_{i,j} = \begin{cases} \frac{1}{2}, & \text{if } i = j \\ -\frac{1}{4}, & \text{if } |i - j| = 1 \\ 0, & \text{otherwise;} \end{cases} \quad (4.19)$$

and, B is a matrix containing only the p field boundary values (the geostrophic pressure field p along the boundary), i.e., the elements $b_{i,j}$ of B are,

$$b_{i,j} = \begin{cases} p_{i,0} & \text{if } 2 \leq i \leq N - 1 \text{ and } j = 1 \\ p_{i,N+1} & \text{if } 2 \leq i \leq N - 1 \text{ and } j = N \\ p_{0,j} & \text{if } i = 1 \text{ and } 2 \leq j \leq N - 1 \\ p_{N+1,j} & \text{if } i = N \text{ and for } 2 \leq j \leq N - 1 \\ p_{1,0} + p_{0,1} & \text{if } i = 1 \text{ and } j = 1 \\ p_{0,N} + p_{1,N+1} & \text{if } i = 1 \text{ and } j = N \\ p_{N,0} + p_{N+1,1} & \text{if } i = N \text{ and } j = 1 \\ p_{N,N+1} + p_{N+1,N} & \text{if } i = N \text{ and } j = N \\ 0 & \text{otherwise.} \end{cases} \quad (4.20)$$

For clarity, Q and B are,

$$Q = \frac{1}{4} \begin{bmatrix} 2 & -1 & 0 & \dots & 0 \\ -1 & 2 & -1 & \ddots & \vdots \\ 0 & -1 & 2 & \ddots & 0 \\ \vdots & \ddots & \ddots & \ddots & -1 \\ 0 & \dots & 0 & -1 & 2 \end{bmatrix} \quad (4.21)$$

and

$$B = \begin{bmatrix} p_{0,1} + p_{1,0} & p_{0,2} & \dots & p_{0,N-1} & p_{0,N} + p_{1,N+1} \\ p_{2,0} & 0 & \dots & 0 & p_{2,N+1} \\ \vdots & \vdots & \ddots & \vdots & \vdots \\ p_{N-1,0} & 0 & \dots & 0 & p_{N-1,N+1} \\ p_{N,0} + p_{N+1,1} & p_{N+1,2} & \dots & p_{N+1,N-1} & p_{N,N+1} + p_{N+1,N} \end{bmatrix}. \quad (4.22)$$

We will see that the solution for the p field can be written as the sum of two independent fields; one which is solely a function of the boundary conditions for p and one which is solely a function of the ζ field. Given that the boundary conditions for the χ field are zero, the solution for the χ field depends only on the δ field.

For later convenience we decompose B into 3 $N \times N$ matrices,

$$B = B^v + B^u + B^r \quad (4.23)$$

where the elements of each matrix are,

$$b_{i,j}^u = \begin{cases} p_{i,0} & \text{if } j = 1, i = 1, \dots, N \\ 0 & \text{otherwise} \end{cases} \quad (4.24)$$

$$b_{i,j}^v = \begin{cases} p_{0,j} & \text{if } i = 1, j = 1, \dots, N \\ 0 & \text{otherwise} \end{cases} \quad (4.25)$$

$$b_{i,j}^r = \begin{cases} p_{i,N+1} & \text{if } 1 \leq i \leq N-1 \text{ and } j = N \\ p_{N+1,j} & \text{if } i = N \text{ and for } 1 \leq j \leq N-1 \\ p_{N,N+1} + p_{N+1,N} & \text{if } i = N \text{ and } j = N \\ 0 & \text{otherwise} \end{cases} \quad (4.26)$$

For clarity,

$$B^u = \begin{bmatrix} p_{1,0} & 0 & \dots & 0 \\ \vdots & \vdots & \ddots & \vdots \\ p_{N,0} & 0 & \dots & 0 \end{bmatrix}, \quad (4.27)$$

$$B^v = \begin{bmatrix} p_{0,1} & \dots & p_{0,N} \\ 0 & \dots & 0 \\ \vdots & \ddots & \vdots \\ 0 & \dots & 0 \end{bmatrix}, \quad (4.28)$$

and

$$B^r = \begin{bmatrix} 0 & \dots & 0 & p_{1,N+1} \\ \vdots & \ddots & \vdots & \vdots \\ 0 & \dots & 0 & p_{N-1,N+1} \\ p_{N+1,1} & \dots & p_{N+1,N-1} & p_{N,N+1} + p_{N+1,N} \end{bmatrix}. \quad (4.29)$$

Using an overbar to denote an $N^2 \times 1$ vector of lexicographic-ordered (row order) elements of an $N \times N$ matrix, Eqs. (4.17) and (4.18) can be reexpressed, as

$$K\bar{P} = \frac{1}{4}\bar{B} + \frac{1}{4}\bar{C} \quad (4.30)$$

$$K\bar{S} = \frac{1}{4}\bar{D} \quad (4.31)$$

where K is an $N^2 \times N^2$ Toeplitz matrix defined, as

$$K \triangleq I \otimes Q + Q \otimes I \quad (4.32)$$

where \otimes is the Kronecker-product [12, 46]. It can be shown that K is invertible and has a simple closed form (see Appendix E).

Since K is invertible, Eqs. (4.30) and (4.31) have the unique solutions,

$$\bar{P} = \frac{1}{4}K^{-1}[\bar{B} + \bar{C}] \quad (4.33)$$

$$= \frac{1}{4}K^{-1}(\bar{B}^u + \bar{B}^v + \bar{B}^r) + \frac{1}{4}K^{-1}\bar{C} \quad (4.34)$$

$$\bar{S} = \frac{1}{4}K^{-1}\bar{D} \quad (4.35)$$

Starting with the first two equations of the FDE system, (4.13) and (4.14), reexpressed as

$$u_{i,j} = -(\psi_{i,j} - \psi_{i,j-1}) + (\chi_{i,j} - \chi_{i-1,j}) \quad (4.36)$$

$$v_{i,j} = (\psi_{i,j} - \psi_{i-1,j}) + (\chi_{i,j} - \chi_{i,j-1}), \quad (4.37)$$

where $i = 1, \dots, N$ and $j = 1, \dots, N$, we can relate the p and χ fields to the velocity field. To write Eqs. (4.36) and (4.37) in matrix form, let U and V be $N \times N$ matrices with elements $u_{i,j}$ and $v_{i,j}$, respectively. These equations can then be written, as

$$U = [P(D^s - I)^T + B^u] + (I - D^s)S \quad (4.38)$$

$$V = [(I - D^s)P - B^v] - S(D^s - I)^T \quad (4.39)$$

where D^s is an $N \times N$ matrix which has a unity sub-diagonal and is zero everywhere else, i.e.,

$$d_{i,j}^s = \begin{cases} 1, & \text{if } j = i - 1 \\ 0, & \text{else} \end{cases} \quad (4.40)$$

For clarity,

$$D^s = \begin{bmatrix} 0 & \dots & & \dots & 0 \\ 1 & 0 & \ddots & & \vdots \\ 0 & \ddots & \ddots & \ddots & \\ \vdots & \ddots & \ddots & \ddots & \vdots \\ 0 & \dots & 0 & 1 & 0 \end{bmatrix} \quad (4.41)$$

Using lexicographic-ordered vectors, Eqs. (4.38) and (4.39) can be written, as

$$\bar{U} = [G\bar{P} + \bar{B}^u] + H\bar{S} \quad (4.42)$$

$$\bar{V} = [H\bar{P} - \bar{B}^v] - G\bar{S} \quad (4.43)$$

where the $N^2 \times N^2$ matrices G and H are defined, as

$$G \triangleq I \otimes [D^s - I] \quad (4.44)$$

$$H \triangleq [I - D^s] \otimes I. \quad (4.45)$$

By using the properties of the Kronecker product and the definition of D it can be shown that G is the block Jordan-form matrix,

$$G = \begin{bmatrix} D^s - I & 0 & \dots & 0 \\ 0 & D^s - I & \ddots & \vdots \\ \vdots & \ddots & \ddots & 0 \\ 0 & \dots & 0 & D^s - I \end{bmatrix} \quad (4.46)$$

while H is a block tridiagonal matrix,

$$H = \begin{bmatrix} I & 0 & 0 & \dots & 0 \\ -I & I & 0 & \dots & 0 \\ 0 & -I & I & \ddots & \vdots \\ \vdots & \ddots & \ddots & \ddots & 0 \\ 0 & \dots & 0 & -I & I \end{bmatrix} \quad (4.47)$$

Both G and H are full rank and invertible. It can be readily verified that the matrix T , with elements $t_{i,j}$, where

$$t_{i,j} = \begin{cases} 1, & \text{if } j \leq i \\ 0, & \text{otherwise} \end{cases} \quad (4.48)$$

is the inverse of the matrix $(I - D^s)$, i.e., $(I - D^s)^{-1} = T$; hence,

$$G^{-1} = I \otimes T \quad (4.49)$$

$$H^{-1} = T \otimes I. \quad (4.50)$$

Note that \bar{B}^u and \bar{B}^v are N^2 element vectors with a maximum of N non-zero elements whereas \bar{B}^r is an N^2 element vector with a maximum of $2N - 1$ non-zero elements. Consequently, there are a maximum of $4N - 1$ non-zero parameters in the \bar{B} vector.

We note that the wind velocity is proportional to the partial derivatives (or, in this formulation, first-order differences) of the p and χ fields. An arbitrary constant can be added or subtracted from the p and χ fields without affecting the results; hence, a constant

can be added to or subtracted from the boundary condition vectors without affecting the results. Since this additive constant is arbitrary and is unimportant, we can normalize the boundary condition vectors \overline{B}^u , \overline{B}^v , and \overline{B}^r so that the first element of \overline{B}^u , $\psi_{0,1}$, is zero. This effectively eliminates one non-zero parameter, reducing the number of non-zero parameters in \overline{B}^u , \overline{B}^v , and \overline{B}^r from $4N - 1$ to $4N - 2$.

With this normalization accomplished, \overline{B}^u and \overline{B}^v will be linearly independent since they have no corresponding non-zero elements. With the exception of the $(n_1 = N)^{th}$ element, where

$$\overline{B}_{n_1}^v = p_{0,N} \quad (4.51)$$

and

$$\overline{B}_{n_1}^r = p_{1,N+1}, \quad (4.52)$$

the vectors \overline{B}^v and \overline{B}^r have no corresponding non-zero elements. Similarly, With the exception of the $(n_2 = N^2 - N + 1)^{th}$ element, where

$$\overline{B}_{n_2}^u = p_{N,0} \quad (4.53)$$

and

$$\overline{B}_{n_2}^r = p_{N+1,1}, \quad (4.54)$$

the vectors \overline{B}^u and \overline{B}^r have no corresponding non-zero elements.

Note, also, that the last element of \overline{B}^r is the sum of two boundary values, $p_{N,N+1}$ and $p_{N+1,N}$; hence, we do not need to separately identify these values and so we need only identify the sum.

Substituting Eqs. (4.33) and (4.35) into Eqs. (4.42) and (4.43), we obtain

$$\overline{U} = \left[\frac{1}{4}GK^{-1}(\overline{B} + \overline{C}) + \overline{B}^u \right] + \frac{1}{4}HK^{-1}\overline{D} \quad (4.55)$$

$$= \frac{1}{4} \left[GK^{-1}(\overline{B}^r + \overline{B}^v + \overline{C}) + (GK^{-1} + 4I)\overline{B}^u \right] + \frac{1}{4}HK^{-1}\overline{D} \quad (4.56)$$

$$\overline{V} = \left[\frac{1}{4}HK^{-1}(\overline{B} + \overline{C}) - \overline{B}^v \right] - \frac{1}{4}GK^{-1}\overline{D} \quad (4.57)$$

$$= \frac{1}{4} \left[HK^{-1}(\overline{B}^r + \overline{B}^u + \overline{C}) + (HK^{-1} - 4I)\overline{B}^v \right] - \frac{1}{4}GK^{-1}\overline{D} \quad (4.58)$$

To write Eqs. (4.56) and (4.58) as a single equation, observe that they have the general form,

$$\overline{U} = {}_1A(\overline{B}^r + \overline{C}) + {}_1A\overline{B}^v + {}_2A\overline{B}^u + {}_3A\overline{D} \quad (4.59)$$

$$\overline{V} = {}_3A(\overline{B}^r + \overline{C}) + {}_3A\overline{B}^u + {}_4A\overline{B}^v - {}_1A\overline{D} \quad (4.60)$$

where the ${}_jA$ matrices are defined, as

$${}_1A = \frac{1}{4}GK^{-1} \quad (4.61)$$

$${}_2A = \frac{1}{4}[GK^{-1} + 4I] \quad (4.62)$$

$${}_3A = \frac{1}{4}HK^{-1} \quad (4.63)$$

$${}_4A = \frac{1}{4}[HK^{-1} - 4I]. \quad (4.64)$$

Let \bar{X} be a $4N - 2$ element vector of the non-zero elements of \bar{B}^r , \bar{B}^u , and \bar{B}^v , where the n^{th} element, \bar{x}_n , of \bar{X} is,

$$\bar{x}_n = \begin{cases} \bar{B}_{n+1}^v & 1 \leq n < N \\ \bar{B}_{(n-N)N+1}^u & N \leq n < 2N \\ \bar{B}_{(n-2N+1)N}^r & 2N \leq n < 3N \\ \bar{B}_{n-4N+N^2+1}^r & 3N \leq n \leq 4N - 2 \end{cases} \quad (4.65)$$

For clarity,

$$\bar{X} = \begin{bmatrix} \bar{x}_1 \\ \bar{x}_2 \\ \vdots \\ \bar{x}_{N-1} \\ \bar{x}_N \\ \bar{x}_{N+1} \\ \bar{x}_{N+2} \\ \vdots \\ \bar{x}_{2N-1} \\ \bar{x}_{2N} \\ \bar{x}_{2N+1} \\ \vdots \\ \bar{x}_{3N-2} \\ \bar{x}_{3N-1} \\ \bar{x}_{3N} \\ \vdots \\ \bar{x}_{4N-2} \end{bmatrix} = \begin{bmatrix} p_{0,2} \\ p_{0,3} \\ \vdots \\ p_{0,N} \\ p_{1,0} \\ p_{2,0} \\ p_{3,0} \\ \vdots \\ p_{N,0} \\ p_{1,N+1} \\ p_{2,N+1} \\ \vdots \\ p_{N-1,N+1} \\ p_{N,N+1} + \psi_{N+1,N} \\ p_{N+1,1} \\ \vdots \\ p_{N+1,N-1} \end{bmatrix} = \begin{bmatrix} \bar{B}_2^v \\ \bar{B}_3^v \\ \vdots \\ \bar{B}_N^v \\ \bar{B}_1^u \\ \bar{B}_{N+1}^u \\ \bar{B}_{2N+1}^u \\ \vdots \\ \bar{B}_{N^2-N+1}^u \\ \bar{B}_N^r \\ \bar{B}_{2N}^r \\ \vdots \\ \bar{B}_{N^2-N}^r \\ \bar{B}_{N^2}^r \\ \bar{B}_{N^2-N+1}^r \\ \vdots \\ \bar{B}_{N^2-1}^r \end{bmatrix} \quad (4.66)$$

Define the N^2 element vector \bar{W} as the concatenation of \bar{U} and \bar{V} , i.e.,

$$\bar{W} = \begin{bmatrix} \bar{U} \\ \bar{V} \end{bmatrix}. \quad (4.67)$$

Then, the wind field model, Eqs. (4.59) and (4.60), can be expressed as the single equation,

$$\overline{W} = F\overline{X} + R^c\overline{C} + R^d\overline{D} \quad (4.68)$$

where F is a $2N^2 \times (4N - 2)$ matrix and R^c and R^d are $2N^2 \times N^2$ matrices. F , R^c and R^d are composed of columns of the A matrices in Eqs. (4.61) through (4.64).

For convenience in defining F , we partition F into 4 rectangular submatrices,

$$F = [F_1 \mid F_2 \mid F_3 \mid F_4] \quad (4.69)$$

where the F_i matrices are defined, as

$$F_1 = \left[\begin{array}{c|c|c|c} \frac{1A_2}{4A_2} & \frac{1A_3}{4A_3} & \dots & \frac{1A_N}{4A_N} \end{array} \right] \quad (4.70)$$

$$F_2 = \left[\begin{array}{c|c|c|c} \frac{2A_1}{3A_1} & \frac{2A_{N+1}}{3A_{N+1}} & \dots & \frac{2A_{N^2-N+1}}{3A_{N^2-N+1}} \end{array} \right] \quad (4.71)$$

$$F_3 = \left[\begin{array}{c|c|c|c} \frac{1A_N}{3A_N} & \frac{1A_{2N}}{3A_{2N}} & \dots & \frac{1A_{N^2}}{3A_{N^2}} \end{array} \right] \quad (4.72)$$

$$F_4 = \left[\begin{array}{c|c|c|c} \frac{1A_{N^2-N+1}}{3A_{N^2-N+1}} & \frac{1A_{N^2-N+2}}{3A_{N^2-N+2}} & \dots & \frac{1A_{N^2-1}}{3A_{N^2-1}} \end{array} \right] \quad (4.73)$$

where ${}_jA_i$ is the i^{th} column of the j^{th} A matrix in Eqs. (4.61) through (4.64). The matrices F_1 and F_4 are $2N^2 \times (N - 1)$ while F_2 and F_3 are $2N^2 \times N$. The matrix R^c is defined, as

$$R^c = \left[\begin{array}{c} \frac{1A}{3A} \end{array} \right] \quad (4.74)$$

whereas the matrix R^d is defined, as

$$R^d = \left[\begin{array}{c} \frac{3A}{-1A} \end{array} \right] \quad (4.75)$$

Eq. (4.68) provides a single matrix-vector equation relating the wind field velocity components contained in the $2N^2$ element vector \overline{W} to the $4N - 2$ element boundary condition vector \overline{X} and the N^2 element vorticity and divergence field vectors \overline{C} and \overline{D} , respectively.

Note that Eq. (4.68) can be expressed, as

$$\overline{W} = \overline{W}^b + \overline{W}^c + \overline{W}^d \quad (4.76)$$

where

$$\overline{W}^b \triangleq F\overline{X} \quad (4.77)$$

$$\overline{W}^c \triangleq R^c\overline{C} \quad (4.78)$$

$$\overline{W}^d \triangleq R^d\overline{D} \quad (4.79)$$

The wind field \overline{W} can therefore be expressed as the sum of a field \overline{W}^b which depends only on the boundary conditions in \overline{X} , a field \overline{W}^c which depends only on the vorticity field in \overline{C} , and a field \overline{W}^d which depends only on the divergence field in \overline{D} .

From our fourth modeling assumption, we assume that the vorticity and divergence fields can be parameterized (or modeled) by a small number of unknown but deterministic parameters which are the coefficients of the bivariate polynomials in Eqs. (4.9) and (4.10). Using this parameterization, the wind field model can then be formulated in terms of the boundary conditions on the p field and the parameters of the vorticity and divergence field model. The number of parameters in the vorticity and divergence field models are $N_C = (M_c + 1)(M_c + 2)/2$ and $N_D = (M_d + 1)(M_d + 2)/2$, respectively.

Using this polynomial parameterization for the vorticity and divergence fields, Eq. (4.68) can be written, as

$$\overline{W} = F\overline{X} + R^c \sum_{m=0}^{M_c} \sum_{\substack{n=0 \\ m+n \leq M_c}}^{M_c} c_{m,n} Q_{m,n} + R^d \sum_{m=0}^{M_d} \sum_{\substack{n=0 \\ m+n \leq M_d}}^{M_d} d_{m,n} Q_{m,n} \quad (4.80)$$

$$= F\overline{X} + \sum_{m=0}^{M_c} \sum_{\substack{n=0 \\ m+n \leq M_c}}^{M_c} c_{m,n} R^c Q_{m,n} + \sum_{m=0}^{M_d} \sum_{\substack{n=0 \\ m+n \leq M_d}}^{M_d} d_{m,n} R^d Q_{m,n} \quad (4.81)$$

where the k^{th} element ${}_k q_{m,n}$ of the N^2 element vector $Q_{m,n}$ is,

$${}_k q_{m,n} = [k]^m + [k]^n \quad (4.82)$$

in which $[k] \triangleq \text{int}[(k-1)/N] + 1$ and $[k] \triangleq \text{mod}(k-1, N) + 1$. The constant vorticity or divergence case corresponds to $M_c = 0$ or $M_d = 0$, respectively. The case when the vorticity or divergence is assumed to be identically zero will be denoted by $M_c = -1$ or $M_d = -1$, respectively.

A simple special case occurs for $M_c = M_d = 1$; then,

$$\zeta_{i,j} = c_{0,0} + c_{1,0}i + c_{0,1}j \quad (4.83)$$

$$\delta_{i,j} = d_{0,0} + d_{1,0}i + d_{0,1}j \quad (4.84)$$

so that Eq. (4.68) can be written, as

$$\overline{W} = F\overline{X} + c_{0,0}\overline{R}^c + c_{1,0}\overline{R}_x^c + c_{0,1}\overline{R}_y^c + d_{0,0}\overline{R}^d + d_{1,0}\overline{R}_x^d + c_{0,1}\overline{R}_y^d \quad (4.85)$$

where \overline{R}^c , \overline{R}^d , \overline{R}_x^c , \overline{R}_y^c , \overline{R}_x^d , and \overline{R}_y^d are $2N^2$ vectors with elements \overline{R}_k^c , \overline{R}_k^d , $\overline{R}_{x_k}^c$, $\overline{R}_{y_k}^c$, $\overline{R}_{x_k}^d$ and $\overline{R}_{y_k}^d$ defined, as

$$\overline{R}_k^c = \sum_{i=1}^N \sum_{j=1}^N r_{k,j+(i-1)N}^c \quad (4.86)$$

$$\overline{R}_k^d = \sum_{i=1}^N \sum_{j=1}^N r_{k,j+(i-1)N}^d \quad (4.87)$$

$$\overline{R}_{x_k}^c = \sum_{i=1}^N i \sum_{j=1}^N r_{k,j+(i-1)N}^c \quad (4.88)$$

$$\overline{R}_{y_k}^c = \sum_{j=1}^N j \sum_{i=1}^N r_{k,j+(i-1)N}^c \quad (4.89)$$

$$\overline{R}_{x_k}^d = \sum_{i=1}^N i \sum_{j=1}^N r_{k,j+(i-1)N}^d \quad (4.90)$$

$$\overline{R}_{y_k}^d = \sum_{j=1}^N j \sum_{i=1}^N r_{k,j+(i-1)N}^d \quad (4.91)$$

where $r_{k,j}^c$ and $r_{k,j}^d$ are the elements of R^c and R^d , respectively.

To express Eq. (4.85) in a simple form, we define a new $4N + 4$ parameter vector \overline{X}_r by augmenting \overline{X} with $c_{0,0}$, $c_{1,0}$, $c_{0,1}$, $d_{0,0}$, $d_{1,0}$ and $d_{0,1}$, i.e.,

$$\overline{X}_r = \begin{bmatrix} \overline{X} \\ c_{0,0} \\ c_{1,0} \\ c_{0,1} \\ d_{0,0} \\ d_{1,0} \\ d_{0,1} \end{bmatrix} \quad (4.92)$$

and let the $2N^2 \times (4N + 4)$ matrix F_r be the matrix created by column-augmenting the matrix F with \overline{R} , \overline{R}_x^c , etc.; i.e.,

$$F_r = \left[F \mid \overline{R}^c \mid \overline{R}_x^c \mid \overline{R}_y^c \mid \overline{R}^d \mid \overline{R}_x^d \mid \overline{R}_y^d \right]. \quad (4.93)$$

Equation (4.85) can then be written, as

$$\overline{W} = F_r \overline{X}_r \quad (4.94)$$

Since G , H and K are invertible, ${}_1A$ and ${}_3A$ are full rank (i.e., they have independent columns) and invertible. It is shown that the columns of F are linearly independent in Appendix E; hence, F is full rank. It follows from the definitions of R^c and R^d that the columns of R^c and R^d are linearly independent. We note that \overline{R}^c , \overline{R}^d , \overline{R}_x^c , \overline{R}_y^c , \overline{R}_x^d and \overline{R}_y^d are linearly independent of each other (for $N > 3$) and, further, that these vectors are independent of the columns of F . It follows that the columns of F_r are linearly independent so that F_r is full rank; hence, there is a unique relationship between a given \overline{W} and the parameters \overline{X}_r . Given \overline{W} , a least-squares estimate of \overline{X}_r is,

$$\overline{X}_r = F_r^\dagger \overline{W} \quad (4.95)$$

where F_r^\dagger is the generalized inverse of F_r . Since the system of equations is overdetermined, $F_r^\dagger = (F_r^T F_r)^{-1} F_r^T$.

The extension of this approach of augmenting the parameters of the vorticity and divergence field models to the boundary conditions for higher-order polynomial orders is straightforward.

4.4 Parameterizing the Boundary Conditions

For a given choice of M_c and M_d , the final wind field model has the form of Eq. (4.94); the wind field is a simple linear function of the boundary conditions for p and the parameters of the vorticity and divergence fields. This model is referred to as the normal boundary (NB) wind field model.

Early in the testing of this wind field model, it became apparent that, since the geostrophic pressure field tends to be very smooth at the mesoscale, the number of unknown boundary values can be reduced by parameterizing the geostrophic pressure field around the region's boundary. While not a required part of our wind field model, minimizing the number of unknown parameters in the model significantly reduces the CPU time required to determine the optimum model parameters, when our model is applied to wind field estimation from wind scatterometer measurements.

We note that the pressure field around the square region of interest will be continuous. Since the boundary is closed, the pressure field along the boundary will be periodic. We now parameterize the pressure p as a one-dimensional function along the boundary of the region \mathcal{L} . We write the pressure field around the boundary as $p(l)$, where l is related to the discretization grid indexes i and j clockwise around the boundary, according to

$$l = \begin{cases} j, & i = 0, 0 \leq j \leq N + 1, \\ i + N + 1, & j = N + 1, 0 < i \leq N + 1, \\ 2N + 2 - j, & i = N + 1, 0 \leq j \leq N + 1, \\ 4N + 4 - i, & j = 0, 0 \leq i < N + 1. \end{cases} \quad (4.96)$$

This formulation provides a one-to-one mapping from l to the region's boundary. Observe

that l runs from 0 to $4N + 4$. For notational simplicity, we write $p(l)$ as p_l .

Since p_l is “smooth” and must be periodic, a low-order Fourier series representation is appropriate for it, i.e.,

$$p_l = s_0 + \sum_{k=1}^{(M_l-1)/2} \left[s_k^c \cos\left(\frac{kl\pi}{2(N+1)}\right) + s_k^s \sin\left(\frac{kl\pi}{2(N+1)}\right) \right] \quad (4.97)$$

where M_l is the order of the pressure boundary condition model. We have already noted that an arbitrary constant can be added to the pressure field without affecting the model formulation, so we can ignore the s_0 term. This requires that we modify the definition of F_1 slightly to incorporate the boundary value $p_{0,1}$. Let F'_1 be the $2N^2 \times N$ rectangular matrix defined, as

$$F'_1 = \left[\begin{array}{c|c|c|c} {}_1A_1 & {}_1A_2 & \dots & {}_1A_N \\ \hline {}_4A_1 & {}_4A_2 & \dots & {}_4A_N \end{array} \right] = \left[\begin{array}{c|c} {}_1A_1 & \\ \hline {}_4A_1 & F_1 \end{array} \right]. \quad (4.98)$$

Let the M_l element vector \bar{Y} be defined, as

$$\bar{Y} \triangleq \begin{bmatrix} s_1^c \\ s_1^s \\ s_2^c \\ s_2^s \\ \vdots \\ s_{(M_l-1)/2}^c \\ s_{(M_l-1)/2}^s \end{bmatrix} \quad (4.99)$$

Equations (4.59) and (4.60) can be then be written as,

$$\bar{W} = \mathcal{F}\bar{Y} + R^c C + R^d D \quad (4.100)$$

where \mathcal{F} is a $2N^2 \times M_l$ rectangular matrix created from the F_j matrices and F'_1 . Let $f_{i,j}$ be

the $(i, j)^{th}$ element of \mathcal{F} and $(F_k)_{i,j}$ be the $(i, j)^{th}$ element of the F_k matrix; then,

$$f_{i,j} = \begin{cases} \sum_{k=1}^N \left\{ (F'_1)_{i,k} \cos[jk\pi/(2N+2)] \right. \\ \quad + (F_2)_{i,k} \cos[j(2-k)\pi/(2N+2)] & \text{for } j \text{ odd} \\ \quad + (F_3)_{i,k} \cos[j(1+k)\pi/(2N+2)] \\ \quad \left. + (F_4)_{i,k} \cos[j(3-k)\pi/(2N+2)] \right\} \\ \sum_{k=1}^N \left\{ (F'_1)_{i,k} \sin[jk\pi/(2N+2)] \right. \\ \quad + (F_2)_{i,k} \sin[j(2-k)\pi/(2N+2)] & \text{for } j \text{ even.} \\ \quad + (F_3)_{i,k} \sin[j(1+k)\pi/(2N+2)] \\ \quad \left. + (F_4)_{i,k} \sin[j(3-k)\pi/(2N+2)] \right\} \end{cases} \quad (4.101)$$

The final parameterized boundary condition (PBC) wind field model is created by augmenting \bar{Y} with the parameters of the vorticity and divergence field model, as previously done for the NB model.

4.5 Evaluating the Wind Field Model

Both the NB and PBC wind field model options have the general form,

$$\bar{W} = F\bar{X} \quad (4.102)$$

where \bar{W} contains the components of the sampled wind field over the region \mathcal{L} , F is a known constant matrix, and \bar{X} is the model parameter vector. We now consider how well these models can represent realistic wind fields for different orders of the vorticity and divergence field models and field size N .

To evaluate the modeling error: (1) a least-squares fit of the model parameters to a real wind field was obtained; (2) the resulting ‘‘model’’ wind field was computed from the model parameters; and, (3) the root-mean-square (RMS) difference between the true field and the model field was computed.

The sampled ‘‘true’’ wind field over \mathcal{L} is denoted by \bar{W}_t . The least-squares fit \bar{X} of the model parameters to \bar{W}_t is

$$\bar{X} = F^\dagger \bar{W}_t \quad (4.103)$$

where $F^\dagger = (F^T F)^{-1} F^T$ is the pseudo-inverse of F [58]. The wind field computed from the model parameter vector, denoted \bar{W} , is

$$\bar{W} = F\bar{X}. \quad (4.104)$$

Table 4.2: RMS difference between the true wind field in Fig. 4.2 and the field in Fig. 4.3.

Normalized Vector	Direction (deg)	Normalized Speed
0.08	4.24	0.06

The vector error between \overline{W}_t and \overline{W} is then,

$$\overline{W}_t - \overline{W} = (I - FF^\dagger)\overline{W}_t = (I - F(F^T F)^{-1}F^T)\overline{W}_t. \quad (4.105)$$

To illustrate the model performance, consider Figs. 4.2 and 4.3. A simulated (described below) mesoscale wind field, sampled at 25 km with $N = 12$, is shown in Fig. 4.2. A vector length equal to the distance between samples corresponds to a wind speed of 15 m/s. The model parameter vector \overline{X} was computed using Eq. (4.103). The model wind field \overline{W} was then computed using Eq. (4.104) and is plotted in Fig. 4.3. For this example, the NB model was used with $M_c = M_d = 2$. The RMS differences between \overline{W}_t and \overline{W} are tabulated in Table 4.2. In this and succeeding tables, the RMS vector error is defined as the square root of the mean squared magnitude of the vector difference between the true field and the estimated field. The value shown is normalized by the RMS vector magnitude of the true wind field. Similarly, the RMS wind speed error has been normalized by the RMS wind speed of the true wind field. Note the close agreement between the true and model wind fields.

To evaluate our model formulation we have used simulated mesoscale wind fields, since little conventional mesoscale wind field data over the ocean is available. A detailed description of how these fields were created is given in Appendix D. A summary is provided here. The test wind fields were generated by state-of-the-art numerical weather prediction models at 1.875 deg resolution. The surface wind fields were interpolated to 10 km and non-divergent small-scale variability with a ak^{-2} spectrum and random phase [9, 33] added. For a given 2000×2000 km region, the value of a was selected to be consistent with the spectrum within the region [33]. The wind fields were selected to span a wide range of meteorological conditions. An example of a portion of one of the test fields is shown in Fig. 4.4. Regions of high vorticity and non-zero divergence are readily observable. The sampling interval is 80 km with a vector length corresponding to the sampling distance equivalent to 15 m/s.

To evaluate the modeling error for a wind field model of size N , each wind field was segmented into $N \times N$ regions. For each region segment, the model parameters were computed using the approach described above, and the model wind field was computed from the model parameters. The RMS of the error between the true and model fields was computed over all possible regions within the original true wind field. The results for various model options are described below.

As a general rule, for fixed N , as M_c and M_d are increased, the modeling error is reduced. For given values of M_c and M_d , as N is increased, the modeling error increases. Since the

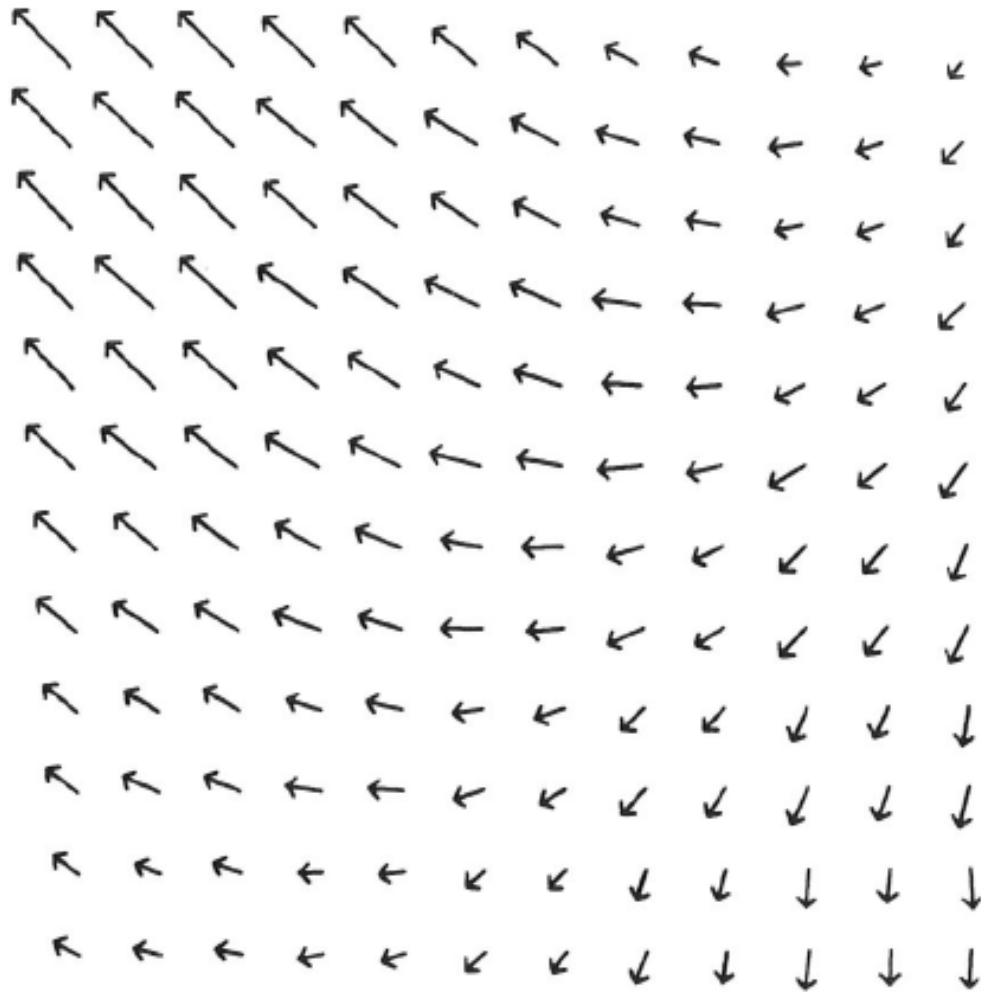


Figure 4.2: An example of a wind field uniformly sampled with $h = 50$ km over a 600×600 km region. A vector length equal to the sample spacing corresponds to 15 m/s.

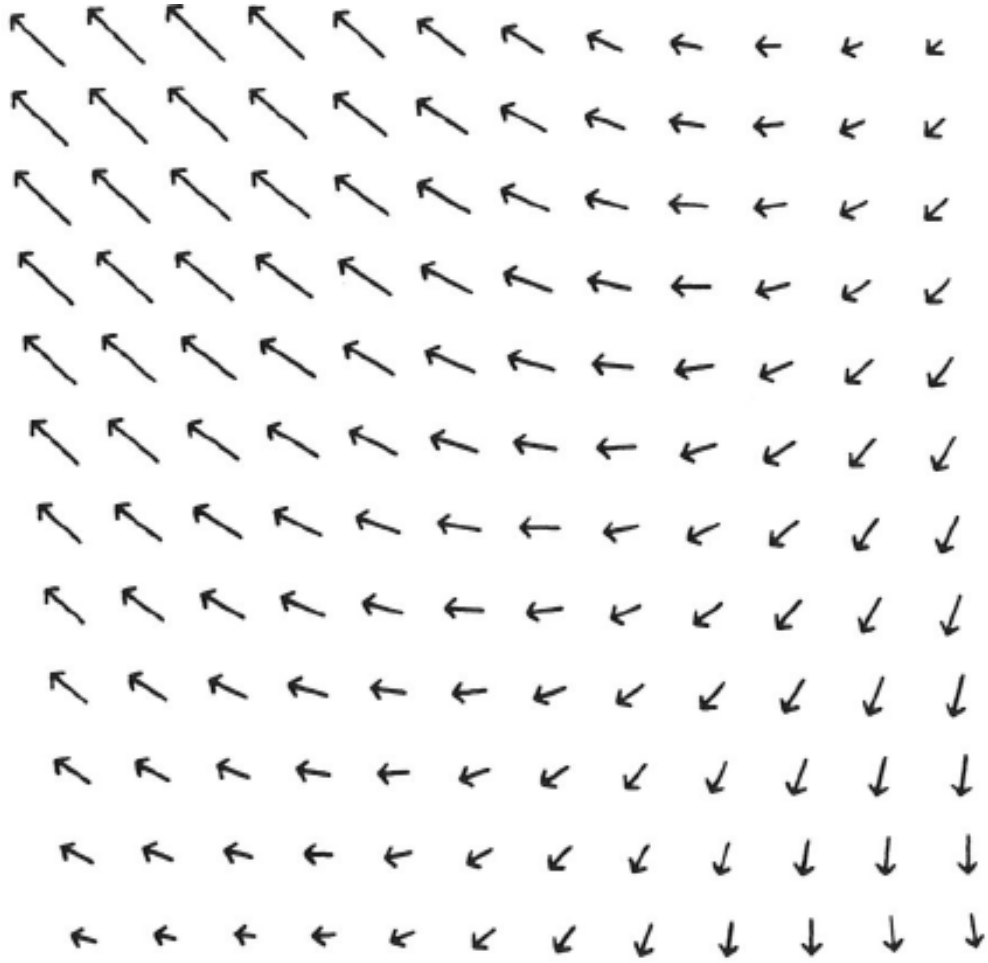


Figure 4.3: The “model” wind field resulting from fitting the NB model with $M_c = M_d = 4$ and $N = 12$ to the wind field shown in Fig. 4.2. Plotting conventions and scale are the same as in Fig. 4.2.

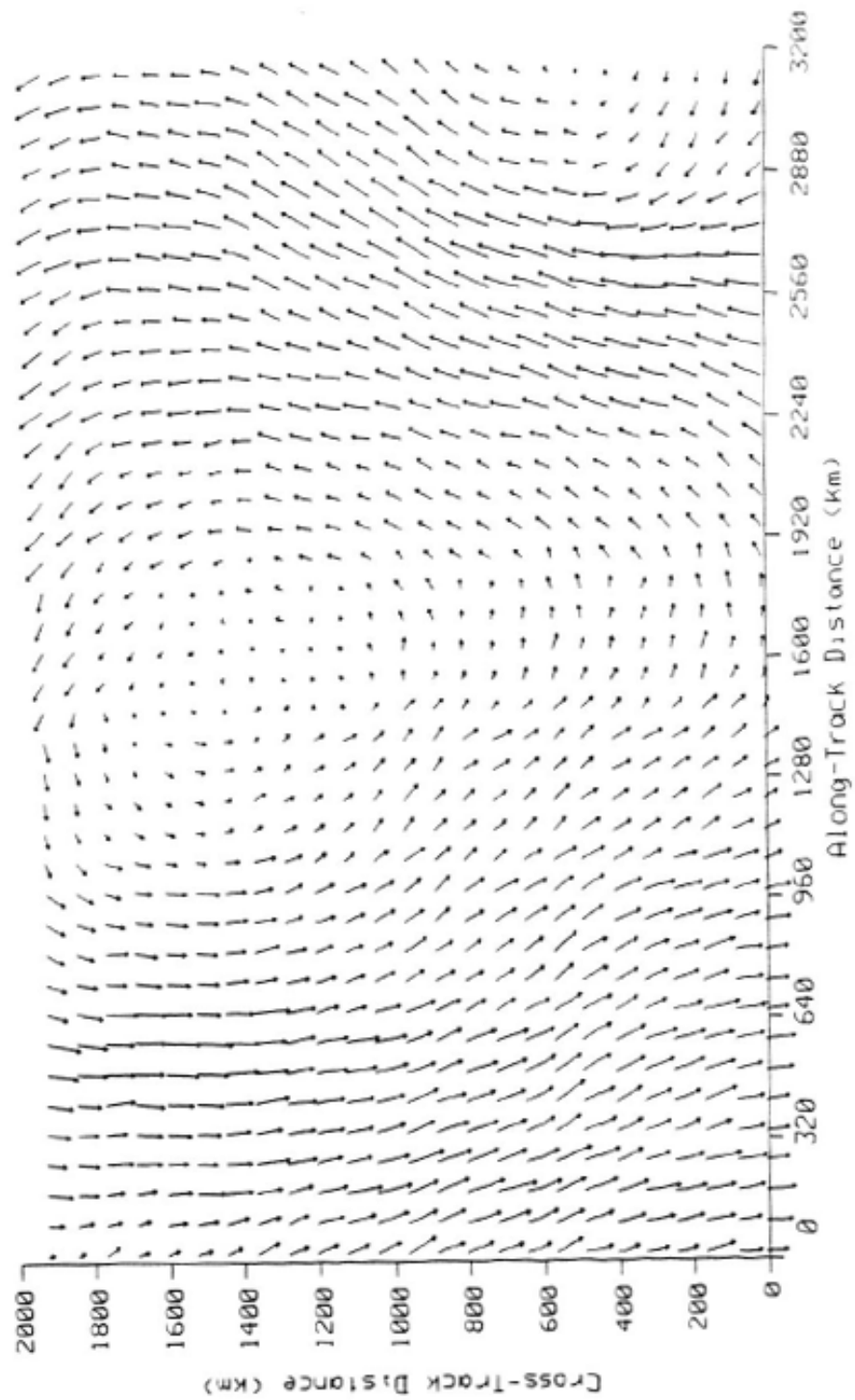


Figure 4.4: An example of the mesoscale wind fields used in evaluating the model accuracy. The field was uniformly sampled with $h = 80$ km. A vector length equal to the sample spacing corresponds to 15 m/s.

Table 4.3: Wind-field-model error for the NB model, with $M_c = M_d = 2$, as a function of N for simulated mesoscale wind fields.

N	Number of Unknowns in $N \times N$ Region	Normalized RMS Error		
		Vector	Direction (deg)	Speed
4	20	0.024	1.06	0.011
6	28	0.080	3.11	0.046
8	36	0.084	3.69	0.050
10	44	0.104	4.92	0.065
12	54	0.083	4.27	0.052
14	66	0.082	4.48	0.054
16	74	0.084	5.04	0.057

number of parameters is a function of M_c , M_d , and N , there is room for tradeoff between the number of model parameters and the accuracy of the wind field model. We will be primarily interested in values of N such as 8 or 12 which evenly divide the swath width.

4.5.1 NB Model Error

Let us first consider the performance of the NB model. For the NB model the number of unknowns, N_u , in each $N \times N$ region segment is related to N , M_c and M_d by the formula,

$$N_u = 4N - 2 + g(M_c) + g(M_d) \quad (4.106)$$

where

$$g(M) = \begin{cases} 0, & M < 0, \\ (M + 1)(M + 2)/2, & M \geq 0. \end{cases} \quad (4.107)$$

$M_c = -1$ is used to denote the case when the vorticity field is identically zero. Similarly, M_d denotes the case when the divergence is identically zero.

Table 4.3 shows RMS modeling error versus N for polynomial vorticity and divergence models with $M_c = M_d = 2$. With the exception of a peak at $N = 10$, the modeling error increases as N increases. Table 4.4 illustrates the effects of varying M_c and M_d for $N = 8$. Table 4.5 is similar to Table 4.4, but for $N = 12$. As M_c and M_d increase, the modeling error is reduced. To minimize the number of unknowns in the model, we desire to keep M_c and M_d small. While other values of M_c and M_d can be chosen, our desired accuracy requirements (see Section 4.1) will be met for $N = 8$ with $M_c = M_d = 0$, i.e., for a constant vorticity and divergence model over the region \mathcal{L} , whereas for $N = 12$, $M_c = M_d = 1$ will meet the desired requirements. In the latter case, the vorticity and divergence files are bilinear over the region \mathcal{L} .

Table 4.4: NB-model Error for $N = 8$, versus M_c and M_d

Field Model		Unknowns N_u	Normalized RMS Error		
M_c	M_d		Vector	Direction (deg)	Speed
-1	-1	30	0.191	8.31	0.115
-1	0	31	0.171	7.22	0.099
-1	1	33	0.165	6.97	0.095
-1	2	36	0.163	6.95	0.093
-1	3	40	0.158	6.74	0.091
-1	4	45	0.144	6.17	0.084
0	-1	31	0.133	6.01	0.084
0	0	32	0.102	4.65	0.063
0	1	34	0.096	4.36	0.059
0	2	37	0.095	4.30	0.058
0	3	41	0.095	4.27	0.058
0	4	46	0.094	4.21	0.057
1	-1	33	0.129	5.79	0.080
1	0	34	0.097	4.35	0.058
1	1	36	0.090	4.01	0.054
1	2	39	0.090	3.96	0.053
1	3	43	0.089	3.92	0.053
1	4	48	0.089	3.91	0.053
2	-1	36	0.125	5.62	0.077
2	0	37	0.092	4.09	0.055
2	1	39	0.085	3.72	0.050
2	2	42	0.084	3.69	0.050
2	3	46	0.084	3.68	0.050
2	4	51	0.084	3.67	0.050
3	-1	40	0.125	5.60	0.077
3	0	41	0.091	4.06	0.055
3	1	43	0.084	3.70	0.050
3	2	46	0.084	3.66	0.049
3	3	50	0.084	3.65	0.049
3	4	55	0.084	3.64	0.049
4	-1	45	0.118	5.30	0.073
4	0	46	0.082	3.68	0.049
4	1	48	0.074	3.25	0.044
4	2	51	0.074	3.20	0.043
4	3	55	0.074	3.20	0.043
4	4	60	0.073	3.20	0.043

4.5.2 PBC Model Error

The PBC model has the advantage of using a smaller number of unknowns than the NB model, but at the expense of a somewhat higher modeling error. For the PBC model the number of unknowns N_u in each $N \times N$ region is related to M_l , M_c and M_d by the formula,

$$N_u = 2M_l + g(M_c) + g(M_d). \quad (4.108)$$

Next we contrast the performance of the previous NB model results with those obtained for the PBC model. Table 4.6 illustrates the effect of varying M_l for $N = 8$ and $M_c = M_d = 2$. Table 4.7 presents the RMS errors for $M_l = 8$ and $M_c = M_d = 2$ versus N . Table 4.7 should be compared to Table 4.3; note that the errors are only slightly larger for the PBC case as compared to the NB case. Table 4.8 shows the effects of varying M_c and M_d for $N = 8$ and $M_l = 8$, whereas Table 4.9 presents similar results for $N = 12$. Table 4.8 should be compared with Table 4.5, whereas Table 4.9 should be compared with Table 4.6. Observe that for $N = 8$, setting $M_l = 8$ and $M_c = M_d = 1$, permits us to meet our desired model accuracy requirements. For $N = 12$ and $M_l = 8$, and $M_c, M_d = 2$, the desired accuracy requirements are met. Greater accuracy is achieved for larger M_l and/or larger M_c and M_d .

Table 4.5: NB-model Error for $N = 12$, versus M_c and M_d

Field Model		Unknowns N_u	Normalized RMS Error		
M_c	M_d		Vector	Direction (deg)	Speed
-1	-1	46	0.234	11.21	0.148
-1	0	47	0.208	9.76	0.127
-1	1	49	0.199	9.23	0.120
-1	2	52	0.197	9.12	0.118
-1	3	56	0.196	9.07	0.117
-1	4	61	0.193	9.05	0.116
0	-1	47	0.163	8.03	0.108
0	0	48	0.123	6.26	0.082
0	1	50	0.109	5.63	0.073
0	2	53	0.106	5.46	0.070
0	3	57	0.105	5.44	0.069
0	4	62	0.107	5.55	0.071
1	-1	49	0.152	7.56	0.098
1	0	50	0.108	5.60	0.070
1	1	52	0.092	4.77	0.059
1	2	55	0.088	4.56	0.056
1	3	59	0.087	4.52	0.056
1	4	64	0.087	4.53	0.056
2	-1	52	0.149	7.44	0.096
2	0	53	0.104	5.43	0.067
2	1	55	0.087	4.52	0.055
2	2	58	0.083	4.27	0.052
2	3	62	0.083	4.23	0.051
2	4	67	0.083	4.24	0.052
3	-1	56	0.149	7.42	0.095
3	0	57	0.103	5.40	0.066
3	1	59	0.086	4.49	0.055
3	2	62	0.083	4.23	0.051
3	3	66	0.082	4.19	0.051
3	4	71	0.086	4.54	0.054
4	-1	61	0.147	7.34	0.094
4	0	62	0.101	5.26	0.065
4	1	64	0.085	4.46	0.054
4	2	67	0.082	4.30	0.052
4	3	71	0.080	4.13	0.050
4	4	76	0.080	4.10	0.050

Table 4.6: PBC-model Error for $N = 8$ and $M_c = M_d = 2$, versus M_l

M_l	Unknowns N_u	Normalized RMS Error		
		Vector	Direction (deg)	Speed
2	14	0.237	10.98	0.153
4	16	0.160	7.48	0.111
6	18	0.116	5.11	0.076
8	20	0.106	4.80	0.068
10	22	0.097	4.40	0.059
12	24	0.096	4.32	0.058

Table 4.7: PBC-model error, with $M_l = 8$ and $M_c = M_d = 2$, as a function of N for simulated mesoscale wind fields.

N	Number of Unknowns in $N \times N$ Region	Normalized RMS Error		
		Vector	Direction (deg)	Speed
4	20	0.057	2.14	0.032
6	20	0.099	4.12	0.060
8	20	0.106	4.80	0.068
10	20	0.107	5.02	0.072
12	20	0.110	5.64	0.075
14	20	0.112	5.91	0.078
16	20	0.116	6.56	0.082

Table 4.8: PBC-model Error for $N = 8$ and $M_l = 8$, versus M_c and M_d

Field Model		Unknowns N_u	Normalized RMS Error		
M_c	M_d		Vector	Direction (deg)	Speed
-1	-1	8	0.203	8.965	0.126
-1	0	9	0.185	7.964	0.112
-1	1	11	0.178	7.716	0.108
-1	2	14	0.177	7.657	0.106
-1	3	18	0.173	7.486	0.104
-1	4	23	0.162	6.998	0.098
0	-1	9	0.150	6.856	0.097
0	0	10	0.123	5.677	0.080
0	1	12	0.117	5.403	0.076
0	2	15	0.116	5.345	0.075
0	3	19	0.115	5.286	0.075
0	4	24	0.112	5.081	0.071
1	-1	11	0.146	6.640	0.094
1	0	12	0.118	5.426	0.076
1	1	14	0.112	5.113	0.072
1	2	17	0.111	5.049	0.071
1	3	21	0.110	5.004	0.071
1	4	26	0.106	4.783	0.067
2	-1	14	0.141	6.443	0.091
2	0	15	0.113	5.177	0.072
2	1	17	0.107	4.866	0.069
2	2	20	0.106	4.798	0.068
2	3	24	0.105	4.779	0.067
2	4	29	0.101	4.528	0.063
3	-1	18	0.140	6.447	0.089
3	0	19	0.111	5.186	0.070
3	1	21	0.106	4.880	0.066
3	2	24	0.105	4.832	0.066
3	3	28	0.104	4.800	0.065
3	4	33	0.099	4.496	0.061
4	-1	23	0.134	6.182	0.085
4	0	24	0.104	4.857	0.065
4	1	26	0.098	4.527	0.061
4	2	29	0.097	4.485	0.060
4	3	33	0.096	4.433	0.060
4	4	38	0.091	4.157	0.056

Table 4.9: PBC-model error for $N = 12$ and $M_l = 8$, versus M_c and M_d

Field Model		Unknowns N_u	Normalized RMS Error		
M_c	M_d		Vector	Direction (deg)	Speed
-1	-1	8	0.247	11.84	0.160
-1	0	9	0.222	10.51	0.141
-1	1	11	0.213	9.98	0.133
-1	2	14	0.211	9.85	0.131
-1	3	18	0.209	9.78	0.131
-1	4	23	0.206	9.63	0.128
0	-1	9	0.181	8.98	0.121
0	0	10	0.145	7.39	0.098
0	1	12	0.132	6.77	0.090
0	2	15	0.129	6.62	0.088
0	3	19	0.128	6.57	0.088
0	4	24	0.125	6.44	0.085
1	-1	11	0.170	8.43	0.114
1	0	12	0.132	6.73	0.089
1	1	14	0.118	6.03	0.080
1	2	17	0.114	5.86	0.078
1	3	21	0.113	5.80	0.078
1	4	26	0.110	5.63	0.075
2	-1	14	0.167	8.28	0.111
2	0	15	0.128	6.53	0.086
2	1	17	0.113	5.81	0.077
2	2	20	0.110	5.64	0.075
2	3	24	0.109	5.60	0.075
2	4	29	0.106	5.51	0.072
3	-1	18	0.166	8.30	0.110
3	0	19	0.127	6.56	0.085
3	1	21	0.112	5.81	0.075
3	2	24	0.109	5.65	0.073
3	3	28	0.108	5.59	0.073
3	4	33	0.104	5.39	0.070
4	-1	23	0.163	8.21	0.107
4	0	24	0.124	6.43	0.082
4	1	26	0.109	5.66	0.072
4	2	29	0.105	5.51	0.070
4	3	33	0.104	5.40	0.070
4	4	38	0.101	5.26	0.067

4.6 Conclusion

In this Chapter the development of a model for near-surface mesoscale wind fields which is suitable for use in model-based estimation of wind fields from wind scatterometer measurements is presented. The modeling error is evaluated by means of simulation. Only a summary of the modeling error computations has been shown here. A more complete set of modeling error tables for various model options are presented in Appendix G. Other options for modeling the vorticity and divergence fields are considered in Appendix F and the modeling error shown in Appendix G.

The parameterized boundary condition model with $N = 8$, $M_l = 8$, and $M_c = M_d = 1$ or $N = 12$, $M_l = 8$, and $M_c = M_d = 2$ provides the desired model accuracy while minimizing the number of unknowns. Larger values of M_l , M_c , and M_d produce more accurate models. $N = 12$ will be used in the sequel since this corresponds to the scatterometer swath width at 50 km resolution.

Chapter 5

Formulating Model-Based Wind Field Estimation

The classic approach to model-based estimation is to form an objective function from the measurements for the parameters of the model and optimize the objective function. The model parameters corresponding to the global minima of the objective function are the parameter estimates [78]. When the objective function is based on maximum likelihood, the resulting estimates are the maximum likelihood estimates of the model parameters.

In this Chapter we consider the formulation of the maximum likelihood objective function for model-based wind field estimation and show the identifiability of the model parameters. For use in optimization of the objective function, the gradient of the objective function is also computed. Optimization of the objective function is considered in the next Chapter.

5.1 Objective Function Formulation

The role of the wind field model in model-based wind field estimation is to provide a description of the wind field over the scatterometer measurement swath at a fixed instant of time and a resolution of 25 km (corresponding to the scatterometer sampling). The wind field model has the general form,

$$\overline{W} = F\overline{X} \quad (5.1)$$

where \overline{W} contains the components of the sampled wind field over the $N \times N$ region \mathcal{L} , F is a full rank $2N^2 \times N_u$ dimension constant matrix with elements $F_{n,p}$, and \overline{X} is a N_u -dimensional model parameter vector. Typically, we choose $N = 8$ or $N = 12$. The value of N_u depends on the order of the wind field model, though typically $N_u = 20$. This model form lends itself to the parameter estimation formulation: the model parameters in \overline{X} are directly estimated from the noisy σ^o measurements and then the wind field is computed from the estimated model parameters.

The components $u_{i,j}$ and $v_{i,j}$ of wind velocity vector $(u_{i,j}, v_{i,j})$ at the sample point (i, j)

within the region are,

$$u_{i,j} = \overline{W}_n = (F\overline{X})_n \quad (5.2)$$

$$v_{i,j} = \overline{W}_{N^2+n} = (F\overline{X})_{N^2+n} \quad (5.3)$$

where $n = (j - 1)N + i$ is the lexicographic index corresponding to i, j .

Following our estimation theory approach, we define an objective function for the model parameters from the available measurements [78]. The parameter estimate is computed by minimizing the objective function. The objective function formulation will be based on maximum likelihood [78].

The true value of σ^o , denoted $\sigma_n^o(k)$, corresponding to the k th observation of the sample point identified by lexicographic index n , can be expressed, as

$$\begin{aligned} \sigma_n^o(k) &= \mathcal{M}\{(u_n, v_n), k\} \\ &= \mathcal{M}\{(\overline{W}_n, \overline{W}_{N^2+n}), k\} \\ &= \mathcal{M}\{((F\overline{X})_n, (F\overline{X})_{N^2+n}), k\} \end{aligned} \quad (5.4)$$

which, for notational convenience, can be written, as

$$\sigma_n^o(k) = \mathcal{M}\{(F\overline{X})_n, k\}. \quad (5.5)$$

As an aid in deriving the likelihood function for \overline{X} , we note that the conditional probability distribution of the k th measurement of σ^o at n , $z_n(k)$, given \overline{X} is [refer to Eq. (2.18)]

$$\begin{aligned} p(z_n(k)|\overline{X}) &= \frac{1}{\sqrt{2\pi}} \frac{1}{[\alpha_n^2(k)\sigma_n^{o2}(k) + \beta_n^2(k)\sigma_n^o(k) + \gamma_n^2(k)]^{1/2}} \cdot \\ &\quad \exp\left\{-\frac{1}{2}[z_n(k) - \sigma_n^o(k)]^2/[\alpha_n^2(k)\sigma_n^{o2}(k) + \beta_n^2(k)\sigma_n^o(k) + \gamma_n^2(k)]\right\} \end{aligned} \quad (5.6)$$

where $\sigma_n^o(k)$ is given by Eq. (5.5). There are L_n measurements available at the sample point n . L_n may vary from its nominal value of 4 when there are missing σ^o measurements due to calibration cycles and coregistration errors [68].

The measurement noise is assumed to be independent for each $z_n(k)$. It follows that the log-likelihood function $l(\overline{X})$, given all the measurements $z_n(k)$, is

$$l(\overline{X}) = \sum_{n=1}^{N^2} \sum_{k=1}^{L_n} \log p(z_n(k)|\overline{X}). \quad (5.7)$$

Disregarding any constants, $l(\bar{X})$ can be written, as

$$l(\bar{X}) = - \sum_{n=1}^{N^2} \sum_{k=1}^{L_n} \left\{ \log[\alpha_n^2(k)\sigma_n^{o2}(k) + \beta_n^2(k)\sigma_n^o(k) + \gamma_n^2(k)] \right. \\ \left. + [z_n(k) - \sigma_n^o(k)]^2 / [\alpha_n^2(k)\sigma_n^{o2}(k) + \beta_n^2(k)\sigma_n^o(k) + \gamma_n^2(k)] \right\} \quad (5.8)$$

where $\sigma_n^o(k)$ is given by Eq. (5.5). We define the objective function $J_f(\bar{X})$ as the negative of the log-likelihood function omitting the constants of proportionality, i.e.,

$$J_f(\bar{X}) \triangleq -l(\bar{X}) \\ = \sum_{n=1}^{N^2} \sum_{k=1}^{L_n} \left\{ \log[\alpha_n^2(k)\sigma_n^{o2}(k) + \beta_n^2(k)\sigma_n^o(k) + \gamma_n^2(k)] \right. \\ \left. + [z_n(k) - \sigma_n^o(k)]^2 / [\alpha_n^2(k)\sigma_n^{o2}(k) + \beta_n^2(k)\sigma_n^o(k) + \gamma_n^2(k)] \right\} \quad (5.9)$$

The maximum-likelihood estimate of \bar{X} is obtained by minimizing $J_f(\bar{X})$.

5.2 Identifiability of the Model Parameters

In Chapter 2 we studied the identifiability of winds estimated on a point-wise basis from wind scatterometer measurements. These results will be used in showing the identifiability of the model parameters from the scatterometer measurements. The wind field model relates the $2N^2$ element wind field vector \bar{W} to the N_u element model parameter vector \bar{X} via the linear equation, (repeated here for convenience)

$$\bar{W} = F\bar{X}. \quad (5.10)$$

where the $2N^2 \times N_u$ constant matrix F has linearly independent columns.

The first question we need to address is, given a wind field \bar{U} and \bar{V} (i.e., given \bar{W}), can we determine \bar{X} ? For an arbitrary \bar{W} , since the system of equations represented by (5.10) is overdetermined, there will be, in general, no solution for \bar{X} ; an arbitrary \bar{W} is contained in the space \mathcal{R}^{2N^2} while \bar{X} spans only a N_u dimensional subspace \mathcal{R}^{N_u} of \mathcal{R}^{2N^2} . However, by the Projection Theorem, there is a unique element of \mathcal{R}^{N_u} which is closest to \bar{W} by the square-norm $\|\bar{W} - F\bar{X}\|_2$ [58]. Such an element is the solution of the over-determined least-squares problem,

$$F^T\bar{W} = F^T F\bar{X}. \quad (5.11)$$

The solution for \bar{X} in Eq. (5.11) is,

$$\bar{X} = F^\dagger\bar{W} = (F^T F)^{-1} F^T\bar{W} \quad (5.12)$$

where F^\dagger is the pseudo-inverse of F [58]. Since F is full rank (the columns of F are linearly independent), there is only a single, unique solution to (5.11) [58]. We note that F^\dagger is a fixed matrix which may be computed ahead of time using singular value decomposition. For the range of N 's of interest in this research ($2 \leq N \leq 24$), the singular values of F (which correspond to the eigenvalues of a square matrix) lie within the range 1 to 0.2. The precise structure of F depends on the order of the curl and divergence field models.

For an arbitrary \overline{W} there exists a unique corresponding $\overline{X} = F^\dagger \overline{W}$, and, for a given \overline{X} , there is a corresponding $\overline{W} = F\overline{X}$; hence, the linear wind field model can be treated as a ‘‘one-to-one’’ system. Consequently, showing that \overline{X} is identifiable from the noisy σ^o measurements is essentially equivalent to showing that \overline{W} is identifiable from the noisy σ^o measurements.

The proof of the identifiability of \overline{X} can be shown using the same approach as the one used in the point-wise case. Let \overline{X}_t be the true value of \overline{X} with a corresponding true wind field $\overline{W}_t = F\overline{X}_t$.

Just as in the point-wise case, there may be several possible wind fields (with corresponding model parameter vectors) which could have given rise to the observed σ^o measurements. Let the set D_f^c denote the set of all \overline{X} which give rise to the same true σ^o observations, i.e.,

$$D_f^c \triangleq \{ \overline{X} \mid \mathcal{M}\{(F\overline{X})_n, k\} = \mathcal{M}\{(F\overline{X}_t)_n, k\} \forall n, k \}. \quad (5.13)$$

As in the point-wise case, due to the nature of \mathcal{M} , the set D_f^c may have more than one member. In general, however, D_f^c will have only a single member. In order for D_f^c to have multiple members, each of the wind fields corresponding to the different \overline{X} must have wind vectors at all corresponding sample points which produce exactly the same values of $\sigma^o(k)$ for all k and n . This is unlikely for most wind fields.

Based on the log-likelihood function, the field-wise objective function $J_f(\overline{X})$ can be written, as [see Eq. (5.9)]

$$J_f(\overline{X}) = \frac{1}{2} \sum_{n=1}^{N^2} \sum_{k=1}^{L_n} \left\{ \log V_n(k) + [z_n(k) - s_n^2(k)]^2 / V_n(k) \right\} \quad (5.14)$$

where

$$V_n(k) = \alpha_n^2(k) s_n^{L_n} + \beta_n^2(k) s_n^2(k) + \gamma_n(k) \quad (5.15)$$

and $s_n^2(k) = \sigma_n^o(k)$ is given by Eq. (5.5).

To show identifiability of the model parameters in model-based wind field estimation, we need to show that as $T \rightarrow \infty$ (corresponding to a longer and longer measurement) the locations of global minima of $J_f(u, v)$ converge in probability to the members of D_f^c . To show this we will, as in the point-wise case, show (A) that $J_f(u, v)/T$ converges in mean-square to $E[J_f(u, v)/T]$ and (B) the maximum likelihood estimates of \overline{X} converge in probability to

some element $\bar{X}_1 \in D_f^c$, i.e.,

$$\lim_{T \rightarrow \infty} E \left[\frac{J_f(\bar{X}_1)}{T} \right] = \min_{\bar{X}} \lim_{T \rightarrow \infty} E \left[\frac{J_f(\bar{X})}{T} \right]. \quad (5.16)$$

To show (A), let us first compute $E[J_f(\bar{X})]$. Taking the expectation of (5.14), we compute $E[J_f(u, v)]$ and find,

$$E[J_f(\bar{X})] = \frac{1}{2} \sum_{n=1}^{N^2} \sum_{k=1}^{L_n} \left\{ \log V_n(k) + \left[V_{nt}(k) + [s_{nt}^2(k) - s_n^2(k)]^2 \right] / V_n(k) \right\} \quad (5.17)$$

where $s_{nt}(k)$ is the true value of $s(k)$ at the sample point n and $V_{nt}(k)$ is the true value of $V(k)$ at the sample point n . Writing this equation explicitly in terms of T and letting $T \rightarrow \infty$ we obtain a deterministic function,

$$\lim_{T \rightarrow \infty} E[J_f(\bar{X})/T] = \frac{1}{2} \sum_{n=1}^{N^2} \sum_{k=1}^{L_n} [s_{nt}^2(k) - s_n^2(k)]^2 / Y_n(k) \quad (5.18)$$

where $Y_n(k)$ is the $Y(k)$ [see Eq. (3.13)] at the sample point n .

We want to show that the field-wise objective function $J_f(\bar{X})$ converges in mean-square to zero, i.e.,

$$\lim_{T \rightarrow \infty} E \left\{ \left[\frac{1}{T} J_f(\bar{X}) - \frac{1}{T} E[J_f(\bar{X})] \right]^2 \right\} = 0. \quad (5.19)$$

We can take advantage of the detailed derivation for the point-wise case given in Chapter 3 by noting that since the noise is independent in both k and n , we can fold the location index n into the k index in the point-wise case and let the k used in the point-wise derivation correspond to $k \leftarrow k + 4(n - 1)$. Additionally, (u, v) is replaced by $F\bar{X}$. Then the results given in Chapter 3 and Appendix B for the point-wise case are valid for the field-wise case by letting the limits on k go from $k = 1$ to $k = 4N^2$. As in the point-wise case we note that,

$$\begin{aligned} E \left\{ \left[\frac{1}{T} J_f(\bar{X}) - \frac{1}{T} E[J_f(\bar{X})] \right]^2 \right\} &= E \left[\frac{1}{T^2} J_f^2(\bar{X}) \right] + \frac{1}{T^2} E^2[J_p(\bar{X})] \\ &\quad - 2E \left[\frac{1}{T^2} J_f(\bar{X}) E[J_f(\bar{X})] \right] \end{aligned} \quad (5.20)$$

Substituting the modified point-wise results from Appendix B into Eq. (5.20) and taking the limit of the resulting expression as $T \rightarrow \infty$, we find that all the terms cancel and we have the desired result (compare the point-wise results given in Chapter 3),

$$\lim_{T \rightarrow \infty} E \left\{ \left[\frac{1}{T} J_f(\bar{X}) - \frac{1}{T} E[J_f(\bar{X})] \right]^2 \right\} = 0; \quad (5.21)$$

hence, (A) is shown.

We now consider result (B). Since $J_f(\bar{X})/T$ converges in the mean-square to the deterministic function $E[J_f(\bar{X})/T]$, the locations of the minima of $J_f(\bar{X})/T$ converge in probability to the minima of $E[J_f(\bar{X})/T]$. We need only show that set A_f^c ,

$$A_f^c = \left\{ \bar{X}_1 \left| \lim_{T \rightarrow \infty} E \left[\frac{J_f(\bar{X}_1)}{T} \right] = \min_{\bar{X}} \lim_{T \rightarrow \infty} E \left[\frac{J_f(\bar{X})}{T} \right] \right\}, \quad (5.22)$$

is equal to D_f^c . As in the point-wise case, from Eq. (5.18) we see,

$$\lim_{T \rightarrow \infty} E \left[\frac{J_f(\bar{X})}{T} \right] = \sum_{n=1}^{N^2} \sum_{k=1}^{L_n} [s_{nt}^2(k) - s_n^2(k)]^2 / Y_n(k) \geq 0. \quad (5.23)$$

Equality occurs only when

$$\sum_{n=1}^{N^2} \sum_{k=1}^{L_n} [s_{nt}^2(k) - s_n^2(k)]^2 = 0 \quad (5.24)$$

which occurs at the minimum of $\lim_{T \rightarrow \infty} E \left[\frac{J_f(\bar{X})}{T} \right]$. It follows that $s_n^2(k) = s_{nt}^2(k)$ for all k and n . Hence, the set A_f^c , which are the \bar{X} which minimize $J_f(\bar{X})$ (corresponding to the s_n 's), is, by definition, the set D_f^c (which correspond to the s_{nt} 's). This proves result (B). Thus, field-wise estimation is identifiable to the multimember set D_f^c .

5.3 Gradient of the Objective Function

Since many numerical optimization algorithms require computation of the gradient of the objective function, this section provides a derivation of the gradient of the ML objective function $J_f(\bar{X})$, i.e., $\nabla J_f(\bar{X})$.

We begin by noting that $(u_n, v_n) = (F\bar{X})_n$ can be written as [refer to Eqs. (5.2) and (5.3)]

$$u_n = \sum_{p=1}^{N_u} F_{n,p} \bar{X}_p \quad (5.25)$$

$$v_n = \sum_{p=1}^{N_u} F_{n+N^2,p} \bar{X}_p; \quad (5.26)$$

hence, the wind speed $U_n^2 = |(u_n, v_n)|^2$ at n and the wind direction $\phi_n = \tan^{-1} v_n/u_n$ at n

can be written, as

$$\begin{aligned} U_n^2 &= u_n^2 + v_n^2 \\ &= \sum_{p=1}^{N_u} \sum_{q=1}^{N_u} (F_{n,p} F_{n,q} + F_{n+N^2,p} F_{n+N^2,q}) \bar{X}_p \bar{X}_q \end{aligned} \quad (5.27)$$

$$\phi_n = \tan^{-1} \left(\frac{\sum_{p=1}^{N_u} F_{n+N^2,p} \bar{X}_p}{\sum_{p=1}^{N_u} F_{n,p} \bar{X}_p} \right). \quad (5.28)$$

where the inverse tangent is four-quadrant ($\phi_n \in [-\pi, \pi]$).

It follows that the partial of U_n^2 with respect to \bar{X}_r is,

$$\begin{aligned} \frac{\partial}{\partial \bar{X}_r} U_n^2(k) &= \frac{\partial}{\partial \bar{X}_r} \sum_{p=1}^{N_u} \sum_{q=1}^{N_u} (F_{n,p} F_{n,q} + F_{n+N^2,p} F_{n+N^2,q}) \bar{X}_p \bar{X}_q \\ &= 2 \sum_{p=1}^{N_u} (F_{n,p} F_{n,r} + F_{n+N^2,p} F_{n+N^2,r}) \bar{X}_p \end{aligned} \quad (5.29)$$

To compute the partial of ϕ_n with respect to \bar{X}_r define w as the ratio of the arguments of the four-quadrant inverse tangent, i.e.,

$$w = \frac{\sum_{p=1}^{N_u} F_{n+N^2,p} \bar{X}_p}{\sum_{p=1}^{N_u} F_{n,p} \bar{X}_p}; \quad (5.30)$$

then,

$$\frac{\partial}{\partial \bar{X}_r} \phi_n(k) = \frac{\partial}{\partial \bar{X}_r} \tan^{-1} \left(\frac{\sum_{p=1}^{N_u} F_{n+N^2,p} \bar{X}_p}{\sum_{p=1}^{N_u} F_{n,p} \bar{X}_p} \right) \quad (5.31)$$

$$= \begin{cases} \frac{1}{1+w^2} \frac{\partial}{\partial \bar{X}_r} w & 1^{st} \text{ or } 4^{th} \text{ quadrant} \\ -\frac{1}{1+w^2} \frac{\partial}{\partial \bar{X}_r} w & 2^{nd} \text{ or } 3^{rd} \text{ quadrant} \end{cases} \quad (5.32)$$

with

$$\frac{\partial}{\partial \bar{X}_r} w = \frac{F_{n+N^2,r} \sum_{p=1}^{N_u} F_{n,p} \bar{X}_p - F_{n,r} \sum_{p=1}^{N_u} F_{n+N^2,p} \bar{X}_p}{\left[\sum_{p=1}^{N_u} F_{n,p} \bar{X}_p \right]^2}. \quad (5.33)$$

We now compute the gradient of the objective function $J_f(\bar{X})$. Starting with Eq. (5.9) it can be shown, that

$$\begin{aligned} \frac{\partial}{\partial \bar{X}_r} J_f(\bar{X}) &= \frac{\partial}{\partial \sigma_n^o(k)} J_f(\bar{X}_r) \frac{\partial}{\partial \bar{X}_r} \sigma_n^o(k) \\ &= \sum_{n=1}^{N^2} \sum_{k=1}^{L_n} \frac{\partial}{\partial \sigma_n^o(k)} \left\{ \log[\alpha_n^2(k) \sigma_n^{o2}(k) + \beta_n^2(k) \sigma_n^o(k) + \gamma_n^2(k)] \right. \\ &\quad \left. + [z_n(k) - \sigma_n^o(k)]^2 / [\alpha_n^2(k) \sigma_n^{o2}(k) + \beta_n^2(k) \sigma_n^o(k) \right. \\ &\quad \left. + \gamma_n^2(k)] \right\} \frac{\partial \sigma_n^o(k)}{\partial \bar{X}_r} \\ &= \sum_{n=1}^{N^2} \sum_{k=1}^{L_n} \left\{ \left[2\alpha_n^2(k) \sigma_n^o(k) + \beta_n^2(k) - 2(z_n(k) - \sigma_n^o(k)) \right] / \right. \\ &\quad \left[\alpha_n^2(k) \sigma_n^{o2}(k) + \beta_n^2(k) \sigma_n^o(k) + \gamma_n^2(k) \right] \\ &\quad \left. - [z_n(k) - \sigma_n^o(k)]^2 [2\alpha_n^2(k) \sigma_n^o(k) + \beta_n^2(k)] / \right. \\ &\quad \left. [\alpha_n^2(k) \sigma_n^{o2}(k) + \beta_n^2(k) \sigma_n^o(k) + \gamma_n^2(k)]^2 \right\} \frac{\partial}{\partial \bar{X}_r} \sigma_n^o(k) \end{aligned} \quad (5.34)$$

For the SASS¹, Wentz, and NSCAT tabular geophysical model functions, the partial of $\sigma_n^o(k)$ with respect to \bar{X}_r can be written in terms of the partials of U_n^2 and ϕ_n , as

$$\frac{\partial}{\partial \bar{X}_r} \sigma_n^o(k) = \frac{\partial \sigma_n^o(k)}{\partial U_n^2} \frac{\partial U_n^2}{\partial \bar{X}_r} + \frac{\partial \sigma_n^o(k)}{\partial \phi_n} \frac{\partial \phi_n}{\partial \bar{X}_r}. \quad (5.35)$$

For the SASS¹ and NSCAT tabular geophysical model functions, the partials of $\sigma_n^o(k)$ with respect to U_n^2 and ϕ_n must be computed numerically. For the Wentz geophysical model function a closed-form expression for the partial of $\sigma_n^o(k)$ with respect to \bar{X}_r exists [refer to

Eq. (2.2)]. It is

$$\begin{aligned}
\frac{\partial}{\partial \bar{X}_r} \sigma_n^o(k) &= \frac{\partial \sigma_n^o(k)}{\partial U_n^2} \frac{\partial U_n^2}{\partial \bar{X}_r} + \frac{\partial \sigma_n^o(k)}{\partial \phi_n} \frac{\partial \phi_n}{\partial \bar{X}_r} \\
&= a_n(k) U_n^{d_n(k)} \left\{ \frac{1}{2} \frac{e_n(k) \cos(\phi_n + \chi_n(k))}{U_n^2} + \right. \\
&\quad \frac{1}{2} \frac{\cos[2(\phi_n + \chi_n(k))]}{U_n^2} \left[(z_n(k) - \sigma_n^o(k))^2 / \right. \\
&\quad (\alpha_n(k) \sigma_n^{o2}(k) + \beta_n(k) \sigma^o(k) + \gamma_n(k)) \\
&\quad \left. \left. + \log(\alpha_n(k) \sigma_n^{o2}(k) + \beta_n(k) \sigma^o(k) + \gamma_n(k)) \right] \right. \\
&\quad \left. + \frac{1}{2} a_n(k) d_n(k) U_n^{d_n(k)-2} \left[1 + \cos(\phi_n + \chi_n(k)) \left(b_n(k) \right. \right. \right. \\
&\quad \left. \left. + \frac{1}{2} e_n(k) \log(\alpha_n(k) \sigma_n^{o2}(k) + \beta_n(k) \sigma^o(k) + \gamma_n(k)) \right) \right. \\
&\quad \left. \left. + \cos[2(\phi_n(k) + \chi_n(k))] \left(c_n(k) + \log U_n \{ (z_n(k) - \sigma_n^o(k))^2 / \right. \right. \right. \\
&\quad \left. \left. \left. (\alpha_n(k) \sigma_n^{o2}(k) + \beta_n(k) \sigma^o(k) + \gamma_n(k)) \right. \right. \right. \\
&\quad \left. \left. \left. + \log(\alpha_n(k) \sigma_n^{o2}(k) + \beta_n(k) \sigma^o(k) + \gamma_n(k)) \right\} \right] \right\} \frac{\partial}{\partial \bar{X}_r} U_n^2 \\
&\quad - \left\{ \left(b_n(k) + e_n(k) \log U_n(k) \right) \sin(\phi_n + \chi_n(k)) - 2 \left(c_n(k) \right. \right. \\
&\quad \left. \left. + \log U_n(k) \left[(z_n(k) - \sigma_n^o(k))^2 / (\alpha_n(k) \sigma_n^{o2}(k) + \beta_n(k) \sigma^o(k) + \gamma_n(k)) \right. \right. \right. \\
&\quad \left. \left. \left. + \log(\alpha_n(k) \sigma_n^{o2}(k) + \beta_n(k) \sigma^o(k) + \gamma_n(k)) \right] \right) \right\} \\
&\quad \left. \sin[2(\phi_n + \chi_n(k))] \right\} \frac{\partial}{\partial \bar{X}_r} \phi_n \tag{5.36}
\end{aligned}$$

Using these results, the gradient of $J_f(\bar{X})$ can be computed.

5.4 Summary

In this Chapter we have formulated the maximum-likelihood objective function for the model parameters in terms of the σ^o measurements. We have shown that the model parameters are set-wise identifiable. Lastly, we have computed the gradient of the ML objective function.

Chapter 6

Objective Function Optimization

In this Chapter the optimization of the objective function for the model parameter formulated in the previous chapter is considered. The optimization approach described here is based on a gradient-search algorithm with initialization obtained from the results of point-wise wind estimation. As shown, this approach is sub-optimal but has the advantage of providing both model-based and point-wise wind field estimates for comparison. Appendix I discusses other optimization and initialization strategies.

A detailed comparison of results obtained using the model-based and the point-wise wind estimation approaches is provided in the next Chapter.

6.1 Optimization Considerations

Due to the tabular nature of \mathcal{M} , a closed form for the minimum of $J(\bar{X})$ is not available; hence, $J(\bar{X})$ must be numerically optimized. Unfortunately, the objective function can be difficult to optimize due to the non-linear properties it inherits from the nature of \mathcal{M} and the dimensionality of the problem. The objective function has numerous local minima with the possibility of several global minima. When multiple minima occur, the maximum-likelihood estimate is a set. Selection of a single solution can not be obtained from just the σ^o measurements, and an additional step is required to select a single solution. This situation is discussed below.

Classic non-linear minimization algorithms include stochastic algorithms such as simulated annealing [55, 76, 79], and various gradient-based search techniques [8, 71, 83]. Recently, Slump and Hoenders [98] developed a technique capable of locating all of the global minima of an objective function; however, the computation requirements of their method for a large dimensional problem such as ours prohibits its use. While random optimization techniques are able to locate global minima, they require an excessive number of function evaluations to find even a single global minimum [76]. Multiple global minima are determined by restarting several times. Gradient-based optimization algorithms can get stuck in a local minimum and fail to find a global minimum. Starting the search at different initial values can be used to find multiple minima with similar objective function values, though

there is often no way to determine if the minima are global.

In spite of its limitations, a gradient search algorithm can be used successfully if appropriate initial values can be determined. Such initial values can be computed for optimization of the field-wise objective function using the results of the traditional point-wise approach to wind field estimation. We will describe one such approach to initial value computation in the sequel. This optimization technique is relatively simplistic; as will be shown, better results can be obtained with more sophisticated initial value and optimization algorithms (see also Appendix I). Even so, our model-based wind field estimates are more accurate than the traditional point-wise wind field estimates. Our simple optimization approach is adopted merely for the purpose of demonstrating the feasibility of model-based estimation.

6.2 Field-Wise Dealiasing

Due to the nature of the geophysical model function \mathcal{M} , it is possible to have several global minima of the objective function. When this occurs, the maximum-likelihood estimate is a set and a single estimate can not be determined from the σ^o measurements alone. In this event, an additional step is required to select a single solution. Such a procedure might be termed “field-wise dealiasing” because of its seeming similarity to the “point-wise dealiasing” which is *always* required by the point-wise wind estimation approach. There is, however, a distinct difference between field-wise and point-wise dealiasing: in the point-wise case the problem is to choose from 2-6 possible solutions at *each sample point* (of which there are N^2 in an $N \times N$ region), while in the field-wise case, we need only choose between a few *fields*. The use of auxiliary data, climatological data, and/or continuity considerations can easily resolve the field-wise ambiguity problem.

Since the occurrence of multiple global minima is very rare and our goal is only to show the feasibility of the model-based wind estimation approach, we do not consider field-wise dealiasing any further.

6.3 Initial Value Computation

In order to successfully use a gradient-search optimization algorithm in this application, proper selection of the initial values is crucial. In this section, we describe a technique for computing an initial value wind field based on a point-wise wind field estimate followed by a median-filter-based dealiasing algorithm. The initial value model parameter vector is computed using Eq. (5.12). Alternate initial value computation schemes are described in Appendix I. While dealiasing errors can result in very poor quality initial values, this approach is suitable for demonstrating the feasibility of model-based wind field estimation. This approach has the additional advantage of providing *both* point-wise and model-based wind field estimates for comparison purposes.

6.3.1 Point-Wise Wind Estimation

In the traditional approach to wind estimation, only the measurements of σ^o associated with each sample point of the measurement swath are used to estimate the wind vector at the sample point, i.e, the wind is estimated on a point-wise basis. Unfortunately, on a point-wise basis, the wind vector is only *set-wise* identifiable from the σ^o measurements, i.e, there is not a unique wind estimate (see Chapter 3). Due to the nature of the σ^o -to-wind relationship \mathcal{M} , there are several (2-6) local minima (one or more are global minima) in the point-wise maximum-likelihood objective function which are near-global. Collectively, the wind vectors corresponding to these local minima are known as the *noisy ambiguity set*. The individual vectors of the noisy ambiguity set are known as *aliases* or *ambiguities* [94, 109]. Typically, the aliases have similar wind speed but differ widely in direction. While all of the aliases have similar values of the objective function, they may be “ranked” according to the objective function value; hence, the “first” alias (corresponding to the alias with the lowest objective function value) would be the classic ML estimate of the wind. However, other members of the ambiguity set are very often closer to the true wind than is the first alias. To select a unique wind estimate a later step, known in the literature as *dealiasing* or *ambiguity removal* is used. Traditionally, dealiasing has been based on various *ad hoc* considerations including pattern recognition of significant wind field features, continuity considerations, etc. [94, 109].

One difficulty with point-wise estimation is that, when there are not enough σ^o measurements at a sample point (due to cell coregistration errors, spacecraft attitude control error, etc.), it is so inaccurate as to not be useful; hence, there may be sample points within the swath at which a point-wise wind estimate is not available, resulting in gaps in the wind field estimate.

As a graphic example of point-wise and model-based wind estimation, consider Fig. 6.1 which shows a section of a wind field, sampled at 25 km over a 300×300 region. This is the true wind field. A least-squares fit of the model parameters to this true field can be made using Eq. (5.12). The resulting model parameter vector is known as the “true model parameters”. The wind field computed from these true model parameters, using Eq. (5.10), termed the “true model field”, is illustrated in Fig. 6.2 which appears identical to the true field shown in Fig. 6.1. The model used is the PBC model with $N = 12$, $M_c = M_d = 2$, and $M_l = 10$ ($N_u = 20$). Simulated σ^o measurements from this field were generated based on the NSCAT scatterometer design; the resulting point-wise ambiguity sets are plotted in Fig. 6.3.

6.3.2 Point-Wise Dealiasing

The point-wise dealiasing algorithm we have used is based on 2-d median filtering [95, 96] (see below). Unlike a low-pass filter, the median filter does not smooth edges or boundaries in the data.

Performance of the dealiasing algorithm is dependent on the underlying wind field, any missing measurements, the σ^o measurements, and the median filter window size. Averaged over a wide range of wind fields, the algorithm correctly selects the ambiguity closest to the

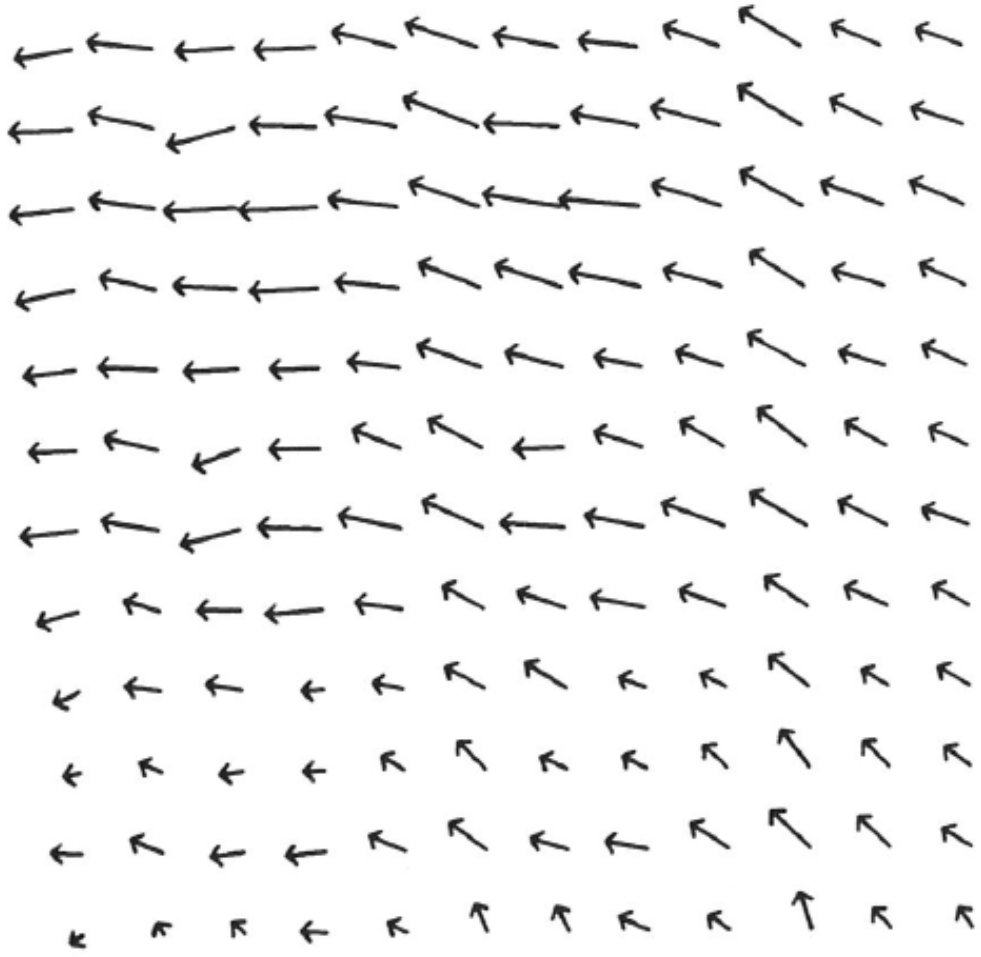


Figure 6.1: An example of a simulated wind field uniformly sampled with $h = 25$ km over a 300×300 km region. A vector length equal to the sample spacing corresponds to 15 m/s.

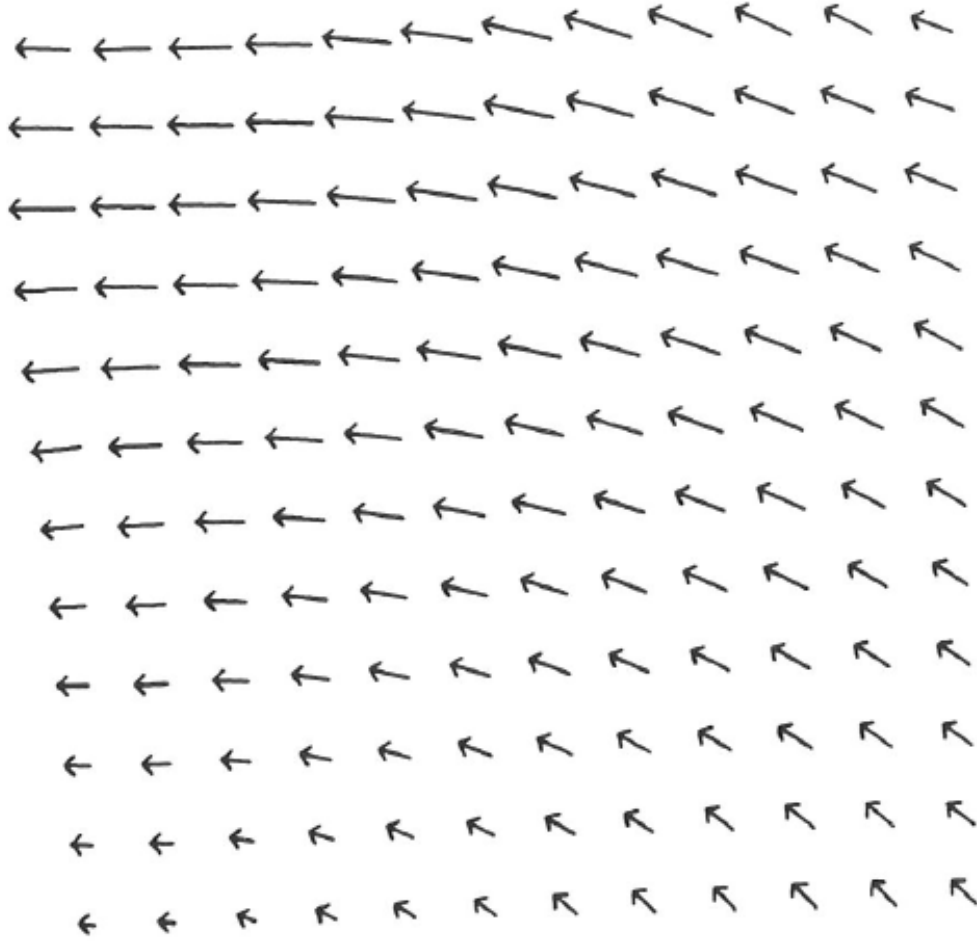


Figure 6.2: The “true model” wind field resulting from fitting the PB model with $M_c = M_d = 2$ and $N = 8$ to the wind field shown in Fig. 6.1. Plotting conventions and scale are the same as in Fig. 6.1.

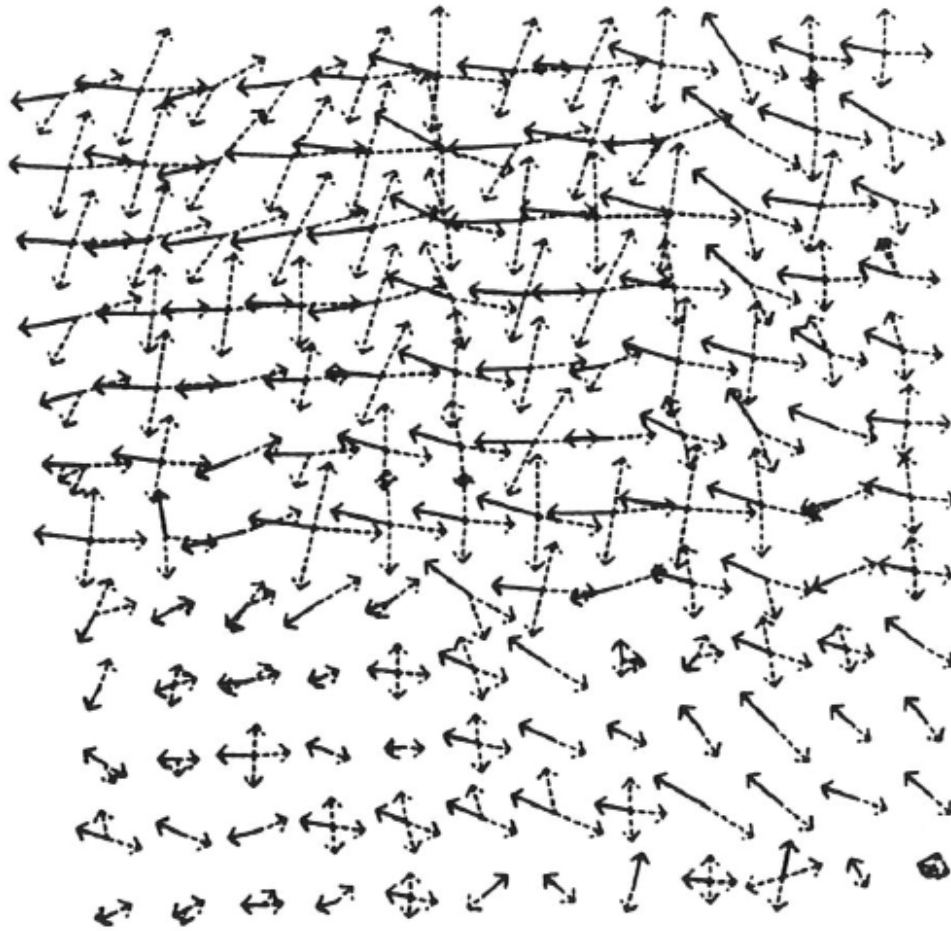


Figure 6.3: Noisy ambiguity sets resulting from point-wise estimation of the wind field in Fig. 6.1 using simulated σ° measurements from NSCAT.

true wind 90-98% of the time. Figure 6.4 illustrates the dealiased wind field corresponding to Fig. 6.3. Careful examination will reveal that, in this example, the dealiasing algorithm was unable to correctly select the ambiguity closest to the true wind vector at every sample point. Compare the dealiased wind field in Fig. 6.4 to the true wind field in Fig. 6.3. Note how “noisy” the wind field estimate appears.

While overall performance is good, ambiguity selection errors tend to be highly clustered, particularly in low wind speed regions [96]. The clustering of the errors is sensitive to the size of the median filter window; large windows result in alias selection errors associated with small scale features while small windows lead to alias selection errors on large scale features.

The steps in the median-filter-based dealiasing algorithm we used are:

1. Initialize a working field by copying the first alias from each of the point-wise ambiguity sets.
2. Repeat steps 3 and 4 until the working field estimate stabilizes.
3. Filter the working field with a vector median-err filter with a square window of size W_s . Any missing data points are ignored. The definition of the “median” vector of the set $\{\mathbf{U}_1, \mathbf{U}_2, \dots, \mathbf{U}_{N_s}\}$ is defined as the vector \mathbf{U}_m which minimizes the squared error

$$\sum_{i=1}^{N_s} |\mathbf{U}_m - \mathbf{U}_i|^2. \quad (6.1)$$

4. For each sample point, replace the median vector with the ambiguity from the corresponding ambiguity set which is closest to the median vector using in the L_2 norm.
5. The dealiased wind field is contained in the working field.

6.3.3 Model Parameter Initial Value Computation

The dealiasing algorithm is applied over as large a region as possible to minimize edge effects. The dealiased field is segmented into adjacent $N \times N$ (typically $N = 12$) regions and the least-squares fit of the model parameters for each region is computed using Eq. (5.12). Missing dealiased wind estimates at a given sample point are filled with an average of adjacent dealiased winds. For each region, the model parameters computed using this least-squares fit to the dealiased wind field are referred to as “initial value model parameters”. These are used as the initial values to begin the optimization of the objective function for the model parameters for the particular region. The wind field computed from the initial value parameters using Eq. (5.10) is known as the “initial wind field”. The model-based estimate of the wind field is computed from the optimized model parameters.

Figure 6.5 illustrates the initial wind field computed from the least-squares fit of the model parameters to the dealiased wind field in Fig. 6.4. Compare this initial value wind field in Fig. 6.5 to the true wind field in Fig. 6.2 and the dealiased wind field in Fig. 6.4. We note that Fig. 6.5 makes a better estimate of the true wind field than Fig. 6.4 *even without further*

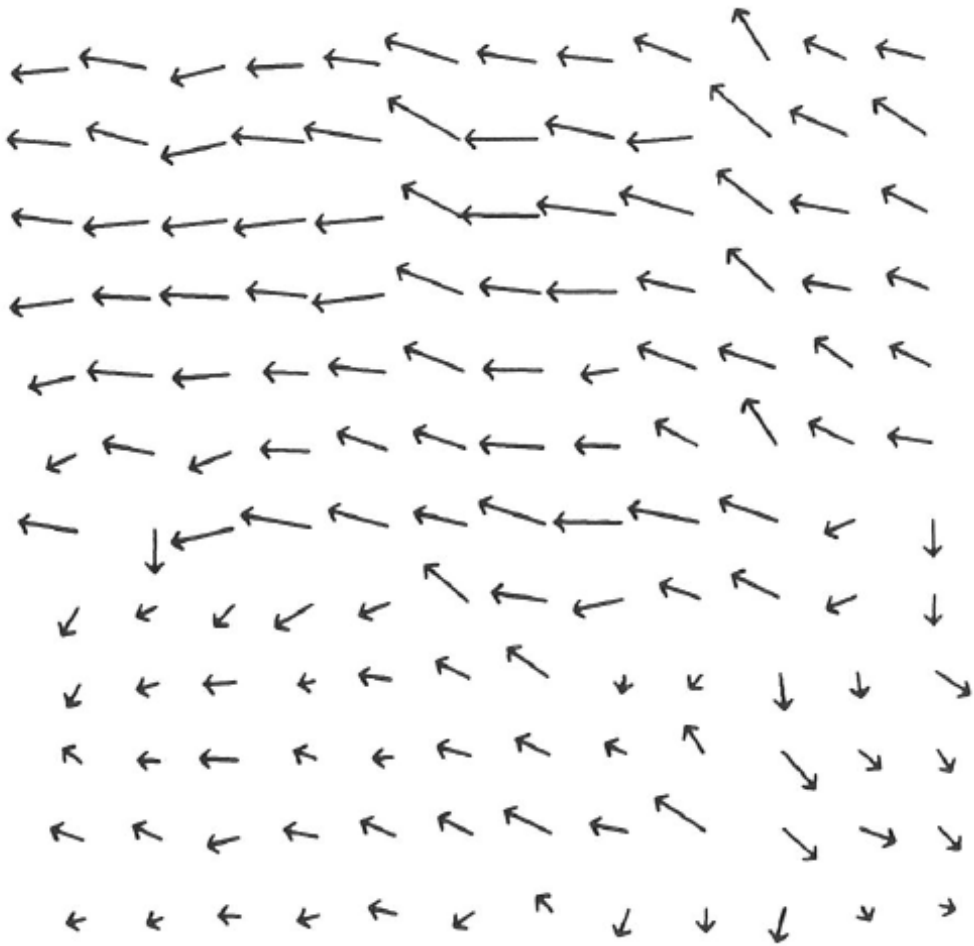


Figure 6.4: The result of applying the median-filter-based dealiasing algorithm described in the text to Fig. 6.3.

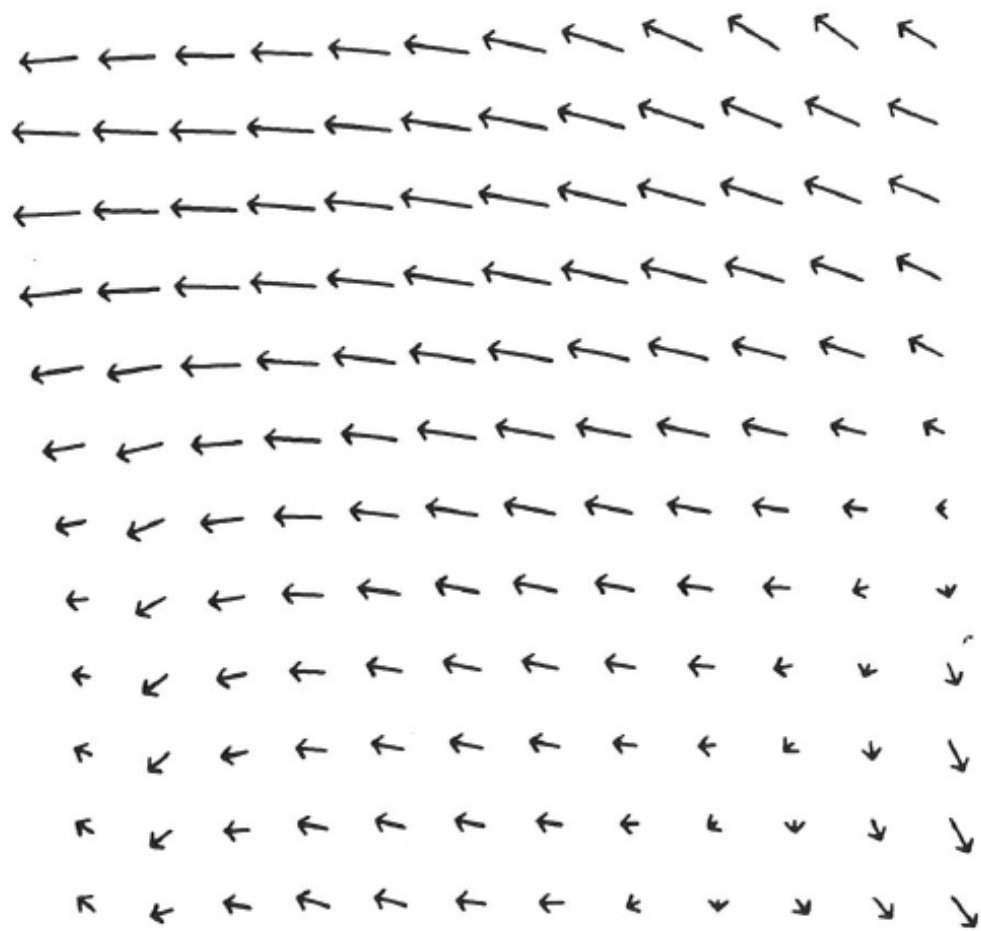


Figure 6.5: The initial value wind field computed from Fig. 6.4 (see text for explanation of computational method).

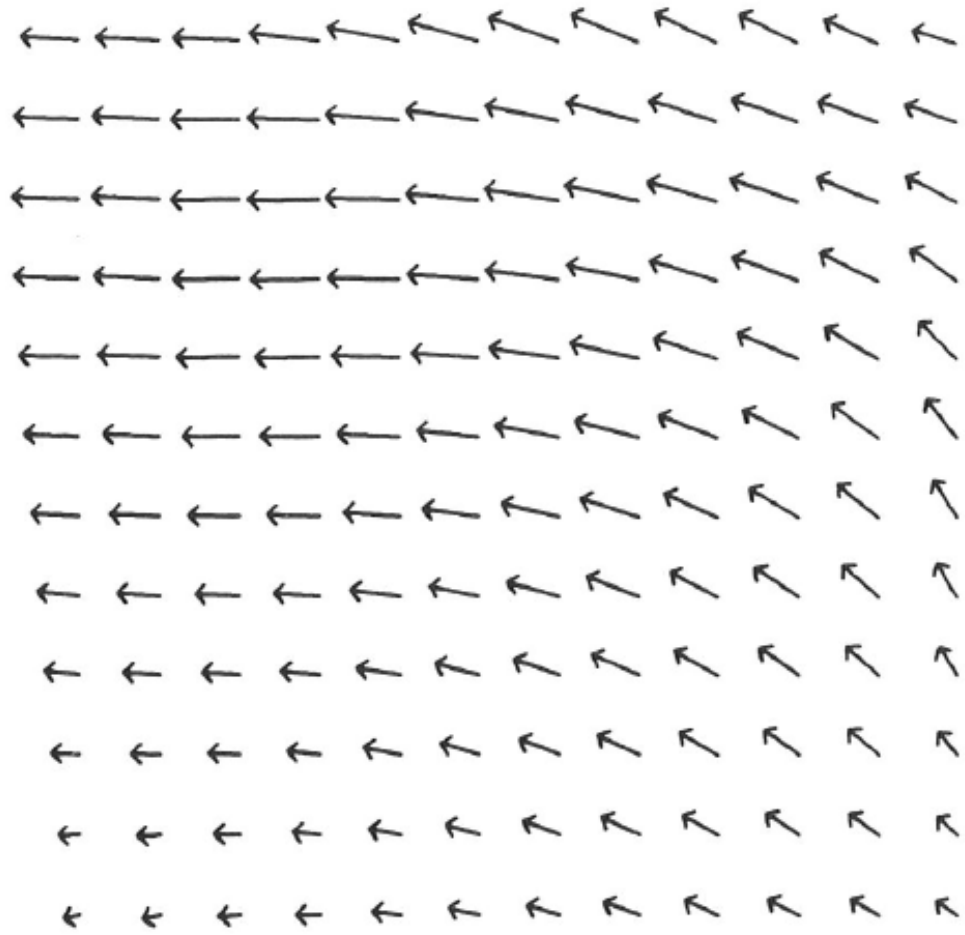


Figure 6.6: The wind field computed using the optimized model parameters.

Table 6.1: Wind Field Estimate Error

Wind Field	Figure Number	RMS Error		
		Vector (m/s)	Direction (deg)	Speed (m/s)
True Model	6.2	0.99	11.62	0.65
Point-wise Closest	6.3	1.33	21.63	0.58
Point-wise Dealiased	6.4	2.42	54.51	0.62
Initial Value	6.5	2.04	47.25	1.13
Model-based Estimate	6.6	1.16	13.81	0.74

Table 6.2: Wind Field Model Fit Error

Field	RMS Model Fit Error		
	Vector (m/s)	Direction (deg)	Speed (m/s)
True Model	0.99	11.62	0.65
Initial Value	1.76	26.07	1.15

optimization. This observation can be used to reduce the computation required to obtain the model-based wind field estimate (discussed below). Table 6.3.3 provides a summary of the root-mean-square (RMS) difference in wind speed, direction, and the magnitude of the vector difference between each case in Figs. 6.2-6.5 (and also Fig. 6.6, which is described in the next section) and the true field in Fig. 6.1.

The difference (known as model-fit error) between the initial value wind field and the dealiased wind field (from which the initial value wind was computed via a least squares fit of the model parameters), provides a measure of the accuracy of the dealiasing. When the dealiasing algorithm chooses the correct ambiguity at each sample point, initial value RMS model-fit direction-error is generally small. However, when there are clustered dealiasing errors, the initial value RMS model-fit direction-error is generally much larger. This leads to a simple threshold-based dealiasing algorithm accuracy check. When the RMS initial value model-fit direction-error is above a threshold (typically, 15-20 deg, depending on wind speed and resolution) the accuracy of the dealiasing for the region may be considered suspect. Table 6.3.3 gives the model-fit error for the initial value wind field for the previous example.

6.4 Gradient-Search Optimization

Given initial values, a gradient-search-based algorithm has been used to perform the optimization. For this purpose we have used the standard IMSL routine IMING for non-linear optimization, which uses quasi-Newton gradient optimization. Starting with the initial value

field in Fig. 6.5, the wind field computed from the optimized model parameters, known as the “optimized wind field”, is shown in Fig. 6.6. Compare Fig. 6.6 with the true field in Fig. 6.1. From Table 6.3.3 we see that the model-based estimate is superior to the point-wise estimate; it is less “noisy” and has smaller RMS vector and direction error. The model-based estimate has a slightly larger RMS speed error since the model-based approach effectively minimizes the RMS vector error at the possible expense of the speed error; point-wise estimation can provide slightly better estimates of the wind speed.

6.5 Resolution Considerations

The NSCAT instrument is designed to provide σ^o measurements at 25 km resolution. However, the wind is typically estimated at 50 km resolution by first resampling the 25 km resolution σ^o measurements onto a 50 km grid. For each grid point, the wind is estimated using point-wise wind estimation followed by dealiasing [60, 61]. Our method can be applied to provide to wind estimation at both 25 km and 50 km resolution. In the next Chapter, we will provide examples of wind estimates obtained at both 25 km and 50 km resolution.

Because of the higher “noise” level in the point-wise wind estimates at 25 km resolution relative to the point-wise 50 km resolution wind estimates (there are more measurements used for computing the 50 km resolution estimates), the dealiasing algorithm performance at 25 km resolution is more often poor, resulting in poor-quality initial values. We have found that better-quality initial values can be obtained by first computing the point-wise wind estimates and dealiasing at 50 km resolution and using the dealiased 50 km resolution field as a reference to select unique wind vectors for the point-wise wind estimates at 25 km resolution. For the four 25 km sample points corresponding to the 50 km resolution dealiased wind estimate, the ambiguities closest to the dealiased wind are selected. The resulting wind vector field is termed the 50 km reference field. The initial value is computed by fitting the model to the 50 km reference field using Eq. (5.12). This approach will be used for the results given in the next Chapter.

6.6 Computational Considerations

A disadvantage of the model-based estimation approach is that it requires significantly more computation than does the point-wise estimation approach. Most of this time is consumed in optimizing the objective function. We have observed that if the initial value wind fields have acceptable accuracy, we can save a significant amount of computation by not optimizing the objective function, i.e., by just using the initial value wind field as our final the result. We have observed that in general, this accuracy is achieved if: (1) the RMS of the estimated wind speed is larger than 4 m/s and (2) the RMS direction difference between the initial value field and the dealiased field is less than a threshold value (about 15 deg for 50 km resolution wind estimation). These conditions can be checked before starting the optimization. If they are met, we can elect not to optimize, and thereby trade off accuracy

of the estimate and computation time.

6.7 Summary

In this Chapter, the optimization of the field-wise objective function is considered. An optimization approach, based on gradient-search with initial values obtained using the point-wise estimation approach, has been described. This simplistic optimization approach is sub-optimal but yields both point-wise and model-based wind field estimates for comparison. Even with this simplistic optimization approach, model-based estimation results in more accurate estimates of the wind than does the traditional wind estimation approach. A more comprehensive comparison of the two estimation approaches is provided in the next Chapter.

Chapter 7

Performance of Model-Based Wind Field Estimation

In this Chapter the performance of the point-wise and model-based wind field estimates are compared using the optimization approach presented in the previous Chapter. The true wind fields used are those first discussed in Chapter 4 for evaluating the wind field model. Greater detail is given in Appendix D. Simulated measurements of σ^o are based on a simulation of the NSCAT Scatterometer. The state-of-the-art simulation of the NSCAT instrument includes all of the effects of spacecraft attitude control errors, uncertainty in the parameters of the radar equation used to compute σ^o from the power measurements made by the scatterometer, and the uncertainty in the correct relationship between σ^o and winds (i.e., geophysical modeling error in \mathcal{M}). The simulation is as realistic as possible (see Appendix H). Examples of wind field estimates at both 25 km and 50 km resolution will be given.

A flow chart of the model-based estimation procedure is shown in Fig. 7.1.

7.1 50 km Resolution Results Example

The simulated σ^o measurements are used to compute the point-wise wind estimates (ambiguity sets). This is followed by point-wise dealiasing using the median-filter-based dealiasing algorithm previously described to compute the initial values for the field-wise objective function optimization. For each region of the measurement swath initial value model parameters are computed using a least-squares fit and the parameter vector optimized.

For model-based wind estimation, the left and right swaths are segmented in the along-track direction into 12×12 (600×600 km) regions as indicated in Fig. 7.2. These region segments are indicated with dotted lines in the following figures. No information sharing between regions has been used. While the actual σ^o measurements are on a 25 km grid, for wind estimation at 50 km resolution, the measurements are resampled onto the 50 km grid. The fact that some of the σ^o associated with a 50 km resolution sample point may actually be as much as 25 km apart is not utilized.

Figure 7.3 shows the wind field over both the left and right swaths with an along-track

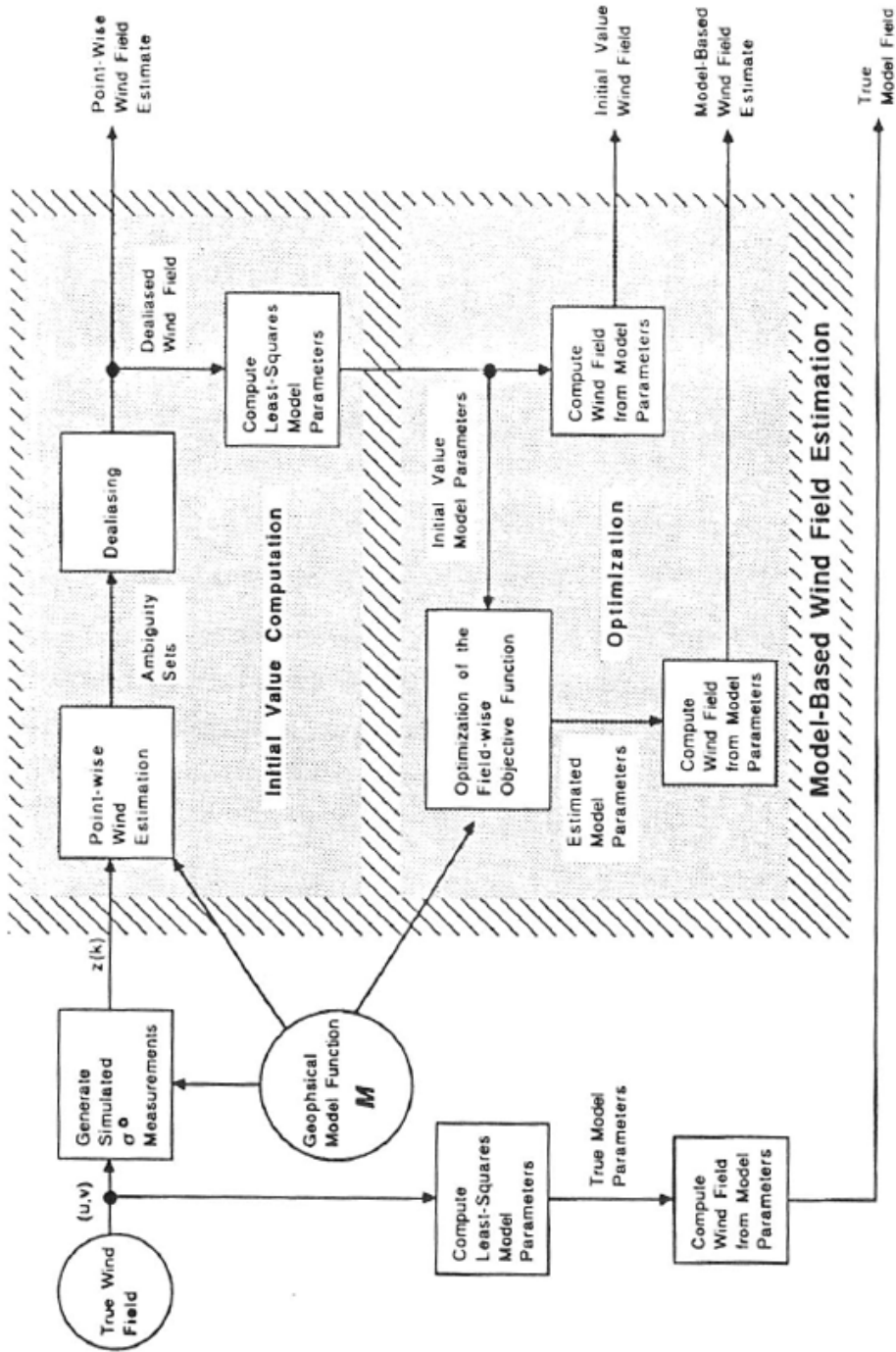


Figure 7.1: Diagram of the model-based estimation procedure.

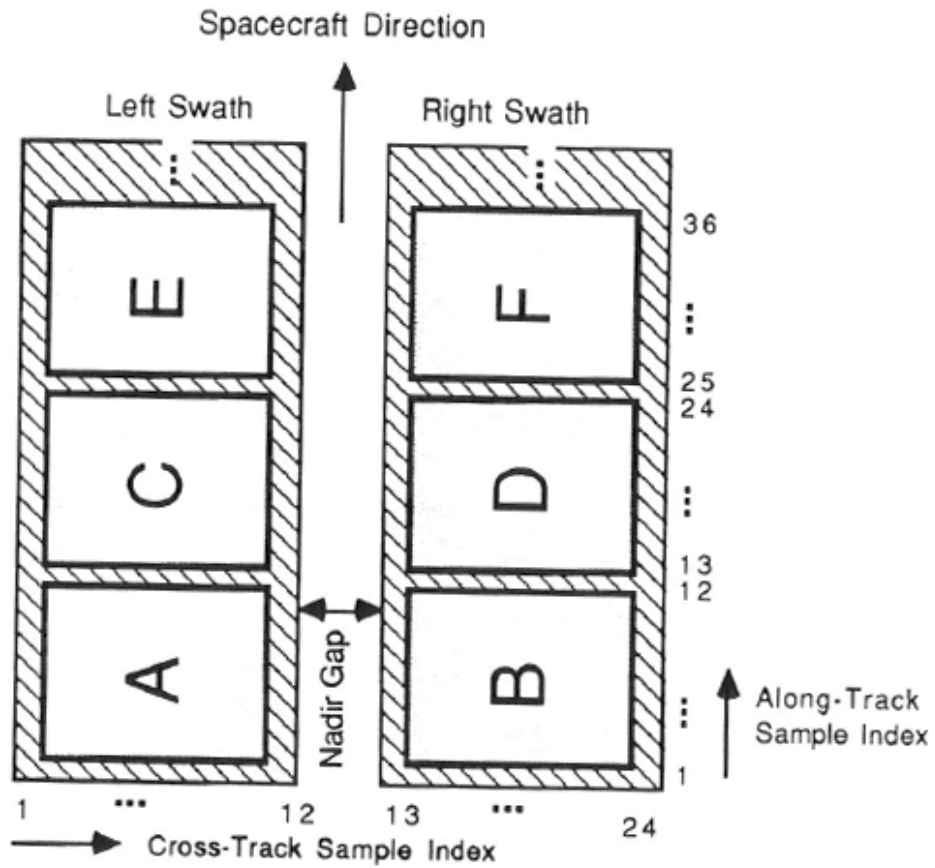


Figure 7.2: Diagram of the region segmentation scheme for the 50 km resolution example.

distance of 3000 km. The sample resolution is 50 km. This will be the “true” wind field in the results that follow. Figure 7.4 shows the results of computing the least-square fit of the model parameters to the true field and computing the resulting field on a region-by-region basis. This true model field represents the best the model-based estimation technique can achieve. For reference, Fig. 7.5 shows the closest alias to the true wind vector at each sample point, obtained from the ambiguity set using point-wise wind estimation. The results in Fig. 7.5 can only be obtained in a simulated example such as ours because this field can only be obtained if the dealiasing is perfect; actual dealiased point-wise results are worse due to dealiasing errors. The dealiased point-wise wind field estimate is shown in Fig. 7.6. Comparison of Figs. 7.3 and 7.6 reveals that in region F the dealiased wind field has significant direction errors. Note that in many regions, the point-wise wind estimates (even the closest ambiguity field) appear very noisy. Figure 7.7 shows the initial value wind field computed from Fig. 7.6. The optimized wind field, which is the model-based estimate of the wind field, is shown in Fig. 7.8. The RMS errors for each region are given in Tables 7.1-7.1.

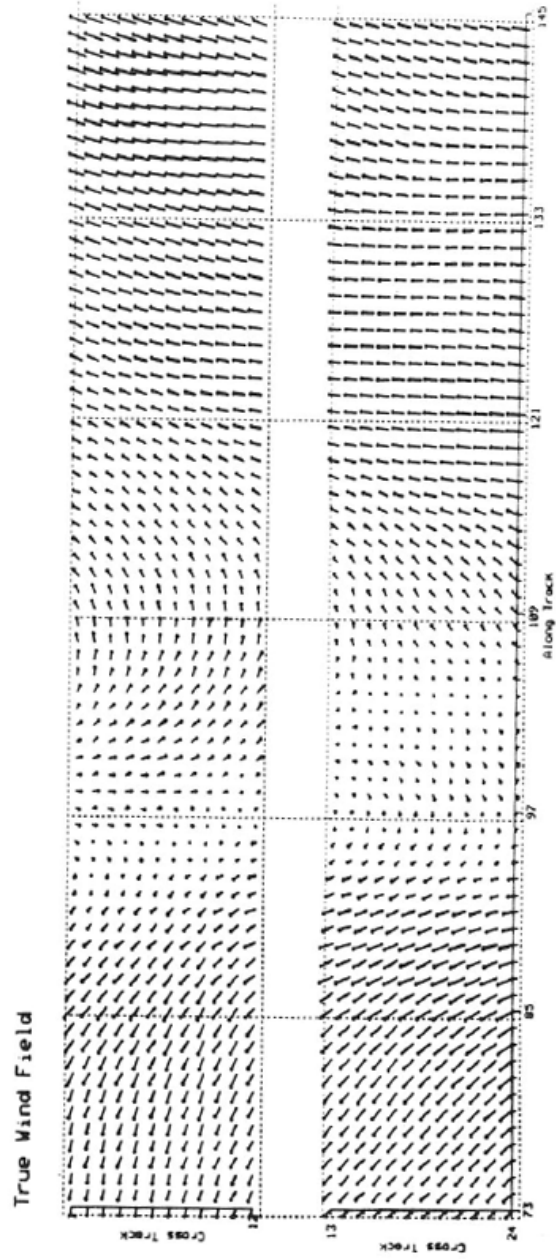


Figure 7.3: True wind field over both NSCAT observation swaths at 50 km resolution.

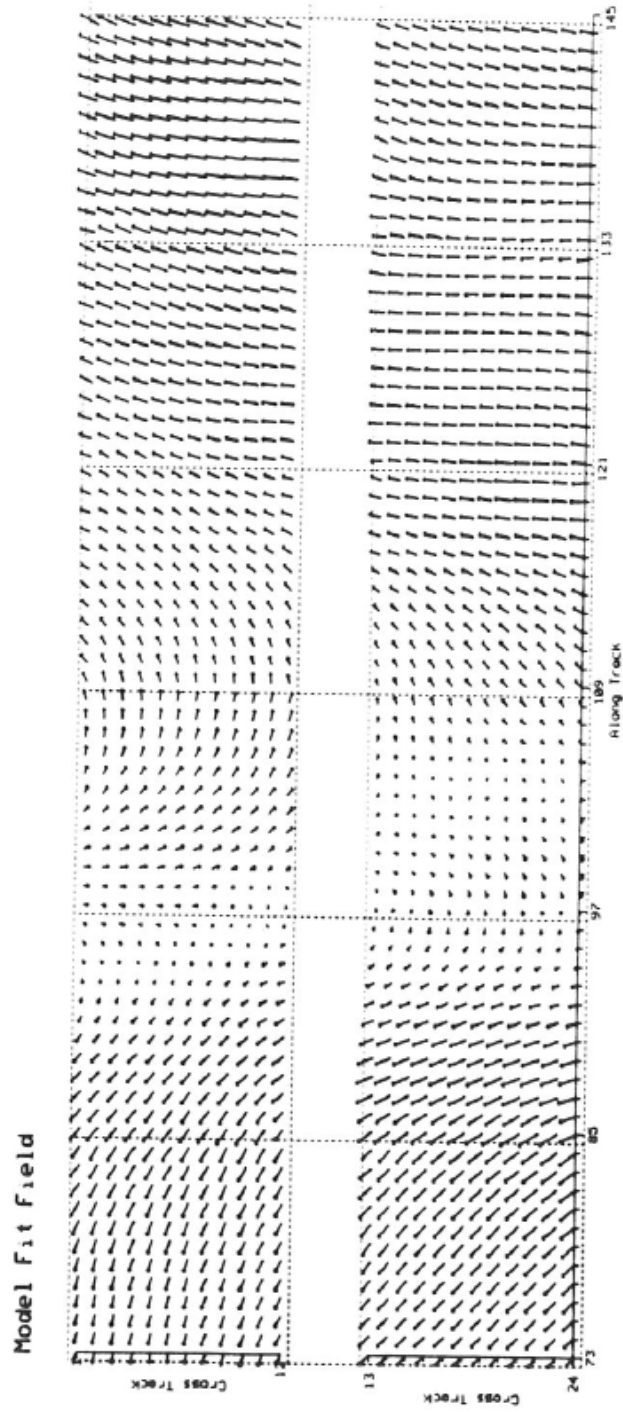


Figure 7.4: True model field corresponding to Fig. 7.3.

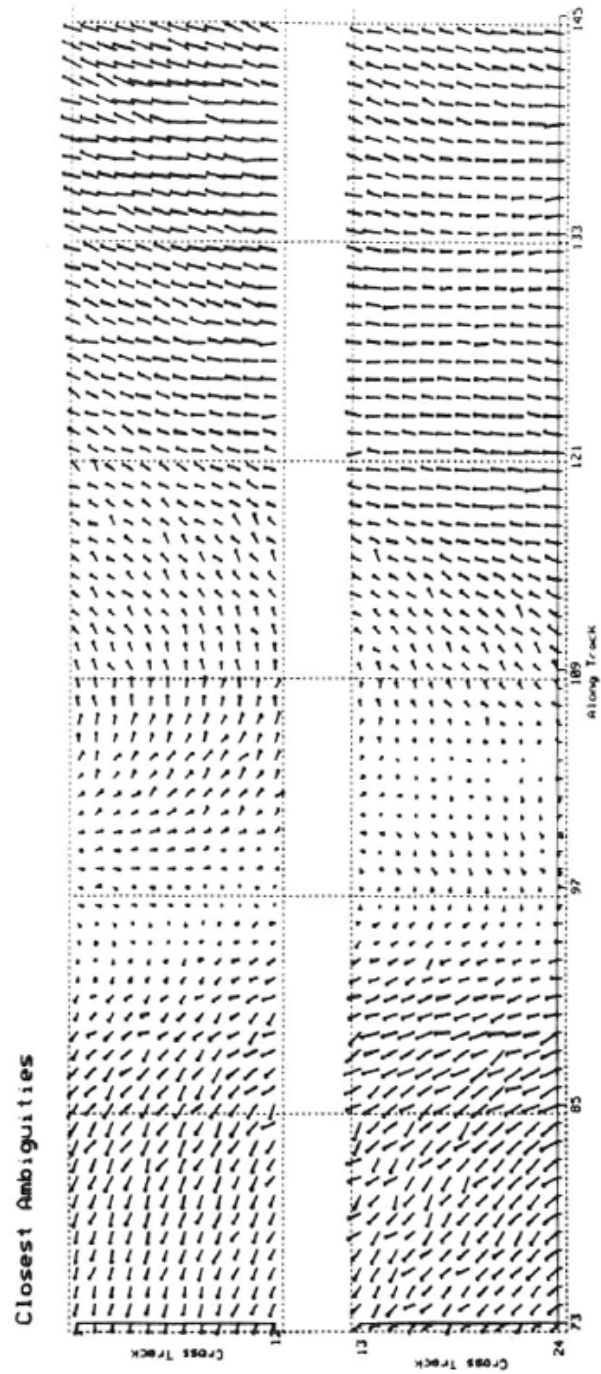


Figure 7.5: The closest alias to the true wind vector in point-wise noisy ambiguity sets computed using simulated σ^o measurements from NSCAT. The true wind field is shown in Fig. 7.3.

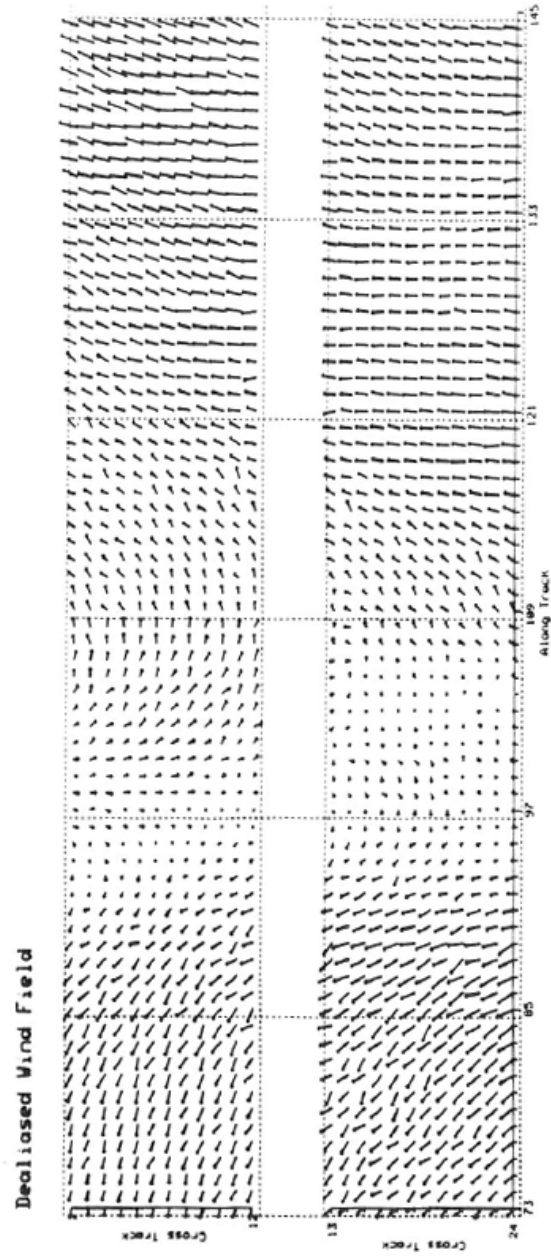


Figure 7.6: Dealiased point-wise wind field estimate.

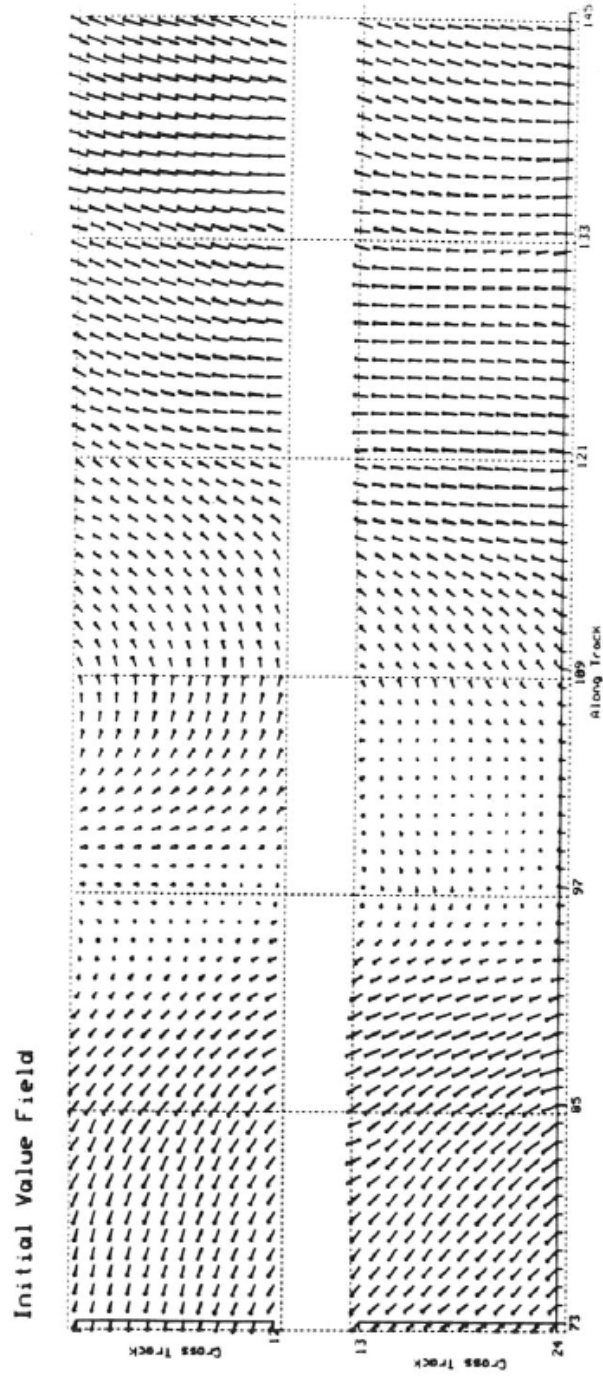


Figure 7.7: Initial value wind field computed from Fig. 7.6.

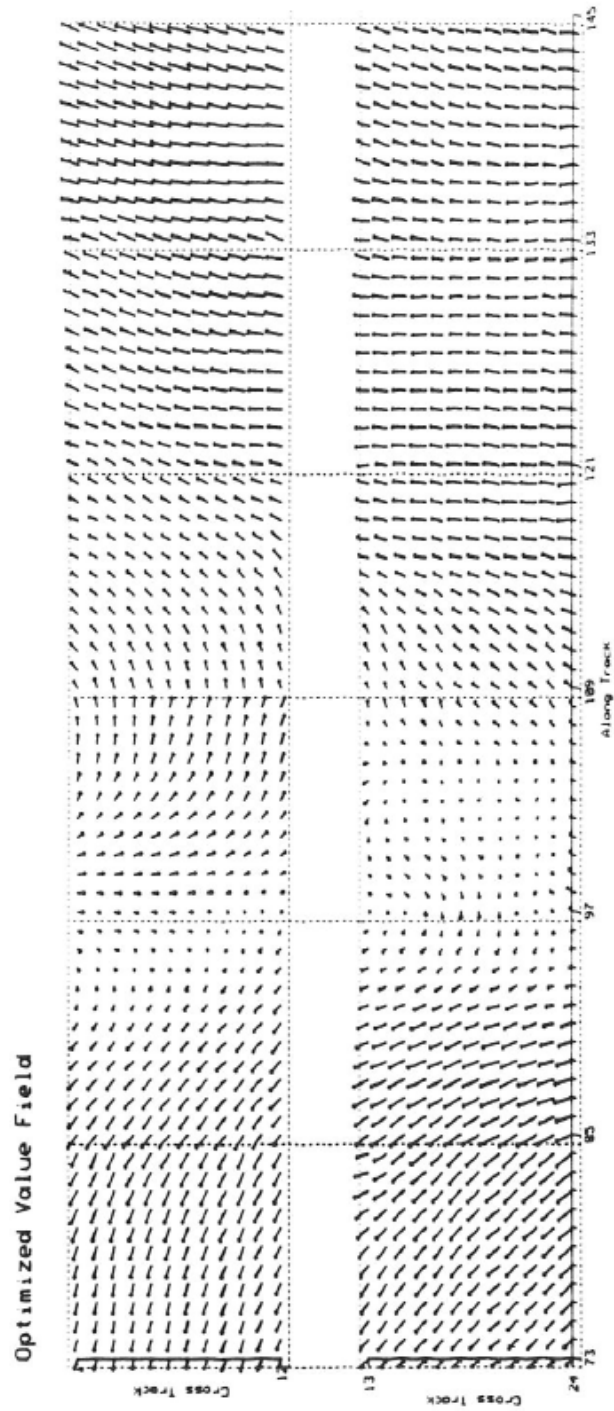


Figure 7.8: Optimized wind field (model-based wind field estimate) resulting from the initial value wind field in Fig. 7.7. Compare Fig. 7.3 and Fig. 7.6.

Table 7.1: Region A (at 1,73) Wind Estimation Performance

Field	Obj Func Value	RMS Err		
		Vector	Direction	Speed
True Model	-5755.80	0.831	4.435	0.634
Point-wise Closest	–	0.898	6.383	0.339
Point-wise Dealiased [†]	–	0.898	6.383	0.339
Initial Value	-5764.86	0.867	4.645	0.646
Optimized from:				
Initial Value	-5879.98	0.968	5.577	0.651
True Model	-5951.15	0.967	5.576	0.651

[†] Perfect dealiasing in this region.

Table 7.2: Region B (at 13,73) Wind Estimation Performance

Field	Obj Func Value	RMS Err		
		Vector	Direction	Speed
True Model	-5748.16	0.775	3.655	0.574
Point-wise Closest	–	1.645	11.095	0.431
Point-wise Dealiased	–	1.679	11.429	0.432
Initial Value	-5692.19	1.103	6.508	0.640
Optimized from:				
Initial Value	-5808.44	1.432	9.510	0.539
True Model	-5799.30	1.227	7.480	0.531

Table 7.3: Region C (at 1,85) Wind Estimation Performance

Field	Obj Func Value	RMS Err		
		Vector	Direction	Speed
True Model	-6319.14	0.783	13.178	0.521
Point-wise Closest	–	1.105	13.577	0.344
Point-wise Dealiased	–	1.141	20.730	0.348
Initial Value	-6280.93	0.858	13.343	0.553
Optimized from:				
Initial Value	-6428.33	1.076	15.757	0.617
True Model	-6428.37	1.081	15.690	0.614

Table 7.4: Region D (at 13,85) Wind Estimation Performance

Field	Obj Func Value	RMS Err		
		Vector	Direction	Speed
True Model	-5791.83	0.741	7.898	0.552
Point-wise Closest	–	1.260	10.327	0.513
Point-wise Dealiased	–	1.361	24.953	0.528
Initial Value	-5722.53	0.913	18.905	0.584
Optimized from:				
Initial Value	-5861.44	0.884	7.881	0.565
True Model	-5861.44	0.884	7.880	0.565

Table 7.5: Region E (at 1,97) Wind Estimation Performance

Field	Obj Func Value	RMS Err		
		Vector	Direction	Speed
True Model	-6341.67	0.727	13.916	0.487
Point-wise Closest	–	0.757	9.221	0.313
Point-wise Dealiased	–	0.813	17.673	0.321
Initial Value	-6337.66	0.756	17.854	0.491
Optimized from:				
Initial Value	-6415.90	0.799	16.668	0.520
True Model	-6413.92	0.783	13.243	0.518

Table 7.6: Region F (at 13,97) Wind Estimation Performance

Field	Obj Func Value	RMS Err		
		Vector	Direction	Speed
Model Fit	-6740.41	0.691	26.257	0.444
Point-wise Closest	–	0.872	23.012	0.344
Point-wise Dealiased	–	2.567	89.739	0.555
Initial Value	-5717.32	2.268	84.218	1.064
Optimized from:				
Initial Value	-6409.16	2.324	78.070	0.758
True Model	-6841.41	0.811	27.058	0.446

Table 7.7: Region G (at 1,109) Wind Estimation Performance

Field	Obj Func Value	RMS Err		
		Vector	Direction	Speed
True Model	-6158.89	0.574	4.356	0.417
Point-wise Closest	–	1.196	12.006	0.293
Point-wise Dealiased	–	1.198	12.039	0.292
Initial Value	-6128.49	0.711	6.056	0.440
Optimized from:				
Initial Value	-6219.37	0.734	6.266	0.445
True Model	-6219.37	0.732	6.236	0.446

Table 7.8: Region H (at 13,109) Wind Estimation Performance

Field	Obj Func Value	RMS Err		
		Vector	Direction	Speed
True Model	-5629.96	0.504	3.477	0.373
Point-wise Closest	–	0.940	9.399	0.331
Point-wise Dealiased	–	0.972	10.013	0.328
Initial Value	-5628.41	0.643	6.245	0.427
Optimized from:				
Initial Value	-5670.99	0.639	5.030	0.417
True Model	-5670.98	0.639	5.032	0.417

Table 7.9: Region I (at 1,121) Wind Estimation Performance

Field	Obj Func Value	RMS Err		
		Vector	Direction	Speed
True Model	-5480.57	0.514	2.544	0.393
Point-wise Closest	–	0.877	5.540	0.354
Point-wise Dealiased [†]	–	0.877	5.540	0.354
Initial Value	-5483.03	0.627	3.409	0.415
Optimized from:				
Initial Value	-5532.36	0.717	4.339	0.398
True Model	-5532.36	0.716	4.337	0.398

[†] Perfect dealiasing in this region.

Table 7.10: Region J (at 13,121) Wind Estimation Performance

Field	Obj Func Value	RMS Err		
		Vector	Direction	Speed
True Model	-5298.27	0.609	2.852	0.472
Point-wise Closest	–	0.678	4.467	0.332
Point-wise Dealiased [†]	–	0.678	4.467	0.332
Initial Value	-5293.66	0.659	3.352	0.470
Optimized from:				
Initial Value	-5349.96	0.808	4.336	0.503
True Model	-5349.96	0.808	4.338	0.504

[†] Perfect dealiasing in this region.

Table 7.11: Region K (at 1,133) Wind Estimation Performance

Field	Obj Func Value	RMS Err		
		Vector	Direction	Speed
True Model	-4936.73	0.595	2.245	0.457
Point-wise Closest	–	1.108	5.502	0.375
Point-wise Dealiased†	–	1.108	5.502	0.375
Initial Value	-4928.98	0.692	2.886	0.466
Optimized from:				
Initial Value	-4993.65	0.883	4.263	0.442
True Model	-4993.65	0.882	4.254	0.442

† Perfect dealiasing in this region.

Table 7.12: Region L (at 13,133) Wind Estimation Performance

Field	Obj Func Value	RMS Err		
		Vector	Direction	Speed
Model Fit	-5429.46	0.364	1.924	0.246
Point-wise Closest	–	0.719	4.419	0.368
Point-wise Dealiased†	–	0.719	4.419	0.368
Initial Value	-5437.86	0.435	2.485	0.267
Optimized from:				
Initial Value	-5446.52	0.455	2.595	0.276
True Model	-5446.52	0.455	2.595	0.276

† Perfect dealiasing in this region.

Table 7.13: Total Wind Field Estimate Error

Field	RMS Error		
	Vector (m/s)	Direction (deg)	Speed (m/s)
True Model	0.669	10.033	0.485
Closest Ambiguity	1.038	10.777	0.366
Point-wise Dealiased	1.266	28.554	0.389
Initial Value	0.994	26.079	0.578
Optimized from Initial Value	1.098	24.243	0.539
Optimized from True Model	0.874	10.946	0.508
Point-wise Dealiased [†]	1.072	12.544	0.370
Initial Value [†]	0.781	9.856	0.511
Optimized from Initial Value [†]	0.907	9.331	0.514
Optimized from True Model [†]	0.880	8.009	0.513

[†] Region F has been excluded.

Again we note that the initial value field (Fig. 7.7) is a good estimate of the true wind field *even without further optimization* everywhere except in region F. In fact, the optimized field (shown in Fig. 7.8) does not look much different than the initial-value field everywhere but in region F. This conclusion is strengthened by the RMS error summary given on a region-by-region basis in Tables 7.1-7.1: with the exception of region F, just the process of fitting the wind field model to the point-wise wind field estimate can dramatically improve the RMS wind error. Optimization generally improves the RMS error though optimization of the objective function may increase the RMS error slightly since the objective function and the RMS error are different “cost” measures.

In region F, where large dealiasing errors were made, the initial model parameter vector was of very poor quality. While optimization improved the objective function value, the optimization algorithm stopped at a local minimum rather than at the global minimum. In this region, the optimization algorithm finds a local minimum which results in a wind field which differs somewhat from the true wind field. Even so, the model-based wind field estimate is better than the point-wise dealiased estimate. In virtually all regions the model-based estimates are better than the point-wise estimates *even when perfect dealiasing occurs*. Table 7.1 contrasts the *total* RMS errors over all regions for the model-based and point-wise estimation results. The values given in the lower half of Table 7.1 were computed with region F excluded.

Since the wind estimates shown above are based on a gradient-search optimization algorithm which uses a very simple technique for computing initial values, the optimization algorithm may get stuck in a local minimum which, while “close” to the global minimum, is not the global minimum; the actual global minimum is closer to the true wind field; thus,

Table 7.14: Total Wind Field Estimate Error for Example 2

Field	RMS Error		
	Vector (m/s)	Direction (deg)	Speed (m/s)
True Model	0.942	5.716	0.696
Closest Ambiguity	1.435	9.409	0.481
Point-wise Dealiased	1.460	9.794	0.483
Initial Value	0.941	5.192	0.667
Optimized from Initial Value	1.036	5.737	0.702
Optimized from True Model	1.036	5.737	0.702

these results represent an upper bound on the performance of the model-based estimation technique. To demonstrate this, we used the true model parameters to initialize the gradient search. In all cases, the optimization starting with the true model parameters either locates the same minimum as previously found (starting with the initial value field) or it locates a minimum with a lower value, which is closer to the true field than the initial value field; see Tables 7.1-7.1. In these tables compare the RMS error and objective function values after optimization starting with the initial value and the true model value, respectively. Of particular interest is region F (Table 7.1). For clarity, the true wind field in region F is shown in Fig. 7.9, the dealiased wind field in Fig. 7.10, the initial value field in Fig. 7.11, and the optimized wind field in Fig. 7.12. The optimized wind field resulting from starting the optimization with the true model parameters is shown in Fig. 7.13. These results indicate that improved initialization/optimization approaches will yield even better estimates of the wind field. Our simple approach to initialization and optimization is, however, adequate for demonstrating the feasibility of model-based wind field estimation.

Another comparison of the model-based and point-wise wind field estimates is illustrated in Figs. 7.12-7.14. Figure 7.12 shows a true wind field. Figure 7.13 shows the corresponding dealiased wind field. For this example, there are fewer, more widely spaced dealiasing errors than in the previous example in Figs. 7.3-7.8. As a result, the initial values were sufficiently close to the global minimum of the objective function to insure that the optimization found this minimum. Figure 7.14 shows the model-based wind field estimated. Table 7.1 summarizes the total error. Again, the model-based wind field estimates are: (1) less noisy and (2) exhibit better RMS vector and direction error than *both* the dealiased wind fields and the closest ambiguity wind field.

7.2 25 km Resolution Results Example

Wind estimates obtained at 25 km resolution will have greater RMS errors than wind estimates at 50 km resolution due to the reduction in the number of measurements used to obtain each estimate. Figures 7.15-7.19 illustrate 25 km resolution wind estimation. Figure

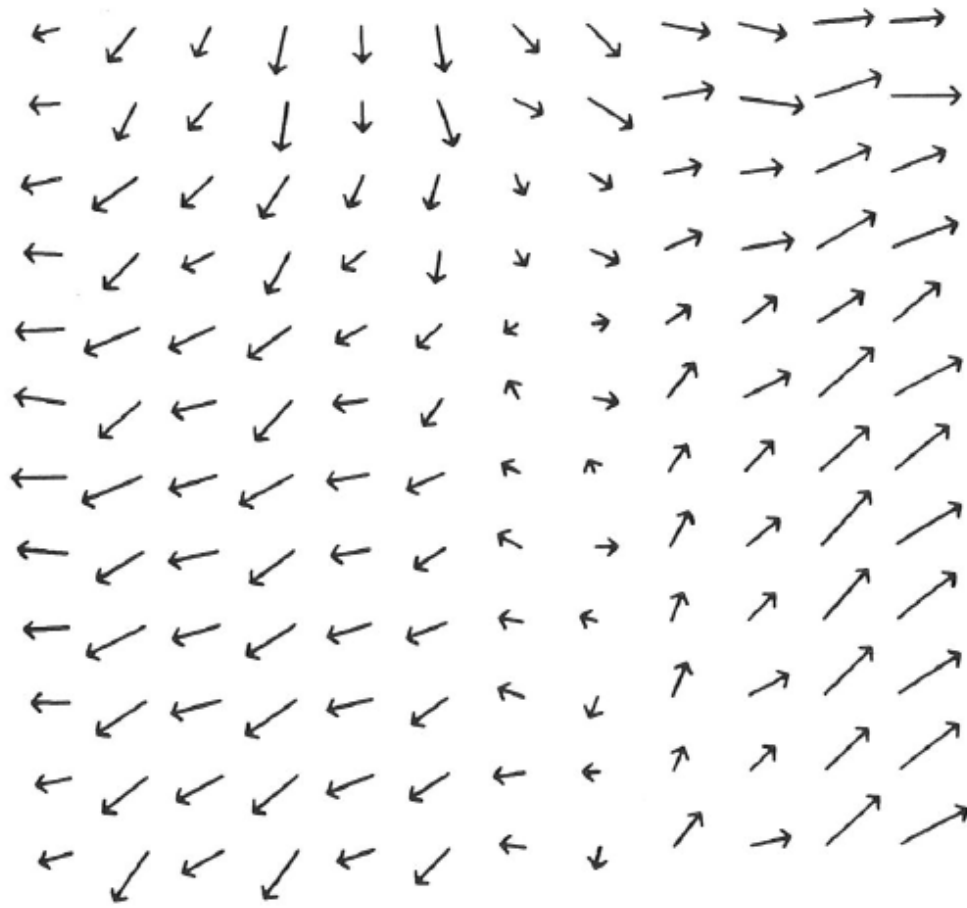


Figure 7.9: Enlargement of region F of the true wind field in Fig. 7.3.

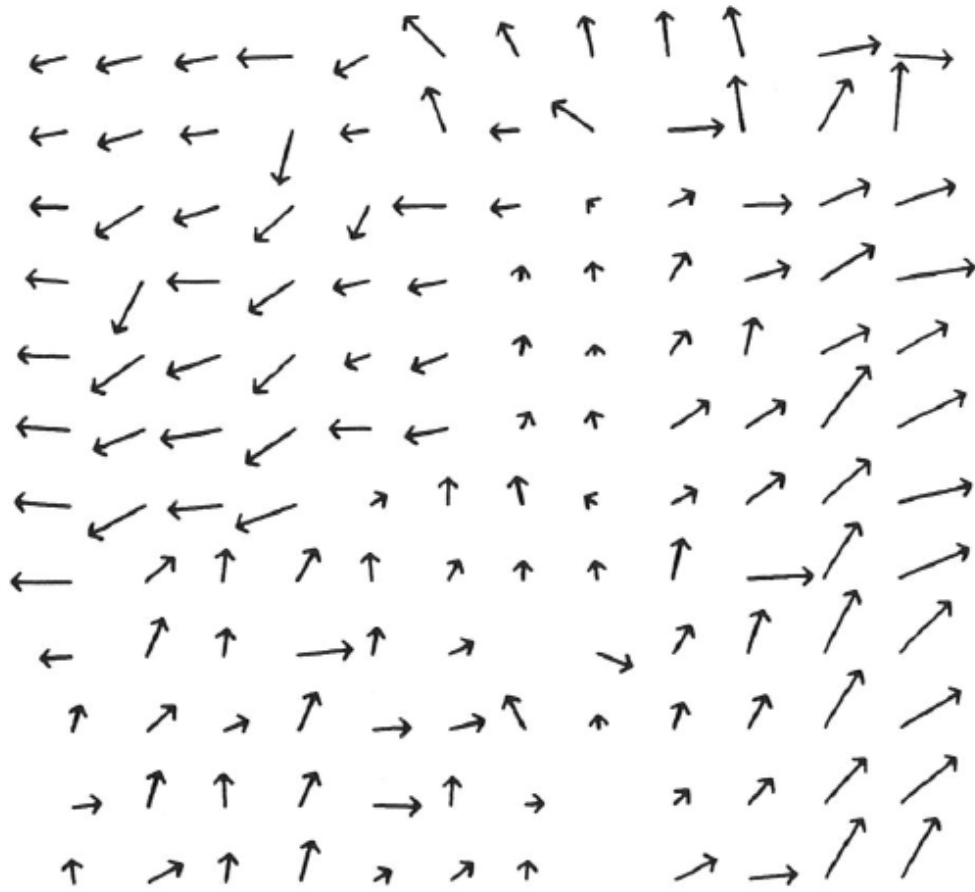


Figure 7.10: Enlargement of region F of the dealiased wind field in Fig. 7.6.

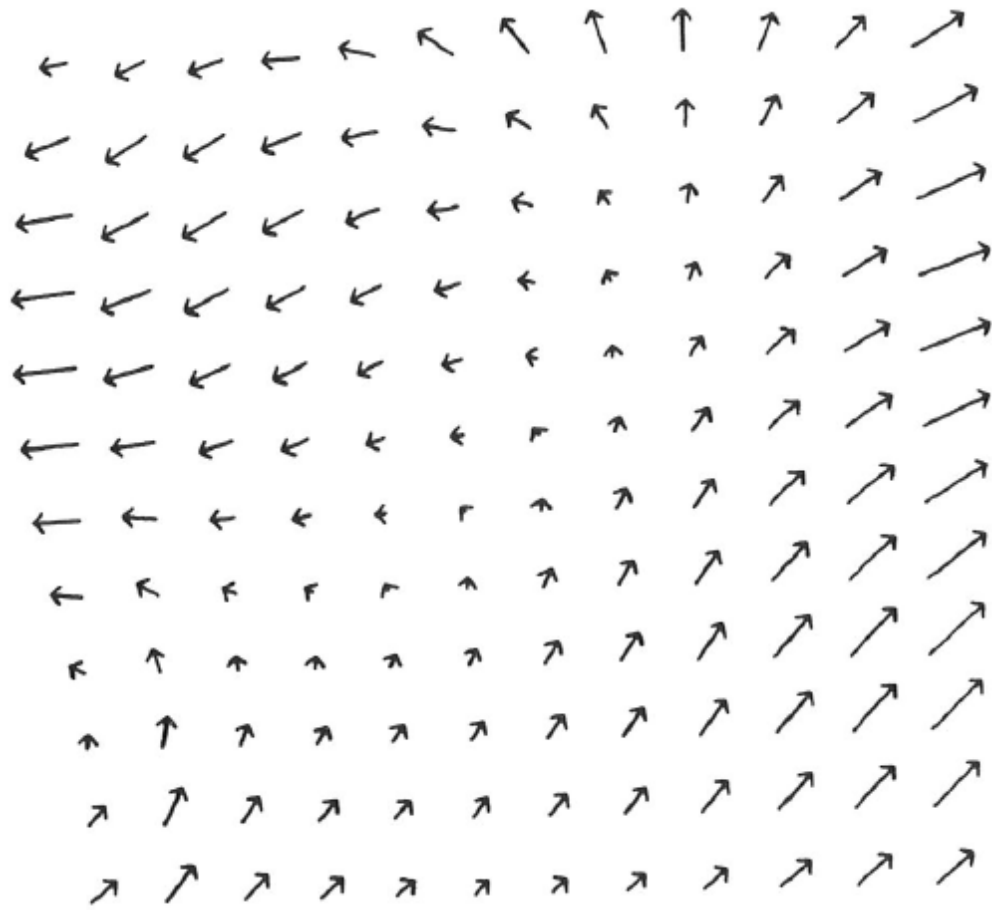


Figure 7.11: Enlargement of region F of the initial value wind field in Fig. 7.7.

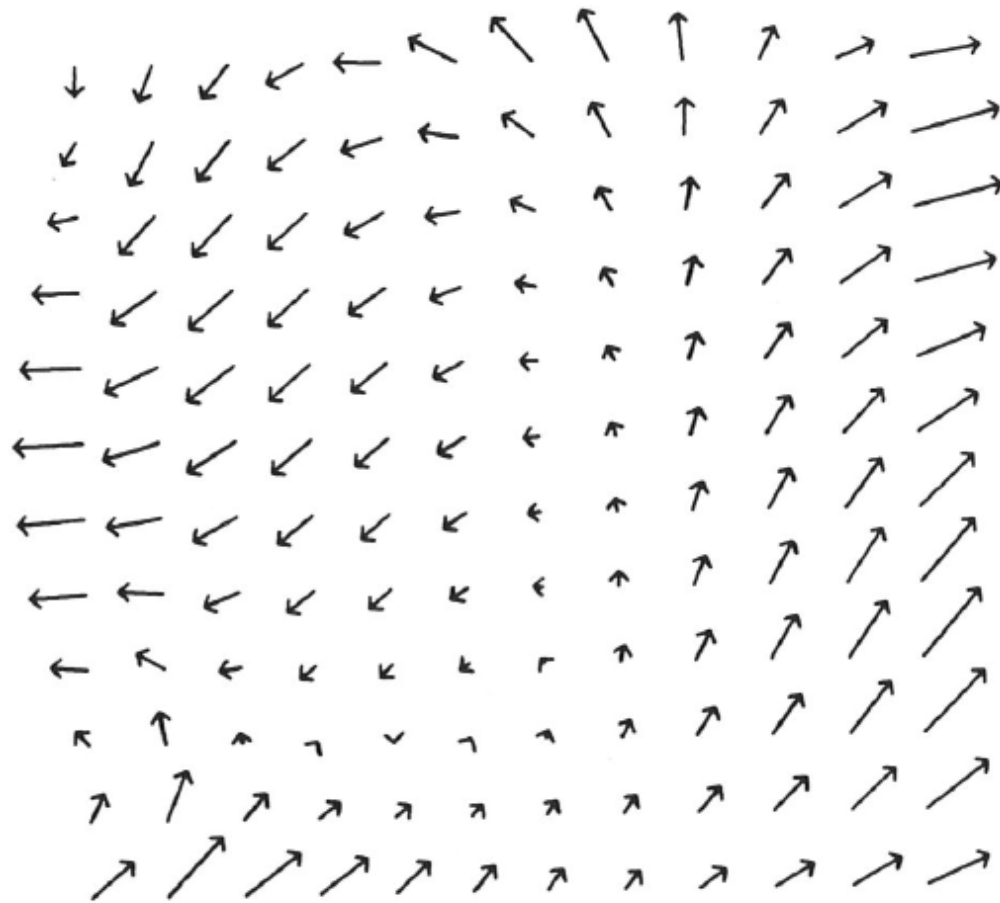


Figure 7.12: Enlargement of region F of the optimized wind field in Fig. 7.8.

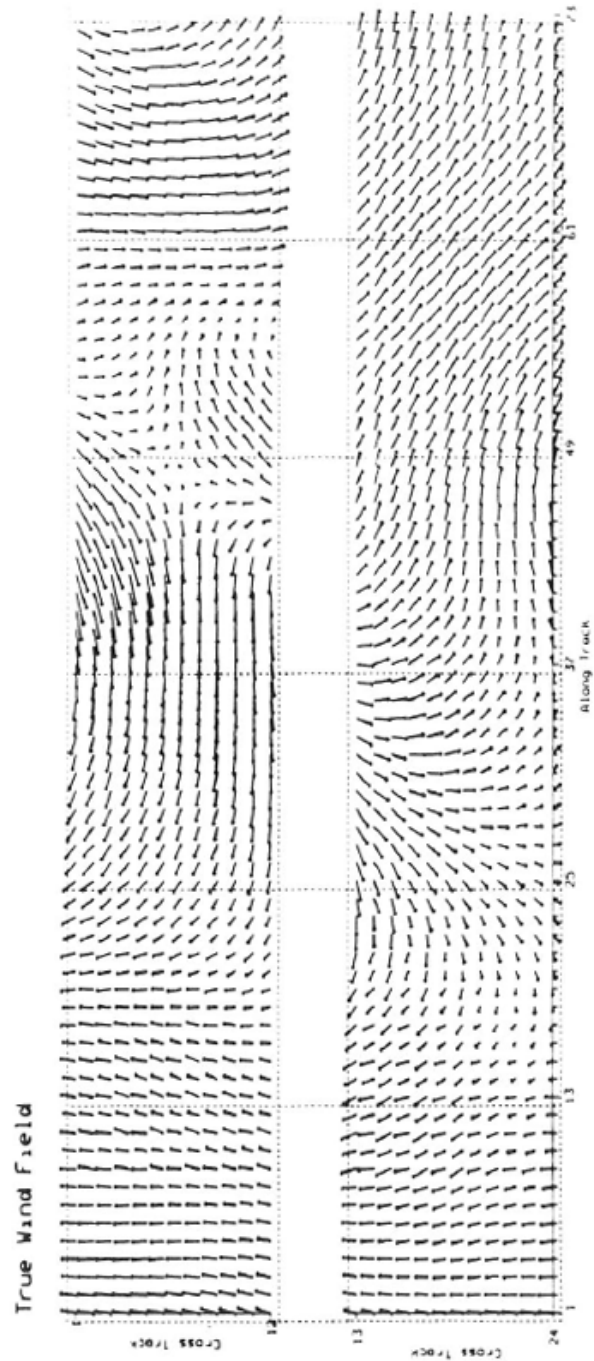


Figure 7.13: A second 50 km resolution example of a true wind field over both NSCAT observation swaths. Plotting convention is similar to Fig. 7.3.

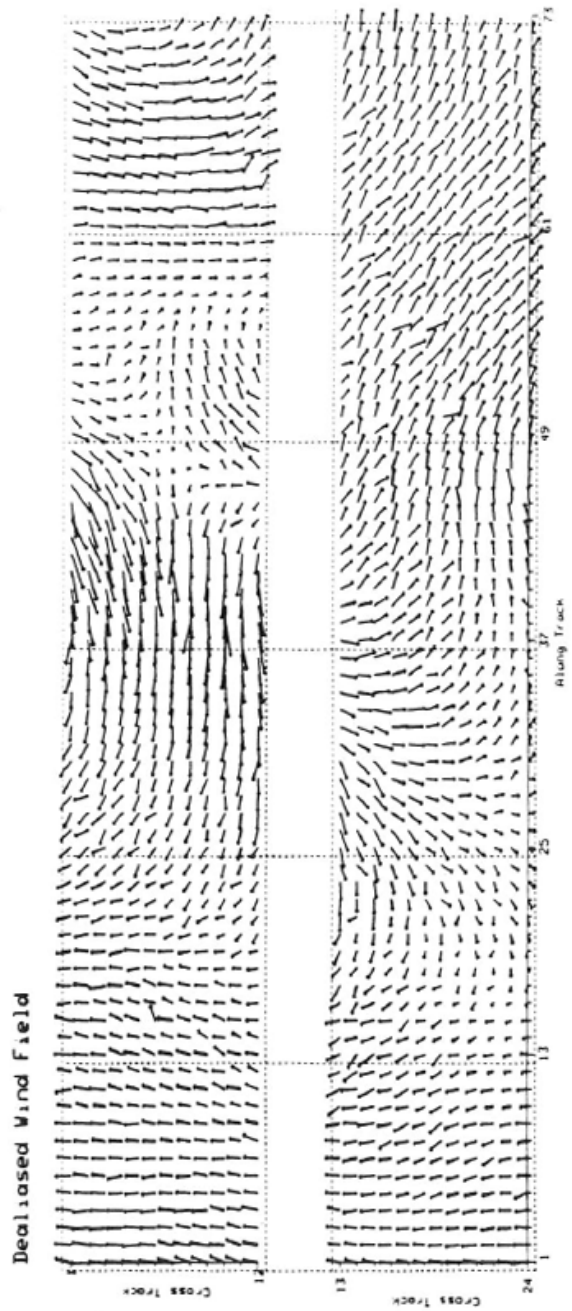


Figure 7.14: Dealiased point-wise wind field estimate corresponding to Fig. 7.12.

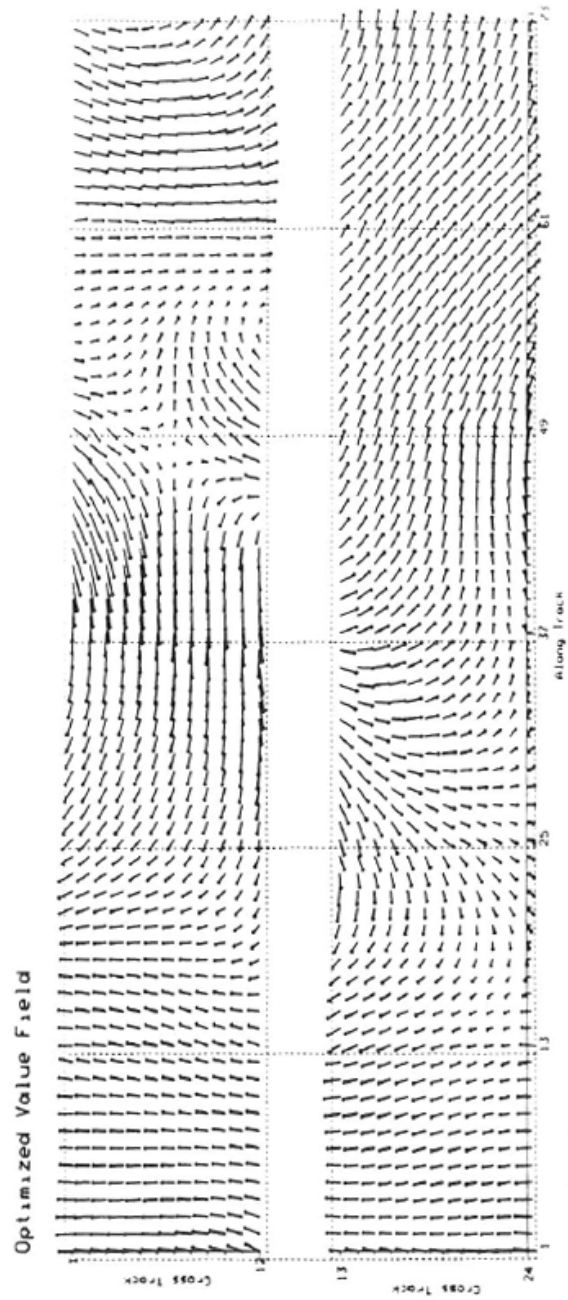


Figure 7.15: Optimized wind field (model-based wind field estimate) corresponding to Fig. 7.12.

Table 7.15: Total Wind Field Estimate Error for the 25 km Resolution Example

Field	RMS Error		
	Vector (m/s)	Direction (deg)	Speed (m/s)
True Model	1.012	14.532	0.718
Closest Ambiguity	1.778	21.747	0.667
Point-wise Dealiased	7.696	101.946	0.874
50 km Resolution Reference	1.895	29.560	0.675
Initial Value	1.256	20.823	0.835
Optimized from Initial Value	1.296	21.783	0.834
Optimized from True Model	1.336	20.026	0.828

7.15 shows a true wind field sampled at 25 km resolution. This example is the same underlying wind field as in Fig. 7.3. Figure 7.16 shows the closest ambiguity to the true wind field. This would be the ideal point-wise wind estimate corresponding to perfect dealiasing. Figure 7.17 shows the actual point-wise wind estimated obtained by dealiasing at 25 km resolution. Figure 7.18 shows the 50 km reference field. The 50 km reference field is computed by first using point-wise estimation and dealiasing at 50 km resolution. The 25 km resolution point-wise ambiguity which is closest to the corresponding 50 km resolution dealiased wind vectors become the 50 km reference field. Figure 7.18 shows the initial value field computed from Fig. 7.17. Figure 7.19 shows the model-based wind field estimate which was optimized from the initial value in Fig. 7.17.

Table 7.2 summarizes the total error for the various fields including the errors for the 25 km resolution point-wise dealiased and the 50 km reference fields. While, the 25 km resolution wind estimates have larger RMS errors than the 50 km resolution wind estimates, the model-based wind field estimates are: (1) less noisy and (2) exhibit better RMS vector and direction error than *both* of the dealiased wind fields *and* the closest ambiguity wind field. For this example, the initial values computed from the 50 km reference field were all good-quality such that the optimization algorithm found the global minimum for each region.

7.3 Summary

In this Chapter we have shown that, even with simplistic initialization/optimization schemes, the model-based estimates are more accurate than the point-wise wind estimates at both 25 km and 50 km resolution. We have shown that better results can be obtained by improved initialization/optimization schemes. Several such schemes are described in Appendix I.

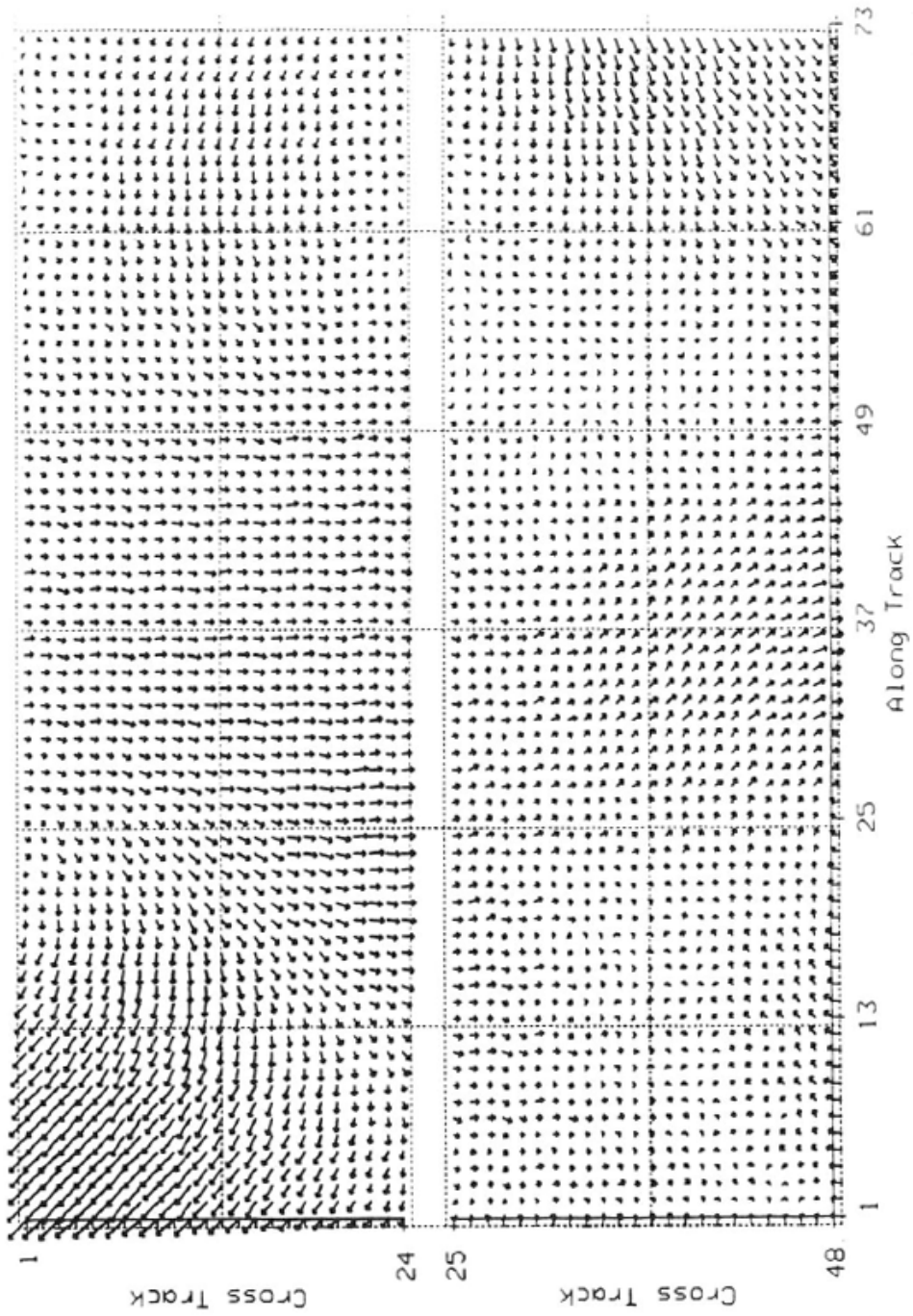


Figure 7.16: A 25 km resolution example of a true wind field over both NSCAT observation swaths. Plotting convention is similar to Fig. 7.3.

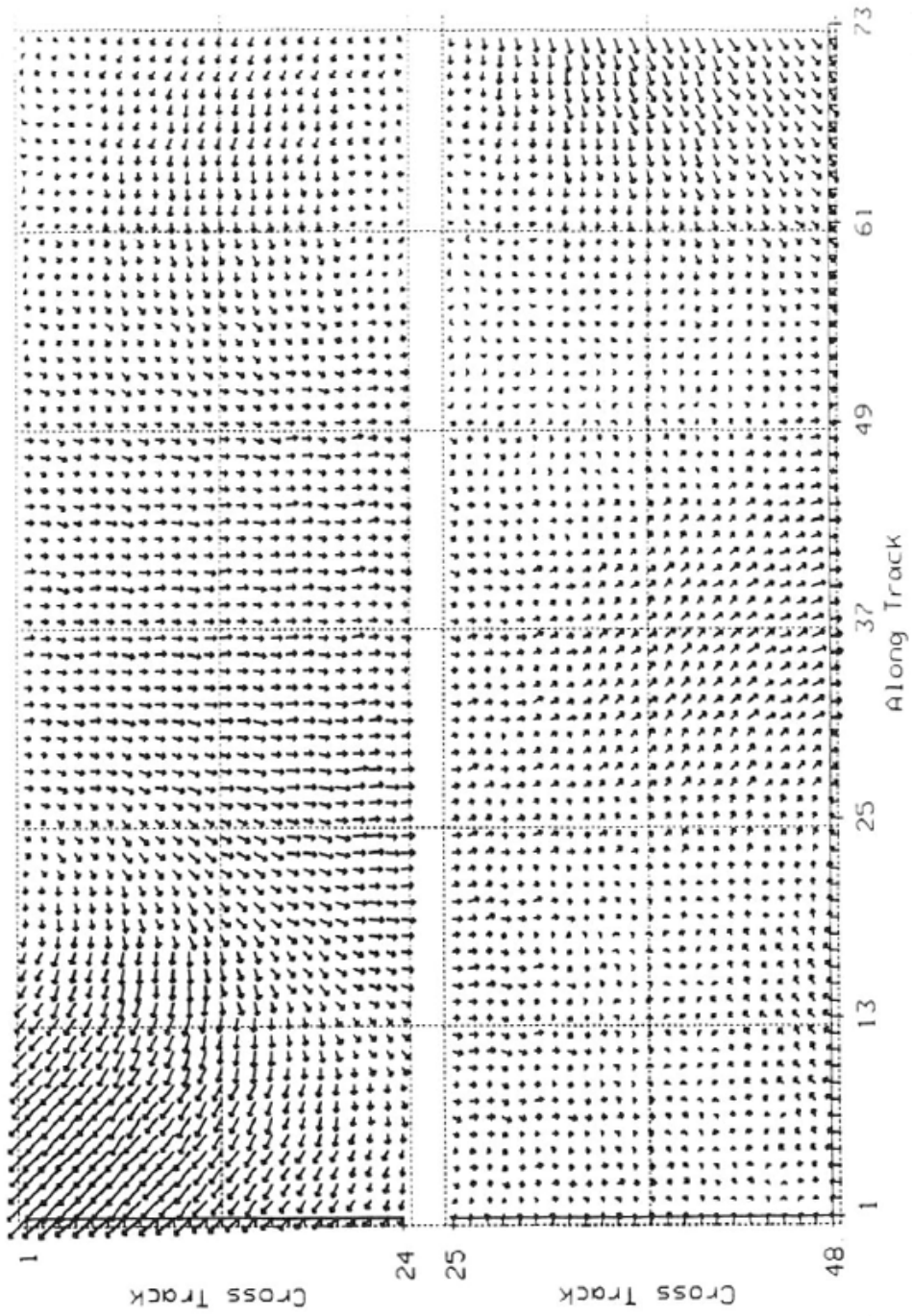


Figure 7.17: Closest ambiguity to the true wind field in Fig. 7.15.

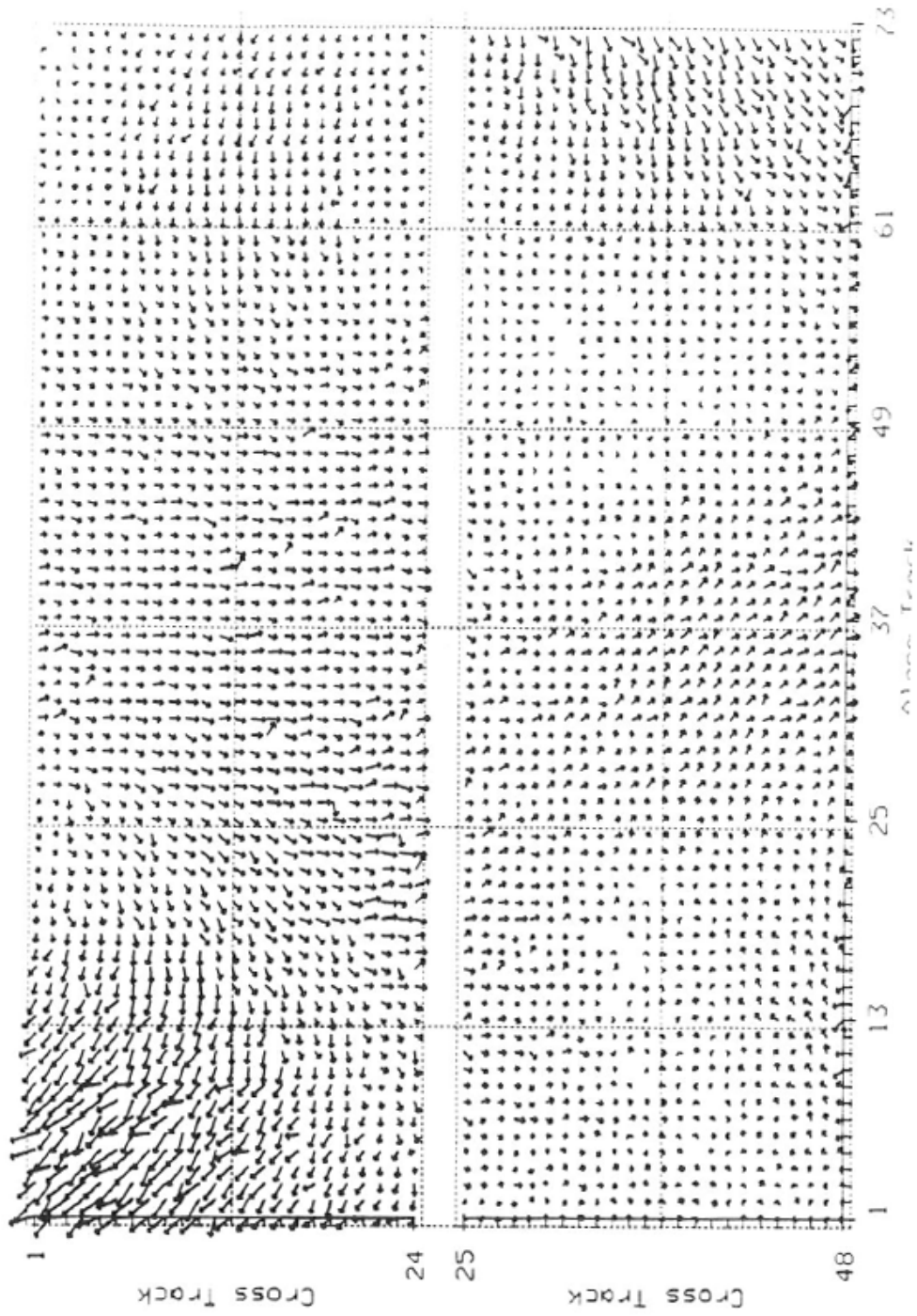


Figure 7.18: Point-wise dealiased wind field estimate corresponding to Fig. 7.15. Dealiasing was done at 25 km resolution.

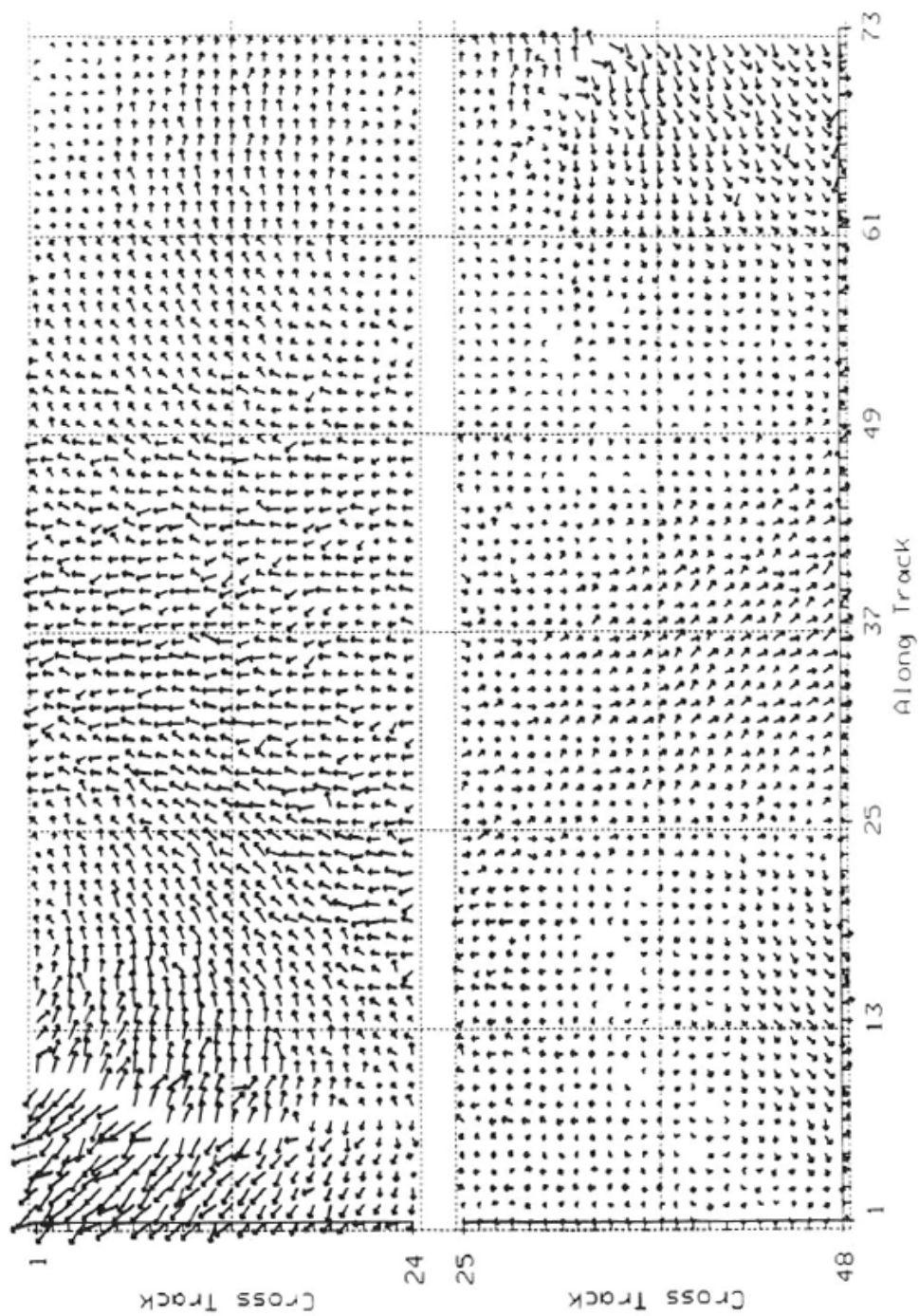


Figure 7.19: The 50 km reference field. This field was determined by first computing the point-wise wind estimates and dealiasing at 50 km resolution. The 25 km resolution point-wise ambiguities closest to the corresponding 50 km dealiased winds are shown.

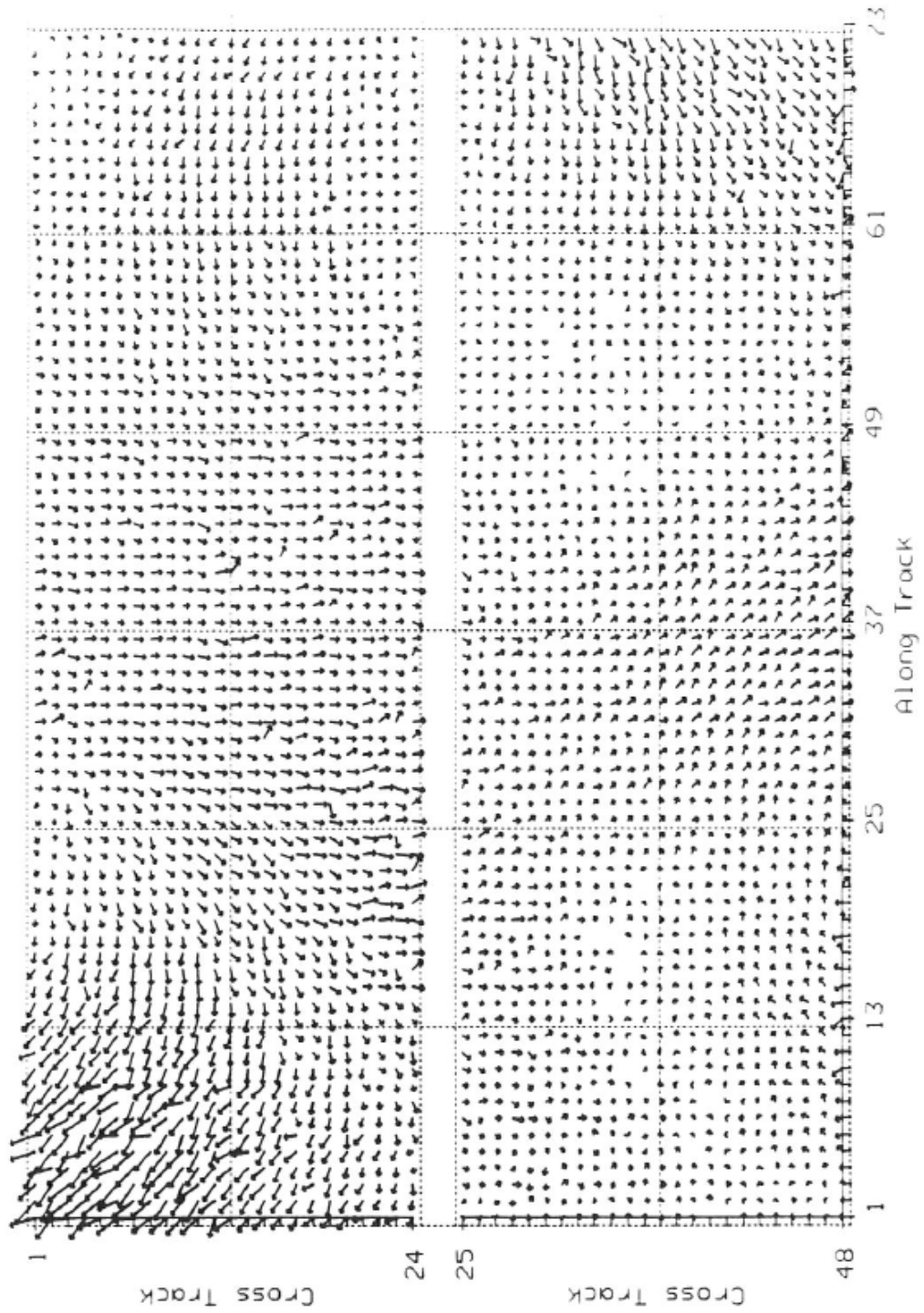


Figure 7.20: The 25 km resolution initial value field computed from Fig. 7.17

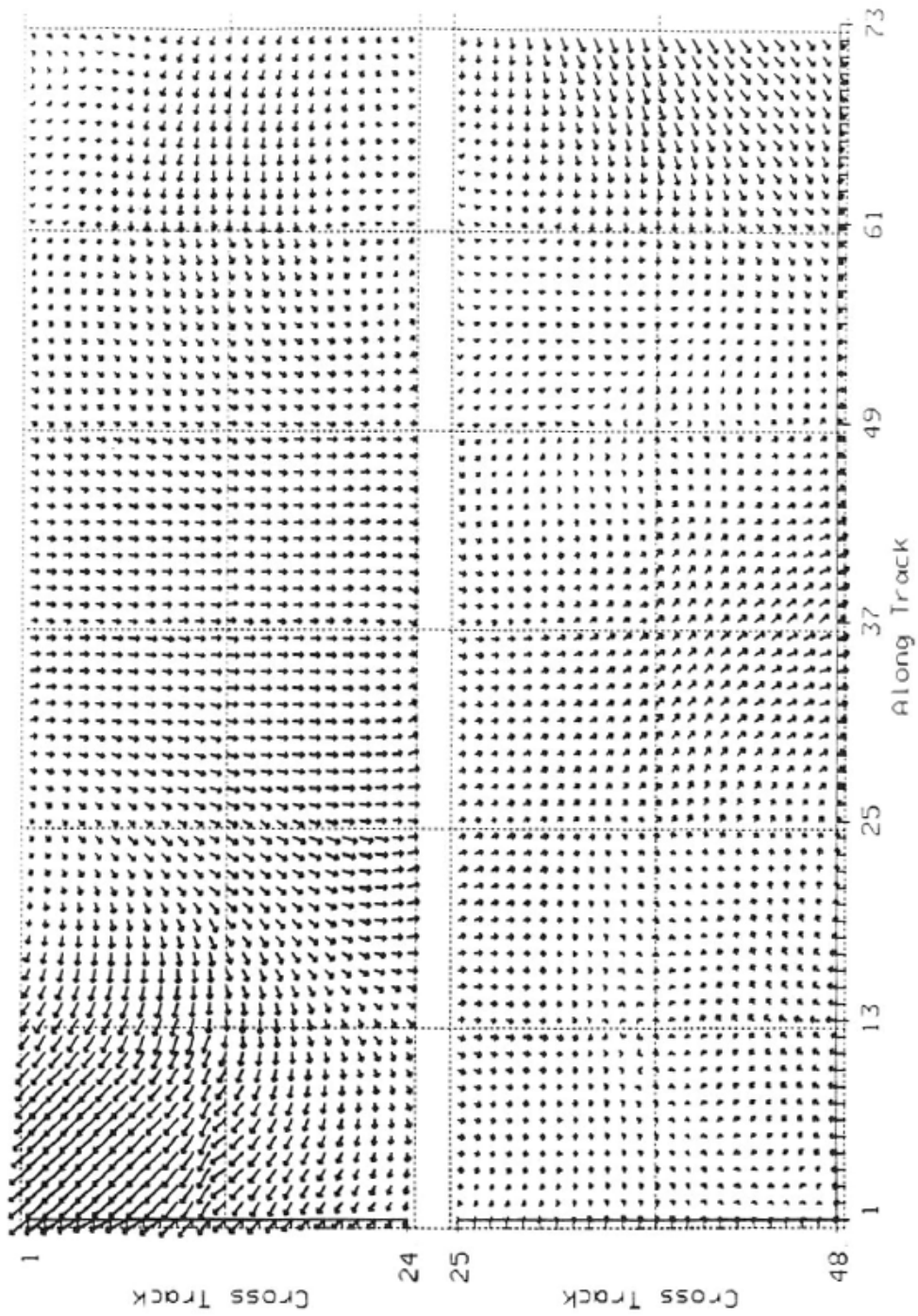


Figure 7.21: Optimized wind field (model-based wind field estimate) corresponding to Fig. 7.17.

Chapter 8

Conclusions and Recommendations for Future Work

8.1 Conclusions

In this research we have: (1) demonstrated the identifiability of the point-wise wind estimates (Chapter 3), (2) developed a model for near-surface mesoscale wind fields (Chapter 4), (3) evaluated the model using realistic wind fields (Chapter 4), (4) formulated the maximum-likelihood objective function for the wind field model parameters from the noisy σ^o measurements (Chapter 5), (5) demonstrated the identifiability of the model parameters (Chapter 5), (6) developed a simple method for optimizing the objective function based on a gradient-search technique with initial values computed using the results of point-wise wind estimation followed by dealiasing (Chapter 6), and (7) evaluated and compared the accuracy of the wind field estimates obtained using point-wise and model-based wind field estimation (Chapter 7). This work has demonstrated the feasibility of model-based wind field estimation. While the simple approach for optimizing the objective function described in Chapter 6 is sub-optimal, the comparisons given in Chapter 7 demonstrate that wind field estimation using a model-based approach, even with this simple optimization approach, yields more accurate estimates of the wind field than does the traditional two-step wind estimation approach using point-wise estimation and dealiasing. When more sophisticated optimization techniques are used in model-based wind field estimation, the accuracy of the resulting wind field estimates are better.

8.2 Recommendations for Future Work

There are a number of potential avenues of research which can be derived from this research. While the feasibility of model-based wind field estimation from wind scatterometer measurements has been demonstrated using a simple initialization and optimization approach, we have seen in Chapter 7 and Appendix I that better model-based wind field estimates are possible using improved optimization techniques; hence, future work should give priority to

the development of improved initialization and optimization algorithms. In particular, in order to use model-based wind field estimation for the operational processing of wind scatterometer data, an efficient implementation of the initial value computation procedure and the objective function optimization will be needed.

In this research, emphasis has been on demonstrating the feasibility of model-based wind estimation based on simulated σ^o measurements obtained using the NSCAT scatterometer. The application of model-based wind field estimation using σ^o measurements for the proposed ScanScat, which is based on a scanning pencil-beam [81], should also be evaluated. In addition, the model-based wind field estimation approach should be adapted for processing of the σ^o measurements collected by SASS. In order to do this, our approach must be modified to take into account the non-uniform sampling of the σ^o measurements obtained by SASS. In particular, a different initialization scheme may be required. In addition, this technique should be evaluated for processing the planned ERS-1 scatterometer. The ERS-1 scatterometer differs from previous and planned scatterometers in that it operates at a different frequency; hence, the model function may be quite different.

Lastly, the wind field model developed in this research is based on rather simplistic assumptions on the vorticity and divergence fields; more sophisticated models should be investigated.

In summary, future work in model-based wind field estimation from wind scatterometer measurements should be done in the following areas: (1) improved initialization and optimization techniques, (2) application of the approach to other classes of wind scatterometers, (3) evaluation using SASS data, and (4) improved wind field models.

The methodology used in this research has application in other areas involving distributed parameter systems. In wind estimation we started with a well-defined measurement equation for a parameter (σ^o) which is related to the quantity of interest (the wind) via a model function. Our approach to the estimation of the wind from measurements of σ^o is to view the wind field as a distributed parameter system which can be approximately modeled using partial differential equations. In effect, this system of equations provides constraints on the estimate of the quantity of interest, thus permitting more accurate estimates.

The partial differential equation system is solved by converting it to a finite-difference system which is then arranged to express the quantity of interest in terms of a set of unknown parameters. This yields a simple model of the distributed parameter system. The quantity of interest is estimated indirectly by first estimating the unknown parameters directly from the measurements, then using the model to compute the quantity of interest from the estimated model parameters.

As the results of this research indicate, this methodology can be successfully used even when the relationship between the measured parameter and the desired quantity is non-unique as is the case with the geophysical model function relating σ^o and winds.

This methodology has possible application in other remote sensing problems such as estimation of atmospheric aerosols, surface topography, and wave height as well as down-to-earth problems such as the thermal control of steel in rolling mills.

Bibliography

- [1] T. D. Allan, ed., *Satellite Microwave Remote Sensing*, West Sussex, England: Ellis Horwood Limited, 1983.
- [2] O. E. Allen, *Atmosphere*, Alexandria, Virginia: Time-Life Books, 1982.
- [3] D. Anderson *et al.*, *A Study of the Feasibility of Using Sea and Wind Information from the ERS-1 Satellite – Part 1: Wind Scatterometer Data*, European Space Agency Contract Report, June 1987.
- [4] R. Atlas *et al.*, “The Impact of Scatterometer Wind Data on Global Weather Forecasting,” NASA Conference Publication 2303, Proceedings of the URSI Commission F Symposium and Workshop, Shoshon, Israel, May 14-23, pp. 567-573, 1984.
- [5] R. Atlas *et al.*, “Global Surface Wind and Flux Fields from Model Assimilation of Seasat Data,” *Journal of Geophysical Research*, Vol. 92, No. C6, pp. 6477-6487, 1987.
- [6] W. E. Baker *et al.*, “Large-Scale Analysis and Forecast Experiments with Wind Data from the Seasat-A Scatterometer,” *Journal of Geophysical Research*, Vol. 89, pp. 4927-4936, 1984.
- [7] G. K. Batchelor, *The Theory of Homogeneous Turbulence*, Cambridge: Cambridge University Press, 1967.
- [8] M. S. Bazaraa and C. M. Shetty, *Nonlinear Programming – Theory and Algorithms*, New York: John Wiley and Sons, 1979.
- [9] R. Beven and M. Freilich, “Wind Fields for Big Sim,” Jet Propulsion Laboratory Interoffice Memorandum, Nov. 1985.
- [10] S. J. Bijlsma, L. M. Hafkenscheid and P. Lynch, “Computation of the Streamfunction and Velocity Potential and Reconstruction of the Wind Field,” *Monthly Weather Review*, No. 114, pp. 1547-1551, 1986.
- [11] E. Bracalente, D. Boggs, W. Grantham, and J. Sweet, “The SASS Scattering Coefficient (σ_o) Algorithm,” *IEEE Journal of Oceanic Engineering*, Vol. OE-5, No. 2, pp. 145-154, April 1980.

- [12] J. W. Brewer, "Kronecker Products and Matrix Calculus in System Theory," *IEEE Transactions on Circuits and Systems*, Vol. CAS-25, No. 9, pp. 772-781, Sept. 1978.
- [13] R. A. Brown and G. Levy, "Ocean Surface Pressure Fields from Satellite-Sensed Winds," *Monthly Weather Review*, Vol. 114, No. 11, pp. 2197-2204, Nov. 1986.
- [14] R. A. Brown *et al.*, "Surface Wind Analyses for SEASAT," *Journal of Geophysical Research*, Vol. 87, No. C5, pp. 3355-3364, April 1982.
- [15] R. A. Brown "On a Satellite Scatterometer as an Anemometer," *Journal of Geophysical Research*, Vol. 88, No. C3, pp. 1663-1673, Feb. 1983.
- [16] C. J. Cats, "Analysis of Surface Wind and Its Gradient in a Mesoscale Wind Observation Network," *Monthly Weather Review*, Vol. 108, pp. 1100-1107, Aug. 1980.
- [17] J. G. Charney, "Geostrophic Turbulence," *Journal of Atmospheric Science*, Vol. 28, pp. 1087-1095, 1971.
- [18] C-Y Chi, "Single-Channel and Multichannel Deconvolution," Dissertation, University of Southern California, April 1983.
- [19] C-Y Chi, D. G. Long, and F. K. Li, "Radar Backscatter Measurement Accuracies Using Digital Doppler Processors in Spaceborne Scatterometers," *IEEE Transactions on Geoscience and Remote Sensing*, Vol. GE-24, No. 3, pp. 426-437, May 1986.
- [20] C-Y Chi, R. Aroian, and F. K. Li, "Simulation Studies for the NASA Scatterometer on NROSS," Proceedings of the International Geoscience and Remote Sensing Symposium, pp. 1673-1676, Sept. 1986.
- [21] C-Y Chi and F.K. Li, "A Comparative Study of Several Wind Estimation Algorithms for Spaceborne Scatterometers," *IEEE Transactions on Geoscience and Remote Sensing*, Vol. GE-26, No. 2, pp. 115-121, March 1988.
- [22] R. Davies-Jones, "On the Formulation of Surface Geostrophic Streamfunction," *Monthly Weather Review*, Vol. 116, pp. 1824-1826, Sept. 1988.
- [23] G. J. Dome, "Oceanic Wind Vector Determination Using SEASAT Satellite," Thesis, University of Kansas at Lawrence, 1980.
- [24] M.A. Donelan and W.J. Pierson, Jr., "Radar Scattering and Equilibrium Ranges in Wind-generated Waves with Application to Scatterometry," *Journal of Geophysical Research*, Vol. 92, pp. 4971-5029, 1987.
- [25] W. L. Donn, *Meteorology*, McGraw-Hill Book Co., New York, New York, 1965.
- [26] J. L. Doob, "Probability and Statistics," *American Mathematical Society Transactions*, Vol. 36, pp. 759-775, 1934.

- [27] D. Duffy and R. Atlas, "The Impact of Seasat-A Scatterometer Data on the Numerical Prediction of the QEII Storm," *Journal of Geophysical Research*, Vol. 90, pp. 2241-2248, 1985.
- [28] S. L. Durden, "Microwave Scattering from the Ocean Surface," Dissertation, Stanford University, 1986.
- [29] C. E. Elachi, *Spaceborne Radar Remote Sensing: Applications and Techniques*, New York: IEEE Press, 1988.
- [30] M. H. Freilich, *Science Opportunities Using the NASA Scatterometer on N-ROSS*, JPL Publication 84-57, Jet Propulsion Laboratory, Pasadena, Feb. 1, 1985.
- [31] M. H. Freilich, "Construction of Wind fields with Known Curl and Divergence," Jet Propulsion Laboratory Interoffice Memorandum, June 28, 1985.
- [32] M. H. Freilich, "Satellite Scatterometer Comparisons with Surface Measurements: Techniques and SEASAT Results," Proceedings of a Workshop on ERS-1 Wind and Wave Calibration, 2-6 June 1986, pp. 57-62, (ESA SP-262, Sept. 1986).
- [33] M. H. Freilich and D. B. Chelton, "Wavenumber Spectra of Pacific Winds Measured by the Seasat Scatterometer," *Journal of Physical Oceanography*, Vol. 16, No. 4, pp. 741-757, April 1986.
- [34] R. E. Fischer, "Standard Deviation of Scatterometer Measurements from Space," *IEEE Transactions on Geoscience Electronics*, Vol. GE-10, No. 2, pp. 106-113, 1972.
- [35] S. B. Goldenberg and J. J. O'Brien, "Time and Space Variability of Tropical Pacific Wind Stress," *Monthly Weather Review*, Vol. 109, pp. 1190-1207, 1981.
- [36] J. F. R. Gower, *Oceanography from Space*, New York: Plenum Press, 1981.
- [37] W. L. Grantham *et al.*, "Performance Evaluation of an Operational Spaceborne Scatterometer," *IEEE Transactions on Geoscience and Remote Sensing*, Vol. GE-20, No. 3, pp. 240-254, July 1982.
- [38] T. H. Guymer, "Remote Sensing of Sea-Surface Winds," R. A. Vaughan, ed., *Remote Sensing Applications in Meteorology and Climatology*, pp. 32-357, D. Reidel Pub. Co., 1987.
- [39] D. Halpern, "The Variability of the Surface Wind Field in the Equatorial Pacific Ocean: Criteria for Satellite Measurements," NASA Conference Publication 2303, Proceedings of the URSI Commission F Symposium and Workshop, Shoshon, Israel, May 14-23, pp. 357-366, 1984.
- [40] G. J. Haltiner and R. T. Williams, *Numerical Prediction and Dynamic Meteorology*, New York: John Wiley and Sons, 1980.

- [41] H. F. Hawkins and S. L. Rosenthal, "On the Computation of Stream Functions from the Wind Field," *Monthly Weather Review*, Vol. 93, pp. 245-253, April 1965.
- [42] J. D. Hawkins and P. G. Black, "SEASAT Scatterometer Detection of Gale-Force Winds Near Tropical Cyclones," *Journal of Geophysical Research*, Vol. 88, No. C3, pp. 1674-1682, Feb. 1983.
- [43] R. N. Hoffman, "SASS Wind Ambiguity Removal by Direct Minimization," *Monthly Weather Review*, Vol. 110, pp. 434-445, May 1982.
- [44] R. N. Hoffman, "SASS Wind Ambiguity Removal by Direct Minimization. Part II: Use of Smoothness and Dynamical Constraints," *Monthly Weather Review*, Vol. 112, pp. 1829-1852, Sept. 1982.
- [45] A. K. Jain, "Partial Differential Equations and Finite Difference Methods in Image Processing—Part I: Image Representation," *Journal of Optimization Theory and Applications*, Vol. 23, No. 1, pp. 65-91, Sept. 1977.
- [46] A. K. Jain and J. R. Jain, "Partial Differential Equations and Finite Difference Methods in Image Processing—Part II: Image Restoration," *IEEE Transactions on Automatic Control*, Vol. AC-23, No. 5, pp. 817-834, Oct. 1978.
- [47] "SEASAT-JASIN Workshop Report – Volume 1: Findings and Conclusions," JPL Publication 80-62, Dec. 1980.
- [48] J. W. Johnson, L. A. Williams, Jr., E. M. Bracalente, F. B. Beck, and W. L. Grantham, "Seasat-A Satellite Scatterometer Instrument Evaluation," *IEEE Journal of Oceanic Engineering*, Vol. OE-5, No. 2, pp. 138-144, April 1980.
- [49] W. L. Jones, L. C. Schroeder, and J. L. Mitchell, "Aircraft Measurements of the Microwave Scattering Signature of the Ocean," *IEEE Transactions on Antennas and Propagation*, Vol. AP-25, No. 1, Jan. 1977.
- [50] W. L. Jones and L. C. Schroeder, "Radar Backscatter from the Ocean: Dependence on Surface Friction Velocity," *Boundary Layer Meteorology*, Vol. 13, pp. 133-149, 1978.
- [51] W. L. Jones *et al.*, "The SEASAT-A Satellite Scatterometer: The Geophysical Evaluation of Remotely Sensed Wind Vectors Over the Ocean," *Journal of Geophysical Research*, Vol. 87, No. C5, pp. 3297-3317, April 1982.
- [52] W. L. Jones, F. J. Wentz, and L. C. Schroeder, "Algorithm for Inferring Wind Stress from SeaSat-A," *J. Spacecraft*, Vol. 15, No. 6, pp. 368-374, Dec. 1978.
- [53] W. L. Jones, V. E. Delnore, and E. M. Bracalente, "The Study of Mesoscale Ocean Winds," R. C. Beal, P. S. DeLeonibus, and I. Katz, eds., *Spaceborne Synthetic Aperture Radar for Oceanography*, Baltimore: The Johns Hopkins University Press, 1981.

- [54] B. Kinsman, *Wind Waves*, Englewood Cliffs, New Jersey: Prentice-Hall, Inc., 1965.
- [55] S. Kirkpatrick, C. D. Gelatt, Jr., and M. P. Vecchi, "Optimization by Simulated Annealing," *Science*, Vol. 220, No. 4598, pp. 671-680, 13 May 1983.
- [56] J. Laycock, "An Analysis of Directional Ambiguities in Wind Scatterometer Measurements," Proceedings of the International Geoscience and Remote Sensing Symposium, pp. 557-560, 1988.
- [57] C. E. Leith, "Atmospheric Predictability and Two-Dimensional Turbulence," *Journal of the Atmospheric Sciences*, Vol. 28, No. 2, pp. 145-161, March, 1971.
- [58] S. J. Leon, *Linear Algebra with Applications*, New York: MacMillan Pub. Co., Inc., 1980.
- [59] D. Leotta and D. G. Long, "Probability Distribution of Wind Retrieval Error Versus True Wind Vector and Swath Location for the NASA Scatterometer," Submitted for publication in the International Geoscience and Remote Sensing Symposium, 1989.
- [60] F. Li, P. Callahan, M. Freilich, D. Long, and C. Winn, "NASA Scatterometer for NROSS – A System for Global Oceanic Wind Measurement," Proceedings of the International Geoscience and Remote Sensing Symposium, pp. 777-780, 1984.
- [61] F. Li, C. Winn, D. Long, and C. Guey, "NROSS Scatterometer – An Instrument for Global Oceanic Wind Observations," Proceedings of SPIE – The International Society for Optical Engineering, Vol. 481, pp. 193-198, 1984.
- [62] F. Li, G. Neumann, S. Shaffer, and S. L. Durden, "Studies of the Location of Azimuth Modulation Minima for K_u Band Ocean Radar Backscatter," *Journal of Geophysical Research*, Vol. 93, No. C7, pp. 8229-8238, July 1988.
- [63] D. K. Lilly and T. Gal-Chen, eds., *Mesoscale Meteorology – Theories, Observations and Models*, Boston: D. Reidel Pub. Co., 1983.
- [64] C. Y. Liu and W. R. Good, "An Iterative Algorithm for Objective Wind Field Analysis," *Monthly Weather Review*, Vol. 104, pp. 784-792, June 1976.
- [65] L. Ljung, *System Identification Theory for the User*, Englewood Cliffs, New Jersey: Prentice-Hall, Inc., 1987.
- [66] D. Long, C-Y Chi, and F. Li, "Digital Filter Processor Design for Spaceborne Scatterometers," Proceedings of the International Geoscience and Remote Sensing Symposium, pp. 569-572, 1984.
- [67] D. G. Long and J. M. Mendel, "Model-based Estimation of Wind Fields Over the Ocean from Wind Scatterometer Measurements," Proceeding of the International Geoscience and Remote Sensing Symposium, pp. 553-556, 1988.

- [68] D. G. Long, C-Y Chi, and F. K. Li, "The Design of an Onboard Digital Doppler Processor for a Spaceborne Scatterometer," *IEEE Transactions on Geoscience and Remote Sensing*, Vol. 26, No. 6, pp. 869-878, Nov. 1988.
- [69] D. G. Long, "Documentation for the NSCAT Simulation Programs," Jet Propulsion Laboratory Internal Memo, 3343-88-177, Dec. 20, 1988.
- [70] D. G. Long, S. Shaffer, and M. Freilich, "Results of a Study on Polarization Selection for the NSCAT Scatterometer," Submitted for publication in the International Geoscience and Remote Sensing Symposium, 1989.
- [71] D. G. Luenberger, *Linear and Nonlinear Programming*, Reading: Addison-Wesley Pub. Co., Mass., 1984.
- [72] P. Lynch, "Deducing the Wind from Vorticity and Divergence," *Monthly Weather Review*, Vol. 116, pp. 86-93, Jan. 1988.
- [73] R. A. Maddox and T. H. Vonder Haar, "Covariance Analyses of Satellite-Derived Mesoscale Wind Fields," *Journal of Applied Meteorology*, Vol. 18, pp. 1327-1334, Oct. 1979.
- [74] G. I. Marchuk, *Numerical Methods in Weather Prediction*, K. N. Trirogoff and V. R. Lamb, Trans., London: Academic Press, 1974.
- [75] B. D. Martin *et al.*, "An Overview of the NSCAT/N-ROSS Program," Proceedings of a Workshop on ERS-1 Wind and Wave Calibration, 2-6 June 1986, pp. 143-149 (ESA Sp-262), 1986.
- [76] S. F. Masri, G. A. Bekey, and F. B. Safford, "A Global Optimization Algorithm Using Adaptive Random Search," *Applied Mathematics and Computation*, Vol. 7, pp. 353-375, 1980.
- [77] J. M. Mendel, *Discrete Techniques of Parameter Estimation*, New York: Marcel Dekker, Inc., 1973.
- [78] J. M. Mendel, *Lessons in Digital Estimation Theory*, Englewood Cliffs, New Jersey: Prentice-Hall, Inc., 1987.
- [79] J. M. Mendel and K. S. Fu, eds., *Adaptive, Learning and Pattern Recognition Systems – Theory and Applications*, New York: Academic Press, 1970.
- [80] A. R. Mitchell, *Computational Methods in Partial Differential Equations*, London: John Wiley and Sons, 1969.
- [81] R. K. Moore and A. K. Fung, "Radar Determination of Winds at Sea," *Proceedings of the IEEE*, Vol. 67, No. 11, pp. 1504-1521, Nov. 1979.

- [82] R. K. Moore, R. G. Kennett, and F. K. Li, "Performance of a Scanning Pencil-Beam Spaceborne Scatterometer for Ocean Wind Measurements," *Proceeding of the International Geoscience and Remote Sensing Symposium*, pp. 563-564, 1988.
- [83] I. M. Navon and D. M. Legler, "Conjugate-Gradient Methods for Large-Scale Minimization in Meteorology," *Monthly Weather Review*, Vol. 115, pp. 1479-1502, Aug. 1987.
- [84] J. O'Brien, "Scientific Opportunities Using Satellite Wind Stress Measurements Over the Ocean," Nova University Press/N.Y.I.T. Press, Fort Lauderdale, Florida, NASS Contract Number NAS5-26714, June 1982.
- [85] S. V. Parter, "Remarks on the Numerical Computation of Solutions of $\Delta u = f(P, u)$," *Numerical Solution of Partial Differential Equations*, J. H. Bramble, ed., New York: Academic Press, pp. 73-82, 1966.
- [86] J. Pailleus, "The Impact of Satellite Data on Global Numerical Weather Prediction," R. A. Vaughan, ed., *Remote Sensing Applications in Meteorology and Climatology*, pp. 32-357, D. Reidel Pub. Co., 1987.
- [87] G. E. Peckham, "Microwave Instrument and Methods," R. A. Vaughan, ed., *Remote Sensing Applications in Meteorology and Climatology*, pp. 32-357, D. Reidel Pub. Co., 1987.
- [88] J. Pedlosky, *Geophysical Fluid Dynamics*, New York: Springer-Verlag, 1979.
- [89] W. J. Pierson, Jr., "The Measurement of the Synoptic Scale Wind Over the Ocean," *Journal of Geophysical Research*, Vol. 88, No. C3, pp. 1683-1708, Feb. 1983.
- [90] W. J. Pierson, Jr., W. B. Sylvester, and R. E. Salfi, "Vector Wind, Horizontal Divergence, Wind Stress, and Wind Stress Curl from SEASAT-SASS at a One Degree Resolution," NASA Conference Publication 2303, Proceedings of the URSI Commission F Symposium and Workshop, Shores, Israel, pp. 557-565, May 14-23, 1984.
- [91] W.J. Plant, "A Two-scale model of short wind-generated waves and Scatterometry," *Journal of Geophysical Research*, Vol. 91, pp. 10735-10749, 1986.
- [92] M. M. Rienecker and L. L. Ehret, "Wind Stress Curl Variability Over the North Pacific from the Comprehensive Ocean-Atmosphere Data Set," *Journal of Geophysical Research*, Vol. 93, No. C5, pp. 5069-5077, May 1988.
- [93] L. Schroeder *et al.*, "The Relationship Between the Wind Vector and the Normalized Radar Cross Section Used to Derive Seasat-A Satellite Scatterometer Winds," *Journal Geophysical Research*, Vol. 87, No. C5, pp. 3318-3336, 1982.
- [94] L. Schroeder *et al.*, "Removal of Ambiguous Wind Directions for a Ku-band Wind Scatterometer Using Measurements at Three Different Azimuth Angles," *IEEE Transactions on Geoscience and Remote Sensing*, Vol. GE-23, No. 2, pp. 91-100, March 1985.

- [95] H. J. Schultz, "A Median Filter Approach for Correcting Errors in a Vector Field," Proceedings of the International Geoscience and Remote Sensing Symposium, pp. 724-728, 1985.
- [96] S. Shaffer, R. S. Dunbar, V. Hsiao, and D. G. Long, "Selection of Optimum Median-Filter-Based Ambiguity Removal Algorithm Parameter Values for NSCAT," Submitted for publication in the International Geoscience and Remote Sensing Symposium, 1989.
- [97] J. Shukla and K. R. Saha, "Computation of Non-Divergent Streamfunction and Irrotational Velocity Potential from the Observed Winds," *Monthly Weather Review*, Vol. 102, pp. 419-425, June 1974.
- [98] C. H. Slump and B. J. Hoenders, "The Determination of the Location of the Global Maximum of a Function in the Presence of Several Local Extrema," *IEEE Transactions on Information Theory*, Vol. IT-31, No. 4, pp. 490-497, July 1985.
- [99] R. H. Stewart, *Methods of Satellite Oceanography*, Berkeley, California: University of California Press, 1985.
- [100] R. H. Stewart, "Seasat Success Statement," JPL Publication D-2841, April 11, 1985.
- [101] D. J. Tritton, *Physical Fluid Dynamics*, Berkshire, England: Van Nostrand Reinhold Co. Ltd., 1982.
- [102] F. T. Ulaby, R. K. Moore, and A. K. Fung, *Microwave Remote Sensing – Active and Passive*, In three volumes, Addison-Wesley Publishing Co., Reading, Mass., 1981.
- [103] M. Van Dyke, *Perturbation Methods in Fluid Mechanics*, New York: Academic Press, 1964.
- [104] J. M. Wallace and P. V. Hobbs, *Atmospheric Science*, New York: Academic Press, 1977.
- [105] F. J. Wentz, S. Peteherych, and L.A. Thomas, "A Model Function for Ocean Radar Cross-sections at 14.6 GHz," *Journal of Geophysical Research*, Vol. 89, pp. 3689-3704, 1984.
- [106] F. J. Wentz, W. J. Cardone, and L. S. Fedor, "Intercomparison of Wind Speeds Inferred by the SASS, Altimeter, and SMMR," *Journal of Geophysical Research*, Vol. 87, No. C5, pp. 3378-3384, April 1984.
- [107] J. Willebrand, "Temporal and Spatial Scales of the Wind Field over the North Pacific and North Atlantic," *Journal of Physical Oceanography*, Vol. 8, pp. 1080-1094, 1978.
- [108] P. M. Woiceshyn *et al.*, "The Necessity for a New Parameterization of an Empirical Model for Wind/Ocean Scatterometry," *Journal of Geophysical Research*, Vol. 91, No. C2, Feb. 1986.

- [109] M.G. Wurtele *et al.*, "Wind Direction Alias Removal Studies of SEASAT Scattermeter-Derived Wind Fields," *Journal of Geophysical Research*, Vol. 87, No. C5, pp. 3365-3377, April 1982.
- [110] T-W Yu, "A Technique for Deducing Wind Direction from Satellite Microwave Measurements of Wind Speed," *Monthly Weather Review*, Vol. 115, pp. 1929-1939, Sept. 1987.

Appendix A

Additional Background

In this Appendix are provided brief tutorials in the fields of meteorology, oceanography, and scattering theory to provide background for the reader. Several sections follow [28] closely and are included for reference purposes.

A.1 Meteorology Fundamentals

Vertically, the atmosphere is divided into 4 distinct regions based on temperature profile and pressure [104]. Wind scatterometry is primarily concerned with the lowest atmospheric layer, the *troposphere*, which extends from sea level to approximately 10 km. The troposphere accounts for more than 80 % of the mass of the atmosphere. Meteorologists express atmospheric pressure in *millibars* (mb) (1 millibar equals 1000 dynes per square centimeter). At sea level, the average air pressure is 1013.25 mb or about 14.7 pounds per square inch. At any given altitude and time the atmospheric pressure can vary depending on local conditions.

At middle and high latitudes, winds tend to blow parallel to the isobars with the low pressure on the left in the northern hemisphere or on the right in the southern hemisphere. At a given latitude the speed of the wind tends to be inverse proportional to the spacing of the isobars. This tendency, due to the *geostrophic relationship* (further discussed below), makes it possible to infer gross features of the wind field from pressure maps and visa versa [104].

A.1.1 Atmospheric Thermodynamics

Temperature also drives atmospheric motion. When a volume of air is colder or contains more moisture and is thus denser than the surrounding air mass, it sinks. Conversely, when a volume of air is less dense than surrounding air due to a lower moisture content or warmer temperature, it is more buoyant than the surrounding air and rises. When this occurs, the atmosphere is termed *unstable*. As an air mass rises it cools due to adiabatic expansion and becomes more dense than the surrounding air. This tends to cancel the effects of buoyancy. When an air mass is less buoyant than the surrounding atmosphere it is termed *stable*. When

there is no net buoyancy, the atmosphere is said to have *neutral stability* [25].

An important factor in determining atmospheric stability is the rate at which temperature changes with height, called the *lapse rate*. As a volume of air ascends, it expands to maintain its internal pressure equal to the pressure of the air surrounding it. This expansion requires work which is extracted in the form of heat from the volume of moving air, cooling it. This is called *adiabatic cooling*. If the rising air contains sufficient moisture, the humidity may reach 100 %, causing the moisture to condense into clouds and if conditions are right, precipitation. The latent heat of vaporization is released into the air, warming it. On the other hand, as a volume of air descends, it is compressed. This heats the air volume [104].

A change of temperature or moisture changes the air density. As the air density in a column of air changes, the pressure at its base changes. The pressure gradient between columns of air at different pressures produces winds. A modified form of the *ideal gas law* is used to relate the pressure p , temperature T , and density ρ of the air.

$$p = \rho RT \quad (\text{A.1})$$

where R is the gas constant. An adjusted value for R is used which considers the moisture constant of the air. The relationship between pressure, height h , and density is known as the *hydrostatic equation*,

$$\frac{dp}{dh} = -g\rho \quad (\text{A.2})$$

where $g = 9.81\text{ms}^{-2}$ is the gravitational constant. Since $p(\infty) = 0$,

$$p(h) = \int_h^\infty g\rho dh. \quad (\text{A.3})$$

The height H required to decrease the pressure by a factor of $e = 2.718$ is known as the *scale height*,

$$H = \frac{RT}{g}. \quad (\text{A.4})$$

As wind blows, friction with the earth's surface tends to slow the wind at the surface level. The lowest region of the troposphere, the portion most affected by the surface, is known as the *surface boundary layer*, the top of which may be from tens to many hundreds of meters above the surface. A wind scatterometer measures boundary layer winds. Within the surface boundary layer the wind speed U profile as a function of height h above the surface can be approximately expressed, as [28]

$$U(h) = \frac{u_*}{0.4} \left(\ln \frac{h}{Z_0} + \psi \right) \text{ m/s} \quad (\text{A.5})$$

where u_* is the *friction velocity* of the wind at the ocean surface, ψ is a function of the atmospheric stability of the surface boundary layer, and Z_0 is the roughness length of the

surface. Z_0 can be related to u_* by the empirical formula [28],

$$Z_0 = \frac{0.00684}{u_*} + 0.428u_*^2 - 0.000443 \text{ m}. \quad (\text{A.6})$$

The friction velocity u_* can be written, as [28]

$$u_* = \frac{\sqrt{C_{Dn}}U}{1 - \sqrt{C_{Dn}}\psi/0.4} \quad (\text{A.7})$$

where C_{Dn} is the drag coefficient for a neutral atmosphere. When the air temperature is different than the ocean temperature, there is a heat flux between the sea and air, increasing the turbulence in the atmosphere and producing and affecting atmospheric stability ($\psi \neq 0$). ψ is positive in a stable atmosphere and negative in an unstable atmosphere. Under the conditions of neutral stability, $\psi = 0$ and Eq. (A.7) for u_* reduces to,

$$u_* = \sqrt{C_{Dn}}U. \quad (\text{A.8})$$

An empirical expression for the neutral stability drag coefficient C_{Dn} at an altitude of $h = 10 \text{ m}$ is [28],

$$C_{Dn[10m]} = \begin{cases} 1.14 \times 10^{-3} & 4 < U \leq 10 \text{ m/s} \\ 0.49 + 0.065U & 10 < U < 26 \text{ m/s} \end{cases} \quad (\text{A.9})$$

For other altitudes in the boundary layer, the neutral stability drag coefficient can be expressed [28],

$$C_{Dn}(h) = \frac{0.16C_{Dn[10 \text{ m}]}}{(\sqrt{C_{Dn[10 \text{ m}]}} \ln(h/10) + 0.4)^2}. \quad (\text{A.10})$$

These formulas relate the wind at the ocean's surface to the wind at an arbitrary height over the ocean's surface within the surface boundary layer. Keeping this relationship in mind, $h = 19.5 \text{ m}$ has historically been used by meteorologists as the standard for specifying the surface wind speed over the ocean.

Until recently, weather forecasting relied exclusively on subjective analysis of synoptic weather charts. The development of computers permitted meteorologists to employ numerical solutions of the equations of motion in their analysis. While the numerical prediction models are far superior to earlier techniques, the lack of a complete knowledge of the current weather conditions still limit their usefulness [104]. Numerical weather prediction (NWP) modeling is based on a set of primitive equations derived from Newton's laws of motions, atmospheric continuity constraints, and the laws of thermodynamics.

The most commonly used coordinate system is a modified spherical system. The horizontal coordinates are latitude ϕ and longitude λ . Cartesian coordinates are often used,

$$dx \triangleq r d\lambda \cos \phi \quad (\text{A.11})$$

$$dy \triangleq r d\phi \quad (\text{A.12})$$

where x and y are the distance east of the Greenwich meridian along a latitude line and the distance north of the equator. r is the distance from the earth's center. For motions in the troposphere, r is invariably replaced by R_E , the radius of the earth (6.36×10^6 m). Rather than use height, the pressure p is more commonly used for the vertical coordinate since this simplifies the resulting expressions. For large scale motions (i.e. mesoscale and larger), there is a monotonic and relatively simple relationship between height and pressure [104]. Since wind scatterometry is primarily concerned with winds only in the surface boundary layer, the distinction is minor.

The three velocity components of general atmospheric motion are,

$$u \triangleq \frac{dx}{dt} = R_E \cos \phi \frac{d\lambda}{dt} \quad (\text{A.13})$$

$$v \triangleq \frac{dy}{dt} = R_E \frac{d\phi}{dt} \quad (\text{A.14})$$

$$\omega \triangleq \frac{dp}{dt} \approx -\frac{dr}{dt} \frac{p}{H} \quad (\text{A.15})$$

where H is the scale height. u is called the *zonal* velocity component. Positive zonal winds are called *westerlies* (from the west) with negative zonal winds called *easterlies* (from the east). v is called the *meridional* velocity component. Positive and negative meridional winds are called *southerly* and *northerly*, respectively. On wind field maps, it is common to use *streamlines* to indicate the wind direction. Streamlines are arbitrarily spaced lines that are everywhere parallel to the horizontal velocity vector [104].

The forces acting on a moving volume of air include gravity, the ‘‘Coriolis’’ force, pressure, and friction. The resulting acceleration is the sum of the effects of these forces. From these effects the equation of horizontal motion can be written [104],

$$\frac{d\mathbf{V}}{dt} = -\nabla\Phi - f\mathbf{k} \times \mathbf{V} - a\mathbf{V} \quad (\text{A.16})$$

where $\mathbf{V} \triangleq u\mathbf{i} + v\mathbf{j}$ is the horizontal velocity vector, f is the *Coriolis parameter* $f = 2\Omega \sin \phi$ where $\Omega = 7.292 \times 10^{-5}$ rad/s is the angular velocity of rotation of the earth, Φ is the *geopotential height*, or gravitational potential energy per unit mass, \mathbf{k} is a unit vector in the vertical direction, and a is the frictional coefficient, the magnitude of which varies according to a myriad of effects including wind speed, ocean roughness and temperature, etc. For large-scale motions the Coriolis force dominates the frictional term, which along with the simplification,

$$\mathbf{k} \times (\mathbf{k} \times \mathbf{V}) = -\mathbf{V} \quad (\text{A.17})$$

produces,

$$\mathbf{V} \approx \frac{1}{f} \mathbf{k} \times \nabla\Phi \quad (\text{A.18})$$

When this relationship is exactly satisfied, the wind is known as *geostrophic*. A more detailed derivation of Eq. (A.18) is provided in Appendix C. The geostrophic wind velocity, \mathbf{V}_g , can

be written,

$$\mathbf{V}_g \triangleq \frac{1}{\rho f}(\mathbf{k} \times \nabla p) \quad (\text{A.19})$$

where ρ is the atmospheric density. Near the ocean’s surface, the frictional term is significant, causing the wind to be *subgeostrophic*. This dampens the surface wind speed and deflects the velocity vector toward lows and away from highs. The analysis is complex and requires many approximations. It is not normally included in numerical modeling for large scale wind fields [104].

The geostrophic wind equation must be combined with the effects of thermal wind gradients. When there is no horizontal thermal gradient, the atmosphere is known as *barotropic* otherwise it is known as *baroclinic*. The *thermal wind equation* relates the the vertical shear of the geostrophic wind to the horizontal temperature gradient.

Kinetic energy in the atmosphere is dissipated by frictional forces. Large scale motions force lesser scale motions in the so-called *energy cascade*. The kinetic energy of the smaller scales is ultimately dissipated through viscosity effects. Since rates of energy dissipation at lower scales is much higher than at higher scales of motion, the energy cascade mechanism can dissipate the energy of large atmospheric motions very rapidly. Instability and irregularities in the earth’s surface also produce small scale eddies and disturbances which extract energy from larger scale wind fields [104].

The energy cascade is important in the development of mesoscale wind fields from synoptic scale motions. It also is important in defining the spectrum of the wind fields. The energy cascade not only occurs in the atmosphere but also is important in ocean wave propagation and extinction.

A.1.2 Turbulence

From the point of view of synoptic-scale motions, mesoscale motions can be viewed as turbulent disturbances in the larger scale motions [17, 57, 88]. The turbulence in the synoptic measurement due to the mesoscale motion adversely affects the performance of numerical weather prediction models. By properly measuring the mesoscale wind fields, the mesoscale turbulence in the synoptic models can be accounted for, resulting in improved weather forecasts. This is one of the primary motivations in the development of wind scatterometers.

Long term empirical observations of the statistics of atmospheric turbulence have shown that the statistics remain relatively stable. This is a distinctive characteristic of turbulent flows. Although the details of the turbulent flow appear random, the statistics of the flow parameters are stable and can be used to characterize it. Because turbulent flow is “random”, deterministic models for the flow can not completely model it. This has lead to the development of *turbulence models* of atmospheric motion [17, 33]. The turbulence models predict an energy spectrum power-law dependence on the wavenumber due to the energy cascade of the form αk^{-b} where k is the spatial spectrum wavenumber $k = 2\pi/L$ and α is a constant [33].

Although the atmosphere is three-dimensional, the flow within the surface boundary layer

can be assumed to be an incompressible, two-dimensional flow for synoptic-scale motions [17, 33, 57]. Conservation of mass dictates that the atmospheric flow will be essentially nondivergent, i.e.,

$$\frac{\partial}{\partial x}u(x, y) + \frac{\partial}{\partial y}v(x, y) = 0 \quad (\text{A.20})$$

where $u(x, y)$ is the x -directed wind velocity component and $v(x, y)$ is the y -directed velocity component of the velocity field $\mathbf{V}(x, y)$. When a fluid is confined to two-dimensional, nondivergent flow, the fluid flow may be described by an *enstrophy* equation. Enstrophy is defined as one-half the squared vorticity (curl).

Turbulence deals with the statistical properties of the solutions to the *Navier-Stokes equation* which describes fluid flow. The solutions to the Navier-Stokes equation for two-dimensional fluid flow require the use of statistical tensor analysis and will not be discussed here (see [57]).

The primary application of turbulence flow models is the determination of the characteristics of the atmospheric kinetic energy spectrum. The turbulent atmospheric flow model discussed by Charney [17] and Leith [57] predicts that the kinetic energy spectrum of the atmosphere has a power-law relationship with the spatial spectrum wavenumber.

The two-dimensional wind fields can be represented by the spatial Fourier coefficients,

$$\Phi_u(k_x, k_y) = \int_{-\infty}^{\infty} \int_{-\infty}^{\infty} u(x, y) e^{-j(k_x x + k_y y)} dx dy \quad (\text{A.21})$$

$$\Phi_v(k_x, k_y) = \int_{-\infty}^{\infty} \int_{-\infty}^{\infty} v(x, y) e^{-j(k_x x + k_y y)} dx dy \quad (\text{A.22})$$

where k_x and k_y are the wave numbers in the x and y directions, respectively. The *two-dimensional component spectra* are,

$$|\Phi_u(k_x, k_y)|^2 = \Phi_u(k_x, k_y) \Phi_u^*(k_x, k_y) \quad (\text{A.23})$$

$$|\Phi_v(k_x, k_y)|^2 = \Phi_v(k_x, k_y) \Phi_v^*(k_x, k_y) \quad (\text{A.24})$$

and the *two-dimensional energy spectrum* $E(k_x, k_y)$ is,

$$E(k_x, k_y) = |\Phi_u(k_x, k_y)|^2 + |\Phi_v(k_x, k_y)|^2 \quad (\text{A.25})$$

For isotropic turbulence, $E(k_x, k_y)$ will be rotationally invariant. It follows that $E(k_x, k_y)$ is a function only of $k = (k_x^2 + k_y^2)^{1/2}$. Applying the nondivergence constraint in Eq. (A.20) to the Fourier coefficients $\Phi(k_x, k_y)$ produces,

$$\int_{-\infty}^{\infty} \int_{-\infty}^{\infty} (k_x \Phi_u(k_x, k_y) + k_y \Phi_v(k_x, k_y)) e^{j2\pi(k_x x + k_y y)} dk_x dk_y = 0 \quad (\text{A.26})$$

It follows, that for nondivergent flow,

$$\Phi_v(k_x, k_y) = \begin{cases} \frac{-k_x}{k_y} \Phi_u(k_x, k_y) & k_y \neq 0 \\ 0 & k_y = 0 \end{cases} \quad (\text{A.27})$$

This equation implies that for nondivergent flow, only the spectrum of one of the velocity components is required to completely specify the velocity field $\mathbf{V}(x, y)$.

The one-dimensional component spectra can be computed from the two-dimensional component spectra, as

$$F_u(k_x) = \int_{-\infty}^{\infty} |\Phi_u(k_x, k_y)|^2 dk_y \quad (\text{A.28})$$

$$F_v(k_x) = \int_{-\infty}^{\infty} |\Phi_v(k_x, k_y)|^2 dk_y. \quad (\text{A.29})$$

The one-dimensional isotropic energy spectrum $\widehat{E}(k)$ is defined as,

$$\widehat{E}(k) = \pi k E(k_x, k_y) \quad (\text{A.30})$$

where $k = (k_x^2 + k_y^2)^{1/2}$ as before. $\widehat{E}(k) = \pi k E(k_x, k_y)$ is related to the one-dimensional spectrum by the following,

$$F_u(k_x) = \frac{2}{\pi} \int_{k_x}^{\infty} \widehat{E}(k) \frac{\sqrt{k^2 - k_x^2}}{k^2} dk \quad (\text{A.31})$$

$$F_v(k_x) = \frac{2k_x^2}{\pi} \int_{k_x}^{\infty} \widehat{E}(k) \frac{1}{k^2 \sqrt{k^2 - k_x^2}} dk. \quad (\text{A.32})$$

Since the two-dimensional isotropic energy spectrum obeys the power-law $\widehat{E}(k) = \alpha k^{-b}$ as predicted by Leith's turbulence model, the one dimensional spectra will also obey a power-law [33, 57]. Leith showed that

$$F_v(k_x) = -k_x \frac{d}{dk_x} F_u(k_x) \quad (\text{A.33})$$

from which follows,

$$F_v(k_x)/F_u(k_x) = b. \quad (\text{A.34})$$

The *two-dimensional cross-spectrum* $H(k_x, k_y)$ is defined in terms of the component spectra,

$$H(k_x, k_y) = \Phi_u(k_x, k_y) \Phi_v^*(k_x, k_y). \quad (\text{A.35})$$

Since the field is non-divergent, the cross-spectrum must be real, i.e.,

$$\text{Im}[H(k_x, k_y)] = 0. \quad (\text{A.36})$$

The *one-dimensional cross-spectrum* is defined by,

$$\hat{H}(k_x) = \int_{-\infty}^{\infty} H(k_x, k_y) dk_y \quad (\text{A.37})$$

which, since the $H(k_x, k_y)$ is real, is identically zero, i.e.,

$$\hat{H}(k_x) = 0. \quad (\text{A.38})$$

Although this derivation has assumed a non-divergent two-dimensional atmosphere, a particular realization of a field may have limited regions of convergence or divergence. These regions occur because the real atmosphere is three-dimensional and vertical transport into upper layers of the atmosphere will appear as convergence zones in the two-dimensional field.

A.2 Oceanography Fundamentals

Nearly 75% of the Earth's surface is covered with saltwater oceans. Since the beginning of time man has struggled to understand the workings of the oceans. The study of the Earth's oceans is termed *oceanography*. Although the field of oceanography includes such diverse topics as ocean currents and hydrology, we will be primarily interested in surface ocean waves generated by the wind. Oceanographers classify waves principally by wave period P or wavenumber $k = 2\pi/L$ where L is the wave length with

$$L = \left(\frac{g}{2\pi} \right) P^2. \quad (\text{A.39})$$

The smallest waves are known as *capillary* waves and range in size up to a centimeter in length [54]. Wind scatterometers are sensitive primarily to capillary waves [99]. *Gravity waves*, which range in size from about 1.5 m to 1.5 km, can distort the scatterometer measurement [28].

The mathematical modeling and analysis of wave generation by the wind is complex. As the wind blows over the ocean's surface, friction between the upper layers of the water and lower layers of the atmospheric boundary layer transfers energy from the wind to the ocean surface. This slows the wind at the surface and induces currents and waves on the ocean's surface. Steady, long term winds over the ocean can establish synoptic scale ocean currents which "pile up" the ocean against one shore, much as blowing over a glass of water piles up the water to one side. When this wind suddenly fails, the ocean returns to a flat state by reversing the current direction. This may be a factor in the reoccurring *El Nino* off the coast of South America [2].

A light breeze over a calm surface, first produces small, ruffled patches of wavelets a few centimeters in length. As the wind grows, larger and larger waves are formed. If no energy were lost from the waves, the wind would continue to force them ever larger to an indefinite size. Friction, however, dissipates the wave energy and limits the wave size. The maximum wave size depends on water temperature, wind speed, wind duration, and *fetch* or length of

ocean surface over which the wind blows [54].

A.2.1 Wind Generated Wave Spectrum

The mathematical modeling and analysis of wave generation is quite complex and is not completely understood. For this discussion, we will not consider the exact mechanism for wave generation but will consider the wave spectrum of the sea when the wave field is fully developed. It will be shown that the wave spectrum is related to the wind frictional velocity u_* and hence by the boundary layer wind profile expression in Eq. (A.5) to the wind at higher levels. Radar scattering theories use the wave spectrum in the scattering problem formulation. Following [28], we outline the development of the wave spectrum.

The ocean's surface is a time-varying rough surface. The space-time power spectrum of the ocean surface is defined by [28, 54],

$$D(\mathbf{K}, \omega) = \frac{1}{(2\pi)^3} \int \int_{-\infty}^{\infty} C(\mathbf{p}, t) e^{-j(\mathbf{K} \cdot \mathbf{p} - \omega t)} d\mathbf{p} dt \quad (\text{A.40})$$

where \mathbf{K} is the vector wavenumber, \mathbf{p} is the position vector, and $C(\mathbf{p}, t)$ is the space-time correlation function,

$$C(\mathbf{p}, t) = \langle h(\mathbf{x}, \tau) h(\mathbf{x} + \mathbf{p}, t + \tau) \rangle. \quad (\text{A.41})$$

Using current techniques the space-time spectrum can not be measured. In general, only the frequency spectrum $Z(\omega)$ can be measured [28, 54], where

$$Z(\omega) = \int \int_{-\infty}^{\infty} E(\mathbf{K}, \omega) d\mathbf{K}. \quad (\text{A.42})$$

The wavenumber spectrum, which is used in radar scattering theory, is

$$\Psi(\mathbf{K}) = \int_{-\infty}^{\infty} E(\mathbf{K}, \omega) d\omega \quad (\text{A.43})$$

The wavenumber spectrum can not be computed without knowledge of the space-time spectrum; however, the dispersion relation between frequency and wave numbers $\omega = \omega(K)$ permits conversion between the frequency spectrum and the wavenumber spectrum. First, we separate the wavenumber spectrum into an amplitude spectrum, $S(K)$ and a directional spectrum $\Phi(\phi)$ [28],

$$\Psi(\mathbf{K}) \triangleq \Psi(K, \phi) = \frac{1}{2\pi} S(K) \Phi(\phi) \quad (\text{A.44})$$

where $K = |\mathbf{K}|$ is the wavevector magnitude and ϕ is the wavevector direction,

$$\mathbf{K} = (K \cos \phi, K \sin \phi). \quad (\text{A.45})$$

In terms of the frequency spectrum $Z(\omega)$ and the dispersion relationship $\omega = \omega(K)$, the

amplitude spectrum $S(K)$ is

$$S(K) = \frac{2}{K} \frac{d\omega}{dK} Z(\omega) \Big|_{\omega=\omega(K)}. \quad (\text{A.46})$$

The dispersion relationship for surface waves can be expressed [28], as

$$\omega^2 = g_* K \quad (\text{A.47})$$

where $g_* \triangleq g + \gamma K^2$. The constant $\gamma = 7.25 \times 10^{-5} \text{ m}^3 \text{ s}^{-2}$ is the ratio of surface tension to water density. For capillary waves, $\gamma K^2 \gg 1$. For smaller wave numbers (corresponding to longer wavelength gravity waves) $g_* \approx g$ [28].

When surface currents are ignored the wavenumber spectrum satisfies the energy transport equation [28],

$$\frac{\partial \Psi(\mathbf{K})}{\partial t} + \frac{\partial \omega}{\partial \mathbf{K}} \cdot \nabla \Psi(\mathbf{K}) = Q_i + Q_n + Q_d \quad (\text{A.48})$$

where Q_i is the input energy due to surface winds, Q_n is the energy exchange between wavenumbers due to nonlinear resonant interactions, and Q_d is the energy dissipation due to wave breaking, etc. In a fully developed wave field the energy input by the wind is equal to the energy dissipated and lost via the energy cascade mechanism, thus [28],

$$Q_i + Q_n + Q_d = 0. \quad (\text{A.49})$$

Wind blowing across a smooth ocean surface generates wave first by pressure variations due to turbulence in the air flow at the surface. Under these conditions, Q_i is roughly constant. Once small waves have been generated, the air flow changes and a turbulence feedback mechanism develops. Under these conditions Q_i is proportional to the ocean wave spectrum.

The energy exchange Q_n between resonant wavenumbers affects different regions of the ocean wavenumber spectrum differently. Nonlinear interactions occur when several wavenumber components combine to produce a new component of a different wavenumber. This effects a transfer of energy between waves of different wave numbers. The interactions are complex and non-linear.

The energy dissipation term, Q_d , is due to wave breaking at lower wavenumbers (larger waves) and viscosity for higher wavenumbers (capillary waves) [28].

Based on empirical observations, the frequency spectrum $Z(\omega)$ for wave frequencies up to 1 Hz (capillary waves) can be expressed,

$$Z(\omega) = 0.008 \frac{g^2}{2\omega^5} e^{-0.74 (g/(\omega U_{19.5}))^4} \quad (\text{A.50})$$

where $U_{19.5}$ is the wind speed at 19.5 m. Using $\omega^2 = gK$ and transforming $Z(\omega)$ to the

amplitude spectrum $S(K)$ using Eq. (A.46) yields [28],

$$S(K) = 0.004 \frac{1}{K^4} e^{-0.74 (g/(KU_{19.5}^2))^2}. \quad (\text{A.51})$$

For higher wavenumbers in the capillary region, the energy transport equation and dimensional analysis define the wave number spectrum as,

$$S(K) = 0.004 \frac{1}{K^4} \left(\frac{bK}{g_*} u_*^2 \right)^{a \ln \frac{K}{K_t}} \quad (\text{A.52})$$

where a and b are constants which must be determined by empirical observation. Based on empirical observations, $a = 0.025$ and $b = 2.25$. $K_t \approx 2 \text{ m}^{-1}$ is the wavenumber where $1 \gg Ku_*^2$ is no longer satisfied [28].

The directional spectrum $\Phi(\phi)$ can be written [28], as

$$\Phi(\phi) = 1 + c(1 - e^{-sK^2}) \cos 2\phi \quad (\text{A.53})$$

where $s = 1.5 \times 10^{-4} \text{ m}^2$ and c is of the form,

$$c = \frac{(1 - R)/(1 + R)}{(1 - D)} \quad (\text{A.54})$$

where R is an affine function of the wind speed at 12.5 m , $U_{12.5}$,

$$R = 0.949 + 0.608 U_{12.5} \quad (\text{A.55})$$

and

$$D = \frac{\int_0^\infty K^2 S(K) e^{-sK^2} dK}{\int_0^\infty K^2 S(K) dK}. \quad (\text{A.56})$$

Combining the directional spectrum in Eq. (A.53) and the two expressions for the amplitude spectrum Eqs. (A.51) and (A.52), the wave number spectrum is [28],

$$\Psi(K, \phi) = \frac{0.004}{2\pi K^4} \begin{cases} e^{-0.74 (\frac{g}{K} \frac{1}{U_{19.5}})^2} [1 + c(1 - e^{-sK^2})] \cos 2\phi & K < 2 \\ \left[\frac{bKu_*^2}{g_*} \right]^{a \ln(K/2)} [1 + c(1 - e^{-sK^2})] \cos 2\phi & K \geq 2 \end{cases}. \quad (\text{A.57})$$

which is a function of the wind speed at 19.5 m and wind direction ϕ . Using the wind profile equation [(A.5)], the wind speed at other altitudes in the atmospheric boundary layer can be computed.

A.3 Scattering Theory

Radar is an acronym originally coined from its purpose, radio detection and ranging. Today,

the term radar has a much broader meaning. For the purposes of this discussion, a radar is an active microwave instrument which transmits a pulse of microwave energy toward a target and receives the echo. We will only consider *monostatic* radars, that is, radars which transmit and receive with the same antenna. A *radar scatterometer* is a radar designed to measure the scattering properties of the target. It measures the returned echo power and with the knowledge of the radar's parameters such as transmit power, antenna gain, etc. determines the *radar cross-section*. The radar cross-section is the equivalent area of the target at microwave frequencies. The *normalized radar cross-section* σ^o is the radar cross-section divided by the target area. In a *wind scatterometer* the σ^o of a region of the ocean's surface is measured. Since σ^o is related to the wind vector by a model function, appropriate measurements of σ^o can be used to measured the wind over the ocean's surface [99, 102].

A.3.1 The Radar Equation

The fundamental equation relating the receive echo, the target characteristics, and the radar parameters is known as the *radar equation*. The radar transmits a signal with power P_t through an antenna with one-way gain G (see Fig. A.1). At the target the transmitted signal has been attenuated by the distance or range R to the target according to $1/(4\pi R^2)$ due to spreading loss. The power intercepted by the target is a function of its effective target area A . Some of the transmitted power is absorbed by the target, some is reflected back toward the radar, and the remainder is scattered in other directions. The amount of power reflected back to the radar is the effective area times the normalized radar scattering cross-section σ^o of the target. The σ^o of the target depends on many factors including incidence and azimuth angle, target roughness, target dielectric constant, etc. The reflected power is again attenuated by the distance to the target. At the radar, the received power is related to the antenna's effective area A_e and the radar wavelength λ by the expression,

$$A_e = \frac{\lambda^2 G}{4\pi} \quad (\text{A.58})$$

Combining these, the radar equation expresses the received power P_r as,

$$P_r = \frac{P_t \lambda^2 A G^2 \sigma^o}{(4\pi)^3 R^4}. \quad (\text{A.59})$$

In wind scatterometry, measurement of P_r are made. From the knowledge of the radar's location relative to the target, and the antenna gain pattern the radar equation can be solved, or *inverted*, to determine σ^o .

$$\sigma^o = C P_r \quad (\text{A.60})$$

where C is

$$C = \frac{(4\pi)^3 R^4}{\lambda^2 P_t G^2 A}. \quad (\text{A.61})$$

While this expression is exact for the ideal case, many of the parameters are not constant

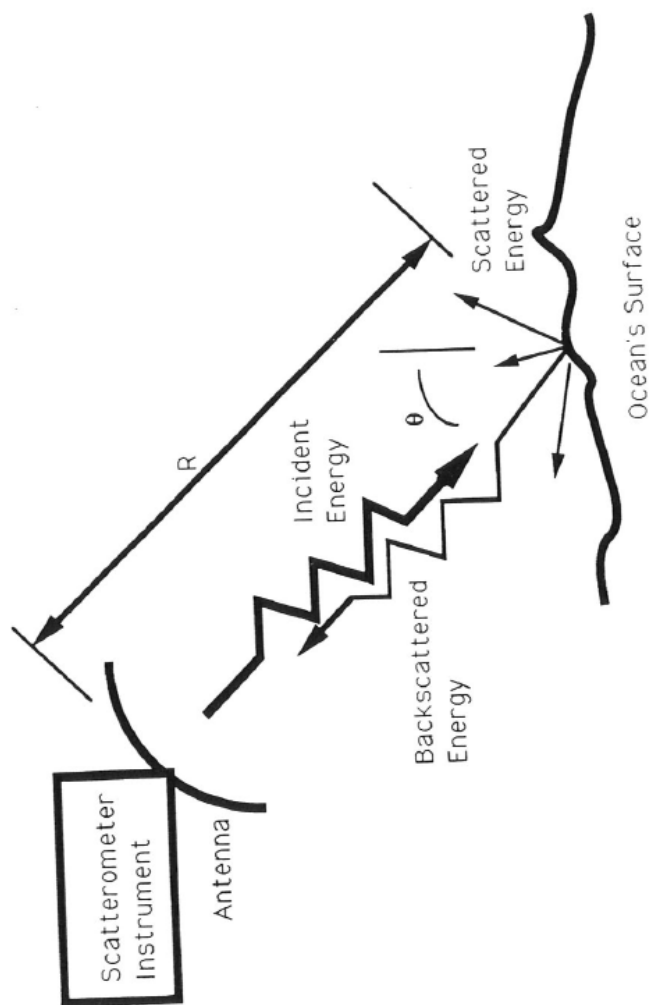


Figure A.1: Schematic diagram of a wind scatterometer.

over the entire target, e.g., antenna gain, σ^o , and R . In this case, the integral form of the radar equation is used,

$$P_r = \frac{\lambda^2}{(4\pi)^3} \int_{\text{area illuminated}} \frac{P_t G^2 \sigma^o}{R^4} dA. \quad (\text{A.62})$$

In this case the inversion of the equation is much more difficult. For inversion of the equation, equivalent values for the antenna gain, \overline{G} , target area, \overline{A} , and range, \overline{R} , are used, so that

$$\overline{\sigma^o} = \frac{P_r (4\pi)^3 \overline{R}^4}{P_t \lambda^2 \overline{G}^2 \overline{A}} = \overline{C} P_r. \quad (\text{A.63})$$

where \overline{C} a function of the equivalent radar system parameters,

$$\overline{C} = \frac{(4\pi)^3 \overline{R}^4}{\lambda^2 \overline{G}^2 P_t \overline{A}}. \quad (\text{A.64})$$

Additive white thermal noise from the radar system and emissive thermal noise in the atmosphere and ocean surface further complicate the return power measurement. Typically, a separate measurement is made of the noise-only power and subtracted from the signal power measurement [68, 102].

A.3.2 Surface Scattering

Following Durden [28], this section will provide an intuitive look at scattering and surface roughness. Scattering of electromagnetic energy from a surface depends on the characteristics of the surface such as roughness, its dielectric constant, etc. and on the radar wavelength. The degree to which a surface is rough greatly influences the scattering properties of the surface. A surface which may appear rough at optical wavelengths can appear smooth at microwave wavelengths. Qualitatively, the rougher the surface the more *isotropic* or non-directional the scattering. An isotropic surface scatters energy equally in all directions. The two most commonly used parameters used to characterize surface roughness are the *standard deviation of the surface height variation* (or rms height) and the *surface correlation length*.

The standard deviation (σ) of the surface height and surface correlation length (l) describe the statistical fluctuations of the “random” component of the surface height relative to a reference surface. For a surface $S_x \times S_y$ in the $x - y$ plane which has a height $h(x, y)$ at the point (x, y) , the mean height and variance of the surface is,

$$\overline{h} = \frac{1}{S_x S_y} \int_0^{S_x} \int_0^{S_y} h(x, y) dx dy \quad (\text{A.65})$$

$$\overline{h^2} = \frac{1}{S_x S_y} \int_0^{S_x} \int_0^{S_y} h^2(x, y) dx dy \quad (\text{A.66})$$

The standard deviation of the surface height is,

$$\sigma = \sqrt{\overline{h^2} - \bar{h}^2}. \quad (\text{A.67})$$

When $h(x, y)$ is statistically independent of the angle from the x axis the equations can be reduced to one-dimensional equations. The normalized autocorrelation $\rho(t)$ of a one-dimensional surface $h(x)$ is defined as,

$$\rho(t) = \frac{\int_0^{S_x} h(x)h(x+t) dx}{\int_0^{S_x} h^2(x) dx}. \quad (\text{A.68})$$

The surface correlation length is the length l for which $\rho(l) = 1/e$.

The two-dimensional surface wavenumber spectrum is defined

$$\Psi(K_x, K_y) = \frac{1}{4\pi^2} \int \int_{-\infty}^{\infty} \langle h(x', y')h(x' + x, y' + y) \rangle e^{-j(K_x x + K_y y)} dx dy. \quad (\text{A.69})$$

The one-dimensional wavenumber spectrum is

$$\Psi(K) = \frac{1}{2\pi} \int_{-\infty}^{\infty} \rho(t)e^{-jKt} dt. \quad (\text{A.70})$$

The *Fraunhofer criterion* for smoothness, states that the surface may be considered smooth if the phase difference between two reflected waves is less than $\pi/8$ [102]. The Fraunhofer criterion will be met if

$$\sigma < \frac{\lambda}{32 \sin \theta} \quad (\text{A.71})$$

where θ is the incidence angle [28]. In scattering theory, the rms surface height, σ , is expressed in terms of the wavelength, λ . As a general guideline, a surface is considered smooth if the quantity $k\sigma$ ($k = 2\pi/\lambda$) is less than 0.02, and very rough if $k\sigma > 1$. The decorrelation distance is also significant [28, 102].

The wave field on the ocean's surface roughens the surface. If the area under consideration is large enough, the surface appears random to the radar wave. In scattering studies, a random ocean surface (subject to power spectrum constraints) is usually assumed [28].

The dielectric constant ϵ of the ocean's surface is dependent on the water temperature, the presence of surface films, salinity, etc. Averaged over a large enough area, however, ϵ can be considered constant.

A.3.3 Scattering Theory

In terms of the incident \mathbf{E}_i and scattered \mathbf{E}_s electromagnetic fields, σ^o can be expressed (where the dependence on incidence angle θ and azimuth angle χ and polarization p is

explicitly shown) [102], as

$$\sigma^o(\theta, \chi, p) = \frac{4\pi R^2 |\mathbf{E}_s(p)|^2}{A |\mathbf{E}_i(p)|^2} \quad (\text{A.72})$$

where A is the illuminated area. If the surface and incident fields are known, the scattered field $|\mathbf{E}_s(p)|$ can be computed. No exact solution for the scattered field exists if the surface is irregular; approximate solutions must then be resorted to [102].

The two most commonly applied approaches to surface-scattering theory are the *Kirchhoff* or the *Physical Optics* formulation and the *Small Perturbation* formulation. The small perturbation formulation applies to surfaces which are slightly rough relative to the radar wavelength, $k\sigma < 0.3$, while the physical optics formulation applies to surfaces which are smooth relative to the radar wavelength, i.e., $k\sigma > 6$ [102].

In the physical optics formulation, an infinite tangent plane is constructed at each point of the surface. The surface fields at the point are the fields produced by incident electromagnetic wave on the tangent plane. *Huygens' principle* is used to derive a relationship between the scattered electric \mathbf{E}_s and magnetic \mathbf{H}_s fields at a point \mathbf{r} outside of a closed surface S to the surface fields \mathbf{E} and \mathbf{H} (far-field approximation) [28, 102],

$$\mathbf{E}_s(\mathbf{r}) = \frac{-jke^{-jk|\mathbf{r}|}}{4\pi|\mathbf{r}|} \hat{\mathbf{r}} \times \oint_S (-\eta_0 \hat{\mathbf{r}} \times (\hat{\mathbf{n}} \times \mathbf{H}) + \hat{\mathbf{n}} \times \mathbf{E}) e^{-jk\hat{\mathbf{r}} \cdot \mathbf{r}'} dS \quad (\text{A.73})$$

$$\mathbf{H}_s(\mathbf{r}) = \frac{-jke^{-jk|\mathbf{r}|}}{4\pi|\mathbf{r}|} \hat{\mathbf{r}} \times \oint_S \left(\frac{1}{\eta_0} \hat{\mathbf{r}} \times (\hat{\mathbf{n}} \times \mathbf{E}) + \hat{\mathbf{n}} \times \mathbf{H} \right) e^{-jk\hat{\mathbf{r}} \cdot \mathbf{r}'} dS \quad (\text{A.74})$$

where η_0 is the impedance of free space, $\hat{\mathbf{r}} = \mathbf{r}/|\mathbf{r}|$, $\hat{\mathbf{n}}$ is the unit normal to the surface, and $k = |\mathbf{k}|$ is the magnitude of the wavevector in the scattering direction. By determination of the tangent fields $\hat{\mathbf{n}} \times \mathbf{E}$ and $\hat{\mathbf{n}} \times \mathbf{H}$ the scattered fields can be computed. Solution of these equations requires the use of two-dimensional Green's functions [28, 102]. Following [28], the discussion can be simplified by considering the scattering from a one-dimensional surface. This allows us to consider the fields as scalars.

For a one-dimensional surface, the incident and scattered fields have the same polarization. The scattered electric field for horizontal polarization (and the magnetic field for vertical polarization) can be expressed [28], as

$$\mathbf{E}_s(\mathbf{p}) = \frac{e^{-j(3\pi/4 + jk|\mathbf{p}|)}}{\sqrt{8\pi k|\mathbf{p}|}} \oint \left(jk \frac{\mathbf{p}}{|\mathbf{p}|} \cdot \hat{\mathbf{n}} \phi - \frac{\partial \phi}{\partial \hat{\mathbf{n}}} \right) e^{jk\mathbf{p} \cdot \mathbf{p}'/|\mathbf{p}|} dl \quad (\text{A.75})$$

where ϕ is the electric field for horizontal polarization or magnetic field for vertical polarization, \mathbf{p} is the position vector of the radar, \mathbf{p}' is the position vector of a point on the surface, and $\hat{\mathbf{n}}$ is the outward pointing surface normal of the one-dimensional surface $h(x)$,

$$\hat{\mathbf{n}} = \frac{1}{\sqrt{1 + h^2(x)}} (\hat{\mathbf{z}} - h^2(x)\hat{\mathbf{x}}) \quad (\text{A.76})$$

Once the surface fields are computed, these expressions can be used to compute the scattered

field, and hence σ^o .

Both of the major scattering theories, small perturbation theory and physical optics theory, will be summarized in the sections that follow. Since most real surfaces (and in particular the ocean's surface) have properties of both smooth and rough surfaces, a two-scale formulation, incorporating both scattering formulations will be discussed.

Small Perturbation Theory Formulation

For surfaces which are slightly rough relative to the electromagnetic wavelength, small perturbation theory can be applied to compute the radar backscatter coefficient. To simplify the discussion, a perfectly conducting surface, rough in only one dimension will be considered. The one-dimensional derivation given in [28] will be followed.

For a finite surface $h(x)$ rough along the x axis on the $x - z$ plane, the incident electric field (horizontal polarization) can be written, as

$$\mathbf{E}_s = e^{-j(k_x x - k_z z)} = 2j e^{-j k_x x} \sin k_z z. \quad (\text{A.77})$$

where $k_x = k \sin \theta$, $k_z = k \cos \theta$, and θ is the angle of incidence. The reflected electric field is,

$$\mathbf{E}_r = -e^{-j(k_x x - k_z z)}. \quad (\text{A.78})$$

Assuming a periodic surface with period L , we can expand it in terms of a Fourier series, as

$$h(x) = \sum_{n=-\infty}^{\infty} P(n) e^{j 2 \pi n x / L} \quad (\text{A.79})$$

where the wavenumber spectrum of the surface and the Fourier coefficients $P(n)$ are related by

$$\langle P(m) P^*(n) \rangle = \begin{cases} a_0 \Psi(n a_0) & m = n \\ 0 & m \neq n \end{cases} \quad (\text{A.80})$$

where $a_0 = 2\pi/L$.

In terms of the periodic surface the scattered field can be expanded in terms of a space harmonic expansion,

$$E_s = \sum_{n=-\infty}^{\infty} B_n e^{-j(k_x + a_0 n)x - j b(n)z} \quad (\text{A.81})$$

where $b(n) \triangleq (k^2 - (k_x + a_0 n)^2)^{1/2}$. The total field at the surface is sum of the incident and the scattered fields,

$$E(x, z) = 2j e^{-k_x x} \sin k_z z + \sum_{n=-\infty}^{\infty} B_n e^{-j(k_x + a_0 n)x - j b(n)z}. \quad (\text{A.82})$$

Ocean water is a reasonably good conductor. For simplicity we will assume it is a perfect

conductor so that the tangential electric field at the ocean surface is zero.

$$E(x, z)|_{z=h(x)} = 0 \quad (\text{A.83})$$

The B_n 's are determined using a perturbation expansion of the height of the surface [28, 103],

$$B_n = B_n^{(1)} + B_n^{(2)} + \dots \quad (\text{A.84})$$

Since the surface is only slightly rough, only the first-order term $B_n^{(1)}$ can be retained. This is substituted into Eq. (A.83) to obtain,

$$e^{-jk_x} \sum_{n=-\infty}^{\infty} B_n^{(1)} e^{ja_0 n x} = 2j e^{-jk_x x} k_z h(x) \quad (\text{A.85})$$

which is substituted into the expression for the Fourier series expansion of $h(x)$ [Eq. (A.79)]. Equating coefficients,

$$B_n^{(1)} = 2jk_z P(n). \quad (\text{A.86})$$

Substituting this expression for the approximate B_n coefficient in the total electric field expression in Eq. (A.82), the electric field on the surface can be calculated. The resulting expression is substituted into Eq. (A.75) to yield the scattered field,

$$E_s = \frac{j e^{j(3\pi/4 + kp)}}{\sqrt{8\pi k p}} \sum_{n=-\infty}^{\infty} A_n L \frac{\sin((2k_x + a_0 n)L/2)}{(2k_x + a_0 n)L/2}. \quad (\text{A.87})$$

where $A_n \triangleq B_n b(n) + k \cos \theta B_n$.

In terms of the electric fields, the normalized radar backscatter coefficient is defined, as

$$\sigma^o = \lim_{L \rightarrow \infty} \frac{2\pi p \langle \mathbf{E}_s \mathbf{E}_s^* \rangle}{L}. \quad (\text{A.88})$$

Taking the limit and simplifying, we obtain

$$\sigma^o = 2\pi k \cos^2 \theta \Psi(-2k_x) 4k^2 \cos^2 \theta. \quad (\text{A.89})$$

As a function of incidence angle, this can be expressed [28], as

$$\sigma_H^o(\theta) = 8\pi k^3 \cos^4 \theta \Psi(-2k \sin \theta) \quad (\text{A.90})$$

which is the horizontal polarization σ^o for a perfectly conducting surface which rough in only one dimension. A similar approach using the magnetic field for vertical polarization, yields the vertically polarized σ^o , [28]

$$\sigma_V^o = 8\pi k^3 (1 + \sin^2 \theta)^2 \Psi(-2k \sin \theta). \quad (\text{A.91})$$

The analysis can be extended to a two-dimensional rough surface which is not a perfect conductor. The results for each polarization P are:

$$\sigma_P^o = 16\pi k^4 \cos^4 \theta \Psi(-2k \sin \theta, 0) |\alpha_P|^2 \quad (\text{A.92})$$

where α_P for horizontal polarization ($P = H$) is,

$$\alpha_H = \frac{(\epsilon - 1)}{(\cos \theta + \sqrt{\epsilon - \sin^2 \theta})^2} \quad (\text{A.93})$$

and for vertical polarization ($P = V$),

$$\alpha_V = \frac{(\epsilon - 1)(\epsilon \sin^2 \theta + (\epsilon - \sin^2 \theta))}{(\epsilon \cos \theta + \sqrt{\epsilon - \sin^2 \theta})^2} \quad (\text{A.94})$$

In both the one- and two-dimensional surfaces, small perturbation theory results in a σ^o which depends on the wavenumber spectrum evaluated at a single wavenumber. This wavenumber is such that the paths from adjacent crests of the wave on the ocean's surface have a phase difference of 2π . This is known as Bragg scattering. Bragg scattering is primarily responsible for the dependence of σ^o on wind speed and direction.

Physical Optics Formulation

The physical optics formulation, also known as the Kirchhoff formulation, models the field on the surface at a point as the field which would exist at that point if the surface were an infinite plane tangent to the surface at that point. Again, to simplify the discussion, a one-dimensional surface $h(x)$ will be assumed. The discussion presented in [28] will be followed. Using a monostatic radar system at \mathbf{p} with our previously defined one-dimensional surface $h(x)$, the electric field on the surface will be zero for horizontal polarization. Equation (A.75) reduces to

$$\mathbf{E}_s(\mathbf{p}, \theta) = \frac{e^{-j(3\pi/4+kp)}}{\sqrt{8\pi kp}} \int \frac{\partial E}{\partial \hat{n}} e^{jk\hat{p}\cdot\mathbf{p}'} dl \quad (\text{A.95})$$

with $p = |\mathbf{p}|$ and $\hat{p} = \mathbf{p}/|\mathbf{p}|$.

Assuming the surface is an infinite plane at the point \mathbf{p}' allows approximation of the derivative of the electric field, as

$$\frac{\partial E}{\partial \hat{n}} \approx 2jk\hat{p} \cdot \hat{n}' e^{jk\hat{p}\cdot\mathbf{p}'} \quad (\text{A.96})$$

Substitution of this derivative into the previous expression, yields

$$\mathbf{E}_s = \frac{2jke^{-j(\pi/4+kp)}}{\sqrt{8\pi kp}} \int \hat{p} \cdot \hat{n}' e^{2jk\hat{p}\cdot\mathbf{p}'} dl \quad (\text{A.97})$$

For vertical polarization the approximation for the magnetic field yields the same expression,

$$\mathbf{H}_s = \frac{2jk e^{-j(\pi/4+kp)}}{\sqrt{8\pi kp}} \int \hat{\mathbf{p}} \cdot \hat{\mathbf{n}}' e^{2jk\hat{\mathbf{p}} \cdot \mathbf{P}'} dl \quad (\text{A.98})$$

Having derived the scattered fields, σ^o is obtained by computing the ensemble average of the magnitude squared field over a surface of length L and letting $L \rightarrow \infty$. Assuming a Gaussian random surface with autocorrelation function $C(u)$ and height variance $h_h^2 = \langle h^2(x) \rangle$ the magnitude squared electric field is,

$$\langle \mathbf{E}_s \mathbf{E}_s^* \rangle = \frac{k}{2\pi p \cos^2 \theta} \int_{-L}^L (L - |u|) e^{-4k_x^2 h_h^2 (1-C(u))} e^{2jk_x u} du \quad (\text{A.99})$$

Taking the limit as $L \rightarrow \infty$, σ^o as a function of incidence angle for both vertical and horizontal polarization θ becomes

$$\sigma^o(\theta) = \frac{k}{\cos^2 \theta} \int_{-\infty}^{\infty} e^{-4k_x^2 h_h^2 (1-C(u))} e^{k_x u} du. \quad (\text{A.100})$$

When the surface is very rough ($4k_x h_h^2 \gg 1$) the integral is dominated by the region near $u = 0$ and $C(u)$ can be approximated by a Taylor series about the origin, as

$$C(u) \approx 1 - \frac{b^2 u^2}{2} + \dots \quad (\text{A.101})$$

where $b^2 = -C''(0)$. Keeping only the first two terms of the series, the integral can be evaluated, to obtain

$$\sigma^o(\theta) = \sqrt{\frac{\pi}{2}} \frac{1}{h_h b \cos^3 \theta} e^{-\tan^2 \theta / 2h_h^2 b^2}. \quad (\text{A.102})$$

Since slope variance S^2 of the surface is $-h_h^2 C''(0) = h_h^2 b^2$, we obtain

$$\sigma^o(\theta) = \sqrt{\frac{\pi}{2}} \frac{1}{S^2 \cos^3 \theta} e^{-\tan^2 \theta / 2S^2}. \quad (\text{A.103})$$

This formulation for σ^o is known as the *quasispecular cross section* since it can be physically interpreted as the cross section due to the quasispecular reflection of the surface which is normal to the incident field.

For a slightly rough two-dimensional surface ($1 \gg k_x^2 h_h^2$), the physical optics formulation produces,

$$\sigma^o(\theta) = 8\pi k^3 \Psi(-2k \sin \theta). \quad (\text{A.104})$$

This expression is similar to the expression for the small perturbation theory but does not include the angular dependence term for the polarization. Since physical observations indicate there is an angular dependence for a slightly rough sea, the small perturbation formulation is used for slightly rough surfaces rather than the physical optics formulation. For a rough

surface the physical optics formulation best matches empirical observations.

Two-Scale Formulation

Since the ocean surface is neither exclusively rough nor smooth, neither small perturbation theory nor physical optics theory can be directly applied. However, we can consider the surface to consist of two independent scales of roughness and apply each theory to the appropriate scale. We will consider the ocean surface to consist of a small scale height fluctuation h_s and a large scale height fluctuation h_l . Assuming independence between the scales of roughness, the wavenumber spectrum can be separated, as

$$\Psi(K) = \Psi_l(K) + \Psi_s(K) \quad (\text{A.105})$$

where $\Psi_l(K)$ is the large-scale spectra and $\Psi_s(K)$ is the small-scale spectra, i.e.,

$$\Psi_l(K) = \Psi(K) \quad K < K_d \quad (\text{A.106})$$

$$\Psi_s(K) = \Psi(K) \quad K \geq K_d \quad (\text{A.107})$$

where K_d is the transition wave number which separates the regions. The total scattering is the sum of the scattering from the large-scale surface (small perturbation theory) and the small-scale surface (physical optics formulation). The large-scale height variations will affect the slope (and hence the Bragg scattering effects) of the small-scale surface scattering. First, however, let us consider the effects of the small-scale roughness on the large-scale.

In the discussion of the physical optics formulation, this was already considered. When $1 \gg 4k_x^2 h_h^2$ the quasispecular σ^o is multiplied by an exponential term,

$$\sigma^o(\theta) = e^{4k_x^2 h_h^2} \sigma_q^o(\theta) \quad (\text{A.108})$$

where $\sigma_q^o(\theta)$ is the large-scale scattering from a surface without small-scale roughness [Eq. (A.91) or Eq. (A.90)].

The effect of the large-scale slope variations (due to large gravity waves) on the small-scale scattering as a function of height $\sigma_s^o(\theta, h(x))$ is the expected value of σ^o over all surface tilts [28],

$$\sigma^o(\theta) = \int_{-\infty}^{\infty} \sigma_s^o(\theta, h(x)) p(h(x)) dh(x) \quad (\text{A.109})$$

where $p(h(x))$ is the slope probability density of the surface. For a Gaussian surface,

$$p(h_x) = \frac{1}{\sqrt{2\pi}\sigma} e^{-h_x^2/2\sigma^2}. \quad (\text{A.110})$$

Equation (A.109) becomes

$$\sigma^o(\theta) = \int \frac{\sigma_s^o(\theta + \psi)}{\cos \psi} p(\tan \psi) d(\tan \psi). \quad (\text{A.111})$$

The final, two-scale σ^o is the sum of the quasispecular large-scale scattering and small-scale scattering with the cross-effects included,

$$\sigma^o(\theta) = e^{-4k^2h_h^2}\sigma_g^o(\theta) + \int \frac{\sigma_s^o(\theta + \psi)}{\cos \psi} p(\tan \psi) d(\tan \psi). \quad (\text{A.112})$$

The choice of the transition wavenumber K_d is important to the accuracy of the results. The two-scale formulation using $K_d = 2 m$ has been very successful in predicting the effects of wind on the ocean scattering coefficient σ^o compared to empirical measurements [28].

A.4 The Geophysical Model Function

The maze of modeling assumptions and equations relating wind to wave interaction and wave to radar backscatter discussed in the previous sections can be avoided by the development of a model which directly relates the wind vector over the ocean to the normalized radar backscatter coefficient σ^o . The SASS¹ G/H table is an example of this approach [11]. The success of the SASS¹ on the Seasat scatterometer data is considered to have validated this technique [102].

This section will briefly review the historical background in relating wind to radar backscatter and the development of a theory for the direct wind-to-backscatter model function as well as discuss the development of the direct wind-to-backscatter model function. A discussion of the comparison wind vector measurements made by Seasat and conventional wind measurements will also be given.

A.4.1 Historical Background

During the early development of radar for the detection of ships at sea it was noticed that the “sea clutter” seemed to be dependent on the *sea state* which includes both wind and wave height. This dependence was initially thought to be on the wave height, but it soon became evident that the dependence was not on large waves, but on the wind speed. This became more apparent after the development of a scattering theory which explained the scattering coefficient in terms of the small capillary waves. This early work is summarized in [81].

The first serious work to quantify the dependence of radar backscatter at microwave frequencies on wind speed was begun using the AAFE Radscat in the 1970’s. The Radscat was an airborne pencil-beam scatterometer. Radscat data first demonstrated the wind direction dependence of the radar backscatter [102]. Radscat and its successor AMSCAT were used to empirically determine the coefficients of the wind-to-backscatter model function.

The first spaceborne scatterometer, a pencil beam scatterometer, was on Skylab [81]. The SeaSat scatterometer demonstrated that accurate measurements of wind speeds over the ocean can be made from space [37, 48]. Other wind and radar scattering studies have been conducted using wave tanks, tower-mounted scatterometers, and airborne scatterometers [102].

While quantitative results have differed slightly between the studies, the qualitative form of the predicted model function have been similar.

A.4.2 Wind-to-Backscatter Modeling

The radar backscatter measurement is sensitive to capillary waves generated by the wind over the ocean's surface. The capillary waves ride on larger gravity waves which modulate the response of the surface to the radar wave to a small degree by tilting the plane of the capillary waves. While the distribution is not well understood, capillary waves are not uniformly distributed over the surface. However, since wind scatterometers observe large regions, the exact distribution is unimportant. Only the average statistics are considered significant.

High winds over the ocean cause breaking waves and foaming. No current theories adequately model the response to foaming and wave breaking, but empirical observations indicate that the wind speed sensitivity remains about the same as for lower wind speeds. At very high incidence angles, larger gravity waves tend to shadow the capillary waves, reducing the sensitivity of σ^o to wind speed.

Using the wind-speed-dependent ocean wave spectrum previously discussed and applying the two-scale formulation for scattering from a random surface, the σ^o response can be calculated by averaging the scattering fields from statistical realizations of ocean waves based on the wave spectrum. This analytical approach produces results which agree closely with empirical observations [28].

The σ^o of the ocean's surface depends primarily on the observation azimuth angle, incidence angle, and wind speed. The variation in σ^o as a function of wind azimuth angle can be expressed as a trigonometric function of the azimuth angle [11, 81, 102]

$$\sigma^o = A + B \cos \chi + C \cos 2\chi. \quad (\text{A.113})$$

The azimuth angle χ between the radar observation angle and the wind vector is defined such that $\chi = 0$ when the vector pointing in the direction of the radar propagation is 180 degrees from the wind vector. The coefficients A , B , and C depend on the angle of radar incidence, wind speed, and polarization. A plot of σ^o versus azimuth angle χ is shown in Fig. 2.1.

The coefficients A , B , and C as a function of wind speed can be expressed as power-law functions of the wind speed [102],

$$A = \beta_a(\theta) U^{\gamma_a(\theta)} \quad (\text{A.114})$$

$$B = \beta_b(\theta) U^{\gamma_b(\theta)} \quad (\text{A.115})$$

$$C = \beta_c(\theta) U^{\gamma_c(\theta)} \quad (\text{A.116})$$

Other similar forms for the coefficients have been proposed, e.g. [105].

In general, $\beta_a(\theta) > \beta_b(\theta) > \beta_c(\theta)$. The γ coefficients vary from about 1.5 to 3. Evaluating the γ coefficients either analytically or from empirical data is difficult and is error prone. Instead, the coefficients A , B , and C are determined from upwind, downwind, and crosswind

measurements of σ^o . This approach was used for deriving the SASS¹ G/H table coefficients from empirical measurements. The σ^o measurements at upwind, downwind, and crosswind are,

$$\sigma_u^o = A + B + C \quad (\text{A.117})$$

$$\sigma_d^o = A - B + C \quad (\text{A.118})$$

$$\sigma_c^o = A - C \quad (\text{A.119})$$

where the subscripts indicate upwind u , downwind d , and crosswind c . Expressing these in the power-law form,

$$\sigma_u^o = \beta_u(\theta) U^{\gamma_u(\theta)} \quad (\text{A.120})$$

$$\sigma_d^o = \beta_d(\theta) U^{\gamma_d(\theta)} \quad (\text{A.121})$$

$$\sigma_c^o = \beta_c(\theta) U^{\gamma_c(\theta)}. \quad (\text{A.122})$$

The coefficients A , B , and C are then,

$$A = \frac{\sigma_u^o + 2\sigma_c^o + \sigma_d^o}{4} \quad (\text{A.123})$$

$$B = \frac{\sigma_u^o - \sigma_d^o}{2} \quad (\text{A.124})$$

$$C = \frac{\sigma_u^o - 2\sigma_c^o + \sigma_d^o}{4} \quad (\text{A.125})$$

This modeling approach was used successfully as the basis for the SASS¹ model function [102].

A.5 The SASS¹ Geophysical Model Function

Based primarily on empirical observations of σ^o from space and from aircraft measurement, but also including the two-scale scattering theory, the science working team for the SeaSat scatterometer developed the SASS¹ model function. The SASS¹ is currently the most commonly used wind-to-backscatter model function. Additional detail is provided in Chapter 2.

During the operation of SASS, an extensive comparison of winds, derived from SASS measurements, was made with a special array of ships and bouys in the North Atlantic Ocean known as the JASIN experiment [47]. This data, obtained early in the SeaSat mission, was used to adjust the coefficients of the SASS¹ model function to eliminate errors in the SASS wind measurements.

Conventional wind measurements over the ocean are made by anemometers mounted on ships or bouys. These measurements consist of fixed-length time averages of the wind speed and direction at a single point. The scatterometer measurement is essentially an instantaneous spatial average of the wind over a large area. A bouy measurement typically

consists of an 8.6 *min* average of the wind speed taken once every hour or so at a single spatial point. The turbulent nature of the atmosphere over the micro-scale and mesoscale may produce differences in the wind measurements due to the different techniques of averaging employed [32].

Furthermore, observational errors in the surface wind measurements from instrument calibration introduce additional uncertainty. An additional error is due to the micro-scale turbulence of the surface wind over the temporal averaging period [32].

These problems make determining the “true” wind over the ocean’s surface very difficult. The “true” wind is required to empirically determine the coefficients of the wind-to-radar backscatter model function as well as for validating the model. Freilich [32] recently reported a comprehensive comparison of the winds measured by SASS and a set of weather bouys. His results, while validating the model function, showed that additional unmodelled effects (for example, sea surface temperature) should be accounted for (see also [108]).

Appendix B

Detailed Derivations for Point-Wise Identifiability

In this appendix detailed derivations are provided for various equations used in the identifiability proof. Noting the independence of the various noise terms in the scatterometer measurement noise model given in Chapter 2, one can easily show the following results,

$$E[z(k)] = s_t^2(k) = \sigma^o(k) \quad (\text{B.1})$$

$$E[z^2(k)] = (1 + \alpha^2(k))s_t^4(k) + \beta^2(k)s_t^2(k) + \gamma^2(k) \quad (\text{B.2})$$

$$= V_t(k) + s_t^4(k) \quad (\text{B.3})$$

$$\text{Var}[z(k)] = V_t(k) \quad (\text{B.4})$$

$$E[z(j)z(k)] = s_t^2(j)s_t^2(k) \quad \forall j \neq k \quad (\text{B.5})$$

$$E[z^2(j)z^2(k)] = [V_t(j) + s_t^4(j)][V_t(k) + s_t^2(k)] \quad \forall j \neq k \quad (\text{B.6})$$

As a reminder, non-subscripted $V(k)$ and $s(k)$ correspond to the estimated $s(k)$ while the t subscript denotes the true value. Using the equations (B.1) through (B.6), and noting the independence of the noise terms, we can show that $E[z(k) - s^2(k)]$, $E[(z(k) - s^2(k))^2]$, and $E[(z(j) - s^2(j))^2(z(k) - s^2(k))^2]$, are, respectively,

$$\begin{aligned} E[z(k) - s^2(k)] &= E[z(k)] - s^2(k) \\ &= s_t^2(k) - s^2(k) \end{aligned} \quad (\text{B.7})$$

$$\begin{aligned} E[(z(k) - s^2(k))^2] &= E[z^2(k)] - 2E[z(k)]s^2(k) + s^4(k) \\ &= V_t(k) + s_t^4(k) - 2s_t^2(k)s^2(k) + s^4(k) \\ &= V_t(k) + [s_t^2(k) - s^2(k)]^2 \end{aligned} \quad (\text{B.8})$$

$$\begin{aligned}
E[(z(j) - s^2(j))^2(z(k) - s^2(k))^2] &= E[s^4(j)s^4(k) + s^4(j)z^2(k) + s^4(k)z^2(j) \\
&\quad + z^2(j)z^2(k) - 2s^2(j)z(j)z^2(k) \\
&\quad - 2s^2(j)s^4(k)z(j) - 2s^4(j)s^2(k)z(k) \\
&\quad - 2s^2(k)z^2(j)z(k) \\
&\quad + 4s^2(j)s^2(k)z(j)z(k)] \\
&= s^4(j)V_t(k) + s^4(j)s^4(k) + s^4(j)s_t^4(k) \\
&\quad + s^4(k)V_t(j) + s^4(k)s_t^4(j) + V_t(j)V_t(k) \\
&\quad + s_t^4(j)V_t(k) + s_t^4(j)s_t^4(k) + s_t^4(k)V_t(j) \\
&\quad - 2s^2(j)s^4(k)s_t^2(j) - 2s^2(j)s_t^2(j)V_t(k) \\
&\quad - 2s^2(j)s_t^2(j)s_t^4(k) - 2s^4(j)s^2(k)s_t^2(k) \\
&\quad - 2s^2(k)s_t^4(j)s_t^2(k) - 2s^2(k)s_t^2(k)V_t(j) \\
&\quad + 4s^2(j)s^2(k)s_t^2(j)s_t^2(k) \\
&\quad + 4\delta_{ij}s^2(j)s^2(k)V_t(k) \\
&= [V_t(j) + s_t^4(j)][V_t(k) + s_t^4(k)] \\
&\quad + s^4(j)[V_t(k) + s_t^4(k)] \\
&\quad + s^4(j)s^4(k) + s^4(k)[V_t(j) + s_t^4(j)] \\
&\quad + 4s^2(j)s^2(k)[\delta_{jk}V_t(k) + s_t^2(j)s_t^2(k)] \\
&\quad - 2s^2(j)s^4(k)s_t^2(j) - 2s^2(j)s_t^2(j)[V_t(k) \\
&\quad + s_t^4(k)] - 2s^4(j)s^2(k)s_t^2(k) \\
&\quad - 2s^2(k)s_t^2(k)[V_t(j) + s_t^4(j)] \\
&= [V_t(j) + (s_t^2(j) - s^2(j))^2] \\
&\quad [V_t(k) + (s_t^2(k) - s^2(k))^2] \tag{B.9}
\end{aligned}$$

where δ_{ij} is the Kronecker delta,

$$\delta_{ij} = \begin{cases} 1 & i = j \\ 0 & \text{otherwise.} \end{cases} \tag{B.10}$$

We next compute $E^2[J_p(u, v)/T]$ using Eq. (3.21), as

$$\begin{aligned}
E^2[J_p(u, v)/T] &= \frac{1}{4} \left[\sum_{k=1}^N \left\{ \frac{1}{T} \log Y(k) - \frac{1}{T} \log T + \right. \right. \\
&\quad \left. \left. \left[Y_t(k)/T + [s_t^2(k) - s^2(k)]^2 \right] / Y(k) \right\}^2 \right] \\
&= \frac{1}{4} \sum_{k=1}^N \sum_{j=1}^N \left\{ \frac{1}{T} \log Y(j) - \frac{1}{T} \log T \right. \\
&\quad \left. + \left[Y_t(j)/T + [s_t^2(j) - s^2(j)]^2 \right] / Y(j) \right\} \left\{ \frac{1}{T} \log Y(k) \right. \\
&\quad \left. - \frac{1}{T} \log T + \left[Y_t(k)/T + [s_t^2(k) - s^2(k)]^2 \right] / Y(k) \right\} \\
&= \frac{1}{4} \sum_{k=1}^N \sum_{j=1}^N \left\{ \frac{1}{T^2} \log Y(j) \log Y(k) + \frac{1}{T^2} \log^2 T \right. \\
&\quad \left. + \frac{1}{Y(j)Y(k)} \left[Y_t(j)/T + [s_t^2(j) - s^2(j)]^2 \right] \left[Y_t(k)/T + [s_t^2(k) \right. \right. \\
&\quad \left. \left. - s^2(k)]^2 \right] + \frac{1}{T^2} \log Y(j) \log T + \frac{1}{T^2} \log Y(k) \log T \right. \\
&\quad \left. + \frac{1}{T} \log Y(k) \left[Y_t(j)/T + [s_t^2(j) - s^2(j)]^2 \right] / Y(j) \right. \\
&\quad \left. + \frac{1}{T} \log Y(j) \left[Y_t(k)/T + [s_t^2(k) - s^2(k)]^2 \right] / Y(k) \right. \\
&\quad \left. + \frac{1}{T} \log T \left[Y_t(j)/T + [s_t^2(j) - s^2(j)]^2 \right] / Y(j) \right. \\
&\quad \left. + \frac{1}{T} \log T \left[Y_t(k)/T + [s_t^2(k) - s^2(k)]^2 \right] / Y(k) \right\} \tag{B.11}
\end{aligned}$$

Taking the limit of Eq. (B.11) as $T \rightarrow \infty$ we obtain

$$\begin{aligned}
\lim_{T \rightarrow \infty} E^2[J_p(u, v)/T] &= \frac{1}{4} \sum_{k=1}^N \sum_{j=1}^N \left\{ \frac{1}{Y(j)Y(k)} \left[s_t^2(j) - s^2(j) \right]^2 \right. \\
&\quad \left. \left[s_t^2(k) - s^2(k) \right]^2 \right\} \tag{B.12}
\end{aligned}$$

We now compute $E[J_p^2(u, v)/T^2]$, using the definitions in Eqs. (B.1) through (B.6), as

$$\begin{aligned}
E[J_p^2(u, v)/T^2] &= E\left\{\left[\sum_k \left\{\frac{1}{2} \log V_t(k) + \frac{1}{2}[z(k) - s^2(k)]^2/V_t(k)\right\}\right]^2/T^2\right\} \\
&= \frac{1}{T^2} E\left\{\frac{1}{4} \sum_j \sum_k \left[\log V(j) \log V(k) \right. \right. \\
&\quad + \log V(j)[z(k) - s^2(k)]^2/V(k) \\
&\quad + \log V(k)[z(j) - s^2(j)]^2/V(j) \\
&\quad \left. \left. + [z(j) - s^2(j)]^2[z(k) - s^2(k)]^2/[V(j)V(k)]\right]\right\} \\
&= \frac{1}{T^2} \frac{1}{4} \sum_j \sum_k \left[\log V(j) \log V(k) + \log V(j) E\{[z(k) - s^2(k)]^2\} \right. \\
&\quad \left. /V(k) + \log V(k) E\{[z(j) - s^2(j)]^2\}/V(j) \right. \\
&\quad \left. + E\{[z(j) - s^2(j)]^2[z(k) - s^2(k)]^2\}/[V(j)V(k)]\right\} \\
&= \frac{1}{T^2} \frac{1}{4} \sum_j \sum_k \left[\log V(j) \log V(k) \right. \\
&\quad + \log V(j)[V_t(k) + (s_t^2(k) - s^2(k))^2]/V(k) \\
&\quad + \log V(k)[V_t(j) + (s_t^2(j) - s^2(j))^2]/V(j) \\
&\quad + \frac{1}{V(j)V(k)} [[V(j) + s_t^4(j)][V(k) + s_t^4(k)] + s^4(j)[V(k) + s_t^4(k)] \\
&\quad + s^4(j)s^4(k) + s^4(k)[V(j) + s_t^4(j)] \\
&\quad + 4s^2(j)s^2(k)[\delta_{ij}V(k) + s_t^2(j)s_t^2(k)] \\
&\quad - 2s^2(j)s^4(k)s_t^2(j) - 2s^2(j)s_t^2(j)[V(k) + s_t^4(k)] \\
&\quad \left. - 2s^4(j)s^2(k)s_t^2(k) - 2s^2(k)s_t^2(k)[V(j) + s_t^4(j)]]\right\} \\
&= \frac{1}{T^2} \frac{1}{4} \sum_j \sum_k \left\{[\log Y(j) - \log T][\log Y(k) - \log T] \right. \\
&\quad + [\log Y(j) - \log T]T[Y_t(k)/T + (s_t^2(k) - s^2(k))^2]/Y(k) + \\
&\quad + [\log Y(k) - \log T]T[V_t(j)/T + (s_t^2(j) - s^2(j))^2]/Y(j) \\
&\quad + \frac{T^2}{Y(j)Y(k)} \left[[Y(j)/T + s_t^4(j)][Y(k)/T + s_t^4(k)] \right. \\
&\quad + s^4(j)[Y(k)/T + s_t^4(k)] \\
&\quad + s^4(j)s^4(k) + s^4(k)[Y(j)/T + s_t^4(j)] \\
&\quad + 4s^2(j)s^2(k)[\delta_{ij}Y(k)/T + s_t^2(j)s_t^2(k)] \\
&\quad - 2s^2(j)s^4(k)s_t^2(j) - 2s^2(j)s_t^2(j)[Y(k)/T + s_t^4(k)] \\
&\quad \left. - 2s^4(j)s^2(k)s_t^2(k) - 2s^2(k)s_t^2(k)[Y(j)/T + s_t^4(j)]\right\} \tag{B.13}
\end{aligned}$$

Taking the limit of Eq. (B.13) as $T \rightarrow \infty$, we obtain,

$$\begin{aligned}
\lim_{T \rightarrow \infty} E[J_p^2(u, v)/T^2] &= \frac{1}{4} \sum_j \sum_k \frac{1}{Y(j)Y(k)} \left[s_t^4(j)s_t^4(k) + s^4(j)s_t^4(k) \right. \\
&\quad + s^4(j)s^4(k) + s^4(k)s_t^4(j) \\
&\quad + 4s^2(j)s^2(k)s_t^2(j)s_t^2(k) \\
&\quad - 2s^2(j)s^4(k)s_t^2(j) - 2s^2(j)s_t^2(j)s_t^4(k) \\
&\quad \left. - 2s^4(j)s^2(k)s_t^2(k) - 2s^2(k)s_t^2(k)s_t^4(j) \right] \tag{B.14}
\end{aligned}$$

We also need $E[J_p(u, v)E[J_p(u, v)]/T^2]$. From Chapter 3, the point-wise objective function $J_p(u, v)$ [see Eq. (3.18)] is

$$J_p(u, v) = \sum_{k=1}^N \left\{ \frac{1}{2} \log V(k) + \frac{1}{2} [z(k) - s^2(k)]^2 / V(k) \right\} \tag{B.15}$$

from which it follows that

$$\begin{aligned}
E[J_p(u, v)] &= E \left[\sum_{k=1}^N \left\{ \frac{1}{2} \log V(k) + \frac{1}{2} [z(k) - s^2(k)]^2 / V(k) \right\} \right] \\
&= \frac{1}{2} \sum_{k=1}^N \left\{ \log V(k) + E \left[[z(k) - s^2(k)]^2 / V(k) \right] \right\} \\
&= \frac{1}{2} \sum_{k=1}^N \left\{ \log V(k) + \left[V_t(k) + [s_t^2(k) - s^2(k)]^2 \right] / V(k) \right\}. \tag{B.16}
\end{aligned}$$

From Eqs. (B.15) and (B.16) we have

$$\begin{aligned}
E\left[J_p(u, v)E[J_p(u, v)/T^2]\right] &= \frac{1}{4}\left[\sum_{k=1}^N\left\{\log V(k) + [z(k) - s^2(k)]^2/V(k)\right\}\right. \\
&\quad \left. \left[\sum_{k=1}^N\left\{\log V(k) + \left[V_t(k) + [s_t^2(k) - s^2(k)]^2\right]\right.\right. \right. \\
&\quad \left. \left. /V(k)\right\}\right]/T^2 \\
&= \frac{1}{4}\sum_{j=1}^N\sum_{k=1}^NE\left\{\log V(j)\log V(k) \right. \\
&\quad + \log V(k)[z(k) - s^2(k)]^2/V(k) \\
&\quad + \log V(j)\left[V_t(k) + [s_t^2(k) - s^2(k)]^2\right]/V(k) \\
&\quad + \frac{1}{V(j)V(k)}[z(j) - s^2(j)]^2[z(k) - s^2(k)]^2 \\
&\quad + \frac{1}{V(j)V(k)}\left[V_t(j) + [s_t^2(j) - s^2(j)]^2\right] \\
&\quad \left. \left[V_t(k) + [s_t^2(k) - s^2(k)]^2\right]\right\}/T^2 \\
&= \frac{1}{4}\sum_{j=1}^N\sum_{k=1}^N\left\{\log V(j)\log V(k) \right. \\
&\quad + \log V(k)E\left\{[z(k) - s^2(k)]^2\right\}/V(k) \\
&\quad + \log V(j)\left[V_t(k) + [s_t^2(k) - s^2(k)]^2\right]/V(k) \\
&\quad + \frac{1}{V(j)V(k)}E\left\{[z(j) - s^2(j)]^2[z(k) - s^2(k)]^2\right\} \\
&\quad + \frac{1}{V(j)V(k)}\left[V_t(j) + [s_t^2(j) - s^2(j)]^2\right] \\
&\quad \left. \left[V_t(k) + [s_t^2(k) - s^2(k)]^2\right]\right\}/T^2 \\
&= \frac{1}{T^2}\frac{1}{4}\sum_{j=1}^N\sum_{k=1}^N\left\{\log V(j)\log V(k) \right. \\
&\quad + \log V(k)\left[V_t(k) + [s_t^2(k) - s^2(k)]^2\right]/V(k) \\
&\quad + \log V(j)\left[V_t(k) + [s_t^2(k) - s^2(k)]^2\right]/V(k) \\
&\quad + \frac{1}{V(j)V(k)}\left\{[V(j) + s_t^4(j)][V(k) + s_t^4(k)] \right. \\
&\quad + s^4(j)[V(k) + s_t^4(k)] \\
&\quad + s^4(j)s_t^4(k) + s^4(k)[V(j) + s_t^4(j)] \\
&\quad + 4s^2(j)s^2(k)[\delta_{ij}V(k) + s_t^2(j)s_t^2(k)] \\
&\quad - 2s^2(j)s^4(k)s_t^2(j) - 2s^2(j)s_t^2(j)[V(k) + s_t^4(k)] \\
&\quad \left. - 2s^4(j)s^2(k)s_t^2(k) - 2s^2(k)s_t^2(k)[V(j) + s_t^4(j)]\right\} \\
&\quad + \frac{1}{V(j)V(k)}\left[V_t(j) + [s_t^2(j) - s^2(j)]^2\right]
\end{aligned}$$

Taking the limit as $T \rightarrow \infty$, we obtain

$$\begin{aligned}
\lim_{T \rightarrow \infty} E \left[J_p(u, v) E[J_p(u, v)/T^2] \right] &= \frac{1}{4} \sum_{j=1}^N \sum_{k=1}^N \left\{ \frac{1}{Y(j)Y(k)} \left[s_t^4(j)s_t^4(k) + s^4(j)s_t^4(k) \right. \right. \\
&+ s^4(j)s^4(k) + s^4(k)s_t^4(j) \\
&+ 4s^2(j)s^2(k)s_t^2(j)s_t^2(k) \\
&- 2s^2(j)s^4(k)s_t^2(j) - 2s^2(j)s_t^2(j)s_t^4(k) \\
&- 2s^4(j)s^2(k)s_t^2(k) - 2s^2(k)s_t^2(k)s_t^4(j) \\
&\left. \left. + [s_t^2(j) - s^2(j)]^2 [s_t^2(k) - s^2(k)]^2 \right] \right\} \quad (\text{B.18})
\end{aligned}$$

Appendix C

The Geostrophic Equation

In this appendix a detailed derivation of the geostrophic equation from the fundamental equations of motion of the atmosphere is provided for background. This is followed by an analysis of the divergence and curl of geostrophic wind fields.

C.1 Derivation of the Geostrophic Equations

In this section an outline of the development of the geostrophic approximation to the Navier-Stokes equation is given. The approach follows Pedlosky [88]. Let L be the characteristic length scale of motion and U be the horizontal velocity scale. Let $\tau = L/U$ be the time scale of motion. The nondimensional *Rossby number*, denoted by ϵ and defined as

$$\epsilon = \frac{U}{2\Omega L}, \quad (\text{C.1})$$

where $\Omega = 7.3 \times 10^{-5} \text{ s}^{-1}$ is the angular velocity of the earth's rotation, is a measure of the effects of the earth's rotation on the atmosphere. For ϵ less than unity, the earth's rotation is a significant factor in the atmospheric motion. For wind scatterometry, $L = 25 \text{ km}$ and $U \approx 3 \text{ m/s}$; hence, $\epsilon \approx 0.8$.

Assuming that there are no sources or sinks of mass, mass conservation considerations lead to the generalized *continuity equation*,

$$\frac{\partial}{\partial t} \rho + \nabla \cdot \rho \mathbf{u} = 0 \quad (\text{C.2})$$

where ρ is the fluid density (which in general varies with space and time), t is time, and $\mathbf{u} = u\mathbf{x} + v\mathbf{y} + w\mathbf{z}$ is the fluid velocity vector where \mathbf{x} , \mathbf{y} and \mathbf{z} are unit vectors in the x , y , and z directions respectively. We begin with Newton's law of motion for fluid flow,

$$\rho \frac{\partial}{\partial t} \mathbf{u} = -\nabla p + \rho \nabla \phi + \mathcal{F}(\mathbf{u}) \quad (\text{C.3})$$

where \mathcal{F} is force and ϕ is the conservative potential (e.g., gravity). This is the generalized Navier-Stokes equation. For Newtonian fluids, such as water or air, the force \mathcal{F} is due only to friction. When the thermodynamic state variables are constant, \mathcal{F} is

$$\mathcal{F} = \mu \nabla^2 \mathbf{u} + \mu \nabla (\nabla \cdot \mathbf{u}) / 3. \quad (\text{C.4})$$

As we shall see, the geostrophic approximation neglects the frictional part of \mathcal{F} and considers only the potential due to the effects of gravity and the earth's rotation. For an observer in a uniformly rotating coordinate frame, Eq. (C.3) can be written, as

$$\rho \left[\frac{d}{dt} \mathbf{u} + 2\boldsymbol{\Omega} \times \mathbf{u} \right] = -\nabla p + \rho \nabla \Phi + \mathcal{F}(\mathbf{u}) \quad (\text{C.5})$$

where $\boldsymbol{\Omega}$ is the planetary angular velocity vector ($\Omega = |\boldsymbol{\Omega}|$), $\Phi = |\boldsymbol{\Omega} \times \mathbf{u}|^2 / 2$ is the magnitude of the centripetal acceleration and $2\boldsymbol{\Omega} \times \mathbf{u}$ is Coriolis force on the atmosphere due to the earth's rotation. An order of magnitude estimate of the relative acceleration is,

$$\frac{d}{dt} \mathbf{u} = \rho \frac{\partial}{\partial t} \mathbf{u} + (\mathbf{u} \cdot \nabla) \mathbf{u} = O(U/\tau, U^2/L) \quad (\text{C.6})$$

where the order is the larger of the two terms in parenthesis on the right. An estimate of the order of magnitude of the Coriolis acceleration is,

$$2\boldsymbol{\Omega} \times \mathbf{u} = O(2\Omega U). \quad (\text{C.7})$$

The order of magnitude estimate of the ratio is,

$$\frac{|\frac{d}{dt} \mathbf{u}|}{|2\boldsymbol{\Omega} \times \mathbf{u}|} = O\left(\frac{1}{2\Omega\tau}, \frac{U}{2\Omega L}\right) \quad (\text{C.8})$$

Both terms in the parenthesis are recognized as the Rossby number. When the Rossby number is small, the relative acceleration $d\mathbf{u}/dt$ is negligible. Using Eq. (C.4), an order of magnitude estimate of \mathcal{F} , is

$$\mathcal{F} = O\left(\frac{\nu U}{L^2}\right) \quad (\text{C.9})$$

where ν is the kinematic viscosity. This estimate is based on the assumption that a single value of U characterizes the variation in \mathbf{u} . When the friction force (and the Rossby number) is sufficiently small, Eq. (C.5) can be approximated by,

$$\rho 2\boldsymbol{\Omega} \times \mathbf{u} = -\nabla p + \rho \nabla \Phi \quad (\text{C.10})$$

The atmosphere is a relatively thin layer above the Earth's surface. Within this layer $\nabla \Phi$ is essentially constant and is equal to the gravitational acceleration g normal to the Earth's

surface. In spherical coordinates, Eq. (C.10) is

$$\rho[-2\Omega v \sin \theta + 2\Omega w \cos \theta] = -\frac{1}{r \cos \theta} \frac{\partial}{\partial \phi} p \quad (\text{C.11})$$

$$\rho 2\Omega u \sin \theta = -\frac{1}{r} \frac{\partial}{\partial \phi} p \quad (\text{C.12})$$

$$-\rho 2\Omega u \cos \theta = -\frac{\partial}{\partial r} p - \rho g \quad (\text{C.13})$$

To understand the next step, it is helpful to partition the pressure p and density ρ fields into two parts. If $u = v = w = 0$, then p and ρ must be independent of ϕ and θ and therefore only a function of r , i.e.,

$$p = p_s(r) + p'(r, \theta, \phi) \quad (\text{C.14})$$

$$\rho = \rho_s(r) + \rho'(r, \theta, \phi) \quad (\text{C.15})$$

where $p_s(r)$ and $\rho_s(r)$ correspond to the fields which would exist without fluid motion and p' and ρ' are due to the fluid motion. It then follows from Eq. (C.13), that

$$\frac{\partial}{\partial r} p_s = \rho_s g \quad (\text{C.16})$$

so that Eqs. (C.11) through (C.13) become,

$$(\rho_s + \rho')[-2\Omega v \sin \theta + 2\Omega w \cos \theta] = -\frac{1}{r \cos \theta} \frac{\partial}{\partial \phi} p' \quad (\text{C.17})$$

$$(\rho_s + \rho') 2\Omega u \sin \theta = -\frac{1}{r} \frac{\partial}{\partial \phi} p' \quad (\text{C.18})$$

$$-(\rho_s + \rho') 2\Omega u \cos \theta = -\frac{\partial}{\partial r} p' - \rho' g \quad (\text{C.19})$$

Let D be the thickness of the region of vertical motion. In wind scatterometry D is at most a few km. The ratio of the vertical to horizontal motion can be estimated, as

$$\frac{w}{u} = O\left(\frac{w}{v}\right) = O\left(\frac{D}{L}\right) \ll 1; \quad (\text{C.20})$$

hence, the $\cos \theta$ term in Eq. (C.17) can be neglected. An order of magnitude estimate of the vertical component of the Coriolis acceleration, $\rho 2\Omega u \cos \theta$, is

$$\rho 2\Omega u \cos \theta = O(\rho 2\Omega U). \quad (\text{C.21})$$

Since the horizontal pressure gradient must balance the Coriolis acceleration,

$$p' = O(\rho 2\Omega U L) \quad (\text{C.22})$$

The order of magnitude estimate of the vertical component of the pressure field gradient, $\partial p'/\partial r$, is then

$$\frac{\partial}{\partial r} p' = O\left(\frac{p'}{D}\right) = O\left(\rho \frac{2\Omega UL}{D}\right) \quad (\text{C.23})$$

so that the ratio of the vertical component of the Coriolis acceleration and the vertical pressure gradient is,

$$\frac{\rho 2\Omega u \cos \theta}{\partial p'/\partial r} = O\left(\frac{D}{L}\right) \ll 1 \quad (\text{C.24})$$

Hence, the terms proportional to $2\Omega \cos \theta$ in both vertical and horizontal equations can be neglected, implying that only the locally normal component of the earth's rotation, $\Omega \sin \theta$, is significant.

An upper bound on the magnitude of ρ' is,

$$\rho' \leq O\left(\frac{p'}{gD}\right) = O\left(\rho \frac{2\Omega UL}{gD}\right) \quad (\text{C.25})$$

so that

$$\frac{\rho'}{\rho} = O\left(\frac{U}{2\Omega L}\right) \frac{4\Omega^2 L^2}{gD} = \epsilon \frac{4\Omega^2 L^2}{gD} \quad (\text{C.26})$$

The term $4\Omega^2 L^2/gD$ depends only on the geometric scale. For the surface wind fields of interest, $4\Omega^2 L^2/gD < 1$. So long as the Rossby number ϵ is small, $\rho'/\rho \leq O(\epsilon) \ll 1$ and $\rho' \ll \rho_s(r)$, so that $(\rho_s + \rho')$ can be approximated by ρ_s .

Based on these approximations, Eqs. (C.17) through (C.19) can be approximated, as

$$C_p v = \frac{1}{\rho_s r \cos \theta} \frac{\partial}{\partial \phi} p \quad (\text{C.27})$$

$$C_p u = -\frac{1}{\rho_s r} \frac{\partial}{\partial \theta} p \quad (\text{C.28})$$

$$\rho g = -\frac{\partial}{\partial r} p \quad (\text{C.29})$$

where

$$C_p = 2\Omega \sin \theta. \quad (\text{C.30})$$

Note that at exactly the equator ($\theta = 0$) the geostrophic equation does not apply. Near the equator C_p can be approximated by $2\Omega\theta$.

The atmosphere is a very thin layer of fluid over the earth's surface. If we define $z = r - r_0$ where r_0 is the radius of the earth's surface and note that $z \ll r$, Eqs. (C.27) through (C.29)

can be written, as

$$C_p v = \frac{1}{\rho_s r_o \cos \theta} \frac{\partial}{\partial \phi} p \quad (\text{C.31})$$

$$C_p u = -\frac{1}{\rho_s r_o} \frac{\partial}{\partial \theta} p \quad (\text{C.32})$$

$$\rho g = -\frac{\partial}{\partial z} p \quad (\text{C.33})$$

These equations are known as the *geostrophic approximation* to the full momentum equation. The horizontal velocity is a balance between the horizontal pressure gradient and the horizontal component of the Coriolis acceleration. In vector form, the first two equations in the geostrophic approximation can be written, as

$$\mathbf{u}_H = \frac{1}{C_p \rho_s} \mathbf{k} \times \nabla p \quad (\text{C.34})$$

where \mathbf{k} is the unit vector perpendicular to the surface of the sphere and $\mathbf{u}_H = (u, v)^T$ is the horizontal velocity vector. This equation is known as the geostrophic equation. The geostrophic approximation provides no information about the vertical velocity w . Note that the density field ρ_s is independent of the fluid motion since it corresponds to the density field which would be present if the fluid were at rest (see Eq. (C.15)).

C.2 Divergence of the Geostrophic Wind Field

In a plane tangent to the earth's surface, the geostrophic equation [Eq. (C.34)] can be written in component form in rectangular coordinates, as

$$u = -\frac{1}{\rho_s C_p} \frac{\partial}{\partial y} p \quad (\text{C.35})$$

$$v = \frac{1}{\rho_s C_p} \frac{\partial}{\partial x} p \quad (\text{C.36})$$

Note that the value of $C_p = 2\Omega \sin \theta$ depends on the latitude θ of the tangent point.

The divergence $\nabla \cdot \mathbf{u}$ and curl $\nabla \times \mathbf{u}$ of a two-component vector field $\mathbf{u} = (u, v)^T$ in rectangular coordinates are, respectively,

$$\nabla \cdot \mathbf{u} = \frac{\partial u}{\partial x} + \frac{\partial v}{\partial y} \quad (\text{C.37})$$

$$\nabla \times \mathbf{u} = \left(\frac{\partial v}{\partial x} - \frac{\partial u}{\partial y} \right) \mathbf{z}, \quad (\text{C.38})$$

where \mathbf{z} is a unit vector in the z direction.

Taking the divergence of the geostrophic equation produces

$$\nabla \cdot \mathbf{u} = \frac{\partial u}{\partial x} + \frac{\partial v}{\partial y} = \frac{1}{\rho_s C_p} \left(-\frac{\partial^2}{\partial x \partial y} + \frac{\partial^2}{\partial x \partial y} \right) p = 0; \quad (\text{C.39})$$

hence, the geostrophic equation results in nondivergent wind fields.

If we take the curl of the geostrophic equation, we have,

$$\nabla \times \mathbf{u} = \left(\frac{\partial v}{\partial x} - \frac{\partial u}{\partial y} \right) \mathbf{z} = -\frac{1}{\rho_s C_p} \left(\frac{\partial^2}{\partial x^2} + \frac{\partial^2}{\partial y^2} \right) p \mathbf{z} \quad (\text{C.40})$$

which, in general, will be nonzero.

C.3 Curl of a Non-divergent, Isotropic Wind Field

In this section, some of the properties of the curl of the velocity field are considered. Following Freilich [31], the curl spectrum of a non-divergent, isotropic wind field is derived. Consider a general two-dimensional vector field $\mathbf{u}(x, y)$ with cartesian components $u(x, y)$ in the x -direction and $v(x, y)$ in the y -direction. Let $d(x, y)$ be the divergence of the field $\mathbf{u}(x, y)$ and $c(x, y)$ be the curl of the field.

The *Helmholtz theorem* states that the vector field $\mathbf{u}(x, y)$ can be written as the sum of two other vector fields $\mathbf{A}(x, y)$ and $\mathbf{B}(x, y)$,

$$\mathbf{u}(x, y) = \mathbf{A}(x, y) + \mathbf{B}(x, y) \quad (\text{C.41})$$

where $\mathbf{A}(x, y)$ is an *irrotational* or curl-free field such that

$$\nabla \times \mathbf{A}(x, y) = 0 \quad (\text{C.42})$$

and $\mathbf{B}(x, y)$ is a non-divergent field such that,

$$\nabla \cdot \mathbf{B}(x, y) = 0 \quad (\text{C.43})$$

For convenience, define the cartesian components of the fields as,

$$\mathbf{A}(x, y) \triangleq a_x(x, y)\mathbf{x} + a_y(x, y)\mathbf{y} \quad (\text{C.44})$$

$$\mathbf{B}(x, y) \triangleq b_x(x, y)\mathbf{x} + b_y(x, y)\mathbf{y} \quad (\text{C.45})$$

Thus, the divergence and curl of \mathbf{A} and \mathbf{B} are,

$$\frac{\partial}{\partial x}a_x(x, y) + \frac{\partial}{\partial y}a_y(x, y) = d(x, y) \quad (\text{C.46})$$

$$\frac{\partial}{\partial x}a_y(x, y) - \frac{\partial}{\partial y}a_x(x, y) = 0 \quad (\text{C.47})$$

$$\frac{\partial}{\partial x}b_y(x, y) - \frac{\partial}{\partial y}b_x(x, y) = c(x, y) \quad (\text{C.48})$$

$$\frac{\partial}{\partial x}b_x(x, y) + \frac{\partial}{\partial y}b_y(x, y) = 0 \quad (\text{C.49})$$

where $d(x, y)$ is the divergence field of \mathbf{A} and $c(x, y)$ is the curl field of \mathbf{B} .

By alternately cross-differentiating and adding the previous equations, we can produce a set of second-order partial differential equations relating the components of the vector fields to the directional partials of the curl and divergence fields, i.e.,

$$\frac{\partial^2}{\partial x^2}a_x(x, y) + \frac{\partial^2}{\partial y^2}a_x(x, y) = \frac{\partial}{\partial x}d(x, y) \quad (\text{C.50})$$

$$\frac{\partial^2}{\partial x^2}a_y(x, y) + \frac{\partial^2}{\partial y^2}b_y(x, y) = \frac{\partial}{\partial y}d(x, y) \quad (\text{C.51})$$

$$\frac{\partial^2}{\partial x^2}b_y(x, y) + \frac{\partial^2}{\partial y^2}b_y(x, y) = \frac{\partial}{\partial x}c(x, y) \quad (\text{C.52})$$

$$\frac{\partial^2}{\partial x^2}b_x(x, y) + \frac{\partial^2}{\partial y^2}b_x(x, y) = -\frac{\partial}{\partial y}c(x, y) \quad (\text{C.53})$$

Solutions of these equations can be obtained using Fourier transforms. The component fields can be defined in terms of their Fourier transforms, as

$$a_x(x, y) = \frac{1}{4\pi^2} \iint A_x(k_x, k_y) e^{j(k_x x + k_y y)} dk_x dk_y \quad (\text{C.54})$$

$$a_y(x, y) = \frac{1}{4\pi^2} \iint A_y(k_x, k_y) e^{j(k_x x + k_y y)} dk_x dk_y \quad (\text{C.55})$$

$$b_x(x, y) = \frac{1}{4\pi^2} \iint B_x(k_x, k_y) e^{j(k_x x + k_y y)} dk_x dk_y \quad (\text{C.56})$$

$$b_y(x, y) = \frac{1}{4\pi^2} \iint B_y(k_x, k_y) e^{j(k_x x + k_y y)} dk_x dk_y \quad (\text{C.57})$$

$$c(x, y) = \frac{1}{4\pi^2} \iint C(k_x, k_y) e^{j(k_x x + k_y y)} dk_x dk_y \quad (\text{C.58})$$

$$d(x, y) = \frac{1}{4\pi^2} \iint D(k_x, k_y) e^{j(k_x x + k_y y)} dk_x dk_y \quad (\text{C.59})$$

where A_x , A_y , B_x , B_y , C , and D are the Fourier coefficients and k_x and k_y are the wavenumbers in the x -direction and y -direction respectively. In terms of the Fourier coefficients the

second-order partial differential Eqs. (C.50) through (C.53) become,

$$\iint \{(k_x^2 + k_y^2)A_x(k_x, k_y) + jk_x D(k_x, k_y)\} e^{j(k_x x + k_y y)} dk_x dk_y = 0 \quad (\text{C.60})$$

$$\iint \{(k_x^2 + k_y^2)A_y(k_x, k_y) + jk_x D(k_x, k_y)\} e^{j(k_x x + k_y y)} dk_x dk_y = 0 \quad (\text{C.61})$$

$$\iint \{(k_x^2 + k_y^2)B_y(k_x, k_y) + jk_x C(k_x, k_y)\} e^{j(k_x x + k_y y)} dk_x dk_y = 0 \quad (\text{C.62})$$

$$\iint \{(k_x^2 + k_y^2)B_x(k_x, k_y) - jk_x C(k_x, k_y)\} e^{j(k_x x + k_y y)} dk_x dk_y = 0. \quad (\text{C.63})$$

The solutions to these equations are [31],

$$A_x(k_x, k_y) = \frac{-jk_x}{k_x^2 + k_y^2} D(k_x, k_y) \quad (\text{C.64})$$

$$A_y(k_x, k_y) = \frac{-jk_y}{k_x^2 + k_y^2} D(k_x, k_y) = \frac{k_y}{k_x} A_x(k_x, k_y) \quad (\text{C.65})$$

$$B_y(k_x, k_y) = \frac{-jk_y}{k_x^2 + k_y^2} C(k_x, k_y) \quad (\text{C.66})$$

$$B_x(k_x, k_y) = \frac{jk_x}{k_x^2 + k_y^2} C(k_x, k_y) = -\frac{k_x}{k_y} B_y(k_x, k_y) \quad (\text{C.67})$$

Thus, given either the spectra of the divergence and curl or realizations of the divergence and curl, the original vector field can be computed.

Using the non-divergent wind field predicted by the geostrophic equation, $\mathbf{A}(x, y) = 0$ and $\mathbf{u}(x, y) = \mathbf{B}(x, y)$. The two-dimensional energy spectrum $E(k_x, k_y)$ of $\mathbf{B}(k_x, k_y)$, is,

$$E(k_x, k_y) = |B_x(k_x, k_y)|^2 + |B_y(k_x, k_y)|^2 = \left(1 + \frac{k_x^2}{k_y^2}\right) |B_x(k_x, k_y)|^2 \quad (\text{C.68})$$

In a paper on the properties of mesoscale wind fields, Freilich and Charney showed that the one-dimensional kinetic energy spectrum of the wind field can be expressed as a power law [33],

$$\widehat{E}(k) = \alpha k^{-b} \quad (\text{C.69})$$

where α is the variance of the wind field, $k = (k_x^2 + k_y^2)^{\frac{1}{2}}$ and $b \approx 2$. Assuming the two-dimensional energy spectrum $E(k_x, k_y)$ is *isotropic*, the energy spectrum will be circularly symmetric and $E(k_x, k_y)$ will be related to the one-dimensional energy spectrum $\widehat{E}(k)$ by [33],

$$\widehat{E}(k) = \pi k E(k_x, k_y) \quad (\text{C.70})$$

so that the power-law for the two-dimensional spectrum becomes,

$$E(k_x, k_y) = \frac{\alpha}{\pi} k^{-3} \quad (\text{C.71})$$

Using Eqs. (C.68) and (C.71), the coefficients $|B_x(k_x, k_y)|^2$ are

$$|B_x(k_x, k_y)|^2 = \frac{\alpha}{\pi} \frac{k_y^2}{(k_x^2 + k_y^2)^{5/2}}. \quad (\text{C.72})$$

It follows that the curl spectrum $C(k_x, k_y)$ is,

$$|C(k_x, k_y)|^2 = \frac{\alpha}{\pi} \frac{1}{\sqrt{k_x^2 + k_y^2}} = \frac{\alpha}{\pi} \frac{1}{k}, \quad (\text{C.73})$$

hence, the curl energy spectrum is isotropic and is proportional to the inverse of the spectral wavenumber. This information is useful in defining a model for the wind field curl. Note that these results are for the *average* curl spectrum. The energy spectrum from wind fields containing fronts may not adhere to the same power-law dependency [17, 33].

Appendix D

Simulation of “Real” Mesoscale Wind Fields

Since there is no existing mesoscale wind field data available at the scatterometer sampling resolution, test wind fields must be generated by simulation. This appendix describes the method used for generating the simulated mesoscale wind fields used in this research. The method was developed by Beven and Freilich [9] for use in generating wind fields for evaluating NSCAT performance. The wind fields used in this research are these same fields generated by Beven and Freilich for NSCAT. Following [9], a brief description of their technique is provided below.

D.1 Computation of “Realistic” Mesoscale Wind Fields

Wind fields at a resolution of 1.875 deg in latitude and longitude were obtained from the European Center for Medium-Range Weather Forecasting (ECMWF). The ECMWF has what is generally considered to be the best global numerical weather prediction model in operation. In 1986 and 1987, ECMWF generated 60 wind fields (two weeks at 6 hour intervals) which assimilated subjectively dealiased SASS winds into their state-of-the-art forecasting model. On plots of these wind fields, templates of the NSCAT swath were laid out and orbit passes which covered significant meteorological features were selected. The choices of the passes were based on a number of subjective criteria including features absent in previous simulations of scatterometer performance such as small-scale cyclones, sharp fronts, small-scale divergence, regions of both high and low wind speeds, etc. A total of 24 passes were selected containing significant small-scale variability.

For each pass, the 1.875 deg wind field data was interpolated to 10 km resolution over the observation swath of the scatterometer using a Laplacian-spline interpolation scheme. Smaller scale variability was then added based on the work of Freilich and Chelton [33]. Freilich and Chelton showed that, assuming the wind was isotropic and non-divergent, the kinetic energy spectrum fell off like k^{-2} (see Appendix C). For each pass, the interpolated wind field was segmented into adjacent 2000×2000 km regions and the variance of the u

and v components were computed separately. A random phase 2000×2000 km isotropic non-divergent wind field with an energy spectrum of k^{-1} with scales of motions from 10 to 100 km was then computed using the Fourier approach described in the last section of Appendix C (see also [32]). This wind field was scaled component-wise by the variances previously computed. The scaled wind field was then added component-wise to the original wind field.

This procedure preserves the small-scale variability of the original field and adds even smaller-scale variability which has consistent kinetic energy spectrum. The result is felt to be “realistic” mesoscale wind fields at 10 km resolution. For use in evaluating the wind field model, the 10 km resolution wind fields were sampled to 25 km resolution after averaging of adjacent 10 km resolution sample points. An example of the resulting wind field is shown in Fig. 4.4.

D.2 The Divergence and Curl of “Realistic” Mesoscale Wind Fields

At large synoptic scales the geostrophic equation is an excellent approximation. At this scale the wind field is nondivergent. At the smaller mesoscale, however, the wind field may contain regions of non-zero divergence. To illustrate this, the vorticity and divergence of the simulated mesoscale wind fields were computed by approximating the directional partials by the first-order finite-difference equation,

$$\frac{\partial}{\partial x} a(x, y) \approx \frac{1}{h} [a(x_i, y_i) - a(x_{i-1}, y_i)] \quad (\text{D.1})$$

where h is the sample spacing. Figures D.1 and D.2 illustrate the vorticity and divergence of a section of one such field. In Fig. D.1, the vorticity is shown as a contour map superimposed on the wind vector field. Similarly, Fig. D.2 shows the divergence superimposed on the wind vector field. The spacing between vectors is approximately 80 km with a vector length corresponding to the sample spacing of 15 m/s. The contour intervals, shown in the legend, are in compatible, but arbitrary, units. Note that the ranges of divergence and curl have nearly the same magnitude though the scales of variation differ. The divergence varies slowly over large regions while the curl shows much more rapid change over shorter scales. The absence of very small scale divergence is consistent with the generation of the wind fields were the smallest scale variations were all non-divergent.

While we expect non-zero vorticity, these figures illustrate that mesoscale wind fields also contain regions of non-zero divergence. Because the wind field contains non-zero divergence, the geostrophic equation can not exactly model the field; hence, the wind field model should be general enough to include (divergent) ageostrophic winds.

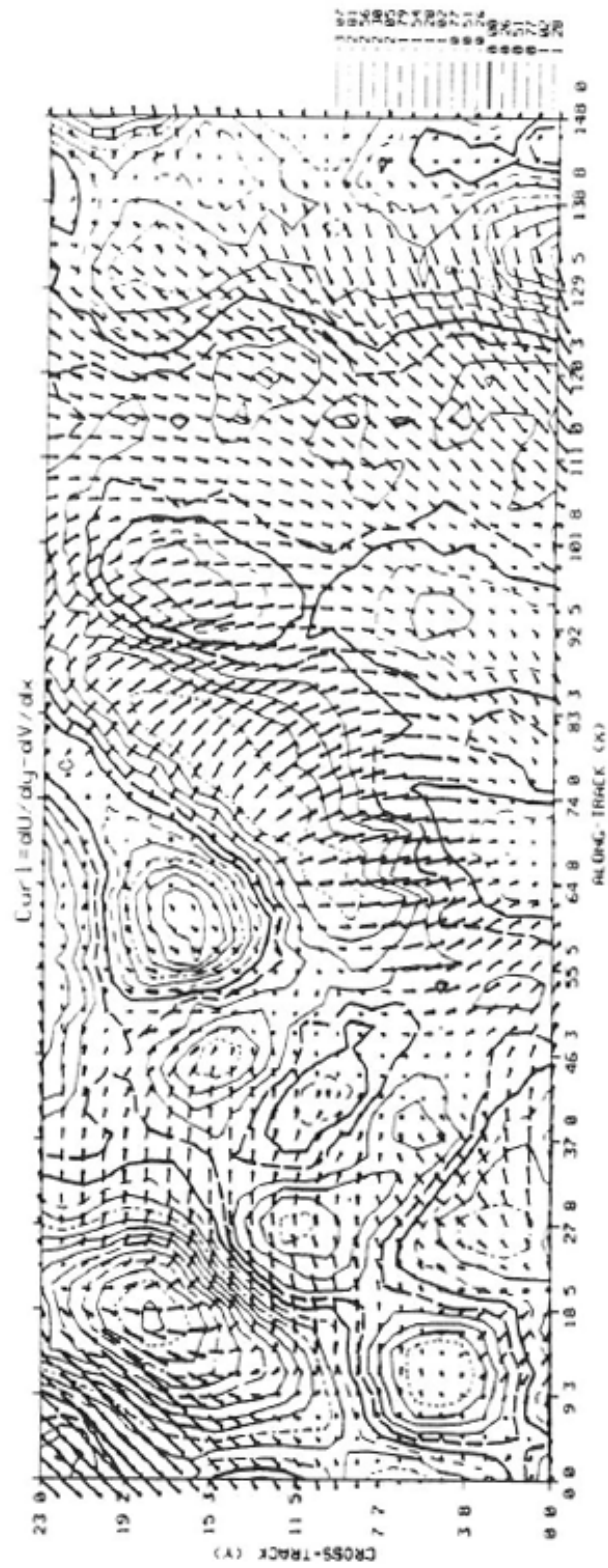


Figure D.1: Example of the vorticity of a mesoscale wind field. The vorticity is shown as a contour plot superimposed on a wind vector field map (see text).

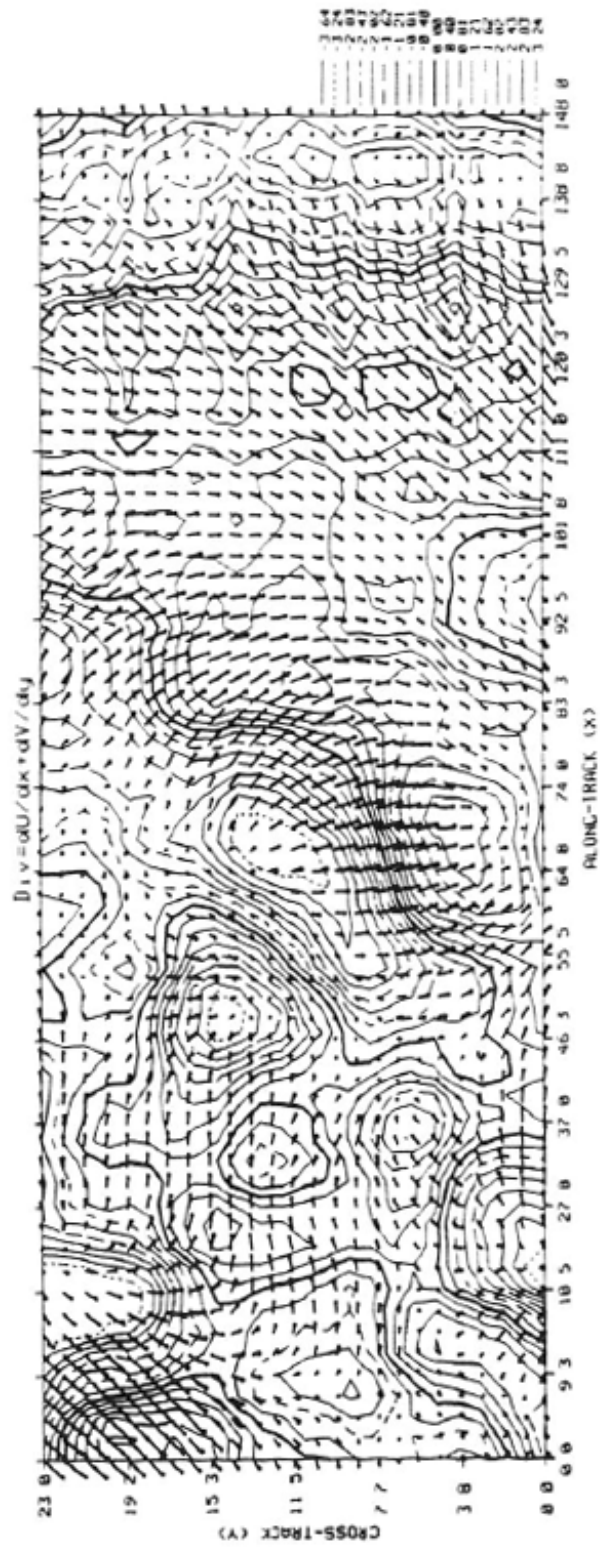


Figure D.2: Example of the divergence of a mesoscale wind field. The divergence is shown as a contour plot superimposed on a wind vector field map (see text).

Appendix E

Detailed Derivations for the Wind Field Model

In this appendix, detailed derivations and proofs used in the derivation of the wind field model are provided. This includes a proof of the invertibility of the K matrix, the computation of K^{-1} , and a proof of the linear independence of the columns of the F matrix.

E.1 Computation of K^{-1}

The $N^2 \times N^2$ matrix K is defined, as

$$K = I \otimes Q + Q \otimes I \tag{E.1}$$

where Q is an $N \times N$ tridiagonal matrix with elements $q_{i,j}$, where

$$q_{i,j} = \begin{cases} \frac{1}{2}, & \text{if } i = j, \\ -\frac{1}{4}, & \text{if } |i - j| = 1, \\ 0, & \text{otherwise} \end{cases} \tag{E.2}$$

and I is an $N \times N$ identity matrix.

We will exploit the well known fact [46, 80] that the unitary sine transform matrix Ψ with elements $\psi_{i,j}$ diagonalizes Q , where

$$\psi_{i,j} = \sqrt{\frac{2}{N+1}} \sin\left(\frac{ij\pi}{N+1}\right) \tag{E.3}$$

and

$$\Psi Q \Psi^T = \Psi Q \Psi = \Lambda^q \tag{E.4}$$

The off-diagonal elements of Λ^q are zero and the diagonal elements $\lambda_{i,i}^q \triangleq \lambda^q(i)$ of Λ^q are

$$\lambda^q(i) = \frac{1}{2} \left[1 - \cos \left(\frac{i\pi}{N+1} \right) \right] \quad (\text{E.5})$$

This permits us to explicitly compute the elements $q_{i,j}^{-1}$ of Q^{-1} , as

$$\begin{aligned} q_{i,j}^{-1} &= \sum_{k=1}^N \psi_{i,k} \psi_{k,j} / \lambda^q(i) \\ &= \frac{4}{N+1} \sum_{k=1}^N \left[\sin \left(\frac{ik\pi}{N+1} \right) \sin \left(\frac{jk\pi}{N+1} \right) \right] / \left[1 - \cos \left(\frac{k\pi}{N+1} \right) \right] \\ &= \frac{2}{N+1} \sum_{k=1}^N \left[\cos \left(\frac{k(i-j)\pi}{N+1} \right) - \cos \left(\frac{k(i+j)\pi}{N+1} \right) \right] / \\ &\quad \left[1 - \cos \left(\frac{k\pi}{N+1} \right) \right] \end{aligned} \quad (\text{E.6})$$

The $N \times N$ matrix Ψ can be used to diagonalize K . Using the elementary properties of the Kronecker product and noting that $\Psi^T \Psi = \Psi \Psi = I$ we see that,

$$\begin{aligned} (\Psi \otimes \Psi)K(\Psi \otimes \Psi) &= (\Psi \otimes \Psi)(I \otimes Q + Q \otimes I)(\Psi \otimes \Psi) \\ &= (\Psi \otimes \Psi)(I \otimes Q)(\Psi \otimes \Psi) + (\Psi \otimes \Psi)(Q \otimes I)(\Psi \otimes \Psi) \\ &= (\Psi \otimes \Psi)([I\Psi] \otimes [Q\Psi]) + (\Psi \otimes \Psi)([Q\Psi] \otimes [I\Psi]) \\ &= ([\Psi I\Psi] \otimes [\Psi Q\Psi]) + ([\Psi Q\Psi] \otimes [\Psi I\Psi]) \\ &= I \otimes (\Psi Q\Psi) + (\Psi Q\Psi) \otimes I \\ &= I \otimes \Lambda^q + \Lambda^q \otimes I \\ &\triangleq \Lambda \end{aligned} \quad (\text{E.7})$$

Note that the matrices $I \otimes \Lambda^q$ and $\Lambda^q \otimes I$ are diagonal matrices with off-diagonal elements zero so that Λ is also diagonal. It follows from (E.5) that the N^2 eigenvalues of Λ (which are also the eigenvalues of K) are,

$$\lambda_{k,k} \triangleq \lambda(k) = \lambda^q(i) + \lambda^q(j) = 1 - \frac{1}{2} \cos[i\pi/(N+1)] - \frac{1}{2} \cos[j\pi/(N+1)] \quad (\text{E.8})$$

where $i = \text{mod}(k-1, N) + 1$ and $j = \text{int}((k-1)/N) + 1$. Note that the eigenvalues of K are strictly positive, i.e.,

$$0 < \lambda(k) < 2 \quad \text{for all } k \quad (\text{E.9})$$

With strictly positive eigenvalues, K is invertible. The eigenvalues of K^{-1} are the inverse of

the eigenvalues of K , i.e.,

$$\lambda_{k,k}^{K^{-1}} \triangleq \lambda^{K^{-1}}(k) = \frac{1}{\lambda^q(i) + \lambda^q(j)} = \frac{2}{2 - \cos[i\pi/(N+1)] - \cos[j\pi/(N+1)]} \quad (\text{E.10})$$

We can explicitly write the elements $k_{m,n}^{-1}$ of K^{-1} , as

$$\begin{aligned} k_{m,n}^{-1} &= \sum_{l=1}^{N^2} (\Psi \otimes \Psi)_{m,l} \lambda^{K^{-1}}(l) (\Psi \otimes \Psi)_{l,n} \\ &= \sum_{l=1}^{N^2} \psi_{\lfloor m \rfloor, \lfloor l \rfloor} \psi_{\lceil m \rceil, \lceil l \rceil} \psi_{\lfloor n \rfloor, \lfloor l \rfloor} \psi_{\lceil n \rceil, \lceil l \rceil} / \lambda(l) \\ &= \frac{8}{(N+1)^2} \sum_{l=1}^{N^2} \sin\left(\frac{\lfloor m \rfloor \lfloor l \rfloor \pi}{N+1}\right) \sin\left(\frac{\lceil m \rceil \lceil l \rceil \pi}{N+1}\right) \\ &\quad \sin\left(\frac{\lfloor n \rfloor \lfloor l \rfloor \pi}{N+1}\right) \sin\left(\frac{\lceil n \rceil \lceil l \rceil \pi}{N+1}\right) / \\ &\quad \left[2 - \cos\left(\frac{i\pi}{N+1}\right) - \cos\left(\frac{j\pi}{N+1}\right) \right] \end{aligned} \quad (\text{E.11})$$

where $\lfloor i \rfloor \triangleq \text{int}((i-1)/N) + 1$ and $\lceil i \rceil \triangleq \text{mod}(i-1, N) + 1$.

E.2 Linear Independence of the Columns of F

In this section the linear independence of the columns of the F matrix is shown. For convenience in defining F , F is partitioned into 4 submatrices,

$$F = [F_1 \mid F_2 \mid F_3 \mid F_4] \quad (\text{E.12})$$

where the F_i matrices are defined, as

$$F_1 = \left[\begin{array}{c|c|c|c} 1A_2 & 1A_3 & \dots & 1A_N \\ \hline 4A_2 & 4A_3 & \dots & 4A_N \end{array} \right] \quad (\text{E.13})$$

$$F_2 = \left[\begin{array}{c|c|c|c} 2A_1 & 2A_{N+1} & \dots & 2A_{N^2-N+1} \\ \hline 3A_1 & 3A_{N+1} & \dots & 3A_{N^2-N+1} \end{array} \right] \quad (\text{E.14})$$

$$F_3 = \left[\begin{array}{c|c|c|c} 1A_N & 1A_{2N} & \dots & 1A_{N^2} \\ \hline 3A_N & 3A_{2N} & \dots & 3A_{N^2} \end{array} \right] \quad (\text{E.15})$$

$$F_4 = \left[\begin{array}{c|c|c|c} 1A_{N^2-N+1} & 1A_{N^2-N+2} & \dots & 1A_{N^2-1} \\ \hline 3A_{N^2-N+1} & 3A_{N^2-N+2} & \dots & 3A_{N^2-1} \end{array} \right] \quad (\text{E.16})$$

in which ${}_jA_i$ is the i^{th} column of the ${}_jA$ matrix,

$${}_1A = \frac{1}{4}GK^{-1} \quad (\text{E.17})$$

$${}_2A = \frac{1}{4}[GK^{-1} + 4I] \quad (\text{E.18})$$

$${}_3A = \frac{1}{4}HK^{-1} \quad (\text{E.19})$$

$${}_4A = \frac{1}{4}[HK^{-1} - 4I]. \quad (\text{E.20})$$

where the $N^2 \times N^2$ matrices G and H are defined as,

$$G \triangleq I \otimes [D^s - I] \quad (\text{E.21})$$

$$H \triangleq [I - D^s] \otimes I \quad (\text{E.22})$$

in which D^s is an $N \times N$ matrix which has a unity sub-diagonal and is zero everywhere else, i.e., the elements $d_{i,j}^s$ of D^s are

$$d_{i,j}^s = \begin{cases} 1, & \text{if } j = i - 1 \\ 0, & \text{else} \end{cases} \quad (\text{E.23})$$

The matrices F_1 and F_4 are $2N^2 \times (N - 1)$ while F_2 and F_3 , are $2N^2 \times N$.

Using the properties of the Kronecker product and the definition of D^s , it can be shown that G is the block Jordan-form matrix,

$$G = \begin{bmatrix} D^s - I & 0 & \dots & 0 \\ 0 & D^s - I & \ddots & \vdots \\ \vdots & \ddots & \ddots & 0 \\ 0 & \dots & 0 & D^s - I \end{bmatrix} \quad (\text{E.24})$$

while H is a block tridiagonal matrix,

$$H = \begin{bmatrix} I & 0 & 0 & \dots & 0 \\ -I & I & 0 & \dots & 0 \\ 0 & -I & I & \ddots & \vdots \\ \vdots & \ddots & \ddots & \ddots & 0 \\ 0 & \dots & 0 & -I & I \end{bmatrix} \quad (\text{E.25})$$

Note that both G and H are full rank and invertible. It can be readily verified that the

matrix T , with elements $t_{i,j}$, where

$$t_{i,j} = \begin{cases} 1, & \text{if } j \leq i \\ 0, & \text{otherwise} \end{cases} \quad (\text{E.26})$$

is the inverse of the matrix $(I - D^s)$, i.e., $(I - D^s)^{-1} = T$; hence,

$$G^{-1} = I \otimes T \quad (\text{E.27})$$

$$H^{-1} = T \otimes I \quad (\text{E.28})$$

Since G and H are invertible, it follows that ${}_1A = GK^{-1}$ and ${}_3A = HK^{-1}$ are full rank with independent columns. From their definition it is readily apparent that the columns of F_3 and F_4 are linearly independent since they are composed of different columns of ${}_1A$ and ${}_3A$. In the following section we show that ${}_2A = (GK^{-1} + 4I)/4$ and ${}_3A = (HK^{-1} - 4I)/4$ are full rank. It then follows that the columns of F_1 and F_2 are linearly independent. Since no F_i matrix shares a column from the same ${}_jA$ matrix with any other F_k matrix, the columns of the F_i matrices are linearly independent.

E.3 Rank of $GK^{-1} + 4I$ and $HK^{-1} - 4I$

We want to show that $GK^{-1} + 4I_{N^2}$ is full rank. Note that,

$$GK^{-1} + 4I_{N^2} = GK^{-1} + 4KK^{-1} = G(I_{N^2} + 4K)K^{-1} \quad (\text{E.29})$$

where I_{N^2} is the $N^2 \times N^2$ identity matrix. Since both G and K^{-1} are full rank, the only question is the rank of $(I_{N^2} + 4K)$. Using the definitions,

$$G = I_N \otimes [D^s - I_N] \quad (\text{E.30})$$

$$K = I_N \otimes Q + Q \otimes I_N \quad (\text{E.31})$$

where I_N is the $N \times N$ identity matrix, we see that

$$\begin{aligned} (I_{N^2} + 4K) &= (I_{N^2} + 4I_N \otimes Q + 4Q \otimes I_N) \\ &= I_N \otimes I_N + 4I_N \otimes Q + 4Q \otimes I_N \\ &= \frac{1}{2}I_N \otimes I_N + 4I_N \otimes Q + 4Q \otimes I_N + \frac{1}{2}I_N \otimes I_N \\ &= \frac{1}{2}I_N \otimes (I_N + 8Q) + \frac{1}{2}(I_N + 8Q) \otimes I_N \\ &= I_N \otimes Q_1 + Q_1 \otimes I_N \\ &\triangleq K_1 \end{aligned} \quad (\text{E.32})$$

where $Q_1 = \frac{1}{2}(I_N + 8Q)$ is an $N \times N$ tridiagonal, symmetric Toeplitz matrix,

$$Q_1 = \frac{1}{2} \begin{bmatrix} 5 & 1 & 0 & \dots & 0 \\ 1 & 5 & 1 & \ddots & \vdots \\ 0 & 1 & 5 & \ddots & 0 \\ \vdots & \ddots & \ddots & \ddots & 1 \\ 0 & \dots & 0 & 1 & 5 \end{bmatrix} \quad (\text{E.33})$$

Q_1 can be readily seen to be full rank and can be diagonalized using the Ψ matrix. Since Q_1 is full rank, it follows that K_1 is full rank and therefore $GK^{-1} + 4I_{N^2}$ is full rank. Using this same procedure it is easy to show that $HK^{-1} - 4I_{N^2}$ is full rank.

Appendix F

Options for the Wind Field Model

In this Appendix, alternatives for the wind field model are considered. In Appendix G, the modelling error for each of these alternatives is evaluated. Sections F.1 through F.5 provide alternatives models for the vorticity and divergence fields. These are applicable for both the normal boundary (NB) and parameterized boundary condition (PBC) models. Section F.6 considers an alternative model for the parameterization of the boundary conditions.

We begin with Eq. (4.68) from Chapter 4, repeated here for completeness,

$$\overline{W} = F\overline{X} + R^c\overline{C} + R^d\overline{D} \quad (\text{F.1})$$

where \overline{W} contains the components of the wind field, \overline{X} contains the pressure field boundary values, and the $2N^2$ elements vectors \overline{C} and \overline{D} contain the lexicographic-ordered vorticity and divergence fields, respectively. R^c and R^d are $2N^2 \times N^2$ matrices.

F.1 Zero Vorticity, Zero Divergence Model

The simplest model for the wind field is obtained when the vorticity and divergence are assumed to be identically zero. In this case, the wind field model in Eq. (F.1) reduces to,

$$\overline{W} = F\overline{X} \quad (\text{F.2})$$

Given \overline{W} , the least-squares estimate of the boundary conditions \overline{X} may be obtained, as

$$\overline{X} = F^\dagger\overline{W} \quad (\text{F.3})$$

where F^\dagger is the generalized inverse of F . Since the system of equations is overdetermined, $F^\dagger = (F^T F)^{-1} F^T$, and, since F is full-rank, the \overline{X} vector will be identifiable (see Chapter 5).

Because mesoscale wind fields tend to have regions with both non-zero vorticity and non-zero divergence, this model is generally unsuitable.

F.2 Constant Vorticity, Constant Divergence Model

A slightly more general model for the vorticity and divergence fields is the case when the vorticity is assumed to a constant c and the divergence is assumed to a constant d . In this case Eq. (F.1) reduces to,

$$\bar{W} = F\bar{X} + c\bar{R}^c + d\bar{R}^d \quad (\text{F.4})$$

where \bar{R}^c and \bar{R}^d are $2N^2$ element vectors with elements \bar{R}_n^c and \bar{R}_n^d which are the sum of the elements $r_{i,j}^c$ and $r_{i,j}^d$ of the R^c and R^d matrices, respectively,

$$\bar{R}_n^c = \sum_{j=1}^{2N^2} r_{n,j}^c \quad (\text{F.5})$$

$$\bar{R}_n^d = \sum_{j=1}^{2N^2} r_{n,j}^d. \quad (\text{F.6})$$

To express the model in a simple form, define a new $4N$ parameter vector \bar{X}_{cd} by augmenting \bar{X} by c and d , i.e.,

$$\bar{X}_{cd} = \begin{bmatrix} \bar{X} \\ c \\ d \end{bmatrix} \quad (\text{F.7})$$

and let the $2N^2 \times 4N$ matrix F_{cd} be the matrix created by column-augmenting the matrix F by \bar{R}^c and \bar{R}^d , i.e.,

$$F_{cd} = \left[F \mid \bar{R}^c \mid \bar{R}^d \right]. \quad (\text{F.8})$$

Then Eq. (F.4) can be written, as

$$\bar{W} = F_{cd}\bar{X}_{cd} \quad (\text{F.9})$$

By construction, \bar{R}^c and \bar{R}^d will be linearly independent and will be linearly independent of the columns of F . It follows that the columns of F_{cd} will be linearly independent so that F_{cd} is full rank; hence, there is a unique relationship between a given \bar{W} and the parameters \bar{X}_{cd} , as required for field-wise identifiability (see Chapter 5). Consequently, the parameters in \bar{X}_{cd} will be identifiable. Given \bar{W} , a least-squares estimate of \bar{X}_{cd} is,

$$\bar{X}_{cd} = F_{cd}^\dagger \bar{W} \quad (\text{F.10})$$

where F_{cd}^\dagger is the generalized inverse of F_{cd} . Since the system of equations is overdetermined, $F_{cd}^\dagger = (F_{cd}^T F_{cd})^{-1} F_{cd}^T$.

F.3 Polynomial Vorticity and Divergence

More general models of the vorticity and divergence fields can be obtained using bivariate polynomials. This is the approach used in Chapter 4. For completeness, it is repeated and expanded here.

The vorticity field $\zeta_{i,j}$ and divergence field $\delta_{i,j}$ may be parameterized as bivariate polynomials, i.e.,

$$\zeta_{i,j} = \sum_{m=0}^{M_c} \sum_{\substack{n=0 \\ m+n \leq M_c}}^{M_c} c_{m,n} i^m j^n \quad (\text{F.11})$$

$$\delta_{i,j} = \sum_{m=0}^{M_d} \sum_{\substack{n=0 \\ m+n \leq M_d}}^{M_d} d_{m,n} i^m j^n \quad (\text{F.12})$$

The number of parameters in each of the vorticity and divergence polynomials is $N_c = (M_c + 1)(M_c + 2)/2$ and $N_d = (M_d + 1)(M_d + 2)/2$, respectively. Using the polynomial parameterization, Eq. (F.1) can then be written, as

$$\bar{W} = F\bar{X} + R^c \sum_{m=0}^{M_c} \sum_{\substack{n=0 \\ m+n \leq M_c}}^{M_c} c_{m,n} Q_{m,n} + R^d \sum_{m=0}^{M_d} \sum_{\substack{n=0 \\ m+n \leq M_d}}^{M_d} d_{m,n} Q_{m,n} \quad (\text{F.13})$$

$$= F\bar{X} + \sum_{m=0}^{M_c} \sum_{\substack{n=0 \\ m+n \leq M_c}}^{M_c} c_{m,n} R^c Q_{m,n} + \sum_{m=0}^{M_d} \sum_{\substack{n=0 \\ m+n \leq M_d}}^{M_d} d_{m,n} R^d Q_{m,n} \quad (\text{F.14})$$

where the k^{th} element ${}_k q_{m,n}$ of the N^2 element vector $Q_{m,n}$ is,

$${}_k q_{m,n} = [k]^m + [k]^n \quad (\text{F.15})$$

in which $[k] \triangleq \text{int}[(k-1)/N] + 1$ and $[k] \triangleq \text{mod}(k-1, N) + 1$. The constant vorticity or divergence case corresponds to $M_c = 0$ or $M_d = 0$, respectively. The case when the vorticity or divergence is assumed to be identically zero will be denoted by $M_c = -1$ or $M_d = -1$, respectively. In Chapter 4 the special case when $M_c = M_d = 1$ is considered.

Equation (F.13) can be written, as

$$\bar{W} = F\bar{X} + R^c \Upsilon^c \bar{X}^c + R^d \Upsilon^d \bar{X}^d \quad (\text{F.16})$$

where \bar{X} contains the pressure field boundary conditions [see Eq. (4.65)], \bar{X}^c and \bar{X}^d contain the $c_{m,n}$ and $d_{m,n}$ parameters, respectively, in row order, and the $N^2 \times N_c$ matrix Υ^c and the $N^2 \times N_d$ matrix Υ^d are constructed from the $Q_{m,n}$ vectors, i.e., the k th column of Υ^c is

$Q_{m,n}$ where $k = m + n(2M_c + 3 - n)/2 + 1$, i.e.,

$$\Upsilon^c = [Q_{0,0} \quad Q_{0,1} \quad Q_{0,2} \quad \cdots \quad Q_{0,M_c} \quad Q_{1,0} \quad Q_{1,1} \quad \cdots \quad Q_{M_c,0}]. \quad (\text{F.17})$$

Similarly, the k th column of Υ^d is $Q_{m,n}$ where $k = m + n(2M_d + 3 - n)/2 + 1$, i.e.,

$$\Upsilon^d = [Q_{0,0} \quad Q_{0,1} \quad Q_{0,2} \quad \cdots \quad Q_{0,M_d} \quad Q_{1,0} \quad Q_{1,1} \quad \cdots \quad Q_{M_d,0}]. \quad (\text{F.18})$$

Note that if $M_c = M_d$ that $\Upsilon^c = \Upsilon^d$. For clarity,

$$\overline{X}^c = \begin{bmatrix} c_{0,0} \\ c_{0,1} \\ c_{0,2} \\ \vdots \\ c_{1,0} \\ c_{1,1} \\ \vdots \\ c_{M_c,0} \end{bmatrix} \quad (\text{F.19})$$

and

$$\overline{X}^d = \begin{bmatrix} d_{0,0} \\ d_{0,1} \\ d_{0,2} \\ \vdots \\ d_{1,0} \\ d_{1,1} \\ \vdots \\ d_{M_d,0} \end{bmatrix}. \quad (\text{F.20})$$

Let \overline{X}^a be defined as the concatenation of \overline{X} , \overline{X}^c , and \overline{X}^d , i.e.,

$$\overline{X}^a = \begin{bmatrix} \overline{X} \\ \overline{X}^c \\ \overline{X}^d \end{bmatrix}. \quad (\text{F.21})$$

Define the $2N^2 \times (4N - 2 + N_c + N_d)$ matrix F^a , as

$$F^a = [F \mid R^c \Upsilon^c \mid R^d \Upsilon^d]. \quad (\text{F.22})$$

Then Eq. (F.16) can be expressed as,

$$\overline{W} = F^a \overline{X}^a. \quad (\text{F.23})$$

F.4 Fourier Series Vorticity and Divergence

In Appendix C, it was shown that for a non-divergent wind field the spectrum of the curl is inversely proportional to the wave number k ; hence, only the first few Fourier series coefficients can be considered to be significant. Based on this consideration, a deterministic model for the vorticity and divergence fields based on a discrete Fourier series representation can be developed using only the first few Fourier series coefficients. The vorticity field $\zeta_{i,j}$ and divergence field $\delta_{i,j}$ are written, as

$$\zeta_{i,j} = \sum_{m=0}^M \sum_{n=0}^M \left[y_{m,n}^c \sin \left(\frac{(mi + nj)\pi}{N} \right) + x_{m,n}^c \cos \left(\frac{(mi + nj)\pi}{N} \right) \right] \quad (\text{F.24})$$

$$\delta_{i,j} = \sum_{m=0}^M \sum_{n=0}^M \left[y_{m,n}^d \sin \left(\frac{(mi + nj)\pi}{N} \right) + x_{m,n}^d \cos \left(\frac{(mi + nj)\pi}{N} \right) \right] \quad (\text{F.25})$$

Eq. (F.1) can then be written, as

$$\begin{aligned} \bar{W} &= F\bar{X} + R^c \sum_{m=0}^M \sum_{n=0}^M \left[x_{m,n}^c Q_{m,n}^s + y_{m,n}^c Q_{m,n}^c \right] \\ &\quad + R^d \sum_{m=0}^M \sum_{n=0}^M \left[x_{m,n}^d Q_{m,n}^s + y_{m,n}^d Q_{m,n}^c \right] \end{aligned} \quad (\text{F.26})$$

where the k^{th} elements ${}_k q_{m,n}^s$ and ${}_k q_{m,n}^c$ of the N^2 element vectors $Q_{m,n}^s$ and $Q_{m,n}^c$ are,

$${}_k q_{m,n}^s = \sin \left(\frac{(m[k] + n[k])\pi}{N} \right) \quad (\text{F.27})$$

$${}_k q_{m,n}^c = \cos \left(\frac{(m[k] + n[k])\pi}{N} \right) \quad (\text{F.28})$$

in which $[k] \triangleq \text{int}[(k-1)/N] + 1$ and $\lceil k \rceil \triangleq \text{mod}(k-1, N) + 1$.

To express the model in a simple form, define a new parameter vector \bar{X}_s by augmenting \bar{X} with the $x_{m,n}^c$, $x_{m,n}^d$, $y_{m,n}^c$ and $y_{m,n}^d$ parameters as before and column-augmenting the matrix F to produce F_s . The F_s matrix will have linearly independent columns (for small M_c and M_d); so it will be of full rank; hence, there is a unique relationship between a given \bar{W} and the parameters \bar{X}_s as required for field-wise identifiability. Consequently, the parameters in \bar{X}_s will be identifiable. Given \bar{W} , a least-squares estimate of \bar{X}_s is,

$$\bar{X}_s = F_s^\dagger \bar{W} \quad (\text{F.29})$$

where F_s^\dagger is the generalized inverse of F_s . Since the system of equations is overdetermined, $F_s^\dagger = (F_s^T F_s)^{-1} F_s^T$.

F.5 Isotropic Vorticity and Divergence

The previous Fourier series representation for the vorticity field did not take into account the (presumed) isotropic nature of the curl. When the curl spectrum is isotropic then $x_{m_1, n_1} = x_{n_2, m_2}$ and $y_{m_1, n_1} = y_{n_2, m_2}$ for all $m_1^2 + n_1^2 = m_2^2 + n_2^2$. Assuming an isotropic curl and an isotropic divergence spectrum, the vorticity and divergence fields can be expressed, as

$$\zeta_{i,j} = x_0^c + \sum_{m=1}^M \left[x_m^c \sin(mk\pi/N) + y_m^c \cos(mk\pi/N) \right] \quad (\text{F.30})$$

$$\delta_{i,j} = x_0^d + \sum_{m=1}^M \left[x_m^d \sin(mk\pi/N) + y_m^d \cos(mk\pi/N) \right] \quad (\text{F.31})$$

where $k = \sqrt{i^2 + j^2}$. Equation (F.1) becomes,

$$\begin{aligned} \bar{W} = F\bar{X} + x_0^c \bar{R}^c + \sum_{m=0}^M \left[x_m^c Q_m^s + y_m^c Q_m^c \right] \\ + x_0^d \bar{R}^d + \sum_{m=0}^M \left[x_m^d Q_m^s + y_m^d Q_m^c \right] \end{aligned} \quad (\text{F.32})$$

where the k^{th} elements ${}_k q_m^s$ and ${}_k q_m^c$ of the N^2 element vectors Q_m^s and Q_m^c are,

$${}_k q_m^s = \sum_{i=1}^N \sum_{j=1}^N r_{k,j+(i-1)N} \sin\left(\frac{m\pi}{N} \sqrt{i^2 + j^2}\right) \quad (\text{F.33})$$

$${}_k q_m^c = \sum_{i=1}^N \sum_{j=1}^N r_{k,j+(i-1)N} \cos\left(\frac{m\pi}{N} \sqrt{i^2 + j^2}\right) \quad (\text{F.34})$$

The \bar{X} vectors are augmented with the x_i parameters and the F matrix with the Q vectors to produce a single equation.

F.6 Parameterization of the Boundary Conditions

Since the pressure field around the region boundary tends to be smooth, the number of unknowns in the wind field model can be reduced by parameterizing the pressure field around the region boundary. This can be done for all of the vorticity and divergence model options discussed above.

Since the boundary is closed, the pressure field around the boundary will be periodic. The boundary conditions for the pressure field for the wind field model are $p(x_0, y_j)$ and $p(x_{N+1}, y_j)$ for $j = 1, \dots, N$ and $p(x_i, y_0)$ and $p(x_i, y_{N+1})$ for $i = 1, \dots, N$. For convenience,

p will be parameterized as a one-dimensional function around the boundary. For the purposes of this dissertation, we will write the pressure field around the boundary as $p(l)$ where l is related to i and j clockwise around the boundary, according to

$$l = \begin{cases} j, & i = 0, 0 \leq j \leq N + 1, \\ i + N + 1, & j = N + 1, 0 < i \leq N + 1, \\ 2N + 2 - j, & i = N + 1, 0 \leq j \leq N + 1, \\ 4N + 4 - i, & j = 0, 0 \leq i < N + 1. \end{cases} \quad (\text{F.35})$$

l runs from 0 to $4(N + 1)$. For notational simplicity, we will write $p(l)$ as p_l .

To formulate Eq. (F.1), when the boundary values are parameterized, the definition of F_1 must be modified slightly to incorporate the boundary value $p_{0,1}$ which was ignored (set to zero). Let F'_1 be the $2N^2 \times N$ rectangular matrix, defined as

$$F'_1 = \left[\begin{array}{c|c|c|c} {}_1A_1 & {}_1A_2 & \dots & {}_1A_N \\ \hline {}_4A_1 & {}_4A_2 & \dots & {}_4A_N \end{array} \right] \quad (\text{F.36})$$

$$(\text{F.37})$$

where ${}_jA_i$ is the i^{th} column of the j^{th} A matrix defined in the main text. Note that

$$F'_1 = \left[\begin{array}{c|c} {}_1A_1 & F_1 \\ \hline {}_4A_1 & \end{array} \right]. \quad (\text{F.38})$$

Since p_l is “smooth” and must be periodic, a low-order Fourier series representation of p_l is appropriate. This was the approach adopted in Chapter 4. An alternate approach is to use Chebychev polynomials. When the boundary conditions are parameterized using Chebychev polynomials, p_l may be written, as

$$p_l = \sum_{k=1}^{M_l} s_k \cos \left[k \arccos \left(\frac{l\pi}{2(N+1)} \right) \right], \quad (\text{F.39})$$

where M_l is the order of the pressure boundary condition model. We have already noted that the DC value of the pressure field is arbitrary and so we can ignore the s_0 term. The number of unknowns is M_l . We can express the elements of \bar{X} in terms of coefficients of the p_l model. Define the vector \bar{Y} , as

$$\bar{Y} = \begin{bmatrix} s_1 \\ s_2 \\ \vdots \\ s_{M_l} \end{bmatrix}. \quad (\text{F.40})$$

The wind field model can be then be written, as

$$\bar{W} = \mathcal{F}'\bar{Y} + R^c C + R^d D \quad (\text{F.41})$$

where \mathcal{F}' is a $2N^2 \times M_l$ rectangular matrix which is created from the F_j matrices. Let $f'_{i,j}$ be the $(i, j)^{th}$ element of \mathcal{F}' and $(F_k)_{i,j}$ be the $(i, j)^{th}$ element of the F_k matrix. Then,

$$\begin{aligned}
f'_{i,j} = & \sum_{k=1}^N (F'_1)_{i,k} \cos\{j \arccos[k/(2N+2)\pi]\} \\
& + \sum_{k=1}^N (F_2)_{i,k} \cos\{j \arccos[(2-k)/(2N+2)\pi]\} \\
& + \sum_{k=1}^N (F_3)_{i,k} \cos\{j \arccos[(1+k)/(2N+2)\pi]\} \\
& + \sum_{k=1}^N (F_4)_{i,k} \cos\{j \arccos[(3-k)/(2N+2)\pi]\} \tag{F.42}
\end{aligned}$$

A procedure similar to the one described in Chapter 4 is used to augment the model parameters of the vorticity C and divergence D fields to the \bar{Y} matrix (details not shown).

Appendix G

Modeling Error for Various Model Options

This Appendix contains modeling error tables for the various wind field model options. To evaluate the modeling error, a least-squares fit of the model parameters to a real wind field was obtained, the resulting “model” wind field was computed from the model parameters, and the RMS difference between the true field and the model field was computed.

To evaluate the modeling error for a wind field model of size N , the wind field was segmented into $N \times N$ regions with $N - 1$ sample overlap in both dimensions. For each region segment, the model parameters were computed using the least-squares approach given in Chapter 4, and the model wind field was computed from the model parameters. The RMS of the error between the true and model fields was computed over all possible regions within the original true wind field. In these tables, the column labeled “Ave” is the average of the region vector error where, for a given region, the region vector error is the square root of the mean-squared magnitude of the vector difference of the fields in that region. The column labeled “RMS” is the square root of the mean-squared magnitude of the vector difference of the fields. The column labeled “Direction” is the RMS of the difference in wind direction in the fields. The column labeled “Speed” is the square root of the mean of the normalized region speed error which, for a given region, is the RMS speed error normalized by the RMS speed of the true wind in that region.

For each model option, the number of unknowns in an $N \times N$ region, N_u , is indicated. The total number of unknowns N_u which must be determined to cover a 24×24 , region using non-overlapping regions is

$$N_u = \left(\frac{24}{N}\right)^2 N_u \quad (\text{G.1})$$

assuming that there is no information sharing between $N \times N$ subregions. When N is not an exact factor of 24 the nearest integer number of unknowns is used and the value of N_t in the tables is tagged with a tilde.

In these tables the designation $M_c = -1$ for the order of the vorticity model is used to indicate that the model has zero vorticity. Similarly, $M_d = -1$ is used to indicate that the

divergence model has zero divergence.

Only a few examples of each model option are given for comparison purposes. The first group of tables (i.e., G.1-G.5) shows the modeling error versus M_d and M_c for various values of N for the NB model which uses normal boundary conditions and polynomial vorticity and divergence fields. The second group of tables (i.e., G.6-G.8) shows the modeling error versus M_d and M_c for various values of N for the normal boundary condition with isotropic Fourier series for the vorticity and divergence fields. The third group of tables (i.e., G.9-G.12) shows the modeling error versus M_d and M_c for various values of N with $M_l = 8$ for the PBC model which uses Fourier series boundary condition parameterization and polynomial vorticity and divergence. The last table (i.e., G.13) shows the modeling error versus M_d and M_c for $N = 8$ and $M_l = 8$ when Chebychev polynomial boundary condition parameterization and polynomial vorticity and divergence is used.

General conclusions drawn from these tables are that the wind field model fits well for small N . The model error increases with N . Model error decreases as M_c and M_d are increased.

The NB model (Tables G.1-G.5) has the lowest model error for a given N and M_c and M_d . The PBC model (Tables G.9-G.12) minimizes the number of unknowns and provides good model performance. Recommendations for which model options to use are provided in Chapter 4.

Appendix H

Simulation of the NSCAT Scatterometer

This Appendix describes the software simulation of the NSCAT system used for generating the simulated σ^o measurements used in this dissertation. The simulation was developed at NASA’s Jet Propulsion Laboratory for the NSCAT Project to perform design tradeoffs and evaluate system performance. Since a description of this simulation is not available in the open literature, this Appendix provides a summary description of the NSCAT instrument measurement simulation model and the overall simulation procedure used to generate simulated σ^o measurements. A description of the instrument design is provided in [68].

H.1 Instrument Measurement Simulation Model

A wind scatterometer does not directly measure σ^o , but instead, measures backscattered power. This measurement is corrupted by noise. A separate measurement of the noise-only power is made and subtracted from the signal+noise measurement to yield a backscatter power “signal” measurement P_r . σ^o is computed from the signal power measurement using the parameters of the radar equation [see Eqs. (A.60) and (A.63)]

$$\sigma^o = CP_r \tag{H.1}$$

where C is a function of the radar wavelength, transmit power, antenna gain, target range, and target area [see Eqs. (A.61) and (A.64)].

In Chapter 2 the measurement noise model for a scatterometer measurement was discussed. This measurement model is based on the noise due to the radar communication noise. In this section, a measurement model is derived which includes the uncertainty in the geometric parameters, i.e., in C , and the uncertainty, or modeling error, in the geophysical model function. This latter error is due to unmodelled effects such as sea surface temperature, surface viscosity, etc., on σ^o . The measurement model given here has been used in generating the simulated NSCAT σ^o measurements.

Let the model σ^o , $\sigma_m^o(k)$, be the value of σ^o computed for the true wind vector (u_t, v_t) using the model function for the k th observation, i.e.,

$$\sigma_m^o(k) = \mathcal{M}\{(u_t, v_t), k\}. \quad (\text{H.2})$$

A commonly used model for the actual value of σ^o , $\sigma^o(k)$, observed by the scatterometer is

$$\sigma^o(k) = \sigma_m^o(k)[1 + K_{pm}(k)\nu_1(k)] \quad (\text{H.3})$$

where $K_{pm}(k)$ is the normalized standard deviation of the error associated with the geophysical model function and $\nu_1(k)$ is a normally-distributed Gaussian random variable. Typically, a value of 17 % is used for $K_{pm}(k)$ with the SASS¹ model function. The true signal power $P_r(k)$ is related to the true σ^o by according to

$$P_r(k) = C(k)\sigma^o(k) \quad (\text{H.4})$$

where $C(k)$ is the true value of C for the k th observation [see Eq. (H.1)]. The measured signal power \widehat{P}_r is corrupted by noise. The measurement noise model is

$$\widehat{P}_r(k) = P_r(k)[1 + K_{pc}(k)\nu_2(k)] \quad (\text{H.5})$$

where $\nu_2(k)$ is a normally-distributed Gaussian random variable and $K_{pc}(k)$ is the normalized standard deviation of the radar communication noise which is a function of the signal-to-noise ratio (SNR) [19, 68, 66], i.e.,

$$K_{pc}^2(k) = \alpha^2(k) + \frac{\beta^2(k)}{\text{SNR}} + \frac{\gamma^2(k)}{(\text{SNR})^2} \quad (\text{H.6})$$

with the SNR defined

$$\text{SNR} \triangleq \frac{P_r}{P_n} \quad (\text{H.7})$$

where P_n is the noise-only power and where the constants $\alpha^2(k)$, $\beta^2(k)$, and $\gamma^2(k)$ depend on the time length T of the measurement, the measurement geometry, and on-board processor design [19, 68]. $\alpha^2(k)$, $\beta^2(k)$, and $\gamma^2(k)$ are inversely proportional to T .

In addition to geophysical model error and communication noise, there are uncertainties in the quantities which go into the computation of C used for computing σ^o from the instrument power measurement [see Eq. (H.1)]. The true value of C may differ from the value $\widehat{C}(k)$ assumed for $C(k)$ due to instrument calibration errors and uncertainties in the spacecraft attitude, position, and velocity. The model used for $\widehat{C}(k)$ is

$$\widehat{C}(k) = C(k)[1 + K_{pr}(k)\nu_3(k)] \quad (\text{H.8})$$

where $K_{pr}(k)$ is the normalized standard deviation of the error associated with the calculation of C and $\nu_3(k)$ is a zero-mean, unit-variance Gaussian random variable. The value of $K_{pr}(k)$

can be computed using the instrument design parameters [68] and can be minimized by proper calibration of the instrument.

The σ^o measurement, $z(k)$, is computed from the power measurement by

$$z(k) = \frac{\widehat{P}_r(k)}{\widehat{C}(k)}. \quad (\text{H.9})$$

Using Eqs. (H.4), (H.5), and (H.9) we have

$$z(k) = \sigma^o(k) \frac{1 + K_{pc}(k)\nu_2(k)}{1 + K_{pr}(k)\nu_3(k)} \quad (\text{H.10})$$

which can be approximated by

$$\begin{aligned} z(k) &\approx \sigma^o(k)[1 + K_{pc}(k)\nu_2(k)][1 - K_{pr}(k)\nu_3(k)] \\ &= \sigma^o(k)[1 + K_{pc}(k)\nu_2(k) - K_{pr}(k)\nu_3(k) \\ &\quad - K_{pr}(k)\nu_3(k)K_{pr}(k)\nu_3(k)] \end{aligned} \quad (\text{H.11})$$

for $K_{pr} \ll 1$. Since $\nu_2(k)$ and $\nu_3(k)$ are independent, it follows from Eq. (H.11) that

$$E[z(k)|\sigma^o(k)] = \sigma^o(k). \quad (\text{H.12})$$

From Eqs. (H.6) and (H.11) we can write,

$$\begin{aligned} E[z^2(k)|\sigma^o(k)] &= \sigma^o(k)[1 + K_{pc}^2(k)][1 + K_{pr}^2(k)] \\ &= [1 + K_{pr}^2(k)] \left\{ [1 + \alpha^2(k)]\sigma^{o2}(k) + \beta^2(k) \frac{P_n}{C(k)} \sigma^o(k) \right. \\ &\quad \left. + \gamma^2(k) \left(\frac{P_n}{C(k)} \right)^2 \right\}. \end{aligned} \quad (\text{H.13})$$

From Eq. (H.3) we see that

$$E[\sigma^o(k)] = \sigma_m^o(k) \quad (\text{H.14})$$

and

$$E[\sigma^{o2}(k)] = [1 + K_{pm}^2(k)]\sigma_m^{o2}(k); \quad (\text{H.15})$$

hence, it follows from Eqs. (H.12) through (H.15) that

$$E[z(k)] = E[E[z(k)|\sigma^o(k)]] = E[\sigma^o(k)] = \sigma_m^o(k) \quad (\text{H.16})$$

which is Eq. (2.12). Using this result and Eqs. (H.12) through (H.15) it follows that

$$\begin{aligned}
E[z^2(k)|\sigma^o(k)] &= \sigma^o(k)[1 + K_{pc}^2(k)][1 + K_{pr}^2(k)] \\
&= [1 + K_{pr}^2(k)] \left\{ [1 + \alpha^2(k)]\sigma^{o2}(k) + \beta^2(k)\frac{P_n}{C(k)}\sigma^o(k) \right. \\
&\quad \left. + \gamma^2(k)\left(\frac{P_n}{C(k)}\right)^2 \right\}. \\
&= [1 + K_{pr}^2(k)] \left\{ [1 + \alpha^2(k)][1 + K_{pm}^2(k)]\sigma_m^{o2}(k) \right. \\
&\quad \left. + \beta^2(k)\frac{P_n}{C(k)}[1 + K_{pm}(k)]\sigma_m^o(k) \right. \\
&\quad \left. + \gamma^2(k)\left(\frac{P_n}{C(k)}\right)^2 \right\}. \tag{H.17}
\end{aligned}$$

The variance of $z(k)$ can be written, as

$$\begin{aligned}
\text{Var}[z(k)] &= E[z^2(k)|\sigma^o(k)] - E^2[z(k)] \\
&= \{[1 + K_{pr}^2(k)][1 + \alpha^2(k)][1 + K_{pm}^2(k)] - 1\}\sigma_m^{o2}(k) \\
&\quad + [1 + K_{pr}^2(k)]\beta^2(k)\frac{P_n}{C(k)}[1 + K_{pm}(k)]\sigma_m^o(k) \\
&\quad + [1 + K_{pr}^2(k)]\gamma^2(k)\left(\frac{P_n}{C(k)}\right)^2 \\
&= \alpha_1^2(k)\sigma_m^{o2}(k) + \beta_1^2(k)\sigma_m^o(k) + \gamma_1^2(k) \tag{H.18}
\end{aligned}$$

[compare Eq. (2.11)] where $\alpha_1^2(k)$, $\beta_1^2(k)$, and $\gamma_1^2(k)$ are defined, as

$$\alpha_1^2(k) = [1 + K_{pr}^2(k)][1 + \alpha^2(k)][1 + K_{pm}^2(k)] - 1 \tag{H.19}$$

$$\beta_1^2(k) = [1 + K_{pr}^2(k)]\beta^2(k)\frac{P_n}{C(k)}[1 + K_{pm}(k)] \tag{H.20}$$

$$\gamma_1^2(k) = [1 + K_{pr}^2(k)]\gamma^2(k)\left(\frac{P_n}{C(k)}\right)^2. \tag{H.21}$$

We note that both $\beta_1^2(k)$ and $\gamma_1^2(k)$ will be inversely proportional to T ; hence, in the limit as $T \rightarrow \infty$, $\beta_1^2(k) = 0$ and $\gamma_1^2(k) = 0$. In the limit as $T \rightarrow \infty$, $\alpha_1^2(k)$ converges to

$$\alpha_1^2(k) = K_{pr}^2(k) + K_{pm}^2(k) + K_{pr}^2(k)K_{pm}^2(k) \tag{H.22}$$

which is a non-zero constant. To reduce the measurement variance to zero as $T \rightarrow 0$ we must also reduce $K_{pr}(k)$ and $K_{pm}(k)$ to zero. To reduce $K_{pr}(k)$ to zero, the time-varying uncertainty in the various instrument and geometric parameters must be eliminated. If we

assume a perfect knowledge of the geophysical model function, $K_{pm}(k)$ will be zero. With these considerations the identifiability results given in Chapter 3 are applicable with this measurement model.

H.2 Simulation Procedure

While the details of the simulation are complex, a brief outline of the procedure for simulating σ^o measurements is outlined below. Details of the computational procedures are contained in [69].

After initialization of the orbit computation, the following procedure is repeated for each antenna beam once every 3.75 seconds. This is the length of time required for the spacecraft subsatellite point to move 25 km along-track. A data loss of 3.75 seconds occurs once every 8 mins when a instrument calibration cycle occurs. For the k antenna beam the procedure for computing the simulated σ^o measurements is:

1. Propagate the orbit to the sample time of the k th antenna beam measurement.
2. Compute the spacecraft position and velocity relative to the Earth.
3. Compute the spacecraft attitude with random variations in the attitude control.
4. For each of the 24 cross-track σ^o cells, do the following:
 - (a) Compute the Doppler frequencies for each of the σ^o cell measurement bandwidths using a simulation of the on-board “binning algorithm”.
 - (b) Compute the antenna pointing vector including random variations due to thermal effects in the antenna.
 - (c) Given the Doppler frequencies, compute the σ^o cell location.
 - (d) Compute needed geometric parameters including incidence angle $\theta(k)$, antenna azimuth angle $\psi(k)$, and the geometric parameters in the radar equation.
 - (e) Compute $C(k)$.
 - (f) Interpolate the true wind field to compute the wind vector at the the center of the σ^o measurement cell.
 - (g) Compute $\sigma_m^o(k)$ from the true wind vector and the antenna pointing direction.
 - (h) Generate Monte Carlo realizations of $\nu_1(k)$, $\nu_2(k)$, and $\nu_3(k)$.
 - (i) Compute $\sigma^o(k)$.
 - (j) Compute P_n , P_r , and SNR.
 - (k) Given the instrument and various calibration parameters, compute $K_{pr}(k)$.
 - (l) Compute the coefficients of $K_{pc}(k)$, $\alpha(k)$, $\beta(k)$, and $\gamma(k)$.
 - (m) Compute $\alpha_1(k)$, $\beta_1(k)$, and $\gamma_1(k)$.
 - (n) Compute $z(k)$.

Appendix I

Initial Value Computation Methods

Proper selection of initial values is critical to the performance of gradient-based optimization in the presence of multiple local minima. In Chapter 6, a simple method for computing initial values for gradient-based optimization of the model-based objective function was given. When large regions of dealiasing errors occur, the initial values computed using this approach may be of poor quality. In this Appendix, two additional methods for computing initial values for the objective function optimization are discussed. The first method is based on an initial objective function optimization using only two dimensions. The second method is based on model extrapolation. Both methods use the parameterized boundary condition (PBC) wind field model.

I.1 The Two-Dimensional Optimization Method

The structure of the model-based objective function can be exploited to generate initial values for optimization. There are numerous schemes which could be developed. The following is a particularly simple scheme based on an initial optimization in two dimensions.

In the PBC model, the two lowest-order coefficients of the boundary condition polynomial dictate the overall wind flow over the region of interest, while the higher-order coefficients and the vorticity and divergence fields impart finer details. Using this fact, we can develop a scheme for selecting initial values based on finding the minima in the objective function with respect to the two lowest-order coefficients in the boundary condition polynomial with all other model parameter unknowns set to zero. Once initial values for these first two coefficients are selected, a gradient search-type algorithm can be used to optimize the objective function with respect to all of the model parameters unknowns using these initial values.

In general, there are a number of local minima of the objective function with respect to the lowest-order coefficients of the objective function; hence, several initial value vectors are produced, each with similar objective function values. Each initial value vector is optimized and the optimized parameter vector resulting in the lowest objective function value is selected as the model parameter estimate. Alternatively, field-wise “dealiasing” can be used.

When all other unknowns are set to zero, the objective function $J(\bar{X})$ with respect to

the two lowest-order coefficients a_0 and a_1 is a two-dimensional function, denoted $J(a_0, a_1)$. This two-dimensional objective function is non-convex; there are a number of local minima, all with similar objective function values. For wind fields with a general wind flow, the lowest-order coefficients seem to account for most of the multiple minima behaviour of the objective function. These local minima of the two-dimensional objective function can be readily located using a ridge search. This may be expedited by expressing the position vector $(a_0, a_1)^T$ in polar form as (r, θ) , i.e., by defining a line in (a_0, a_1) space, radiating from the origin at $(a_0 = 0, a_1 = 0)$ with an angle θ with respect to the a_0 axis. Along this radial line the objective function is generally convex with a monotonically increasing derivative and has a single local minimum. Along this radial line, this minimum can be readily found using a simple gradient-type algorithm. By varying the value of θ and choosing the radial distance r which minimizes the objective function along the radial, a one-dimensional function $\mathcal{J}(\theta)$ is generated. The local minima of $\mathcal{J}(\theta)$ are the local minima of $J(a_0, a_1)$.

From empirical observations, the local behavior of the objective function $J(\bar{X})$ near a local minima of $J(a_0, a_1)$ is generally convex; thus, a local minimum of $J(\bar{X})$ can be found using a gradient-based search starting with an initial value corresponding to the location of the local minimum of $J(a_0, a_1)$. Each of the local minima of $J(a_0, a_1)$ are used as initial values to optimize $J(\bar{X})$. Choosing the value of \bar{X} which gives the lowest value of the objective function gives the global minimum.

This approach reasonably well for wind fields in which there is a general trend in wind direction over the region. However, when the wind field changes significantly over the region (e.g., at a col point or a cyclone center), $J(\bar{X})$ may not be convex in the region of the local minima of $J(a_0, a_1)$; there may be several local minima of $J(\bar{X})$ with respect to the other unknowns (e.g., the vorticity and divergence coefficients) given the (a_0, a_1) which locally minimize $J(a_0, a_1)$. In this event, a more sophisticated version of the initial ridge search which uses multiple dimensions must be used to locate these multiple minima.

I.2 Model Extrapolation

From the results presented in Chapter 7 we can observe that initial values computed from dealiased point-wise wind estimates are generally of good quality if the wind speed is sufficiently high. When a region contains an area of low wind speed, dealiasing errors may result in poor-quality initial values. Adjacent regions, however, are fine. With this in mind, the following question arises: once we have determined the model parameters for a given region, can we use this information to estimate the model parameters of an adjacent or overlapping region? While there are a number of ways to address this question, we will consider a particular technique which we have termed model extrapolation. In this approach, the model parameters determined for a given $N \times N$ region are extrapolated to an overlapping region where the overlap is $N - 1$ points in one dimension. The extrapolated model parameter vector can then be used as an initial value for optimization of the model-based objective function for the new region.

I.2.1 Preliminaries

Before proceeding, we need to introduce some additional notation to simplify later development.

Let the elements $b_{i,j}^{ru}$ of the $N \times N$ matrix B^{ru} be defined, as

$$b_{i,j}^{ru} = \begin{cases} p_{i,N+1} & \text{if } 1 \leq i \leq N \text{ and } j = N \\ 0 & \text{otherwise.} \end{cases} \quad (\text{I.1})$$

For clarity,

$$B^{ru} = \begin{bmatrix} 0 & \dots & 0 & p_{1,N+1} \\ \vdots & \ddots & \vdots & \vdots \\ 0 & \dots & 0 & p_{N,N+1} \end{bmatrix}. \quad (\text{I.2})$$

Let \bar{B}^{ru} be the lexicographic-ordered vector corresponding to B^{ru} .

In the PBC model, the pressure field boundary conditions in the vector \bar{X} are parameterized using an M_l -order polynomial [see Eq. (4.97)] using the M_l element vector \bar{Y} contain the coefficients of the boundary polynomial [see Eq. (4.99)]. Define the $N^2 \times M_l$ matrix Υ such that,

$$\bar{B} = \Upsilon \bar{Y}; \quad (\text{I.3})$$

define the $N^2 \times M_l$ matrix Υ^u such that,

$$\bar{B}^u = \Upsilon^u \bar{Y}; \quad (\text{I.4})$$

and define the $N^2 \times M_l$ matrix Υ^{ru} such that,

$$\bar{B}^{ru} = \Upsilon^{ru} \bar{Y}. \quad (\text{I.5})$$

General expressions for Υ , Υ^u , and Υ^{ru} are complicated and so are not given here.

I.2.2 Model Parameter Vector Extrapolation

Consider an $N \times N$ region \mathcal{L}_1 which overlaps a given $N \times N$ region \mathcal{L} by $N - 1$ points in the j index (along-track) and is aligned in the i index (cross-track). This corresponds to a region shifted just one sample in the j index (see Fig. I.1). We will consider both $+1$ or -1 shifts. Essentially, we will be extrapolating the wind field along one edge just outside of the region \mathcal{L} from the wind field within the region. While this approach can be extended for the normal boundary (NB) model, the development will be given for the parameterized boundary (PBC) model.

The boundary conditions are the pressure field along the outside edge of the region \mathcal{L} boundary (see Fig. A.1). The vector \bar{B}^u contains the values of the pressure field at ($j = 0, i = 1, \dots, N$). If we examine the region \mathcal{L}_1 which is one sample in the $-j$ direction (see Fig. I.1), we find that the boundary conditions in \bar{B}^u contain the values of the pressure

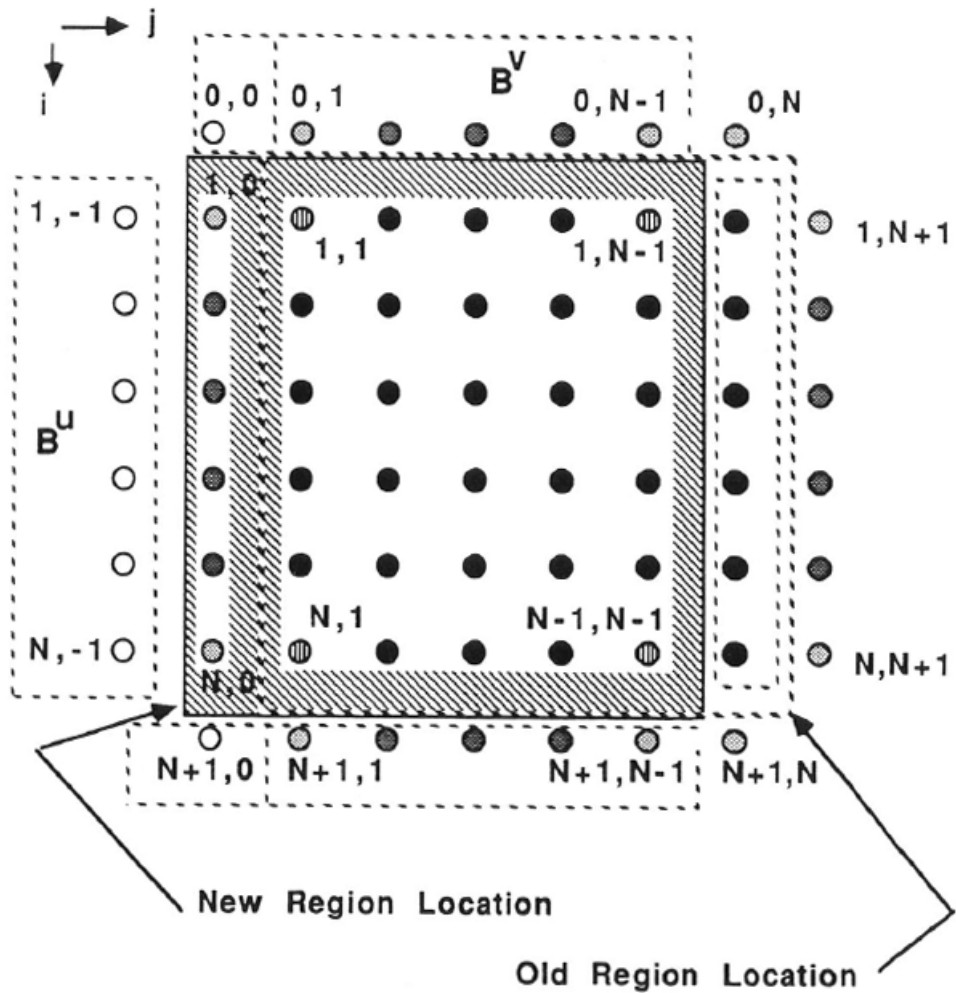


Figure I.1: An illustration showing two $N \times N$ regions with $N-1$ overlap in the $-j$ direction. Note that the old B^u boundary conditions are now part of the pressure field in the region of interest. New boundary conditions needed are indicated with open circles (see text). Compare with Fig. 4.1

field at the new location \mathcal{L}_1 . Further, the pressure field in \mathcal{L} at $(i = N, j = 1, \dots, N)$ are the boundary conditions at the new location \mathcal{L}_1 included in the vector \bar{B}^r for \mathcal{L}_1 . The only new boundary conditions needed are at $(i = 0, j = 0)$, $(i = 0, j = N + 1)$, and $(i = -1, j = 1, \dots, N)$. These we can compute from the known pressure field values at the old location and the extrapolated the vorticity and divergence fields at $(i = 0, j = 1, \dots, N)$.

Let us start by assuming that we have the model parameter vector \bar{X} at the starting region \mathcal{L} . Using the definition of \bar{X} we can compute $\bar{B} = \bar{B}^u + \bar{B}^v + \bar{B}^r$, \bar{C} , and \bar{D} . The pressure field is computed using Eq. (4.33) (repeated here for clarity of presentation),

$$\bar{P} = \frac{1}{4}K^{-1}[\bar{B} + \bar{C}]. \quad (\text{I.6})$$

Quantities for region \mathcal{L}_1 (the new location) will be identified by an underline while no underline indicates region \mathcal{L} (the old location). The pressure field at the new location, \underline{P} , can be appropriately computed from B^u and P , i.e.,

$$\underline{P} = PT^T + B^u \quad (\text{I.7})$$

where the $N \times N$ matrix T with elements $t_{i,j}$ is defined in Eq. (4.48), (repeated here for convenience),

$$t_{i,j} = \begin{cases} 1, & \text{if } j \leq i \\ 0, & \text{otherwise.} \end{cases} \quad (\text{I.8})$$

Using lexicographic vectors and matrix notation, Eq. (I.7) can be written, as

$$\underline{\bar{P}} = (I \otimes T)\bar{P} + \bar{B}^u \quad (\text{I.9})$$

Note that, $I \otimes T = G + I_{N^2}$.

The vorticity field at the new location \mathcal{L}_1 , $\underline{\bar{C}}$, is computed by extrapolating the vorticity bivariate polynomial. Our model for the vorticity field $\zeta_{i,j}$ may be expressed as

$$\zeta_{i,j} = \sum_{m=0}^{M_c} \sum_{\substack{n=0 \\ m+n \leq M_c}}^{M_c} c_{m,n} i^m j^n. \quad (\text{I.10})$$

The number of parameters in the vorticity model is $N_c = (M_c + 1)(M_c + 2)/2$ and the number of parameters in the divergence model is $N_d = (M_d + 1)(M_d + 2)/2$. The model parameter vector has dimension $N_p = M_l + N_c + N_d$ for the PBC model.

Table I.1: Extrapolated vorticity coefficients for region \mathcal{L}_1 in terms of the vorticity coefficients for region \mathcal{L}

n	$\forall m$	
	$(j-1)$ case	$(j+1)$ case
0	$c_{m,0} - c_{m,1} + c_{m,2} - c_{m,3} + c_{m,4}$	$c_{m,0} + c_{m,1} + c_{m,2} + c_{m,3} + c_{m,4}$
1	$c_{m,1} - 2c_{m,2} + 3c_{m,3} - 4c_{m,4}$	$c_{m,1} + 2c_{m,2} + 3c_{m,3} + 4c_{m,4}$
2	$c_{m,2} - 3c_{m,3} + 6c_{m,4}$	$c_{m,2} + 3c_{m,3} + 6c_{m,4}$
3	$c_{m,3} - 4c_{m,4}$	$c_{m,3} + 4c_{m,4}$
4	$c_{m,4}$	$c_{m,4}$

The vorticity field $\underline{\zeta}_{i,j}$ at the new location will be

$$\underline{\zeta}_{i,j} = \sum_{m=0}^{M_c} \sum_{\substack{n=0 \\ m+n \leq M_c}}^{M_c} c_{m,n} i^m (j-1)^n \quad (\text{I.11})$$

$$= \sum_{m=0}^{M_c} \sum_{\substack{n=0 \\ m+n \leq M_c}}^{M_c} \underline{c}_{m,n} i^m j^n \quad (\text{I.12})$$

Equating powers of j , $\underline{c}_{m,n}$ can be computed in terms of the coefficients $c_{m,n}$. Table I.1 summaries the results for a given value of m . Results for both $j-1$ and $j+1$ are shown.

To obtain a matrix equation we note that the vorticity field \overline{C} can be written, as

$$\overline{C} = \Upsilon^c \overline{X}^c \quad (\text{I.13})$$

where Υ^c and \overline{X}^c are defined in Eq. (F.17) and Eq. (F.19), respectively (\overline{X}^c contains the lexicographic-order vorticity field parameters $c_{m,n}$). The shifted and extrapolated vorticity field, $\underline{\overline{C}}$, can be written, as

$$\underline{\overline{C}} = \Upsilon^c \mathcal{T}_{-1}^c \overline{X}^c \quad (\text{I.14})$$

where the $N_c \times N_c$ matrix \mathcal{T}_{-1}^c contains the transformation of parameter values indicated above. Due to the complexity of a general definition of \mathcal{T}_{-1}^c , we give numerical examples of \mathcal{T}_{-1}^c for the range of M_c values of primary interest ($M_c \leq 4$). For $M_c = 0$,

$$\mathcal{T}_{-1}^c = [1]. \quad (\text{I.15})$$

For $M_c = 1$,

$$\mathcal{T}_{-1}^c = \begin{bmatrix} 1 & 0 & -1 \\ 0 & 1 & 0 \\ 0 & 0 & 1 \end{bmatrix}. \quad (\text{I.16})$$

For $M_c = 2$,

$$\mathcal{T}_{-1}^c = \begin{bmatrix} 1 & 0 & 0 & -1 & 0 & 1 \\ 0 & 1 & 0 & 0 & -1 & 0 \\ 0 & 0 & 1 & 0 & 0 & 0 \\ 0 & 0 & 0 & 1 & 0 & -2 \\ 0 & 0 & 0 & 0 & 1 & 0 \\ 0 & 0 & 0 & 0 & 0 & 1 \end{bmatrix}. \quad (\text{I.17})$$

For $M_c = 3$,

$$\mathcal{T}_{-1}^c = \begin{bmatrix} 1 & 0 & 0 & 0 & -1 & 0 & 0 & 1 & 0 & -1 \\ 0 & 1 & 0 & 0 & 0 & -1 & 0 & 0 & 1 & 0 \\ 0 & 0 & 1 & 0 & 0 & 0 & -1 & 0 & 0 & 0 \\ 0 & 0 & 0 & 1 & 0 & 0 & 0 & 0 & 0 & 0 \\ 0 & 0 & 0 & 0 & 1 & 0 & 0 & -2 & 0 & 3 \\ 0 & 0 & 0 & 0 & 0 & 1 & 0 & 0 & -2 & 0 \\ 0 & 0 & 0 & 0 & 0 & 0 & 1 & 0 & 0 & 0 \\ 0 & 0 & 0 & 0 & 0 & 0 & 0 & 1 & 0 & -3 \\ 0 & 0 & 0 & 0 & 0 & 0 & 0 & 0 & 1 & 0 \\ 0 & 0 & 0 & 0 & 0 & 0 & 0 & 0 & 0 & 1 \end{bmatrix}. \quad (\text{I.18})$$

For $M_c = 4$,

$$\mathcal{T}_{-1}^c = \begin{bmatrix} 1 & 0 & 0 & 0 & 0 & -1 & 0 & 0 & 0 & 1 & 0 & 0 & -1 & 0 & 1 \\ 0 & 1 & 0 & 0 & 0 & 0 & -1 & 0 & 0 & 0 & 1 & 0 & 0 & -1 & 0 \\ 0 & 0 & 1 & 0 & 0 & 0 & 0 & -1 & 0 & 0 & 0 & 1 & 0 & 0 & 0 \\ 0 & 0 & 0 & 1 & 0 & 0 & 0 & 0 & -1 & 0 & 0 & 0 & 0 & 0 & 0 \\ 0 & 0 & 0 & 0 & 1 & 0 & 0 & 0 & 0 & 0 & 0 & 0 & 0 & 0 & 0 \\ 0 & 0 & 0 & 0 & 0 & 1 & 0 & 0 & 0 & -2 & 0 & 0 & 3 & 0 & -4 \\ 0 & 0 & 0 & 0 & 0 & 0 & 1 & 0 & 0 & 0 & -2 & 0 & 0 & 3 & 0 \\ 0 & 0 & 0 & 0 & 0 & 0 & 0 & 1 & 0 & 0 & 0 & -2 & 0 & 0 & 0 \\ 0 & 0 & 0 & 0 & 0 & 0 & 0 & 0 & 1 & 0 & 0 & 0 & 0 & 0 & 0 \\ 0 & 0 & 0 & 0 & 0 & 0 & 0 & 0 & 0 & 1 & 0 & 0 & -3 & 0 & 6 \\ 0 & 0 & 0 & 0 & 0 & 0 & 0 & 0 & 0 & 0 & 1 & 0 & 0 & -3 & 0 \\ 0 & 0 & 0 & 0 & 0 & 0 & 0 & 0 & 0 & 0 & 0 & 1 & 0 & 0 & 0 \\ 0 & 0 & 0 & 0 & 0 & 0 & 0 & 0 & 0 & 0 & 0 & 0 & 1 & 0 & -4 \\ 0 & 0 & 0 & 0 & 0 & 0 & 0 & 0 & 0 & 0 & 0 & 0 & 0 & 1 & 0 \\ 0 & 0 & 0 & 0 & 0 & 0 & 0 & 0 & 0 & 0 & 0 & 0 & 0 & 0 & 1 \end{bmatrix}. \quad (\text{I.19})$$

For shifts in the positive j direction, the signs of all the negative values in \mathcal{T}_{-1}^c are changed

to positive. For example, \mathcal{T}_{+1}^c , for $M_c = 3$ is,

$$\mathcal{T}_{+1}^c = \begin{bmatrix} 1 & 0 & 0 & 0 & 1 & 0 & 0 & 1 & 0 & 1 \\ 0 & 1 & 0 & 0 & 0 & 1 & 0 & 0 & 1 & 0 \\ 0 & 0 & 1 & 0 & 0 & 0 & 1 & 0 & 0 & 0 \\ 0 & 0 & 0 & 1 & 0 & 0 & 0 & 0 & 0 & 0 \\ 0 & 0 & 0 & 0 & 1 & 0 & 0 & 2 & 0 & 3 \\ 0 & 0 & 0 & 0 & 0 & 1 & 0 & 0 & 2 & 0 \\ 0 & 0 & 0 & 0 & 0 & 0 & 1 & 0 & 0 & 0 \\ 0 & 0 & 0 & 0 & 0 & 0 & 0 & 1 & 0 & 3 \\ 0 & 0 & 0 & 0 & 0 & 0 & 0 & 0 & 1 & 0 \\ 0 & 0 & 0 & 0 & 0 & 0 & 0 & 0 & 0 & 1 \end{bmatrix}. \quad (\text{I.20})$$

The new vorticity field parameters $\underline{c}_{m,n}$ in \overline{X}^c can be expressed in terms of the old vorticity field parameters $c_{m,n}$ in \overline{X}^c , as

$$\underline{\overline{X}}^c = \mathcal{T}_{-1}^c \overline{X}^c. \quad (\text{I.21})$$

Similarly, the new divergence field parameters $\underline{d}_{m,n}$ in \overline{X}^d can be expressed in terms of the old divergence field parameters $d_{m,n}$ in \overline{X}^d , as

$$\underline{\overline{X}}^d = \mathcal{T}_{-1}^d \overline{X}^d. \quad (\text{I.22})$$

Having obtained the vorticity field \overline{C} at the new location, we can compute the new boundary conditions. Note that we will compute all of the boundary conditions simultaneously from the new pressure field and extrapolated vorticity field. The new boundary condition vector \overline{B} is,

$$\begin{aligned} \overline{B} &= 4K\overline{P} - \overline{C} \\ &= 4K[(I \otimes T)\overline{P} + \overline{B}^u] - \overline{C} \\ &= K[(I \otimes T)K^{-1}(\overline{B} + \overline{C}) + 4\overline{B}^u] - \overline{C} \end{aligned} \quad (\text{I.23})$$

Let the $N^2 \times N^2$ matrix \mathcal{K}_{-1} be defined, as

$$\mathcal{K}_{-1} \triangleq K(I \otimes T)K^{-1}. \quad (\text{I.24})$$

The boundary condition vector \overline{B} is,

$$\overline{B} = \Upsilon \overline{Y}, \quad (\text{I.25})$$

while the boundary condition vector \overline{B}^u is, the $N^2 \times M_l$ matrix Υ^u for which

$$\overline{B}^u = \Upsilon^u \overline{Y}. \quad (\text{I.26})$$

Note that a least-squares estimate of \bar{Y} given \bar{B} is,

$$\bar{Y} = \Upsilon^\dagger \bar{B} = (\Upsilon^T \Upsilon)^{-1} \Upsilon^T \bar{B} \quad (\text{I.27})$$

where Υ^\dagger is the pseudo-inverse of Υ . Then Eq. (I.23) can be written, as

$$\begin{aligned} \underline{\bar{B}} &= \mathcal{K}_{-1}(\bar{B} + \bar{C}) + 4K\bar{B}^u - \bar{C} \\ &= \mathcal{K}_{-1}(\Upsilon\bar{Y} + \Upsilon^c\bar{X}^c) + 4K\Upsilon^u\bar{Y} - \Upsilon^c\mathcal{T}_{-1}^c\bar{X}^c \\ &= \mathcal{K}_{-1}(\Upsilon + 4K\Upsilon^u)\bar{Y} + (\mathcal{K}_{-1}\Upsilon^c - \Upsilon^c\mathcal{T}_{-1}^c)\bar{X}^c. \end{aligned} \quad (\text{I.28})$$

The least-squares estimate of the shifted boundary parameters $\underline{\bar{Y}}$ is then,

$$\begin{aligned} \underline{\bar{Y}} &= \Upsilon^\dagger \underline{\bar{B}} \\ &= \Upsilon^\dagger \left\{ \mathcal{K}_{-1}(\Upsilon + 4K\Upsilon^u)\bar{Y} + (\mathcal{K}_{-1}\Upsilon^c - \Upsilon^c\mathcal{T}_{-1}^c)\bar{X}^c \right\}. \end{aligned} \quad (\text{I.29})$$

Defining $\underline{\bar{X}}^b$ as the concatenation of \bar{Y} , \bar{X}^c , and \bar{X}^d , i.e.,

$$\underline{\bar{X}}^b = \begin{bmatrix} \bar{Y} \\ \bar{X}^c \\ \bar{X}^d \end{bmatrix}, \quad (\text{I.30})$$

the new model parameter vector $\underline{\bar{X}}^b$ can be computed from the old parameter vector \bar{X}^b , as

$$\underline{\bar{X}}^b = M_{-1} \bar{X}^b \quad (\text{I.31})$$

where the $N_p \times N_p$ matrix M_{-1} can be partitioned as,

$$M_{-1} = \left[\begin{array}{c|c|c} M_{-1}^{bb} & M_{-1}^{bc} & 0 \\ \hline 0 & M_{-1}^{cc} & 0 \\ \hline 0 & 0 & M_{-1}^{dd} \end{array} \right] \quad (\text{I.32})$$

where each of the partitions of M_{-1} are defined as follows: the $M_l \times M_l$ matrix M_{-1}^{bb} is,

$$M_{-1}^{bb} = \Upsilon^\dagger (\mathcal{K}_{-1}\Upsilon + 4K\Upsilon^u); \quad (\text{I.33})$$

the $M_l \times N_c$ matrix M_{-1}^{bc} is,

$$M_{-1}^{bc} = \Upsilon^\dagger (\mathcal{K}_{-1}\Upsilon^c - \Upsilon^c\mathcal{T}_{-1}^c); \quad (\text{I.34})$$

the $N_c \times N_c$ matrix M_{-1}^{cc} is,

$$M_{-1}^{cc} = \mathcal{T}_{-1}^c; \quad (\text{I.35})$$

and the $N_d \times N_d$ matrix M_{-1}^{dd} is,

$$M_{-1}^{dd} = \mathcal{T}_{-1}^d. \quad (\text{I.36})$$

The result is the model parameter vector extrapolated to the new region. This can be used to compute an initial value, which can be updated using the pointwise results for wind field estimation.

These results can be extended to motion in the $+j$ direction. For $+j$ movement, the boundary values which become part of the pressure field are at $(j = N + 1, i = 1, \dots, N)$ which are contained as part of the \bar{B}^r vector, \bar{B}^{ru} . The derivation of the matrix to extrapolate the model parameter vector to the new location in the $+j$ direction is similar to the derivation for the $-j$ direction. The pressure field at the new location, \underline{P} , can be appropriately computed from B^{ru} and P , i.e.,

$$\underline{P} = PT + B^{ru} \quad (\text{I.37})$$

(The difference between Eqs. (I.7) and (I.37) is the transpose on the T matrix.) Using lexicographic vectors and matrix notation, Eq. (I.37) can be written, as

$$\underline{P} = (I \otimes T^T)\bar{P} + \bar{B}^u \quad (\text{I.38})$$

Note that, $I \otimes T^T = (G - I_{N^2})^T$. The shifted and extrapolated vorticity field \bar{C} is

$$\bar{C} = \Upsilon^c \mathcal{T}_{+1}^c \bar{X}^c \quad (\text{I.39})$$

The new boundary condition vector \bar{B} can be written, as

$$\begin{aligned} \bar{B} &= 4K\underline{P} - \bar{C} \\ &= 4K[(I \otimes T^T)\bar{P} + \bar{B}^{ru}] - \bar{C} \\ &= K[(I \otimes T^T)K^{-1}(\bar{B} + \bar{C}) + 4\bar{B}^{ru}] - \bar{C} \end{aligned} \quad (\text{I.40})$$

Let the $N^2 \times N^2$ matrix \mathcal{K}_{+1} be defined, as

$$\mathcal{K}_{+1} \triangleq K(I \otimes T^T)K^{-1}. \quad (\text{I.41})$$

Noting that

$$\bar{B}^{ru} = \Upsilon^{ru}\bar{Y}, \quad (\text{I.42})$$

a least-squares estimate of \bar{Y} given \bar{B} is,

$$\bar{Y} = \Upsilon^\dagger \bar{B} = (\Upsilon^T \Upsilon)^{-1} \Upsilon^T \bar{B} \quad (\text{I.43})$$

where Υ^\dagger is the pseudo-inverse of Υ . Then Eq. (I.40) can be written, as

$$\begin{aligned}\underline{\overline{B}} &= \mathcal{K}_{+1}(\overline{B} + \overline{C}) + 4K\overline{B}^{ru} - \overline{C} \\ &= \mathcal{K}_{+1}(\Upsilon\overline{Y} + \Upsilon^c\overline{X}^c) + 4K\Upsilon^{ru}\overline{Y} - \Upsilon^c\mathcal{T}_{+1}^c\overline{X}^c \\ &= \mathcal{K}_{+1}(\Upsilon + 4K\Upsilon^{ru})\overline{Y} + (\mathcal{K}_{+1}\Upsilon^c - \Upsilon^c\mathcal{T}_{+1}^c)\overline{X}^c.\end{aligned}\quad (\text{I.44})$$

The least-squares estimate of the shifted boundary parameters $\underline{\overline{Y}}$ is then,

$$\begin{aligned}\underline{\overline{Y}} &= \Upsilon^\dagger \underline{\overline{B}} \\ &= \Upsilon^\dagger \left\{ \mathcal{K}_{+1}(\Upsilon + 4K\Upsilon^{ru})\overline{Y} + (\mathcal{K}_{+1}\Upsilon^c - \Upsilon^c\mathcal{T}_{+1}^c)\overline{X}^c \right\}.\end{aligned}\quad (\text{I.45})$$

Then the new model parameter vector $\underline{\overline{X}}^b$ can be computed from the old parameter vector \overline{X}^b , as

$$\underline{\overline{X}}^b = M_{+1}\overline{X}^b \quad (\text{I.46})$$

where the $N_p \times N_p$ matrix M_{+1} can be partitioned as,

$$M_{+1} = \left[\begin{array}{c|c|c} M_{+1}^{bb} & M_{+1}^{bc} & 0 \\ \hline 0 & M_{+1}^{cc} & 0 \\ \hline 0 & 0 & M_{+1}^{dd} \end{array} \right] \quad (\text{I.47})$$

where each of the partions of M_{+1} are defined as follows: the $M_l \times M_l$ matrix M_{+1}^{bb} is,

$$M_{+1}^{bb} = \Upsilon^\dagger(\mathcal{K}\Upsilon + 4K\Upsilon^{ru}); \quad (\text{I.48})$$

the $M_l \times N_c$ matrix M_{+1}^{bc} is,

$$M_{+1}^{bc} = \Upsilon^\dagger(\mathcal{K}\Upsilon^c - \Upsilon^c\mathcal{T}_{+1}^c); \quad (\text{I.49})$$

the $N_c \times N_c$ matrix M_{+1}^{cc} is,

$$M_{+1}^{cc} = \mathcal{T}_{+1}^c; \quad (\text{I.50})$$

and the $N_d \times N_d$ matrix M_{+1}^{dd} is,

$$M_{+1}^{dd} = \mathcal{T}_{+1}^d. \quad (\text{I.51})$$

The result is the model parameter vector extrapolated to the new region in the positive j direction.

I.2.3 Discussion

The matrix M_{-1} (or M_{+1}) gives us a very simple way of ‘‘predicting’’ (by extrapolation) what the model parameter vector for an $N - 1$ overlapped region (in the $-j$ or $+j$ direction) will be from the model parameters of a given region. Using the point-wise wind estimation and dealiasing procedure described in Chapter 6, we can first select a region which has a high wind speed using the average wind speeds from the point-wise ambiguity sets. For high

wind speed regions, the dealiased wind fields provide good initial values. Given an initial wind field, we compute the initial model parameters and optimize the field-wise objective function. Using the model extrapolation technique described here we can use M_{-1} (M_{+1}) to predict the model parameters for an adjoining region containing a large area of low wind speeds. This approach can give better initial values than the point-wise dealiasing approach.

As with any extrapolation, one must apply the model extrapolation approach with great care. This is especially true in regions where the wind field model does not fit the underlying wind field well. Improved performance for the model extrapolation approach can be obtained by first computing the extrapolated model parameter vector, computing the resulting wind field, and then, for each sample point, selecting the ambiguity from the point-wise wind estimate set which is closest to the predicted wind field. The initial value is then computed from this closest ambiguity field. The model vector is then optimized and the process repeated with the region sliding along the measurement swath to cover the low wind speed area.